BEILSTEIN JOURNAL OF NANOTECHNOLOGY

Vapor-based polymers: from films to nanostructures

Edited by Meike Koenig and Joerg Lahann

Imprint

Beilstein Journal of Nanotechnology
www.bjnano.org
ISSN 2190-4286
Email: journals-support@beilstein-institut.de

The *Beilstein Journal of Nanotechnology* is published by the Beilstein-Institut zur Förderung der Chemischen Wissenschaften.

Beilstein-Institut zur Förderung der Chemischen Wissenschaften
Trakehner Straße 7–9
60487 Frankfurt am Main
Germany
www.beilstein-institut.de

BEILSTEIN JOURNAL OF NANOTECHNOLOGY

Vapor-based polymers: from films to nanostructures

Meike Koenig*[1] and Joerg Lahann*[1,2]

Editorial

Open Access

Address:
[1]Karlsruhe Institute of Technology (KIT), Institute of Functional Interfaces (IFG), Hermann-von-Helmholtz-Platz 1, 76344 Eggenstein-Leopoldshafen, Germany, and [2]Biointerfaces Institute, University of Michigan (UM), 2800 Plymouth Rd., Ann Arbor, MI 48109, USA

Email:
Meike Koenig* - meike.koenig@kit.edu; Joerg Lahann* - lahann@umich.edu

* Corresponding author

Keywords:
nanostructures; vapor-based polymers

Beilstein J. Nanotechnol. **2017,** *8,* 2219–2220.
doi:10.3762/bjnano.8.221

Received: 19 September 2017
Accepted: 22 September 2017
Published: 24 October 2017

This article is part of the Thematic Series "Vapor-based polymers: from films to nanostructures".

Editor-in-Chief: T. Schimmel

While the traditional and popular realm of polymer synthesis is the liquid phase, the use of vapor-based techniques to deposit polymers has been met with increasing interest over the past decades. The perhaps most relevant example, the deposition of poly(*p*-xylylenes) via the Gorham process, has been of industrial use in the fabrication of isolating or protective coatings in electronics and biomaterials for many years [1,2]. More recently, vapor deposition polymerization has been extended to a broad variety of reactive polymers [3], additionally using techniques such as plasma-, initiated-, or oxidative chemical vapor deposition polymerization [4,5]. The reason for the ongoing interest in this research field is that, analogue to the deposition of inorganic coatings by chemical vapor deposition, the deposition of polymer coatings from the vapor phase has many advantages over traditional, wet chemistry methods. These advantages result in a variety of benefits for vapor-based polymer coatings and their broad utility.

Due to the absence of solvents, dewetting effects are less pronounced, which together with the fact that small monomers instead of larger polymers are used, enable the highly conformal character of vapor-based coatings. The review article by Moni et al., within this Thematic Series, highlights this feature and discusses how to assess it, as well as its applications [6]. In their research article, Cheng and Gupta present another exemplary application of vapor-borne coatings. Here, a 3D-printed device can be equipped with the desired functionality on its surface, while the bulk material can be chosen independently, according to the requirements of the printing process and the desired mechanical properties [7]. The conformal character of vapor-based coatings can furthermore be used to create nanostructures. Balkan et al. report the formation of coaxial nanotubes by the consecutive deposition of polyaniline and poly(hydroxyethyl methacrylate) on a template with mesoscopic pores [8]. The dissolution of the template results in the desired nanostructures. This combination of a conductive polymer with a hydrogel in a single nanostructure shows potential for the use in humidity sensors.

Without the need for additives or solvents, a high purity of the resulting film is ensured, which is of paramount importance in the area of electronic applications. In this context, the versatility of poly(chloro-*p*-xylylene) in the application of flexible organic electronics is presented in a review article by Marszalek

et al. [9]. The absence of small molecule compounds or solvents in CVD films mitigates the risk of potential leakage of hazardous residues from the coating material, which, in turn, often results in superior biocompatibility [10]. This, together with the conformal character of the coating, is of importance in a novel antibacterial catheter introduced by Franz et al. [11] Here, poly(*p*-xylylene), which is deposited via chemical vapor deposition, is used as a top layer above an electro-deposited silver coating, ensuring the prolonged release of antibacterial silver ions.

Another advantage of vapor deposition techniques is the potential of synthesizing copolymers of chemically or functionally distinct monomers [12]. Alternatively, vapor deposition enables coatings of polymers that have only low levels of solubility in solvents. This highlights the importance of vapor deposition techniques in the field of conductive polymers, which are often insoluble and hard to process. Smolin et al. report the deposition of polyaniline using oxidative chemical vapor deposition [13]. A variation of the process parameters influences the quality of the deposited film as the oligomer content or the oxidation state. Another example of polymers with low solubility are fluoropolymers. Christian and Coclite investigated the deposition of fluoroacrylate polymer thin films via initiated chemical vapor deposition and the impact of crosslinking on the mechanical and chemical stability [14].

Vapor-based techniques can also be used to create chemically or topographically structured coatings on various substrates, which is of interest for example in the development of sensors or biomaterials. A general overview of the different techniques used to create structures can be found in the review by H.-Y. Chen [15]. In our own review, on the other hand, we focus on techniques to directly create structures in situ during the vapor deposition [16].

In summary, this Thematic Series highlights the broad utility of polymers deposited from the vapor phase used in the development of novel coating materials for a manifold of applications. We strongly hope that this Thematic Series stimulates further research into new applications of vapor-deposited polymers.

Meike Koenig and Joerg Lahann

Karlsruhe, September 2017

References

1. Gorham, W. F. *J. Polym. Sci., Part A: Polym. Chem.* **1966,** *4,* 3027–3039. doi:10.1002/pol.1966.150041209
2. Gazicki-Lipman, M. *J. Vac. Soc. Jpn.* **2007,** *50,* 601–608. doi:10.3131/jvsj.50.601
3. Chen, H.-Y.; Lahann, J. *Langmuir* **2011,** *27,* 34–48. doi:10.1021/la101623n
4. Alf, M. E.; Asatekin, A.; Barr, M. C.; Baxamusa, S. H.; Chelawat, H.; Ozaydin-Ince, G.; Petruczok, C. D.; Sreenivasan, R.; Tenhaeff, W. E.; Trujillo, N. J.; Vaddiraju, S.; Xu, J.; Gleason, K. K. *Adv. Mater.* **2010,** *22,* 1993–2027. doi:10.1002/adma.200902765
5. Ozaydin-Ince, G.; Coclite, A. M.; Gleason, K. K. *Rep. Prog. Phys.* **2012,** *75,* 016501. doi:10.1088/0034-4885/75/1/016501
6. Moni, P.; Al-Obeidi, A.; Gleason, K. K. *Beilstein J. Nanotechnol.* **2017,** *8,* 723–735. doi:10.3762/bjnano.8.76
7. Cheng, C.; Gupta, M. *Beilstein J. Nanotechnol.* **2017,** *8,* 1629–1636. doi:10.3762/bjnano.8.162
8. Balkan, A.; Armagan, E.; Ozaydin Ince, G. *Beilstein J. Nanotechnol.* **2017,** *8,* 872–882. doi:10.3762/bjnano.8.89
9. Marszalek, T.; Gazicki-Lipman, M.; Ulanski, J. *Beilstein J. Nanotechnol.* **2017,** *8,* 1532–1545. doi:10.3762/bjnano.8.155
10. Lahann, J.; Klee, D.; Thelen, H.; Bienert, H.; Vorwerk, D.; Höcker, H. *J. Mater. Sci.: Mater. Med.* **1999,** *10,* 443–448. doi:10.1023/A:1008939400812
11. Franz, G.; Schamberger, F.; Zare, H. H.; Bröskamp, S.; Jocham, D. *Beilstein J. Nanotechnol.* **2017,** *8,* 1982–2001. doi:10.3762/bjnano.8.199
12. Deng, X.; Friedmann, C.; Lahann, J. *Angew. Chem., Int. Ed.* **2011,** *50,* 6522–6526. doi:10.1002/anie.201101581
13. Smolin, Y. Y.; Soroush, M.; Lau, K. K. S. *Beilstein J. Nanotechnol.* **2017,** *8,* 1266–1276. doi:10.3762/bjnano.8.128
14. Christian, P.; Coclite, A. M. *Beilstein J. Nanotechnol.* **2017,** *8,* 933–942. doi:10.3762/bjnano.8.95
15. Chen, H.-Y. *Beilstein J. Nanotechnol.* **2017,** *8,* 1366–1374. doi:10.3762/bjnano.8.138
16. Koenig, M.; Lahann, J. *Beilstein J. Nanotechnol.* **2017,** *8,* 1250–1256. doi:10.3762/bjnano.8.126

License and Terms

BEILSTEIN JOURNAL OF NANOTECHNOLOGY

Vapor deposition routes to conformal polymer thin films

Priya Moni[1], Ahmed Al-Obeidi[1] and Karen K. Gleason[*2]

Review

Open Access

Address:
[1]Department of Materials Science and Engineering, Massachusetts Institute of Technology, 77 Massachusetts Ave, Cambridge, MA 02139, USA and [2]Department of Chemical Engineering, Massachusetts Institute of Technology, 77 Massachusetts Ave, Cambridge, MA 02139, USA

Email:
Karen K. Gleason[*] - kkg@mit.edu

* Corresponding author

Keywords:
conformal; polymers; thin films; vapor deposition

Beilstein J. Nanotechnol. **2017,** *8,* 723–735.
doi:10.3762/bjnano.8.76

Received: 27 December 2016
Accepted: 13 March 2017
Published: 28 March 2017

This article is part of the Thematic Series "Vapor-based polymers: from films to nanostructures".

Guest Editor: M. Koenig

Abstract

Vapor phase syntheses, including parylene chemical vapor deposition (CVD) and initiated CVD, enable the deposition of conformal polymer thin films to benefit a diverse array of applications. This short review for nanotechnologists, including those new to vapor deposition methods, covers the basic theory in designing a conformal polymer film vapor deposition, sample preparation and imaging techniques to assess film conformality, and several applications that have benefited from vapor deposited, conformal polymer thin films.

Review

Introduction

Conformal coverage is achieved when a film of uniform thickness precisely follows the geometry of the underlying substrate. Conformal coatings allow for surface properties to be optimized independently from the choice of the bulk material and shape of the substrate. Conformality has become an increasingly important characteristic in the fabrication of optoelectronic and medical devices having high aspect ratio features, 3D geometries, and textured/nanostructured surfaces. Conformal coating methods are also desired for modifying the internal surfaces of porous materials, including membranes, foams, and textiles, or irregular surface geometries, as well as for encapsulating fibers, nanowires, or particles [1]. For example, tailoring the surface energy of the pore walls of a separation membrane without obstructing the pore can enhance the passage of the desired liquid or gas [2-4]. Conformal coatings can also ensure that micro or nano-device properties (e.g., conductance, capacitance) do not vary due to large thickness variations [5-7].

One motivation for vapor phase synthesis of polymer thin films over traditional solution methods (e.g., spin casting, dip coating) is the ability to form conformal films on high aspect ratio structures, as seen in Figure 1. In traditional methods, polymers are pre-synthesized and dispersed in a solvent. This solution is then spread on the substrate of interest, typically by

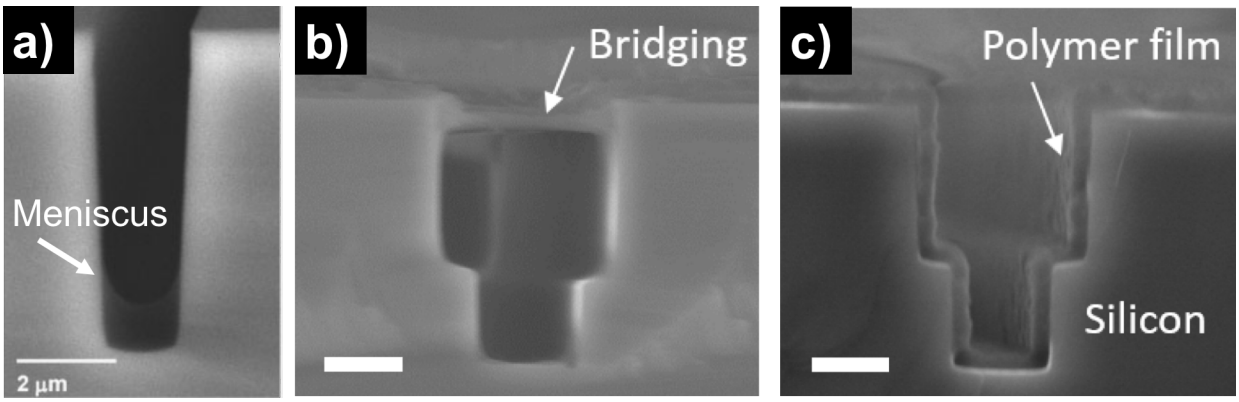

Figure 1: Micro-trenches with polymer coatings by a) solution with low substrat–interface energy, b) solution with high substrate–interface energy and c) iCVD (scale bar 2 μm). a) Reproduced with permission from [8], Copyright 2008 John Wiley and Sons. b),c) Reproduced with permission from [9], Copyright 2016 Massachusetts Institute of Technology.

dip or spinning coating, and dried so that only the polymer, in film form, remains on the surface. While this technique works reasonably well for flat substrates, the interaction energies between solution components coupled with its overall interfacial energy with the substrate can result either meniscus formation inside a feature (Figure 1a) or capillary bridge formation over a feature (Figure 1b). By contrast, vapor phase techniques are controlled by the individual adsorption of small molecules and their subsequent surface reaction to form a polymer film. In this case, the only interaction energy of concern is between the molecule and an available surface. Controlling the reactor conditions to ensure the Knudsen number is greater than unity (i.e., the mean free path of the molecule is greater than the relevant substrate geometric length scale) results in molecular adsorption deep in a structure so that the final film evenly coats the substrate geometry (Figure 1c) [1].

Several chemical vapor deposition (CVD) techniques result in highly conformal polymer films. For instance, emerging techniques such as molecular layer deposition (MLD) and oxidative CVD (oCVD) form conformal metalucone and step-growth polymer films [10,11]. However, no systematic studies of conformality have been devoted solely to these techniques thus far. Practitioners of MLD can look at existing models for its inorganic analogue, atomic layer deposition (ALD), as a starting point for studying conformal MLD films [12]. This review will focus on two, well-studied, conformal polymer CVD techniques: parylene CVD and initiated CVD (iCVD), with both deriving from free radical polymerization mechanisms. The four parts of this review will address reaction mechanisms of the aforementioned techniques, necessary deposition conditions for conformal film growth, imaging conformal polymer films, and finally applications for conformal polymer films.

Reaction mechanisms

Parylene CVD

Parlyene CVD is a well-established, free radical polymerization technique that results in poly[*p*-xylene] films [13]. The reaction mechanism proceeds as shown in Figure 2a, where [2,2]paracyclophane (22PCP) molecules are first sublimed, then thermally cracked at >500 °C to form two, resonance stabilized *p*-xylylene diradicals that eventually adsorb on a substrate near room temperature and react to form poly[*p*-xylene] [13,14]. Functionalized derivatives of the 22PCP monomer precursor enable the introduction of new chemistries into the final poly[*p*-xylene] structure such as halogens, amines, and esters [15,16].

Initiated CVD

iCVD is another free radical polymerization technique where instead of a single reactive species, a monomer and an initiating radical are needed to form the final polymer film. As seen in Figure 2b, gas phase monomers containing a reactive bond first adsorb on the substrate near room temperature. An initiator, such as di-*tert*-butyl peroxide is thermally cleaved by a hot filament (≈250 °C) and the resulting radicals collide with surface adsorbed monomers to initiate polymerization. The most common monomers polymerizable by iCVD are acrylates, methacrylates, and other vinyl (>C=C<) containing monomers [17,18]. However, acetylenic (–C≡C–) monomers have been polymerized as well [19].

The effect of deposition conditions

Depending on the conditions used, a CVD process can vary from extremely conformal to extremely non-conformal (planarization). Therefore, it is important to know what factors enable conformal film deposition and how these are related to the deposition conditions used.

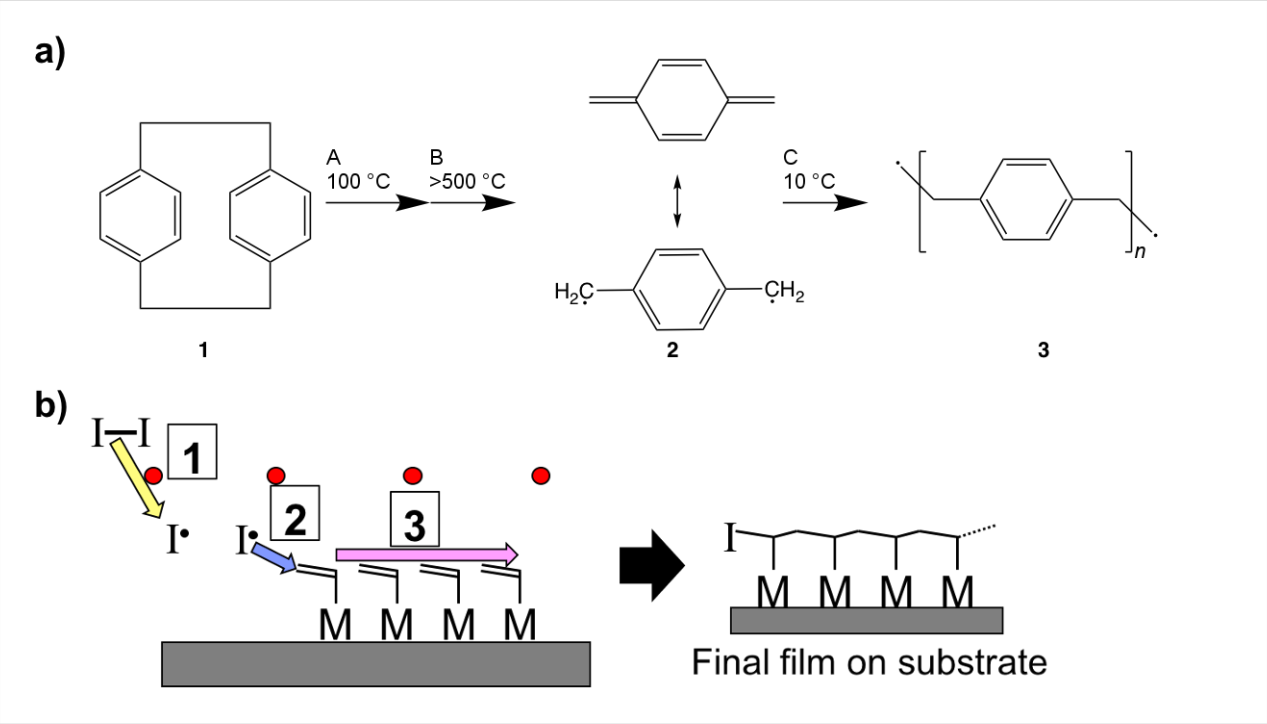

Figure 2: a) Mechanism of parylene CVD. **(1)** [2,2]paracyclophane **(2)** *p*-xylylene diradical intermediate **(3)** poly[*p*-xylene]; A) Sublimation, B) pyrolysis, C) substrate adsorption. b) Mechanism of iCVD: 1) decomposition of initiator by hot filament, 2) initiator attack of adsorbed monomer, 3) propagation to form polymer film.

Thin film depositions on well-defined micron-sized trench structures are often used to study the process' conformality. When studying the conformality on a trench structure, step coverage (SC) and side wall coverage (SWC) are the most important properties to assess. SC and SWC are defined in Equation 1 and Equation 2, respectively:

$$\mathrm{SC} = \frac{t_{\mathrm{bottom}}}{t_{\mathrm{flat}}} \tag{1}$$

$$\mathrm{SWC} = \frac{t_{\mathrm{side}}}{t_{\mathrm{flat}}} \tag{2}$$

where t_{bottom}, t_{side}, and t_{flat} are the film thicknesses at the bottom of trench, side wall of a trench, and flat surface at the top of a trench, respectively. For perfect conformality, SC and SWC should be unity, where any deviation indicates some degree of non conformality. Several theoretical models regarding conformal depositions of parylene-CVD and iCVD in high aspect ratio structures have been published elsewhere [1,3,20,21]. However all systems share a common dependence on the sticking probability, Γ, or the probability that a gas molecule will chemisorb on a surface [22]. In CVD reactions, film conformality improves as reactant sticking probabilities decreases since this enables gas diffusion deeper into deep structures [1,21]. Γ has many dependencies, but the fractional coverage of chemisorbed species, θ, and various chemical reaction rates, R, can play a significant role for polymer growth systems [3]. In general, increasing θ and/or reducing R results in a reduced Γ. In order to develop process optimization strategies for deposition process having more than one gas phase reactant, it is important to determine which species has the Γ which controls the degree of conformality.

Parlyene CVD

During parylene CVD, the adsorption of a single *p*-xylylene diradical usually results in no chemical reaction. However, when a *p*-xylylene diradical collides with a cluster of two adsorbed diradicals, it can react to form a new, heavy chain that does not desorb from the surface [13]. Analysis by Fortin and Lu using the chemisorption model and Langmuir isotherm determined the following relationship between Γ and θ

$$\Gamma = \frac{(1-\theta)}{\left[1 + A\exp\left[\frac{(E_{\mathrm{D}} - E_{\mathrm{A}})}{RT}\right]\right]} \tag{3}$$

where E_{D} and E_{A} are the energies of desorption and adsorption, respectively, R is the gas constant, T is temperature, and A is a pre-exponential factor [20]. In parylene depositions, gaseous diradical monomers can chemisorb directly on the reactive

chain ends, thus growing the chain while still maintaining the active chain ends. This results in (1 − θ), the fraction of available sites for chemisorption, remaining essentially constant during the deposition, since it is proportional to the number of growing chains [13]. To reduce Γ, the overall number of sites for chemisorption must decrease, meaning that the density of monomers adsorbed on the substrate surface must be reduced. This can be achieved by reducing the partial pressure of the monomer either by introducing an inert gas flow or by reducing the total pressure of the deposition. Another approach to reduce the sticking coefficient is to increase the substrate temperature to hinder monomer adsorption. The functional dependence of temperature on Γ is seen in Equation 3 and plotted in Figure 3a. While a reduction both in chamber pressure or increase in substrate temperature allow for more conformal film growth, Figure 3b and Figure 3c show that the deposition rate also decreases in these conditions. Thus highly conformal processes come at the expense of fast film growth rates.

Initiated CVD

During iCVD, clusters of unreacted monomers adsorb on the substrate and quickly polymerize upon the impingement of an initiator radical. The initiator radicals are quite volatile and are expected to have negligible adsorption on the bare surface. Additionally, once a monomer undergoes polymerization, it is no longer a site for initiator chemisorption. Therefore, the number surface sites available for the initiator is directly related to the monomer fractional surface coverage given by P_m/P_{sat} where P_m is the partial pressure of the monomer in the chamber and P_{sat} is the monomer's saturation pressure under the given deposition conditions [23]. Operating at lower P_m/P_{sat} values thus reduces the sticking probability of the initiator radical, as seen in Figure 4a. In Figure 4b, a general trend of decreasing step coverage is seen with an increase in aspect ratio. However, by decreasing the P_m/P_{sat}, step coverages closer to unity are possible even at higher aspect ratios. Finally, like parylene CVD, conformal deposition conditions in iCVD come at the cost of deposition rate. In Figure 4c, a positive relationship between P_m/P_{sat} and deposition rate is demonstrated. In iCVD, conformality can be maintained for rates up to ≈50 nm/min [21].

To confirm that conformality is controlled by the sticking probability of the initiator, the same monomer, cyclohexylmethacrylate, was iCVD polymerized holding P_m/P_{sat} fixed using two different initiators [24]. The first initiator was *tert*-butyl peroxide (TBPO) which decomposes over the heated filament to give two *tert*-butoxy radicals. The second initiator was *tert*-butyl peroxybenzoate (TBPOB) which decomposes to give one *tert*-butoxy radical and one high molecular weight benzoate radical. Figure 4d shows that the sticking coefficients for the higher molecular weight radicals produced for TBPOB, are consistently greater than for TBPO. The sticking coefficient of both initiator radicals is independent of filament temperature. Since the filament temperature determines the fraction of initiators cleaved to radicals, the sticking probability of the initiator radicals is independent of their gas phase concentration. This study confirms that volatile initiators are desirable for conformal iCVD growth.

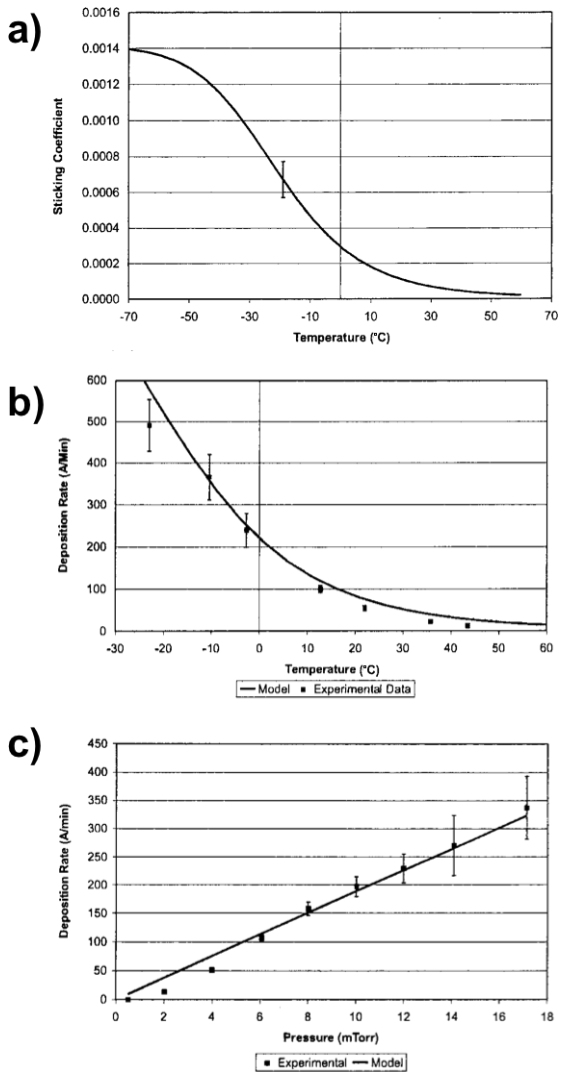

Figure 3: a) Sticking coefficient of *p*-xylylene diradicals as a function of temperature, b) deposition rate as function of temperature at pressure = 4.0 mTorr, c) deposition rate as function of pressure at temperature = 22 °C. Adapted with permission from [20], copyright 2002 American Chemical Society.

Diffusion and reaction controls. As aspect ratios of geometries increase, both the rate of reaction and diffusion of reactants down the feature play a much larger role in the process conformality. Uniform film growth requires reactants to be

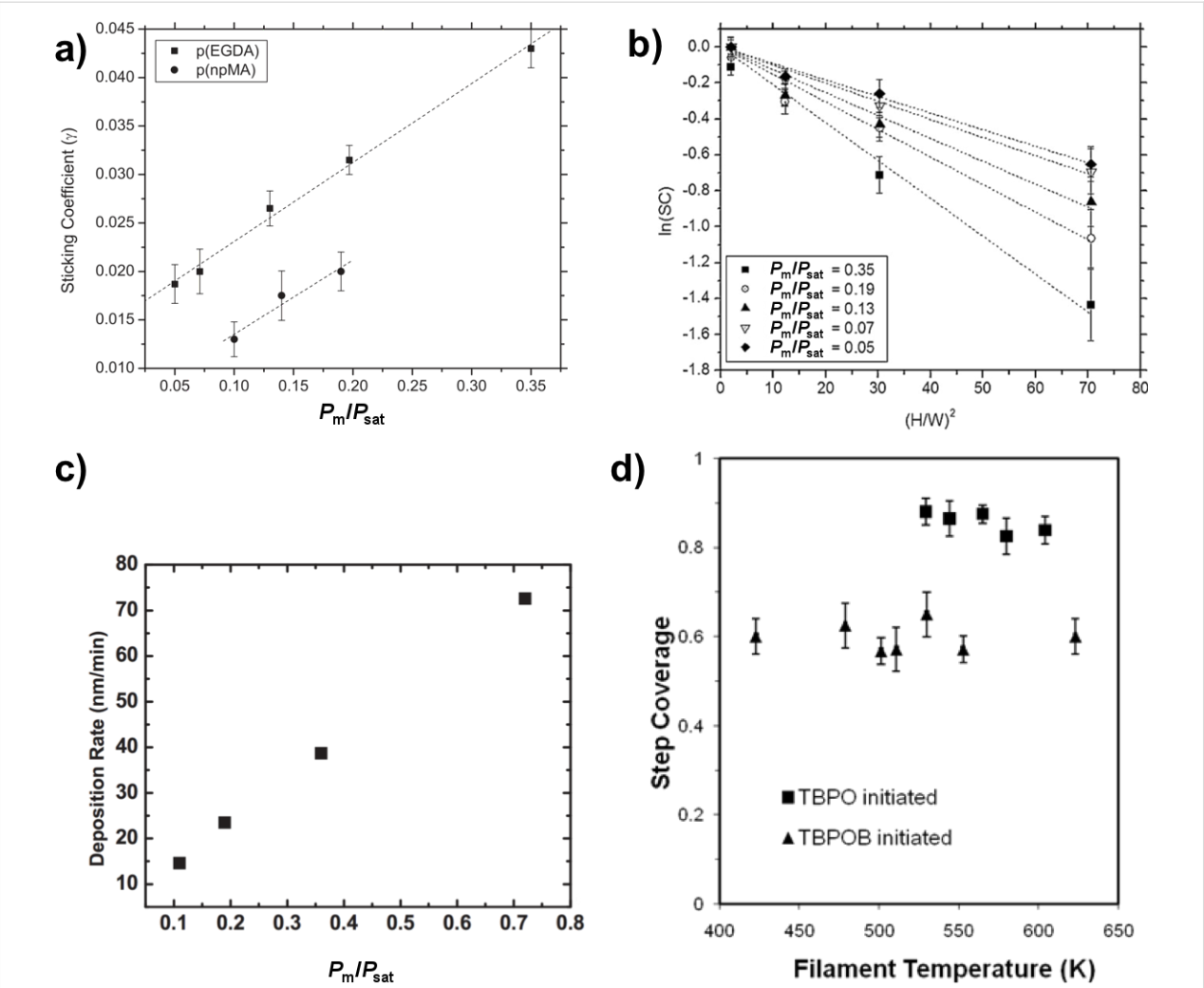

Figure 4: a) Sticking coefficients of *tert*-butoxy initiator radicals as function of P_m/P_{sat} and monomer type where EGDA, a di-acrylate monomer, has a higher Γ than npMA, a methacrylate monomer, due to the presence of a second reactive moiety. b) Step coverage as a function of trench aspect ratio at varying P_m/P_{sat} values. c) iCVD deposition rate as function of P_m/P_{sat}. d) Step coverage as a function of filament temperature and type of initiator. Parts a) and b) reprinted with permission from [25], copyright 2010 John Wiley and Sons. c) Reprinted with permission from [21], copyright 2008 John Wiley and Sons. d) Reprinted with permission from [24], copyright 2011 American Chemical Society.

readily available at all point down a high aspect ratio structure. However, if the rate of propagation for chain growth is much higher than the rate monomer diffusion, this can result in a concentration profile down the geometry. In this case, the monomer sticking probability must also be considered.

Asatekin et al. studied the impact of the Thiele modulus, Φ, which compares the consumption of a reactant to its replenishment by diffusion, on conformality of iCVD film formation [3]. For a pore of depth L and radius r, the following equation was derived for the iCVD system

$$\Phi = \sqrt{\frac{2Lv^2}{rD_i c_{i,0}}} = \frac{\sqrt{3\Gamma_i}}{2}\frac{L}{r} \quad (4)$$

Where v is the deposition rate, and D_i, $c_{i,0}$, and Γ_i are the diffusivity, concentration at pore entrance, and sticking coefficient of species i respectively. The Thiele modulus can then be used to modify Fick's second law to yield the following equation describing the concentration profile at position x down the pore's length:

$$\frac{d^2\psi_i}{d\lambda^2} = \Phi_i^2\psi_i \quad (5)$$

with dimensionless variables $\lambda = x/L$ and $\psi_i = c_i/c_{i,0}$, where c_i is the concentration of species i at position x [1]. The combined impact of the monomer concentration profile, ψ_M, and initiator

concentration profile, ψ_I, on the step coverage at the bottom of the pore is then given by Equation 6 [1].

$$SC = \psi_I^{\frac{1}{2}} \psi_M \tag{6}$$

The ratio of monomer to initiator sticking coefficients has a substantial impact on the final value of step coverage for a given aspect ratio. Numerical solutions to Equation 6 are plotted in Figure 5a. High step coverage at higher aspect ratios requires the monomer sticking coefficient to be substantially smaller than the initiator sticking coefficient.

The propagation rate also affects the monomer sticking probability and concentration profile within a pore. If the $\Phi_M < 1$, the monomers in a pore are continuously replenished meaning the monomer concentration profile within the pore is essentially constant [1,3]. This can occur in reactions with low radical reaction propagation rates, like the polymerization of vinyl monomers, which results in very low monomer sticking coefficients. An example of this is seen in Figure 5b, where the dashed line representing the divinyl benzene concentration profile is relatively constant. Thus only the initiator sticking probability affects step coverage, as given by the following relationship [1,21].

$$\ln SC = -\frac{3}{8}\left(\frac{L}{r}\right)^2 \Gamma_I \tag{7}$$

However, if $\Phi_M > 1$, a gradient in the monomer concentration develops down the length of the pore. In this regime, polymerization consumes monomer faster than monomers can be replenished by diffusion down the pore. This is common for methacrylate and acrylate monomers, which have high radical polymerization rates [3]. An example of the increased reduction of monomer concentration down a pore is seen for perfluorodecyl acrylate, the solid in line Figure 5b. The high propagation rate also results in a corresponding increase in the monomer sticking coefficient, since monomer chemisorption on a growing surface chain has become kinetically favored. Step coverage is poor in this case, as bottlenecks often form, completely obstructing the pores.

Assessing conformality

Experimentally, conformality is determined using electron microscopy. Depending on the substrate structure, material, polymer film thickness, and final application, additional or varied techniques may be needed. The simplest case is a polymer film thicker than 200 nm on a micron-sized structure with sufficient material atomic number contrast (e.g., Si). In this case, physically cleaving the sample and taking a cross-sectional scanning electron microscopy (SEM) image will show how the film is coated on the substrate, as seen in Figure 1c and Figure 6a–d. Conformality of a given process can be assessed by creating a series of trenches of varying aspect ratios, as seen in the top panel of Figure 6. However, conformal depositions are desirable on more geometries than just trenches. For instance, an insulating polymer film uniformly enveloping a conductive wire may be required for an application. As seen in Figure 6e, a simple cross section of the wire can reveal the conformal coating [26]. Imaging a series of cross sections can inform conformality along the length of the wire. Not all complex substrates are amenable to forming physical cross sections. In this case, ion or electron beam ablation can expose the substrate so that the film–substrate interface can be imaged [27,28]. In Figure 6f, an iCVD coated textile fiber has been ion beam ablated to reveal the conformal polymer film [27].

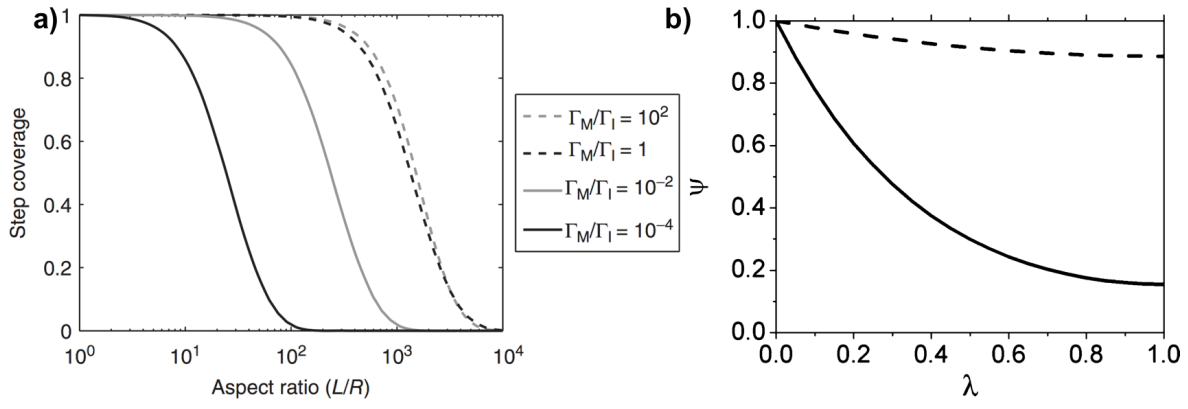

Figure 5: a) Step coverage as function of aspect ratio and ratio of sticking coefficients from numerical solutions of Equation 6. b) Concentration profile of perfluorodecyl acrylate (solid line) and divinyl benzene (dashed line) down a pore. a) Reprinted with permission from [1], copyright 2015 John Wiley and Sons. b) Reprinted with permission from [3], copyright 2011 American Chemical Society.

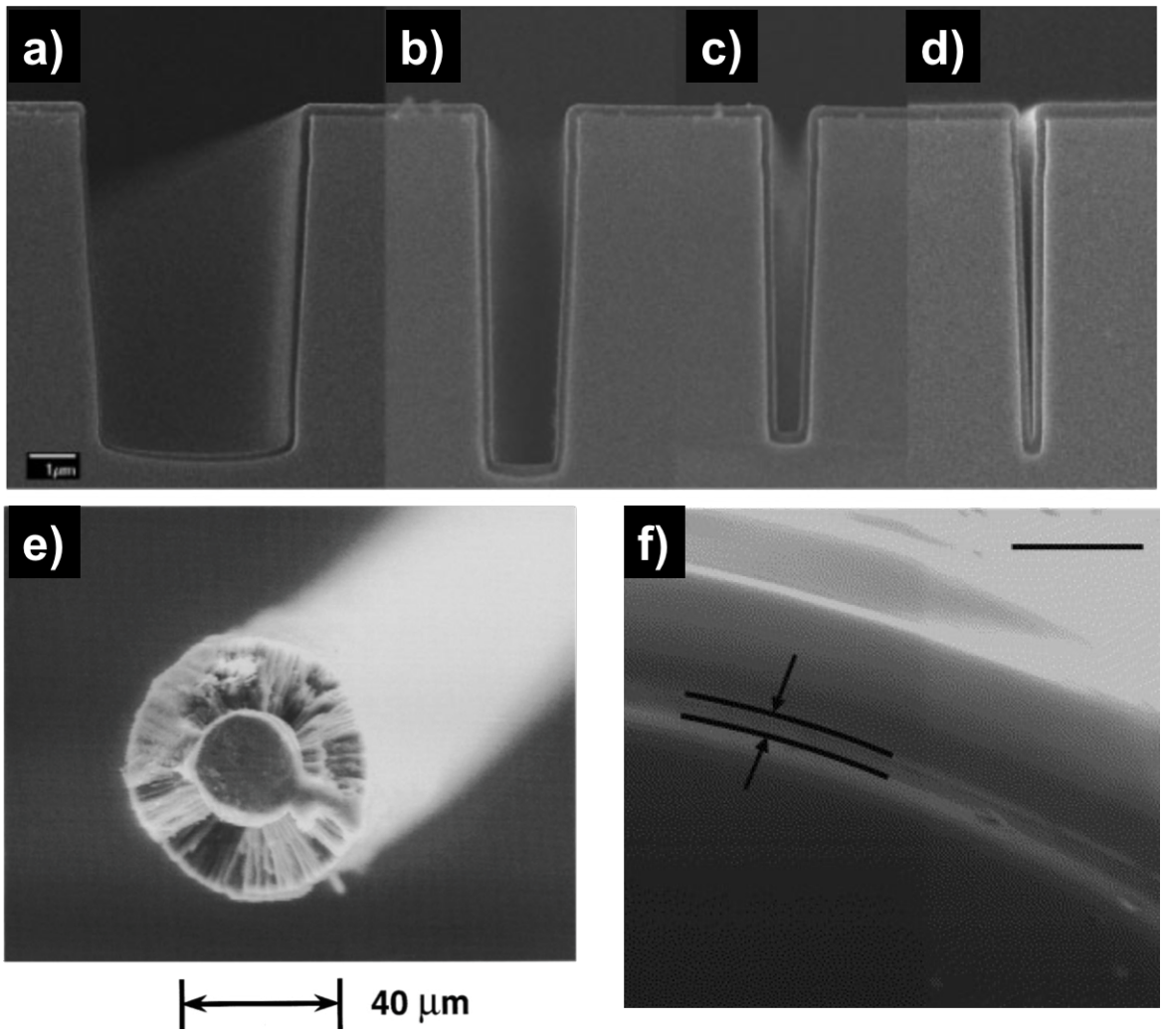

Figure 6: SEM images of iCVD pEGDA on micro-trenches with aspect ratios of a) 1.4 b) 3.5, c) 5.5 and d) 8.4. e) Cross-sectional SEM of 25 µm stainless-steel wire with 16 µm fluoropolymer coating formed via iCVD. f) iCVD pDMAMS on nylon fiber ion beam ablated to reveal substrate, scale bar is 1 µm. Parts a), b), c) and d) reprinted with permission from [25], copyright 2010 Wiley. e) Reprinted with permission from [26], copyright 1996, AIP Publishing LLC. f) Reprinted with permission from [27], copyright 2007, Elsevier.

As substrates become more complex and polymer film thicknesses fall below 100 nm, verifying film conformality becomes increasingly difficult. Insufficient Z contrast and charging effects makes SEM cross sections difficult to analyze. Using a focus ion beam (FIB) system to make transmission electron microscopy (TEM) samples is a route often used with inorganic materials. However, ion damage, particularly for very thin films, is an issue when it comes to this method. An alternate method, particularly to demonstrate the practicality of coatings, is to use SEM images before and after film deposition coupled with a relevant change in a device's property. For example, Servi et al. used iCVD to deposit thin films (≈10 nm) of hydrophobic polymers on nylon membranes to be used in membrane distillation [2]. Conformal film coverage of the membrane microstructure is essential to prevent the wetting of liquid water, a critical property for this application. As seen in Figure 7a and Figure 7b, the overall structure of a nylon membrane before and after coating by iCVD shows little to no change. However, coated membranes can withstand water pressures upwards of 100 kPa before liquid water leakage whereas uncoated membranes are immediately soaked upon contact with water (0 kPa). In this work, the combination of SEM imaging with final device properties prove the conformality of the polymer films. Many applications, particularly those involving surface property changes, require retention of the precursor functionality down the depth of feature as well. Gupta et al. used iCVD to coat 10–150 nm thick perfluorodecyl acrylate films to modify the wetting properties of capillary pore mem-

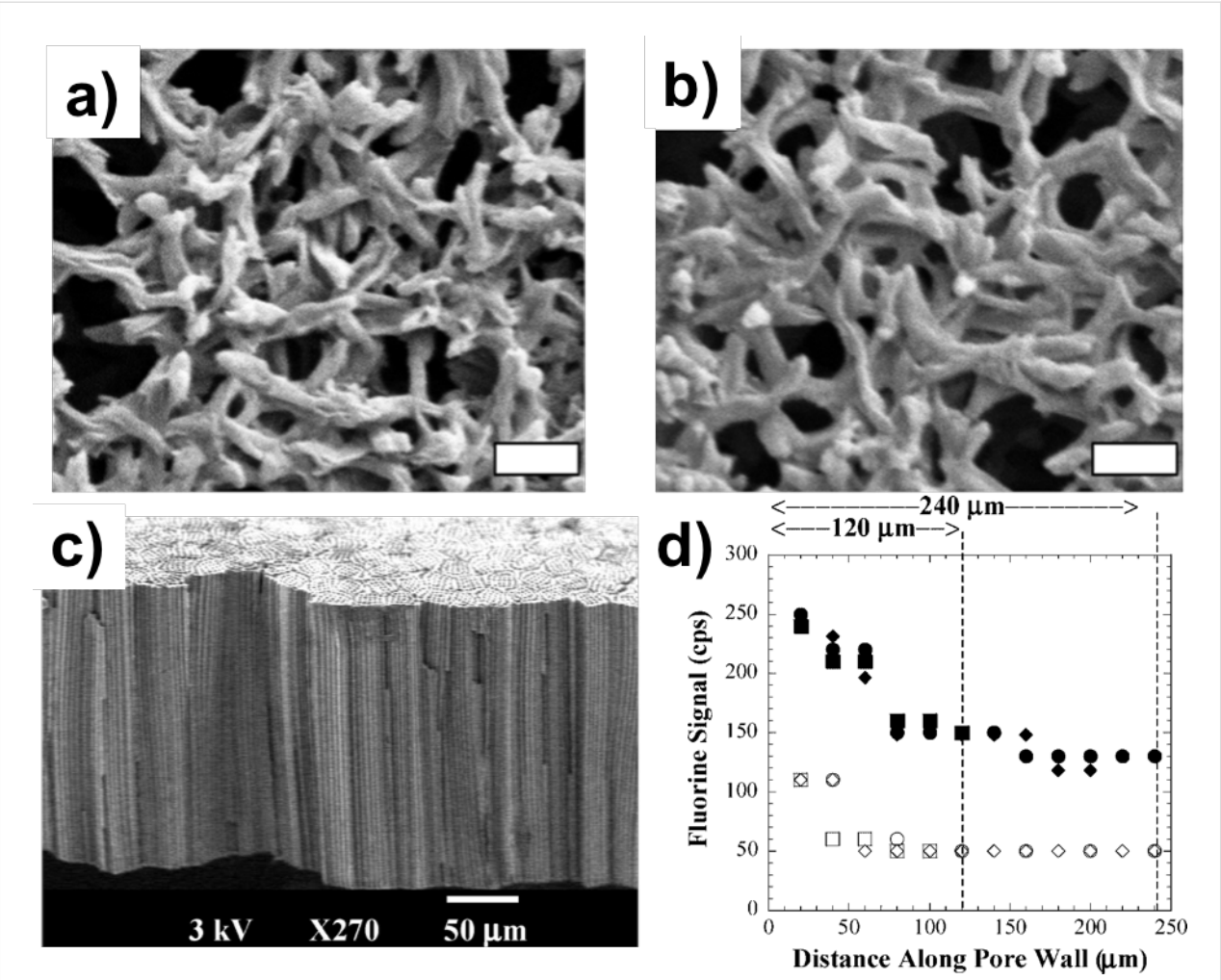

Figure 7: SEM of Nylon membranes a) uncoated and b) coated with 10 nm of iCVD pDVB (scale bar 1 µm). c) Cross-sectional SEM of capillary pore membrane. d) EMPA fluorine signal down 3 µm diameter pore with 2 minute deposition (unfilled) and 5 minute deposition (filled). Parts a) and b) reprinted with permission from [2], copyright 2016 Elsevier. Parts c) and d) reprinted with permission from [4], copyright 2008 American Chemical Society.

branes, as seen in Figure 7c [4]. To determine the coating conformality, electron microprobe analysis (EMPA) was used to measure the fluorine signal down the pore wall of a coated membrane and presented in Figure 7d. While the fluorine signal is detected at the bottom of the pore, the functional side wall coverage, estimated to be between 0.5 and 0.6, indicates a degree of conformality.

In some cases, TEM images are necessary to verify film conformality. For instance, a conformal polysiloxane coating on an Si nanowire array is difficult to image using SEM, as creating nanowire cross sections by physical cleavage is nearly impossible. Using EMPA to determine the signal of constituent atoms fails as both the nanowire and polymer film contain nearly the same elements (Si and O). Previously unpublished work by Gleason and coworkers used a combination of SEM and TEM to verify the conformality of iCVD poly(1,3,5,7-tetramethyl-1,3,5,7-tetravinylcyclotetrasiloxane) (pV4D4) films on vertically aligned Si nanowire arrays. Figure 8a and Figure 8b show SEM images (Zeiss Merlin HR SEM) of the nanowire array before and after deposition, with no apparent change in wire structure except for e-beam induced electrostatic attraction between the coated wire tops. There is no thinning of the coated nanowires down the vertical axis, indicating good side wall coverage. TEM samples were made by sonicating the nanowire arrays in IPA to create a nanowire solution. A drop of solution on a TEM grid allows for wire dispersal and subsequent imaging. Figure 8c and Figure 8d show TEM images (FEI Tecnai G2 Spirit TWIN) of an uncoated and coated Si nanowire. The false colored amorphous layer is a ≈25 nm pV4D4 film exhibiting good SWC of approximately 0.75 within the imaged section. For very thin films, conformal protection

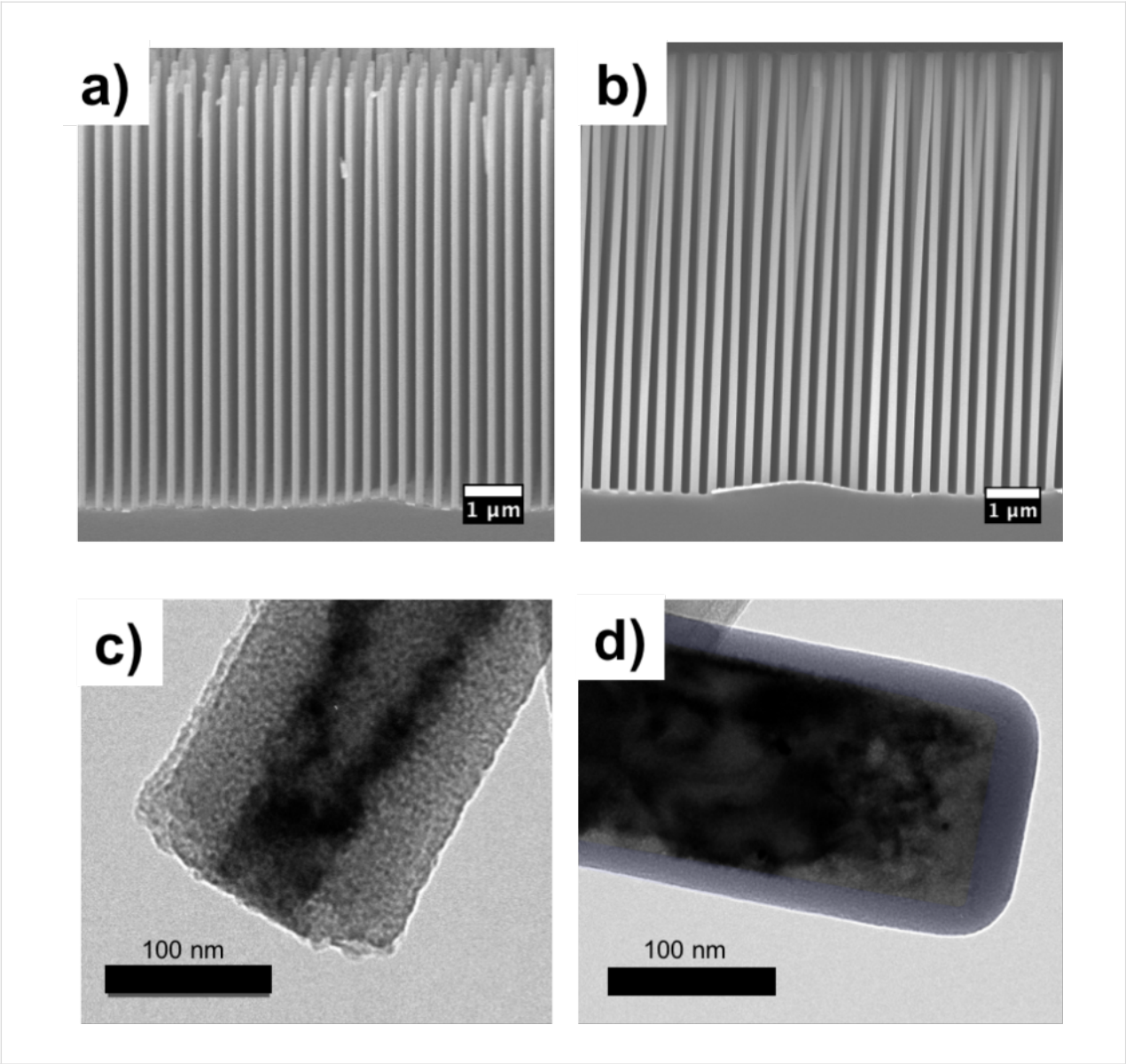

Figure 8: SEM images of a) uncoated ordered Si nanowire array and b) 25 nm iCVD pV4D4 coated ordered Si nanowire array. TEM image of single Si nanowire c) uncoated d) with 25 nm iCVD pV4D4 highlighted in purple.

requires that the deposited film has a smooth, pin-hole free morphology, with the root mean square roughness much smaller than film thickness.

Applications

To date, a variety of conformal polymer thin films have on many substrates from nanometer length to sub millimeter length scales, as summarized in Table 1. These films have found utility in a diverse array of applications. Several biological applications have found uses for vapor deposited polymer thin films. For instance, Baxamusa et al. used iCVD to deposit conformal poly(hydroxyethyl methacrylate) hydrogels silica microspheres for biological sensors, as seen in Figure 9a [29]. Lahann and coworkers used parylene CVD to form thin films of poly[(*p*-xylene-4-methyl-2-bromoisobutyrate)-co-(*p*-xylene)] which served as a conformal initiating layer for atom transfer radical polymerization to produce conformal brushes that controlled protein adsorption [16]. Martin et al. used iCVD deposited conformal coatings of poly(dimethylaminomethylstyrene) on nylon fabric as antimicrobial agents again *E. Coli* and *B. subtilis*, as shown in Figure 6f [27]. Xu et al. demonstrated the benefit of iCVD over plasma enhanced polymer CVD both in conformality and functional group retention for the deposition of conformal sensing molecules on microfluidic devices [30]. This concept was later used to enable PDMS-free microfluidic devices for oxygen-free flow-lithography, a process that can

Table 1: Vapor deposited conformal polymer films by substrate, relevant length scale, method, and polymer chemistry.

Substrate	Width	Aspect ratio (H/W)	Method	Film chemistry and thickness	Ref
Si trench	300 nm	1.67:1	paryleneCVD	halogenated poly(*p*-xylene) 100 nm	[32]
	1 μm	5:1	iCVD	poly(methacrylate)	[8]
	500 nm	10:1	paryleneCVD	parylene-N, 200 nm	[33]
Si cantilever overhang	14 μm 1 μm opening	1:14	paryleneCVD	parylene-N, 200 nm	[33]
	20 μm 3 μm opening	3:20	iCVD	poly(tetrafluoroethylene), 300 nm	[34]
Vertical pores	3 μm	80:1	iCVD	poly(pefluorodecyl acrylate), 250 nm	[4]
	50 nm	400:1	iCVD	poly(divinyl benzene), 20 nm	[3]
Gold wires	50 μm	20:1	iCVD	poly(trivinyl-trimethyl cyclotrisiloxane), 3 μm	[28]
Nylon fibers	10 μm	100:1	iCVD	poly(dimethylaminomethyl styrene), 200 nm	[27]
PDMS micro-pillars	22 μm	2.9:1	iCVD	poly(hydroxyethyl acrylate), 1 μm	[35]
Glass microspheres	25–32 μm	1:1	iCVD	poly(glycidyl methacrylate) 135 nm	[36]
Rose petal micro-molds	20 μm	1:1 + nano-texture	iCVD	poly(glycidyl methacrylate), poly(pefluorodecyl acrylate) 500 nm	[37]
Particles	120 nm	1:1	MLD	poly(aluminum ethylene glycol) 13 nm	[38]
	200 nm	1:1	iCVD	poly(meta-diethynylbenzene) 13 nm	[19]
Bulk Ag nanowires	60 nm	166:1	iCVD	poly(tetravinyl-tetramethyl cyclotetrasiloxane), 10 nm	[39]
Bulk carbon Nanotubes	20 nm	750:1	MLD	glycercol alucone, 10 nm	[40]
Nano trenches	200 nm	2:1	oCVD	poly(3,4-ethylene dioxythiophene)	[41]
NAA	200 nm	285:1	oCVD	poly(thiophene), 30 nm	[42]
Vertically aligned Si nanowires	150 nm	50:1	iCVD	poly(tetravinyl-tetramethyl cyclotetrasiloxane), 25 nm	this work
Vertically aligned carbon nanotubes	50 nm	40:1	iCVD	poly(tetrafluoroethylene), 50 nm	[43]
	8 nm	10,000:1	oCVD	poly(3,4-ethylene dioxythiophene), 10 nm	[44]
	100 nm	20:1	iCVD	poly(methacrylic acid-co-ethylene glycol diacrylate), 50 nm	[45]

generate multifunctional micro and nano-particles [31]. Finally, O'Shaughnessy et al. showed conformal coatings of iCVD grown poly(1,3,5-trivinyl-1,3,5-trimethylcyclotrisiloxane) (pV3D3) for biopassive insulation of neural nodes [28].

Several situations requiring the formation of composite structures have benefited from iCVD deposited polymer films. The aforementioned work by Servi et al. showed how conformal poly(divinyl benzene) coatings allowed only water vapor transport through membranes used in membrane distillation [2]. Im and coworkers fabricated self-cleaning, superamphiphobic sponges by coating poly(heptadecafluorodecyl methacrylate) on a commercial sponge using iCVD [46]. Figure 9b shows the iCVD coating conformally covering the sponge's microstructure. Previously, Lau et al. demonstrated conformal coverage of iCVD grown fluoropolymers on vertically aligned carbon nanotube (CNT) forests to prevent capillary densification as seen in Figure 9c [43]. These coated nanotube forests were later shown to be beneficial to flexographic printing by Hart et al. [47]. Brown et al. showed that MLD could create 10 nm, conformal aluminum alkoxide derivative films on CNT sheets, as seen in Figure 9d, to create a composite material with 4 times the Young's Modulus of a bare CNT sheet [40].

Emerging applications for ultrathin polymer films on nanostructured high aspect ratio structures include various energy storage devices and soft electronics. For instance, silicon based anodes are of interest for lithium ion batteries since Li–Si alloys have an incredibly high gravimetric lithium storage capacity. He at al. have used MLD to encapsulate Si nanoparticles with alucone for this application [49]. The alucone layer prevents the formation of a resistive secondary electrolyte interphase (SEI), thus yielding improved electrode performance. Gleason and coworkers, having previously shown pV4D4 as potential solid electrolyte, are exploring the Si nanowire assembly in Figure 8a as a route toward anodes for micro lithium ion batteries [39]. Figure 9e shows a corresponding, conformal pV4D4 coating on a lithium spinel oxide particle, a material that can be used as a cathode for micro lithium ion batteries. Composite electrodes for supercapacitors have been developed by forming pseudocapacitive, conjugated polymer thin films on various electrodes such as vertically aligned CNTs, aligned graphene flakes, and

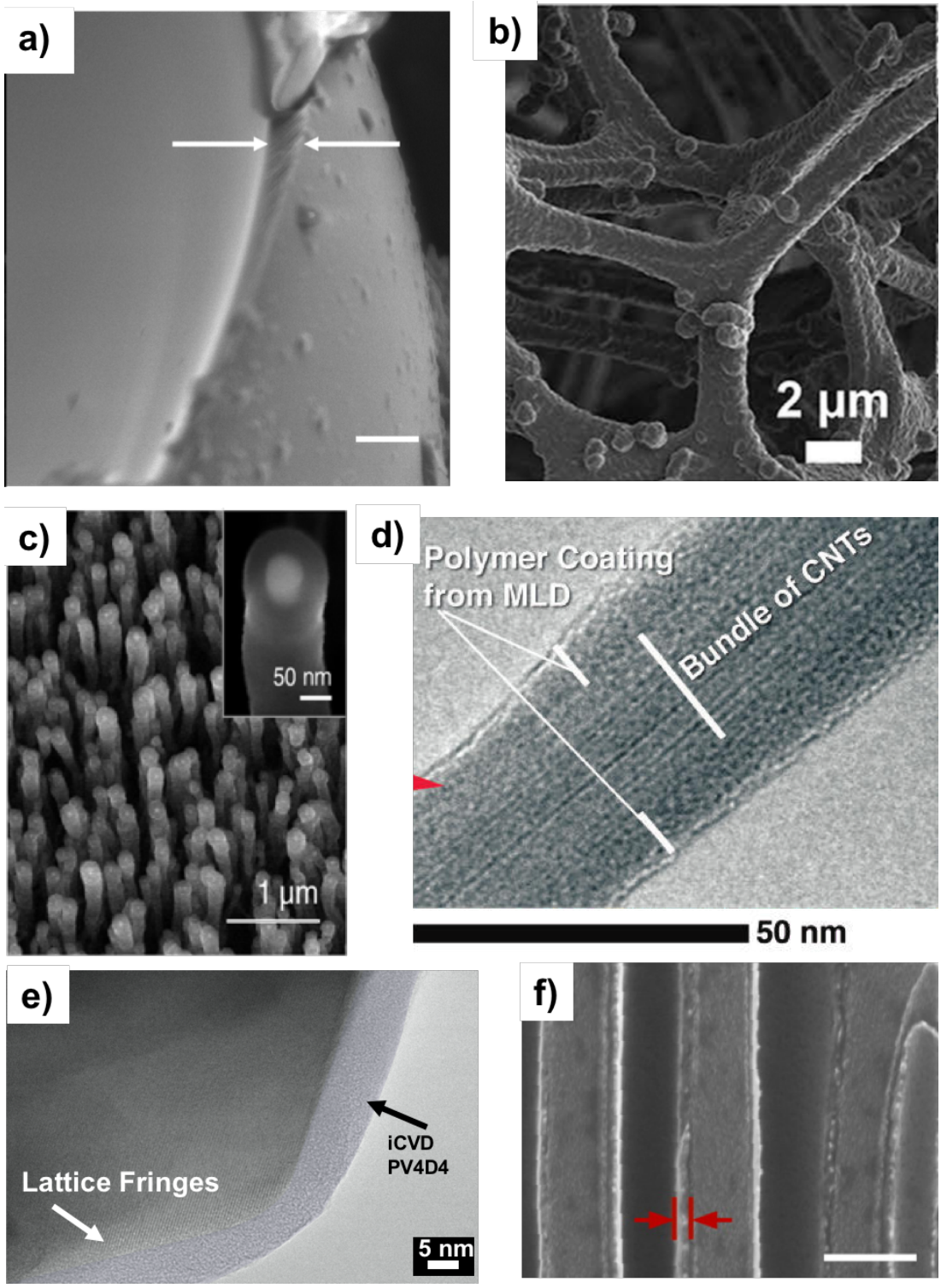

Figure 9: a) SEM image of silica micro-bead with conformal iCVD pHEMA coating, b) SEM image of commercial sponge with pHDFMA coating, c) SEM image of carbon nanotube forest with iCVD PTFE coating, d) TEM image of CNT bundle coated with MLD alucone coating, e) TEM image of lithium spinel oxide particle coated with iCVD pV4D4 coating, f) SEM image of NAA electrode with polythiophene coating (scale bar 200 µm). a) Reprinted with permission from [29], copyright 2008 American Chemical Society. b) Adapted from [46], Copyright 2016 Nature Publishing Group, published in [46] under a Creative Commons CC-BY license, http://creativecommons.org/licenses/by/4.0/, c) Reprinted with permission from [43], copyright 2003 American Chemical Society. d) Reprinted with permission from [40], copyright 2013 American Chemical Society. e) Reprinted with permission from [48], copyright 2016 John Wiley and Sons. f) Adapted with permission from [42], copyright 2014 American Chemical Society.

nano-porous anodized alumina (NAA) [42,50,51]. Figure 9f shows a conformal oCVD synthesized polythiophene coating on a NAA electrode. In soft electronics, conformal dielectric iCVD films have found uses in both field effect transistors and non-volatile memory [7,52].

Conclusion

In summary, vapor based polymerization techniques, such as parylene CVD and iCVD, yield much better conformal thin polymer films on high aspect ratio structures than traditional solution methods. Different categories of monomers are associated with the conformal polymer CVD methods discussed here. Thus, the type of resulting polymeric film desired is one criterion for selecting between the methods. The deposition rate and reactor conditions are other considerations in selecting between the methods. In all cases, depositions must operate under regimes with low reactive molecule sticking coefficients to ensure step coverage and side wall approach unity. To date, the iCVD method has shown the highest rate of vapor depositing conformal polymeric films. The degree of film conformality is typically assessed using a combination of electron microscopy and other characterization techniques. A diverse array of applications have benefited from conformal polymer films including, but not limited to, separation processes, biomedical devices, and micro/nano electronic and energy storage devices.

Acknowledgements

The authors would like to thank funding from the Office of Naval Research (funding Contract N00014-13-1-0466) and National Science Foundation (Award Number: 1344891). Use of the Center for Materials Science and Engineering (CMSE) electron microscopes was funded in part through the National Science Foundation (Grant number DMR-1419807).

The authors also thank Prof. Carl V. Thompson of the Massachusetts Institute of Technology for the use of his laboratories to fabricate the Si nanowire arrays and Dr. Nan Chen for the iCVD pV4D4 coating on the nanowire arrays used in Figure 8.

The image of micro-trench with vapor deposited polymer coating in the graphical abstract was reproduced with permission from [8], copyright 2008 John Wiley and Sons.

References

1. Baxamusa, S. Conformal Polymer CVD. In *CVD Polymers: Fabrication of Organic Surfaces and Devices;* Gleason, K. K., Ed.; Wiley-VCH Verlag GmbH & Co. KGaA: Weinheim, Germany, 2015; pp 87–109. doi:10.1002/9783527690275.ch5
2. Servi, A. T.; Kharraz, J.; Klee, D.; Notarangelo, K.; Eyob, B.; Guillen-Burrieza, E.; Liu, A.; Arafat, H. A.; Gleason, K. K. *J. Membr. Sci.* **2016,** *520,* 850–859. doi:10.1016/j.memsci.2016.08.021
3. Asatekin, A.; Gleason, K. K. *Nano Lett.* **2011,** *11,* 677–686. doi:10.1021/nl103799d
4. Gupta, M.; Kapur, V.; Pinkerton, N. M.; Gleason, K. K. *Chem. Mater.* **2008,** *20,* 1646–1651. doi:10.1021/cm702810j
5. Chen, N.; Reeja-Jayan, B.; Liu, A.; Lau, J.; Dunn, B.; Gleason, K. K. *Macromol. Rapid Commun.* **2016,** *37,* 446–452. doi:10.1002/marc.201500649
6. Reeja-Jayan, B.; Chen, N.; Lau, J.; Kattirtzi, J. A.; Moni, P.; Liu, A.; Miller, I. G.; Kayser, R.; Willard, A. P.; Dunn, B.; Gleason, K. K. *Macromolecules* **2015,** *48,* 5222–5229. doi:10.1021/acs.macromol.5b00940
7. Jang, B. C.; Seong, H.; Kim, S. K.; Kim, J. Y.; Koo, B. J.; Choi, J.; Yang, S. Y.; Im, S. G.; Choi, S.-Y. *ACS Appl. Mater. Interfaces* **2016,** *8,* 12951–12958. doi:10.1021/acsami.6b01937
8. Tenhaeff, W. E.; Gleason, K. K. *Adv. Funct. Mater.* **2008,** *18,* 979–992. doi:10.1002/adfm.200701479
9. Servi, A. T. Advancing Hydrophobic Desalination Membranes using Initiated Chemical Vapor Deposition (iCVD). Ph.D. Thesis, Massachusetts Institute of Technology, Cambridge, MA, 2016; pp 1–159.
10. Zhou, H.; Bent, S. F. *J. Vac. Sci. Technol., A* **2013,** *31,* 040801–040819. doi:10.1116/1.4804609
11. Howden, R. M. In *CVD Polymers: Fabrication of Organic Surfaces and Devices;* Gleason, K. K., Ed.; Wiley-VCH Verlag GmbH & Co. KGaA: Weinheim, Germany, 2015; pp 233–253. doi:10.1002/9783527690275.ch11
12. Kim, J.-Y.; Ahn, J.-H.; Kang, S.-W.; Kim, J.-H. *J. Appl. Phys.* **2007,** *101,* 073502–073508. doi:10.1063/1.2714685
13. Fortin, J. B.; Lu, T.-M. *Chemical vapor deposition polymerization: the growth and properties of parylene thin films;* Springer Science+Business Media, LLC, 2003. doi:10.1007/978-1-4757-3901-5
14. Tan, C. P.; Craighead, H. G. *Materials* **2010,** *3,* 1803–1832. doi:10.3390/ma3031803
15. Elkasabi, Y.; Chen, H.-Y.; Lahann, J. *Adv. Mater.* **2006,** *18,* 1521–1526. doi:10.1002/adma.200502454
16. Jiang, X.; Chen, H.-Y.; Galvan, G.; Yoshida, M.; Lahann, J. *Adv. Funct. Mater.* **2008,** *18,* 27–35. doi:10.1002/adfm.200700789
17. Coclite, A. M.; Howden, R. M.; Borrelli, D. C.; Petruczok, C. D.; Yang, R.; Yagüe, J. L.; Ugur, A.; Chen, N.; Lee, S.; Jo, W. J.; Liu, A.; Wang, X.; Gleason, K. K. *Adv. Mater.* **2013,** *25,* 5392–5423. doi:10.1002/adma.201301878
18. Gleason, K. K., Ed. *CVD Polymers: Fabrication of Organic Surfaces and Devices;* Wiley-VCH Verlag GmbH & Co. KGaA: Weinheim, Germany, 2015. doi:10.1002/9783527690275
19. Reeja-Jayan, B.; Moni, P.; Gleason, K. K. *Nanosci. Nanotechnol. Lett.* **2015,** *7,* 33–38. doi:10.1166/nnl.2015.1902
20. Fortin, J. B.; Lu, T.-M. *Chem. Mater.* **2002,** *14,* 1945–1949. doi:10.1021/cm010454a
21. Baxamusa, S. H.; Gleason, K. K. *Chem. Vap. Deposition* **2008,** *14,* 313–318. doi:10.1002/cvde.200806713
22. Kisliuk, P. *J. Phys. Chem. Solids* **1957,** *3,* 95–101. doi:10.1016/0022-3697(57)90054-9
23. Lau, K. K. S.; Gleason, K. K. *Macromolecules* **2006,** *39,* 3688–3694. doi:10.1021/ma0601619
24. Xu, J.; Gleason, K. K. *ACS Appl. Mater. Interfaces* **2011,** *3,* 2410–2416. doi:10.1021/am200322k
25. Ozaydin-Ince, G.; Gleason, K. K. *Chem. Vap. Deposition* **2010,** *16,* 100–105. doi:10.1002/cvde.200906821
26. Limb, S. J.; Labelle, C. B.; Gleason, K. K.; Edell, D. J.; Gleason, E. F. *Appl. Phys. Lett.* **1996,** *68,* 2810–2812. doi:10.1063/1.116332

27. Martin, T. P.; Kooi, S. E.; Chang, S. H.; Sedransk, K. L.; Gleason, K. K. *Biomaterials* **2007,** *28,* 909–915. doi:10.1016/j.biomaterials.2006.10.009
28. O'Shaughnessy, W. S.; Murthy, S. K.; Edell, D. J.; Gleason, K. K. *Biomacromolecules* **2007,** *8,* 2564–2570. doi:10.1021/bm070242s
29. Baxamusa, S. H.; Montero, L.; Dubach, J. M.; Clark, H. A.; Borros, S.; Gleason, K. K. *Biomacromolecules* **2008,** *9,* 2857–2862. doi:10.1021/bm800632d
30. Xu, J.; Gleason, K. K. *Chem. Mater.* **2010,** *22,* 1732–1738. doi:10.1021/cm903156a
31. Bong, K. W.; Xu, J.; Kim, J.-H.; Chapin, S. C.; Strano, M. S.; Gleason, K. K.; Doyle, P. S. *Nat. Commun.* **2012,** *3,* 805. doi:10.1038/ncomms1800
32. Carrow, B. P.; Bakhru, H.; Wang, P.-I.; Chen, Y.; Senkevich, J. J. *Chem. Vap. Deposition* **2006,** *12,* 239–244. doi:10.1002/cvde.200506426
33. Ganguli, S. Step coverage of metals and interlayer dieletrics in multilevel metallization. Ph.D. Thesis, Troy, NY, 1997.
34. Alf, M. E.; Asatekin, A.; Barr, M. C.; Baxamusa, S. H.; Chelawat, H.; Ozaydin-Ince, G.; Petruczok, C. D.; Sreenivasan, R.; Tenhaeff, W. E.; Trujillo, N. J.; Vaddiraju, S.; Xu, J.; Gleason, K. K. *Adv. Mater.* **2009,** *22,* 1993–2027. doi:10.1002/adma.200902765
35. Chen, B.; Seidel, S.; Hori, H.; Gupta, M. *ACS Appl. Mater. Interfaces* **2011,** *3,* 4201–4205. doi:10.1021/am200836n
36. Lau, K. K. S.; Gleason, K. K. *Adv. Mater.* **2006,** *18,* 1972–1977. doi:10.1002/adma.200600896
37. Karaman, M.; Çabuk, N.; Özyurt, D.; Köysüren, Ö. *Appl. Surf. Sci.* **2012,** *259,* 542–546. doi:10.1016/j.apsusc.2012.07.079
38. Dameron, A. A.; Seghete, D.; Burton, B. B.; Davidson, S. D.; Cavanagh, A. S.; Bertrand, J. A.; George, S. M. *Chem. Mater.* **2008,** *20,* 3315–3326. doi:10.1021/cm7032977
39. Chen, N.; Reeja-Jayan, B.; Lau, J.; Moni, P.; Liu, A.; Dunn, B.; Gleason, K. K. *Mater. Horiz.* **2015,** *2,* 309–314. doi:10.1039/C4MH00246F
40. Brown, J. J.; Hall, R. A.; Kladitis, P. E.; George, S. M.; Bright, V. M. *ACS Nano* **2013,** *7,* 7812–7823. doi:10.1021/nn402733g
41. Howden, R. M.; Flores, E. J.; Bulović, V.; Gleason, K. K. *Org. Electron.* **2013,** *14,* 2257–2268. doi:10.1016/j.orgel.2013.05.004
42. Nejati, S.; Minford, T. E.; Smolin, Y. Y.; Lau, K. K. S. *ACS Nano* **2014,** *8,* 5413–5422. doi:10.1021/nn500007c
43. Lau, K. K. S.; Bico, J.; Teo, K. B. K.; Chhowalla, M.; Amaratunga, G. A. J.; Milne, W. I.; McKinley, G. H.; Gleason, K. K. *Nano Lett.* **2003,** *3,* 1701–1705. doi:10.1021/nl034704t
44. Vaddiraju, S.; Cebeci, H.; Gleason, K. K.; Wardle, B. L. *ACS Appl. Mater. Interfaces* **2009,** *1,* 2565–2572. doi:10.1021/am900487z
45. Ye, Y.; Mao, Y.; Wang, H.; Ren, Z. *J. Mater. Chem.* **2012,** *22,* 2449–2455. doi:10.1039/C1JM14547A
46. Kim, D.; Im, H.; Kwak, M. J.; Byun, E.; Im, S. G.; Choi, Y.-K. *Sci. Rep.* **2016,** *6,* 29993. doi:10.1038/srep29993
47. Kim, S.; Sojoudi, H.; Zhao, H.; Mariappan, D.; McKinley, G. H.; Gleason, K. K.; Hart, A. J. *Sci. Adv.* **2016,** *2,* e1601660. doi:10.1126/sciadv.1601660
48. Wang, M.; Wang, X.; Moni, P.; Liu, A.; Kim, D. H.; Jo, W. J.; Sojoudi, H.; Gleason, K. K. *Adv. Mater.* **2016,** *29,* 1604606–1604620. doi:10.1002/adma.201604606
49. He, Y.; Piper, D. M.; Gu, M.; Travis, J. J.; George, S. M.; Lee, S.-H.; Genc, A.; Pullan, L.; Liu, J.; Mao, S. X.; Zhang, J.-G.; Ban, C.; Wang, C. *ACS Nano* **2014,** *8,* 11816–11823. doi:10.1021/nn505523c
50. Zhou, Y.; Lachman, N.; Ghaffari, M.; Xu, H.; Bhattacharya, D.; Fattahi, P.; Abidian, M. R.; Wu, S.; Gleason, K. K.; Wardle, B. L.; Zhang, Q. M. *J. Mater. Chem. A* **2014,** *2,* 9964–9969. doi:10.1039/c4ta01785d
51. Zhou, Y.; Xu, H.; Lachman, N.; Ghaffari, M.; Wu, S.; Liu, Y.; Ugur, A.; Gleason, K. K.; Wardle, B. L.; Zhang, Q. M. *Nano Energy* **2014,** *9,* 176–185. doi:10.1016/j.nanoen.2014.07.007
52. Moon, H.; Seong, H.; Shin, W. C.; Park, W.-T.; Kim, M.; Lee, S.; Bong, J. H.; Noh, Y.-Y.; Cho, B. J.; Yoo, S.; Im, S. G. *Nat. Mater.* **2015,** *14,* 628–635. doi:10.1038/nmat4237

License and Terms

BEILSTEIN JOURNAL OF NANOTECHNOLOGY

Synthesis of coaxial nanotubes of polyaniline and poly(hydroxyethyl methacrylate) by oxidative/initiated chemical vapor deposition

Alper Balkan[‡1], Efe Armagan[‡1] and Gozde Ozaydin Ince[*1,2]

Full Research Paper

Open Access

Address:
[1]Materials Science and Nanoengineering Program, Faculty of Engineering and Natural Sciences, Sabanci University, Tuzla, Istanbul 34956, Turkey and [2]Nanotechnology Application Center, Sabanci University, Orhanli, Tuzla, Istanbul 34956, Turkey

Email:
Gozde Ozaydin Ince[*] - gozdeince@sabanciuniv.edu

* Corresponding author ‡ Equal contributors

Keywords:
coaxial nanotubes; humidity sensors; initiated chemical vapor deposition; oxidative chemical vapor deposition; polyaniline

Beilstein J. Nanotechnol. **2017,** *8,* 872–882.
doi:10.3762/bjnano.8.89

Received: 15 January 2017
Accepted: 21 March 2017
Published: 18 April 2017

This article is part of the Thematic Series "Vapor-based polymers: from films to nanostructures".

Guest Editor: M. Koenig

Abstract

Vapor-phase synthesis techniques of polymeric nanostructures offer unique advantages over conventional, solution-based techniques because of their solventless nature. In this work, we report the fabrication of coaxial polymer nanotubes using two different chemical vapor deposition methods. The fabrication process involves the deposition of an outer layer of the conductive polyaniline (PANI) by oxidative chemical vapor deposition, followed by the deposition of the inner layer of poly(2-hydroxyethyl methacrylate) (pHEMA) hydrogel by initiated chemical vapor deposition. The vapor-phase techniques allowed for fine-tuning of the thickness of the individual layers, keeping the functionalities of the polymers intact. The response of the single components and the coaxial nanotubes to changes in humidity was investigated for potential humidity sensor applications. For single-component conductive PANI nanotubes, the resistance changed parabolically with relative humidity because of competing effects of doping and swelling of the PANI polymer under humid conditions. Introducing a hydrogel inner layer increased the overall resistance, and enhanced swelling, which caused the resistance to continuously increase with relative humidity.

Introduction

In recent years, with the advances in nanotechnology, the use of nanostructured materials has become widespread in various applications, such as biotechnology [1,2], food industry [3,4], sensors [5] or photovoltaics [6]. Polymeric nanostructures have attained special interest because of their prominent advantages, such as cost-effectiveness, ease of fabrication and biocompatibility making these nanostructures applicable in different areas [7,8]. Among these, the conducting polymer (CP) nanostruc-

tures, such as nanowires, nanorods, nanotubes or nanospheres have been extensively studied through solution-based techniques, such as chemical polymerization [9-11] or electrochemical polymerization [12-14] for applications in light emitting diodes [15], photovoltaic cells [16,17], supercapacitors [18], sensors [19] and drug delivery [20]. During synthesis of these nanostructures, the use of solvents is a major drawback for homogeneity and conformal coatings, especially on high-aspect-ratio templates, due to wetting effect and surface tension. Thus, vapor-phase polymerization techniques have emerged for the deposition of conducting polymers that facilitate the fabrication of conformal polymeric structures [21,22].

Polyaniline (PANI) is one of the well-known conducting polymers with applications in supercapacitors [18], sensors [23], solar cells [24] and membranes [25] because of its great thermal and environmental stability, ease of synthesis, excellent conductivity, cost-effectiveness and redox-tunability [26-29]. One of the original aspects of PANI is that its electrical conductivity can be tuned through oxidation and protonation steps. Depending on the oxidation level, PANI can exist in three different states: leucomeraldine base (fully reduced), emeraldine base (half-oxidized) and pernigraniline base (fully oxidized). However, only the emeraldine salt which is the protonated form of emeraldine has a good conductivity of 1–130 S/cm [30,31].

PANI is a good candidate material for sensor applications due to the change of oxidation/reduction level in response to changes in the environmental conditions, which, in turn, affect the electrical conductivity [32]. However, studies on PANI as humidity sensors are very limited. Zeng et al. [33] studied the resistance change of PANI nanofibers depending on the humidity level. They observed that the resistance changed parabolically as the humidity of the environment increased, and a minimum value for the resistance at a certain humidity level existed. The parabolic behavior with the same resistance readings for two different humidity levels is problematic for sensor applications, making the sensor unreliable. In order to modify this parabolic behavior, Parvatikar et al. [34] fabricated PANI/CeO_2 composites, whose resistance values decreased linearly as humidity increased due to charge transfer between CeO_2 and PANI. However, incorporating CeO_2 in the polymer decreases flexibility and increases the overall electrical resistance, which may limit the range of applications. Lin et al. [35] fabricated electrospun PANI nanofibers and introduced hydrophilic poly(ethylene oxide) and hydrophobic poly(vinyl butyral) into PANI to tune the sensitivity towards humidity. It was observed that increasing the fraction of the hydrophilic material within the sensor decreased resistance, whereas increasing the hydrophobicity resulted in higher resistance.

Our work here demonstrates the advantages of fabricating PANI nanotubes in combination with a hydrophilic material, namely poly(2-hydroxyethyl methacrylate) (pHEMA), enabling PANI to be used in humidity sensors with higher humidity sensitivity due to the open-mouth structure and the high surface area of the nanotubes. Furthermore, fabricating conductive nanotubes using templates with mesoscopic pores resulted in the alignment of polymer chains parallel to the tube axis, increasing conductivity above that of nonaligned films [36]. In this study, the fabrication of PANI nanotubes and PANI/pHEMA coaxial nanotubes were done via oxidative chemical vapor deposition (oCVD) and initiated chemical vapor deposition (iCVD) to enhance the control and sensitivity level of humidity sensors. By using the vapor deposition method oCVD, we achieved conformal coatings of PANI, which allowed us to produce nanotubes with high purity and controlled wall thickness. Furthermore, the oxidation state of PANI could be controlled by varying the oxidant flowrate for the purpose of achieving conductive emeraldine salt. The oCVD technique is based on step-growth polymerization where the polymerization takes place directly on the surface of the substrate. The oxidant, either liquid [37] or solid [38], and the monomers are delivered into the vacuum system simultaneously, initiating the polymerization reaction on the surface. The key advantages of oCVD are good homogeneity, retention of polymer functional groups due to low reaction temperature (25–100 °C), adequate electrical conductivity for a wide range of applications and high-quality conformal CP thin films on various non-planar surfaces [39-41]. In this study, the vapor-phase oCVD and iCVD techniques were used to conformally coat the walls of the pores of anodized aluminium oxide (AAO) track-etch membranes. The ability to control the thickness with high sensitivity using these vapor phase techniques allowed to produce coaxial nanotubes. The response of these nanotubes to the changes in humidity could be tuned by introducing the hydrogel inner layer.

Results and Discussion

The deposition of PANI films on a Si wafer was confirmed by Fourier-transform infrared (FTIR) analysis (Figure 1a). The broad peaks at 2850–3100 cm^{-1} and 3100–3600 cm^{-1} correspond to C–H and N–H stretching vibrations, respectively. The peak at 1590 cm^{-1} can be attributed to the quinoid ring stretching, while the peak at 1495 cm^{-1} is due to the benzenoid ring stretching [42].

A complementary structural analysis was performed with Raman spectroscopy (Figure 1b). The peak at 1193 cm^{-1} is due to C–H vibrations bending in benzoid units. The peaks at 1223 and 1272 cm^{-1} correspond to the bands related to amine groups. Between 1332 and 1376 cm^{-1}, the vibrations of delocalized polaronic structures can be observed. The peaks at 1458 and

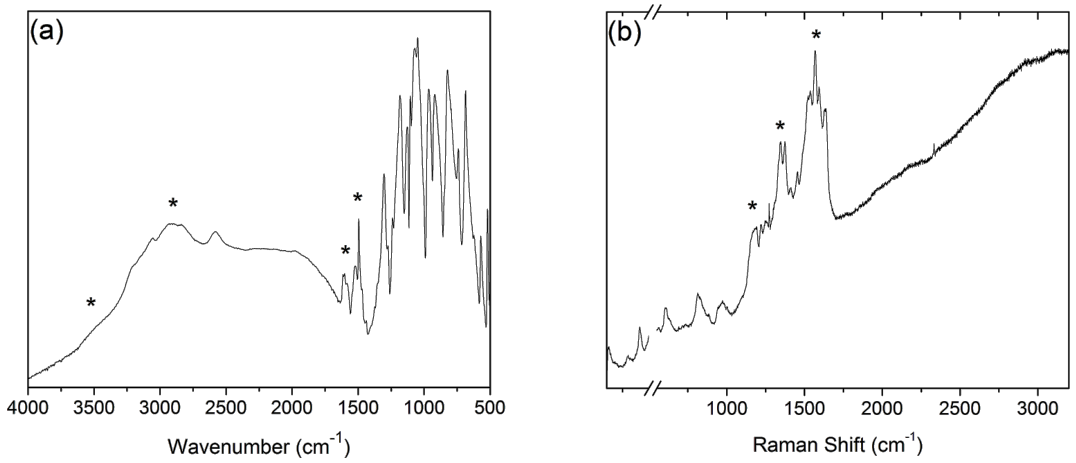

Figure 1: (a) FTIR spectra of PANI emeraldine thin film on a Si wafer. The peaks at 1590 and 1495 cm^{-1} correspond to stretching vibrations of the quinoid and benzenoid rings, respectively. (b) RAMAN spectra of PANI emeraldine thin film on a Si wafer. The peak at 1638 cm^{-1} corresponds to the C–C stretching vibrations in benzoid units, while the peaks due to the C=N and C=C stretching vibrations in quinoid units appear at 1458 and 1569 cm^{-1}, respectively. Both the FTIR and RAMAN spectra confirm the polymerization of PANI.

1569 cm^{-1} correspond to C=N and C=C stretching vibrations in quinoid units, respectively. At 1638 cm^{-1}, the peak for C–C stretching vibrations in benzoid units is present. The results obtained are in good agreement with literature confirming the successful polymerization of PANI thin films [43].

In order to confirm the formation of the protonated emeraldine salt form of PANI, UV–vis analysis was performed on the thin film samples. Figure 2a shows the UV–vis spectra of the as-deposited PANI films with three characteristic peaks at 360, 430 and 796 nm, indicating the formation of a polaron band transition. Furthermore, the peak at 430 nm originates from polaron–bipolaron band transitions consistent with the emeraldine salt form of PANI [44].

The band gaps of both annealed (80 °C) and as-deposited PANI samples were found using the UV–vis spectra (Figure 2b). The band gap of PANI can be calculated from the wavelength of the polaron band excitation [45]. The onset of absorption of the polaron band excitation was used to find the band gap energies, E_g, of both samples. The E_g of as-deposited and annealed samples were calculated as 2.38 and 2.26 eV, respectively. The slight decrease in the band gap with increasing annealing temperature is consistent with previous PANI studies. Joshi et al. reported that the band gap of PANI decreases as the annealing temperature increases up to 100 °C because of the formation of a new crystalline region and the rearrangement of the existing crystalline region [46]. However, annealing at temperatures above 100 °C initiates deformation and causes damage in the

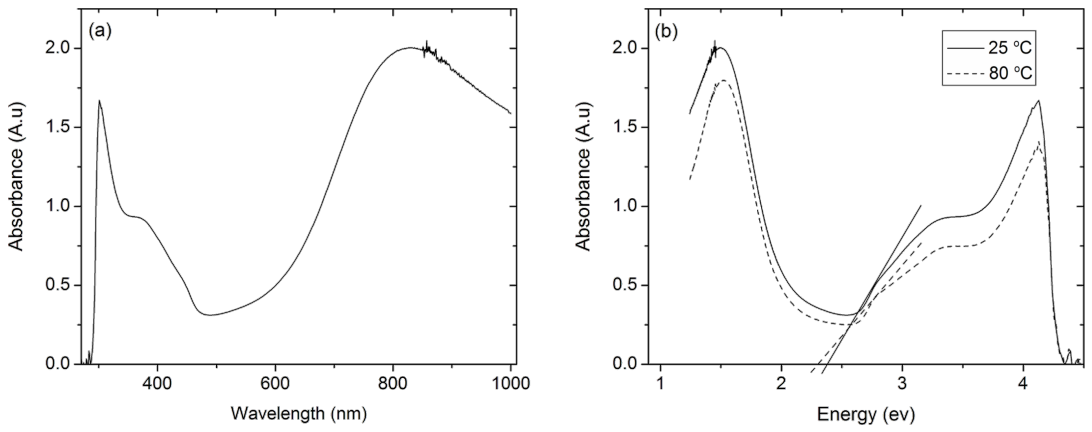

Figure 2: (a) UV–vis spectrum of as-deposited PANI thin films. Three characteristic peaks at 360, 430 and 796 nm indicate the formation of a polaron band transition. The peak at 430 nm due to the polaron–bipolaron band transition confirms the deposition of the emeraldine salt form of PANI. (b) UV–vis spectra of as-deposited and annealed PANI thin films. Bandgaps of 2.38 and 2.26 eV were calculated for the as-deposited and annealed samples, respectively, confirming the formation of the protonated emeraldine salt form of PANI.

crystalline structure of PANI polymer chains resulting in the increase of the band gap energy.

The crystallinity of the deposited films was studied by using XRD analysis (Figure 3). The spectra of the non-annealed, as-deposited samples did not show any distinct peaks, indicating the amorphous state of the films. However, after an annealing process at 80 °C for 4 h, the measurements revealed two peaks at the characteristic 2θ angles of PANI, 16° and 25°, which correspond to the (011) and (200) planes, respectively. These results are attributed to the reorganization of the chains during annealing to form crystalline regions. However, the broadness of the peaks indicate a low degree of crystallinity [47].

The surface morphology of the PANI thin films was examined by using AFM analysis (Figure 4). The RMS surface roughness of the as-deposited thin films of 350 nm thickness was measured as 30 nm on a flat substrate, and the roughness increased with film thickness. When the annealing temperature was increased, the RMS roughness of the PANI thin films decreased. The decrease in surface roughness with increasing temperatures can be explained by the rearrangement of amorphous part of polymer chains and formation of new crystalline regions on the surface that reduce the irregularity and increase the percentage of crystalline regions on the surface [48,49].

The conductivity studies of the thin film samples were performed with a four-point probe in air. Figure 5 shows the conductivity values of the as-deposited (25 °C) samples and samples annealed at temperatures ranging from 40 to 180 °C for 4 h. The highest conductivity value of ca. 26 S/cm was obtained with the sample annealed at 100 °C. This conductivity increase is attributed to the increase in crystallinity with annealing, which leads to reduced hopping distance between chains and crystal domains [50]. However, above 100 °C the polymer starts degrading, resulting in damage to the crystalline structure and reduction of the conductivity.

For sensor applications, the long-term stability of the deposited films was investigated. The conductivities of the PANI coated glass were recorded with a four-point probe in air over 30 days. Figure 6 shows that the decrease in the conductivities of the samples was less than 2% at the end of 30 days, indicating the electrical stability of the films required for long-term applications. Furthermore, the electrical stability of the samples was observed to be independent of the annealing temperatures.

For humidity experiments, circular gold electrodes were evaporated on the PANI films and the resistance was measured using a two-point probe to ensure consistency with the electrical characterization of the nanotube samples. The diameters of the gold electrodes were optimized at 200 μm in order to provide better DC resistance. The lower resistance of 3772 kΩ of PANI-coated glass with electrodes compared to the resistance of 65664 kΩ of PANI-coated glass without electrodes measured in air can be explained by the reduced contact resistance between the PANI thin film and the probes in the presence of gold electrodes.

For PANI flat films, the actual resistance values (R) versus relative humidity (RH%) are plotted in Figure 7. The resistance slightly decreases as RH% increases up to a certain value (RH% of 84.3%). Above 84.3% resistance starts to increase with humidity. The change in the conductivity of the PANI polymer with humidity is the result of the increasing doping level of the polymer due to the proton exchange facilitated by the H-bonds between the water molecules and N-atoms in the backbone [51]. The ionizable water molecules dissociate into positive protons and negative hydroxyl ions upon entering the polymer chain.

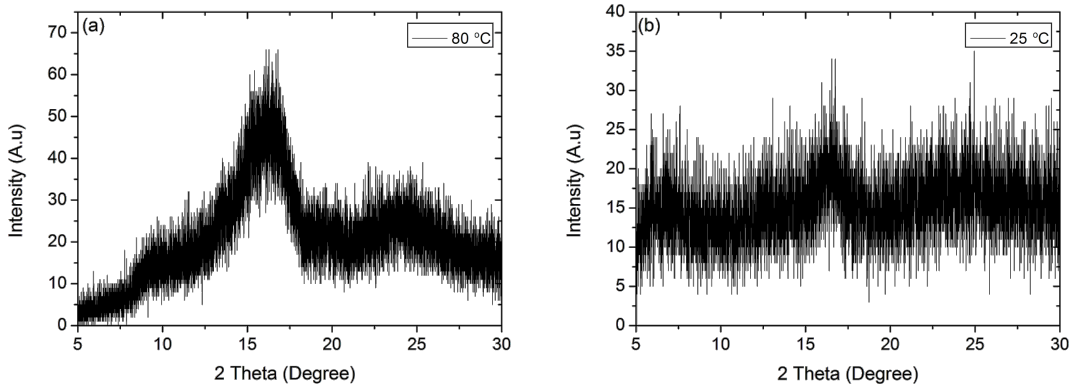

Figure 3: XRD spectra of (a) annealed and (b) as-deposited PANI thin films. After annealing at 80 °C for 4 h, characteristic peaks of PANI appear at 16° and 25°, which correspond to (011) and (200) planes, respectively, confirming the crystallinization of the polymer film upon annealing.

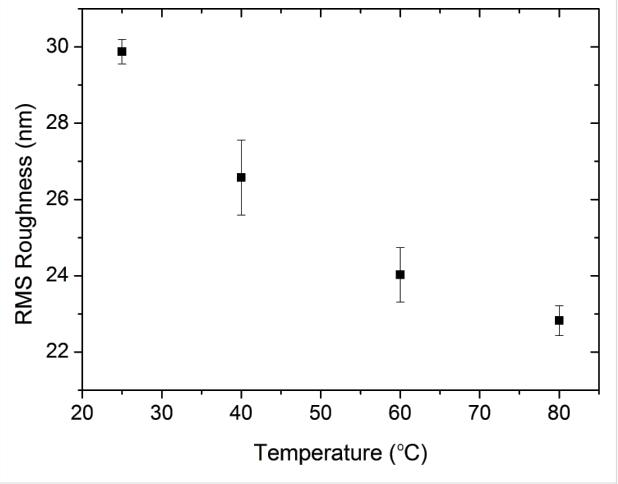

Figure 4: Surface roughness of PANI thin films annealed at 25, 40, 60 and 80 °C. The surface roughness of the polymer thin films decreases as a result of the increased crystallinity as the annealing temperature increases.

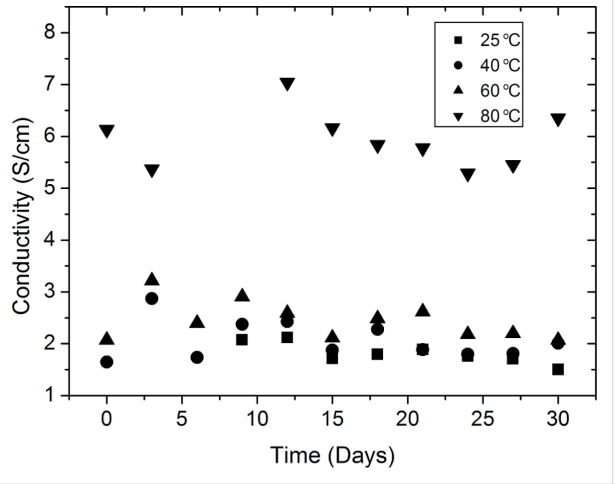

Figure 6: Time dependence of the electrical conductivity of PANI thin films annealed at different temperatures. The decrease in the conductivity after 30 days was less than 2% and did not depend on the annealing temperature.

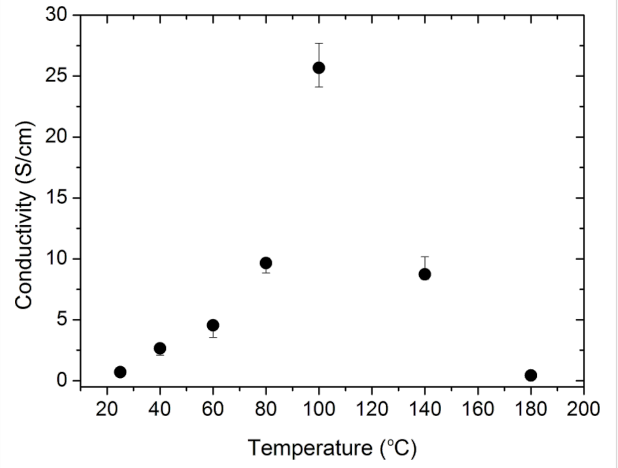

Figure 5: Electrical conductivity of PANI thin films at different annealing temperatures. The conductivity of the films increases with increasing annealing temperatures up to 100 °C because of the increase in crystallinity. Above 100 °C the crystalline structure is damaged leading to the reduction of conductivity.

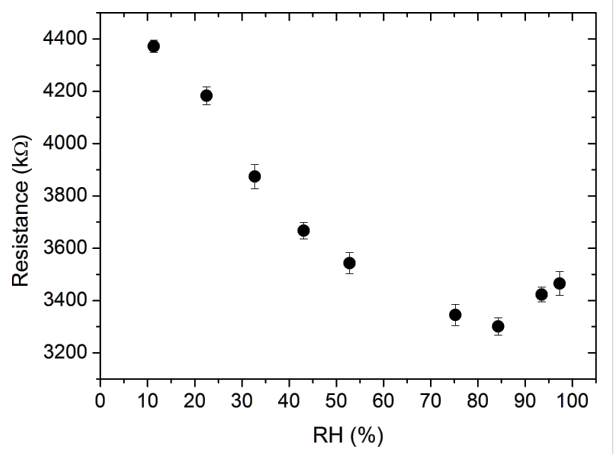

Figure 7: Resistance of PANI thin films as a function of the relative humidity measured using a two-point probe. The parabolic dependency is the result of the competitive effects of doping and swelling of the polymer.

The protons dope the polymer further until the undoped parts of the emeraldine salt is mostly doped with the H^+ ions, after which swelling starts dominating. Swelling of the polymer due to excess water in the ambient results in higher hoping distances and creates distortion in the polymer chains, reducing the conductivity. The maximum resistance of 4372 kΩ was obtained at RH% of 11.3%, whereas the minimum was obtained at 84.3% which is 3301 kΩ.

Single-component PANI and coaxial PANI/pHEMA nanotubes were fabricated using sacrificial AAO membranes. The same process parameters during the polymer deposition were used during the fabrication of both nanotubes and thin films. Figure 8 shows the SEM images of the coaxial and single component PANI nanotubes after removal of the AAO membrane. The fabricated nanotubes are approximately 200 ± 10 nm in diameter with lengths of 3–4 μm.

Circular gold electrodes were evaporated on the nanotubes for the resistance measurements and the change in the resistance of the nanotubes with humidity was measured using two-point probe. For pure PANI nanotubes the resistance at different relative humidity values is shown in Figure 9. The maximum resistance, which is obtained at 97.3%, is 1023 kΩ while the minimum resistance was measured as 75 kΩ at 52.8%. It should

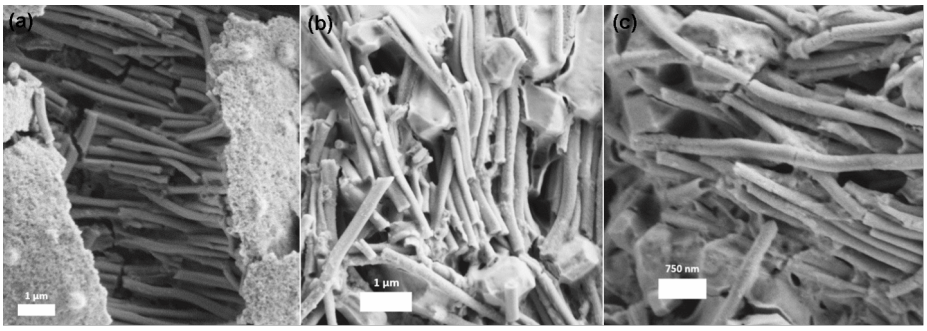

Figure 8: High resolution SEM images of (a) coaxial PANI/pHEMA and (b-c) PANI single component nanotubes.

be noted that since the measurements are taken 30 s after the samples are removed from the humid environment, the measured resistance values may be smaller than the resistances when the samples are in the humid atmosphere. However, the trend of the resistance change with the humidity is not expected to be affected by this delay.

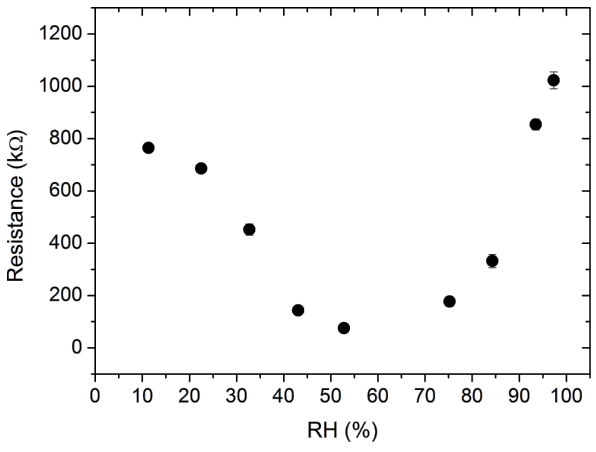

Figure 9: Resistance of single-component PANI nanotubes as a function of the relative humidity. The competing effects of doping and swelling lead to the parabolic behavior, which is similar to the observed behavior in PANI thin films.

The significant resistance difference between PANI nanotubes and PANI thin film stems from the alignment of the polymer chains when deposited inside the pores of a template [36]. This supermolecular order leads to improved conjugation lengths with fewer bends and kinks in the linear polymer chains [52] leading to increased conductivities in nanotubes compared to thin films.

A similar parabolic dependence of resistance on the humidity as observed in the thin films was also observed in the nanotube samples (Figure 9). This type of parabolic dependence of resistance on the humidity was previously reported for PANI nanotubes [53]. The competition between the doping and swelling effects determines at which RH% value the reversal in the behavior of resistance will occur [33]. Comparing the RH% value at which this reversal occurs for the PANI thin films to that of the nanotubes, it is observed that for PANI nanotubes this transition occurs at 52.8%. This is significantly lower than 84.3% that is observed for thin films. This difference can be explained by the high surface-to-volume ratios of the nanotubes compared to the thin films. Due to their high surface-to-volume ratios, more polymer chains are exposed to water molecules in the nanotubes. Even lower humidity levels enable the undoped regions of polymer chains of the nanotubes to be doped with H^+ ions, resulting in an early onset of this transition behavior.

Comparing PANI thin films (Figure 7) to the nanotubes (Figure 9) in terms of the dependence of their resistance on relative humidity, it is observed that the dependence of resistance on RH% is significantly stronger for nanotubes compared to the thin films. The resistance of nanotubes changes from 1023 kΩ to 75 kΩ whereas for the thin films, the change of resistance is only 25%. The higher sensitivity of the nanotubes to the changes in relative humidity can again be explained by the high surface-to-volume ratio of the nanotubes, enabling more water molecules to interact with polymer chains. This improved sensitivity is especially desirable for humidity sensors.

The main issue with the nanotubes sensor is that within the measurement range of 0–100% relative humidity, the resistance values go through a minimum, resulting in same resistance values at two different humidity levels [33]. As explained in the earlier sections, this minimum is due to the competition between the swelling and doping effects. Incorporating another polymer layer that is sensitive purely to humidity is expected to distinguish between low and high humidity levels, causing differences in the measured resistance values. For this purpose,

coaxial nanotubes with pHEMA inner layers and PANI outer layers were fabricated. pHEMA is an insulating hydrogel that is highly sensitive to ambient humidity. The effect of relative humidity on the resistance changes for the coaxial nanotubes is plotted in Figure 10a. According to these results, the resistance values increase parabolically with increasing humidity levels. The increase of resistance is limited (5%) between the humidity levels of 11.3% and 32.7%, indicating poor sensitivity, which is not desirable for a sensor. However, above 32.7% resistance values increase significantly until 97.3% of relative humidity. The maximum resistance of 4027 kΩ was obtained at 97.3%, whereas the minimum resistance was 957 kΩ at the humidity level of 22.5%.

Figure 10b compares coaxial nanotubes to the single-component nanotubes in terms of the dependence of their resistance on relative humidity. The significant difference between the single-component and the coaxial nanotubes in terms of the resistance dependence on the humidity levels stems from the existence of hydrogel pHEMA in the coaxial nanotubes. As stated earlier, pHEMA is sensitive to humidity and swells or shrinks in response to the water level in the ambient. As humidity increases, pHEMA swells which results in an increased distance between each polymer chain, affecting the electronic structure of the nanotubes. The swelling of the inner pHEMA layer, leads to an overall increase in the nanotube diameter, and thus swelling of the outer PANI layer. The longer distances between PANI chains increase the hoping resistance of polymer structure so that the resistance of coaxial nanotubes increases with increasing humidity levels. The doping effect, therefore, is dominated by the swelling effect in the presence of pHEMA layer. At low humidity levels (up to 22.5%), on the other hand, due to the limited swelling of the pHEMA layer, doping effect balances out the swelling effect, resulting in weaker dependence of resistance on humidity.

The stability of single-component and coaxial PANI nanotubes sensors was studied by performing cyclic measurements at two different RH% values. Figure 11a shows the measured resistance of the single-component nanotubes at RH% values of 35% and 52.8%. In the first cycle, the resistance was measured as 336 kΩ and 79 kΩ at 35% and 52.8%, respectively, whereas, in the tenth cycle, the PANI resistance was 334 kΩ and 87 kΩ at 35% and 52.8%, respectively. The change in measured resistance values at both humidity levels is lower than 10%, indicating the stability of the sensors at the end of 10 cycles. The cyclic measurements of coaxial nanotubes were repeated 10 times at RH% values of (35%) and 22.5% (Figure 11(b)). In the first cycle, the resistance was measured as 1154 kΩ and 943 kΩ at 35% and 22.5%, respectively. In the tenth cycle, the resistance was 1246 kΩ and 983 kΩ, at 35% and 22.5%, respectively. The change in the resistance values at the end of 10 cycles is less than 10%, confirming the stability of the nanotubes.

Conclusion

Single-component conducting PANI nanotubes and coaxial polymer nanotubes with PANI outer layer and hydrogel pHEMA inner layer were synthesized using iCVD and oCVD techniques. Ability to control the thickness during deposition via these vapor-phase methods allowed depositing two layers of different polymers inside the pores of AAO track-etch membranes.

The characterization of the PANI thin films deposited by the vapor-phase oCVD method showed that crystalline PANI thin

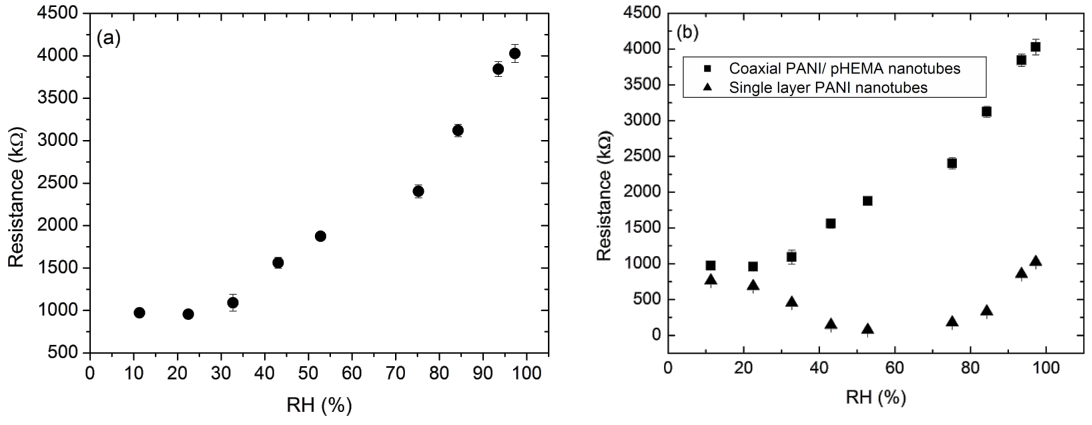

Figure 10: (a) Change in the resistance of coaxial PANI/pHEMA nanotubes with relative humidity. (b) Comparison of the single component and coaxial nanotubes in terms of humidity effect on resistance. The parabolic behavior observed in single-component nanotubes is not observed in the coaxial nanotubes, suggesting the dominance of the swelling effect in the presence of pHEMA hydrogel inner layer.

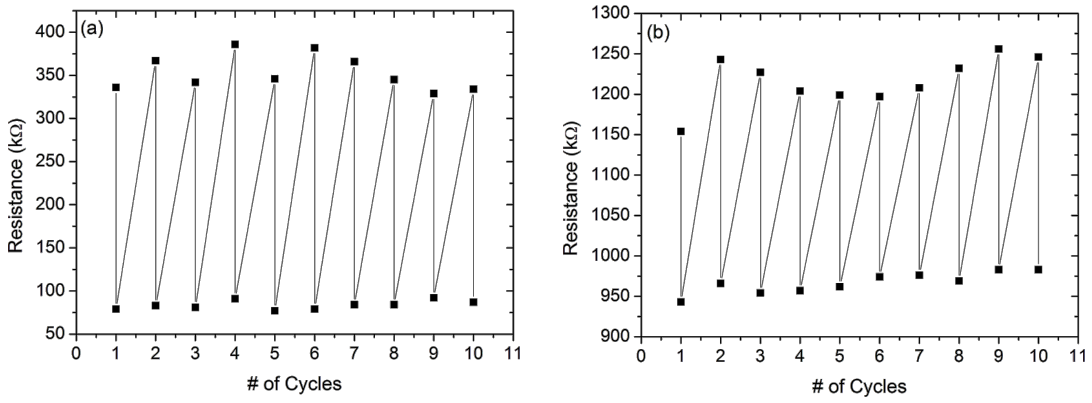

Figure 11: Cyclic resistance measurements of (a) the single component PANI nanotubes at RH% of 35% and 52.8% and (b) coaxial PANI/pHEMA nanotubes at RH% of 35% and 22.5%. At the end of 10 cycles, the change in the resistance is less than 10%.

films could be obtained upon annealing the samples. Conductivity also increased with annealing temperature due to the reduced hopping distance between chains and crystal domains. The results obtained agree with the conventional, solution-based PANI deposition methods reported in literature.

Performance of the single-component and coaxial nanotubes as humidity sensors were tested under different humidity conditions. The competition between the doping and swelling mechanisms of the polymer upon exposure to humidity leads to an increase in the conductivity with humidity until a specific humidity level, above which conductivity decreases. To improve the sensitivity of the sensors an inner hydrogel layer was introduced, delaying the response of the PANI layer. The hydrogel layer in the coaxial nanotubes might further facilitate the swelling effect, which dominates doping, resulting in resistance values that continuously increase with humidity.

The ability to tune the response of the nanotube sensors to humidity by introducing a hydrogel layer will help to improve the sensitivity of the sensors. Furthermore, by incorporating different polymers in the coaxial sensors application areas of these sensors can be extended.

Experimental

The monomers aniline (99.5%, Sigma-Aldrich), HEMA (99%, Sigma Aldrich), the crosslinker ethylene glycol dimethacrylate (98%, Sigma Aldrich) (EGDMA), the initiator *tert*-butyl peroxide (98%, Sigma Aldrich) (TBPO) and the oxidant antimony pentachloride (99%, Sigma Aldrich) ($SbCl_5$) were used as received.

Aniline was heated in a metal jar up to 60 °C while $SbCl_5$ was kept at room temperature in a glass jar. Both chemicals were delivered to the system in vapor phase through different ports facing the substrate surface. Glass slides, Si(100) wafers and anodic aluminum oxide template (AAO) with pore sizes of 200 nm were used as substrates and were coated simultaneously. Glass slides were used for electrical conductivity measurements and UV–visible spectroscopy (UV–vis). Si wafers were used for Fourier-transform infrared (FTIR) spectrophotometry, Raman spectroscopy, atomic force microscopy (AFM) and electron microscopy. AAO templates were used for PANI nanotube synthesis. During deposition, the flowrates of aniline and $SbCl_5$ were maintained at 1.6 sccm and 1.2 sccm, respectively, at 25 mTorr of operating pressure for 15 min. The stage temperatures varied between 25 and 80 °C for different experiments. After the polymer coating, PANI-coated Si wafers were annealed at temperatures ranging between 40 and 180 °C for 4 h in a vacuum oven.

For PANI flat thin film characterization, FTIR spectrophotometry (Thermo Fischer Scientific Model NICOLETiS10) and Raman spectrometry (Renishaw, inVia Reflex) were used to analyze chemical properties of PANI. FTIR spectra were acquired with 4 cm^{-1} resolution. Raman measurements were carried out at 532 nm wavelength and 50 mW power. Furthermore, UV–vis spectrometry (Shimadzu, UV-VIS 3150) was used on PANI-coated glass slides in order to find the band gap of fabricated PANI and to confirm the electrical conductivity of the film by calculating band-transition energies. Atomic force microscopy (Bruker Multimode 8, ScanAsyst) was used to acquire topography and surface roughness of as-deposited and annealed PANI samples.

X-ray diffraction (XRD) (Bruker, D8 Advance XRD) analysis was performed to study the crystalline state of the annealed and as-deposited PANI films. The measurements were taken on as-deposited PANI and PANI samples annealed at 80 °C at 2θ angles of 5–40° in order to eliminate the peak originating

from the Si(100) planes. Each measurement took 4 h for an adequate signal-to-noise ratio. Thickness of the films on Si wafer and glass substrates was measured with a spectroscopic ellipsometer (M-2000, J. A. Woollam) at 65, 70, and 75° within a range of 300–800 nm. For electrical characterization of the PANI thin films, *I–V* curves were obtained using a four-point probe at 0.01 μA and the measurements were taken at four different locations (Lucas Labs Pro 4, Keithley 2400 Sourcemeter).

For the fabrication of the coaxial PANI/pHEMA nanotubes PANI was first deposited on AAO templates via oCVD and then the coated templates were exposed to oxygen plasma to remove excess polymer layer on top of AAO membranes. Subsequently, PANI-coated templates were put inside an iCVD chamber for pHEMA deposition. During iCVD depositions, HEMA and EGDMA were heated up to 70 and 85°C, respectively, and TBPO was kept at room temperature. The deposition was performed at 120 mTorr with a stage temperature of 40 °C. The flowrates of HEMA, EGDMA and TBPO were set to 0.8, 0.11 and 1 sccm, respectively. After the deposition, AAO templates coated with PANI and pHEMA were exposed to oxygen plasma (Torr) at 50 W to remove the excess film on the top of the templates. Afterwards, AAO templates were attached to Si wafers and immersed in 0.5 M HCl solution for 48 h to release the coaxial nanotubes, which were then allowed to dry in the air for two days. This allowed immobilization of the free-standing nanotubes on Si wafers for imaging and sensor studies. Figure 12 shows the fabrication steps of nanostructures used in this study. The synthesized coaxial nanotubes had PANI on the outer side and pHEMA inside. Images of the nanotubes were taken with a field-emission scanning electron microscope (FESEM, Zeiss, SUPRA VP 35).

For the electrical characterization of the PANI thin films and PANI/pHEMA nanotubes, an array of chrome (3 nm) and gold (150 nm) electrodes with a diameter of 200 μm and a spacing of 200 μm were deposited on the nanotubes and thin films using an e-beam evaporator (Torr). Prior to the e-beam evaporation, conventional lithography with a shadow mask was used to create a pattern for the electrodes. The photoresist AZ 5214 E

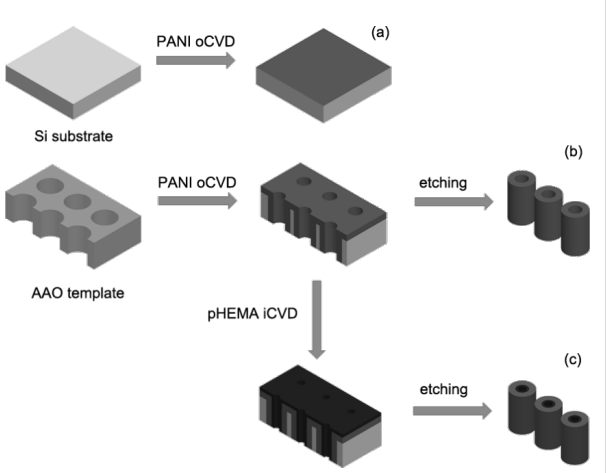

Figure 12: Fabrication steps of nanostructures. (a) PANI thin films are prepared by coating thin layer of PANI on Si surfaces using oCVD. (b) Single-component PANI nanotubes are fabricated by coating the pores of templates with PANI using oCVD. The templates are then etched to release the nanotubes. (c) Coaxial PANI/pHEMA nanotubes are prepared by first coating the pores of templates with PANI polymer using oCVD, followed by iCVD coating of the pores with pHEMA. As the final step the templates are etched to release the nanotubes.

(Merck GmbH), the developer AZ 726 (MIF) (Merck GmbH) and deionized water (stopper) were used for the lithography. After the e-beam evaporation, samples were annealed at 100 °C for 4 h. Optical microscope (Zeiss, Axio Scope A1 MAT) image was taken to show the gold electrodes on the PANI thin film surface.

Both thin film and nanotube samples were then tested for sensor performance. For this purpose, a 2-Point probe (Keithley, 2401 Sourcemeter) was used for resistance measurements with constant DC current of 1 μA. In order to vary ambient humidity, several saturated salt solutions with different humidity levels were prepared in DI water. Table 1 lists the salt solutions and their relative humidity (RH) at room temperature.

Each salt solution and the samples were placed in a sealed box to isolate them from air (Figure 13) For resistance measurements, the samples were taken out from the sealed box and put on the two-point probe station. The initial measurements were

Table 1: Salt solutions and the relative humidity levels obtained in a sealed box by using these solutions.

salt solution	LiCl	CH_3CO_2K	$MgCl_2$	K_2CO_3	$Mg(NO_3)_2$
relative humidity	11.3%	22.5%	32.7%	43.1%	52.8%
salt solution	NaCl	KCl	KNO_3	K_2SO_4	
relative humidity	75.2%	84.3%	93.5%	97.3%	

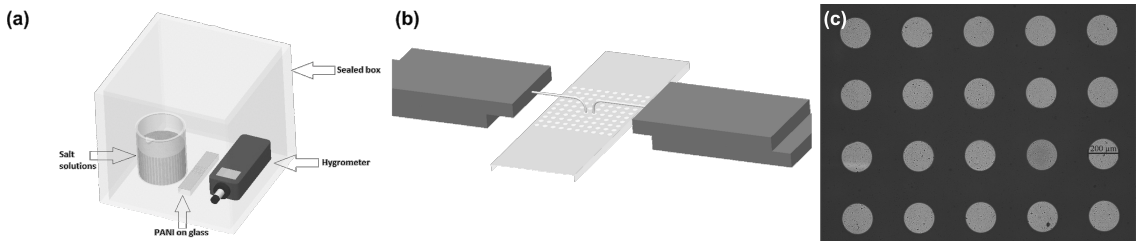

Figure 13: Experimental setup of humidity sensor measurements. (a) The sealed box containing the salt solution, the hygrometer and the nanotube sample. (b) The two-point probe station used for the resistance measurements. The probe station is outside the sealed box. (c) Optical microscope image of the gold electrodes.

taken 30 s after removing the samples from the sealed box. The cyclic resistance measurements were done by leaving the sample in ambient air (35% RH) for 10 min then measuring the resistance of the sample and repeating the same process for 52.8% RH environment within a sealed box.

Acknowledgements

This work was supported by the TUBITAK (The Scientific and Technological Research Council of Turkey) Support Program for Scientific and Technological Research Projects (Grant 114M165) and TUBA (Turkish Academy of Sciences) Young Scientist Award Program.

References

1. Gaharwar, A. K.; Peppas, N. A.; Khademhosseini, A. *Biotechnol. Bioeng.* **2014,** *111,* 441–453. doi:10.1002/bit.25160
2. Rapoport, N. *Prog. Polym. Sci.* **2007,** *32,* 962–990. doi:10.1016/j.progpolymsci.2007.05.009
3. Peteu, S. F.; Oancea, F.; Sicuia, O. A.; Constantinescu, F.; Dinu, S. *Polymers (Basel, Switz.)* **2010,** *2,* 229–251. doi:10.3390/polym2030229
4. de Azeredo, H. M. C.; Mattoso, L. H. C.; McHugh, T. H. Nanocomposites in Food Packaging – A Review. In *Advances in Diverse Industrial Applications of Nanocomposites;* Reddy, B., Ed.; In Tech, 2011; pp 57–78. doi:10.5772/14437
5. Liu, L.; Ye, X.; Wu, K.; Han, R.; Zhou, Z.; Cui, T. *Sensors* **2009,** *9,* 1714–1721. doi:10.3390/s90301714
6. Krogstrup, P.; Jørgensen, H. I.; Heiss, M.; Demichel, O.; Holm, J. V.; Aagesen, M.; Nygard, J.; Morral, A. F. *Nat. Photonics* **2013,** *7,* 306–310. doi:10.1038/nphoton.2013.32
7. Du, F.-S.; Wang, Y.; Zhang, R.; Li, Z.-C. *Soft Matter* **2010,** *6,* 835–848. doi:10.1039/B915020J
8. Chen, J.; Wang, F.; Liu, Q.; Du, J. *Chem. Commun.* **2014,** *50,* 14482–14493. doi:10.1039/C4CC03001J
9. Jang, J.; Yoon, H. *Langmuir* **2005,** *21,* 11484–11489. doi:10.1021/la051447u
10. Jang, J.; Chang, M.; Yoon, H. *Adv. Mater.* **2005,** *17,* 1616–1620. doi:10.1002/adma.200401909
11. Li, G.; Zhang, Z. *Macromolecules* **2004,** *37,* 2683–2685. doi:10.1021/ma035891k
12. Koo, Y. K.; Kim, B. H.; Park, D. H.; Joo, J. *Mol. Cryst. Liq. Cryst.* **2004,** *425,* 55–60. doi:10.1080/15421400490506496
13. Higuchi, T.; Nishiyama, H.; Suga, M.; Watanabe, H.; Takahara, A.; Jinnai, H. *Microscopy (Oxford, U. K.)* **2015,** *64,* 205–212. doi:10.1093/jmicro/dfv013
14. Huang, J.; Wang, K.; Wei, Z. *J. Mater. Chem.* **2010,** *20,* 1117–1121. doi:10.1039/B919928D
15. Boroumand, F. A.; Fry, P. W.; Lidzey, D. G. *Nano Lett.* **2005,** *5,* 67–71. doi:10.1021/nl048382k
16. Habisreutinger, S. N.; Leijtens, T.; Eperon, G. E.; Stranks, S. D.; Nicoholas, R. J.; Snaith, H. J. *Nano Lett.* **2014,** *14,* 5561–5568. doi:10.1021/nl501982b
17. Peng, S.; Zhu, P.; Wu, Y.; Mhaisalkar, S. G.; Ramakrishna, S. *RSC Adv.* **2012,** *2,* 652–657. doi:10.1039/C1RA00618E
18. Sumboja, A.; Tefashe, U. M.; Wittstock, G.; Lee, P. S. *Adv. Mater. Interfaces* **2015,** *2,* 1400154. doi:10.1002/admi.201400154
19. Liu, M.-C.; Dai, C.-L.; Chan, C.-H.; Wu, C.-C. *Sensors* **2009,** *9,* 869–880. doi:10.3390/s90200869
20. Abidian, M. R.; Kim, D.-H.; Martin, D. C. *Adv. Mater.* **2006,** *18,* 405–409. doi:10.1002/adma.200501726
21. Mohammedi, A.; Hassan, M.-A.; Liedberg, B.; Lundstrom, I.; Salaneck, W. R. *Synth. Met.* **1986,** *14,* 189–197. doi:10.1016/0379-6779(86)90183-9
22. Winther-Jensen, B.; Chen, J.; West, K.; Wallace, G. *Macromolecules* **2004,** *37,* 5930–5935. doi:10.1021/ma049365k
23. Virji, S.; Huang, J.; Kaner, R. B.; Weiller, B. H. *Nano Lett.* **2004,** *4,* 491–496. doi:10.1021/nl035122e
24. Takhira, P. Y.; Versimaha, Y. I.; Aksimentyeva, O. I.; Cizh, B. R.; Cherpak, V. V. *Phys. Chem. Solid State* **2005,** *6,* 96–98.
25. Anderson, M. R.; Mattes, B. R.; Reiss, H.; Kaner, R. B. *Science* **1991,** *252,* 1412–1415. doi:10.1126/science.252.5011.1412
26. Macdiarmid, A. G.; Chiang, J. C.; Richter, A. F.; Epstein, A. J. *Synth. Met.* **1987,** *18,* 285–290. doi:10.1016/0379-6779(87)90893-9
27. Gospodinova, N.; Terlemezyan, L. *Prog. Polym. Sci.* **1998,** *23,* 1443–1484. doi:10.1016/S0079-6700(98)00008-2
28. Bhadra, S.; Khastgir, D.; Singha, N. K.; Lee, J. H. *Prog. Polym. Sci.* **2009,** *34,* 783–810. doi:10.1016/j.progpolymsci.2009.04.003
29. Kulkarni, V. G.; Campbell, L. D.; Mathew, W. R. *Synth. Met.* **1989,** *30,* 321–325. doi:10.1016/0379-6779(89)90654-1
30. Yoo, J. E.; Cross, J. L.; Bucholz, T. L.; Lee, K. S.; Espe, M. P.; Loo, Y.-L. *J. Mater. Chem.* **2007,** *17,* 1268–1275. doi:10.1039/b618521e
31. Zhang, Y.; Rutledge, G. C. *Macromolecules* **2012,** *45,* 4238–4246. doi:10.1021/ma3005982
32. Wang, J.; Chan, S.; Carlson, R. R.; Luo, Y.; Ge, G.; Ries, R. S.; Heath, J. R.; Tseng, H.-R. *Nano Lett.* **2004,** *4,* 1693–1697. doi:10.1021/nl049114p

33. Zeng, F.-W.; Liu, X.-X.; Diamond, D.; Lau, K. T. *Sens. Actuators, B* **2010,** *143,* 530–534. doi:10.1016/j.snb.2009.09.050
34. Parvatikar, N.; Jain, S.; Bhoraskar, S. V.; Prasad, M. V. N. A. *J. Appl. Polym. Sci.* **2006,** *102,* 5533–5537. doi:10.1002/app.24636
35. Lin, Q.; Li, Y.; Yang, M. *Sens. Actuators, B* **2012,** *161,* 967–972. doi:10.1016/j.snb.2011.11.074
36. Cai, Z.; Martin, C. R. *J. Am. Chem. Soc.* **1989,** *111,* 4138–4139. doi:10.1021/ja00193a077
37. Chelawat, H.; Vaddiraju, S.; Gleason, K. *Chem. Mater.* **2010,** *22,* 2864–2868. doi:10.1021/cm100092c
38. Lee, S.; Gleason, K. K. *Adv. Funct. Mater.* **2015,** *25,* 85–93. doi:10.1002/adfm.201402924
39. Vaddiraju, S.; Cebeci, H.; Gleason, K. K.; Wardle, B. L. *ACS Appl. Mater. Interfaces* **2009,** *1,* 2565–2572. doi:10.1021/am900487z
40. Baxamusa, S. H.; Im, S. G.; Gleason, K. K. *Phys. Chem. Chem. Phys.* **2009,** *11,* 5227–5240. doi:10.1039/b900455f
41. Trujillo, N. J.; Barr, M. C.; Im, S. G.; Gleason, K. K. *J. Mater. Chem.* **2010,** *20,* 3968–3972. doi:10.1039/b925736e
42. Ping, Z. *J. Chem. Soc., Faraday Trans.* **1996,** *92,* 3063–3067. doi:10.1039/FT9969203063
43. Gomes, E. C.; Oliveira, M. A. S. *Am. J. Polym. Sci.* **2012,** *2,* 5–13. doi:10.5923/j.ajps.20120202.02
44. Flavel, B. S.; Yu, J.; Shapter, J. G.; Quinton, J. S. *Soft Matter* **2009,** *5,* 164–172. doi:10.1039/B809609K
45. Stafström, S.; Brédas, J. L.; Epstein, A. J.; Woo, H. S.; Tanner, D. B.; Huang, W. S.; MacDiarmid, A. G. *Phys. Rev. Lett.* **1987,** *59,* 1464–1467. doi:10.1103/PhysRevLett.59.1464
46. Joshi, G. P.; Saxena, N. S.; Sharma, T. P.; Mishra, S. C. K. *Indian J. Pure Appl. Phys.* **2006,** *44,* 786–790.
47. Chaudhari, H. K.; Kelkar, D. S. *Polym. Int.* **1997,** *42,* 380–384. doi:10.1002/(SICI)1097-0126(199704)42:4<380::AID-PI727>3.0.CO;2-F
48. Motaung, D. E.; Malgas, G. F.; Arendse, C. J.; Mavundla, S. E.; Oliphant, C. J.; Knoesen, D. *J. Mater. Sci.* **2009,** *44,* 3192–3197. doi:10.1007/s10853-009-3425-8
49. Chen, J.-T.; Chen, W.-L.; Fan, P.-W.; Yao, I.-C. *Macromol. Rapid Commun.* **2014,** *35,* 360–366. doi:10.1002/marc.201300290
50. Varma, S. J.; Xavier, F.; Varghese, S.; Jayalekshmi, S. *Polym. Int.* **2012,** *61,* 743–748. doi:10.1002/pi.4131
51. Travers, J. P.; Nechtschein, M. *Synth. Met.* **1987,** *21,* 135–141. doi:10.1016/0379-6779(87)90077-4
52. Martin, C. R. *Acc. Chem. Res.* **1995,** *28,* 61–68. doi:10.1021/ar00050a002
53. Long, Y.; Chen, Z.; Wang, N.; Ma, Y.; Zhang, Z.; Zhang, L.; Wan, M. *Appl. Phys. Lett.* **2003,** *83,* 1863. doi:10.1063/1.1606864

License and Terms

BEILSTEIN JOURNAL OF NANOTECHNOLOGY

Vapor-phase-synthesized fluoroacrylate polymer thin films: thermal stability and structural properties

Paul Christian and Anna Maria Coclite*

Full Research Paper

Open Access

Address:
Institute of Solid State Physics, Graz University of Technology, 8010 Graz, Austria

Email:
Anna Maria Coclite* - anna.coclite@tugraz.at

* Corresponding author

Keywords:
EGDMA; iCVD; in situ; PFDA; spectroscopic ellipsometry; temperature dependent; X-ray diffraction

Beilstein J. Nanotechnol. **2017,** *8,* 933–942.
doi:10.3762/bjnano.8.95

Received: 17 January 2017
Accepted: 05 April 2017
Published: 26 April 2017

This article is part of the Thematic Series "Vapor-based polymers: from films to nanostructures".

Guest Editors: M. Koenig and J. Lahann

Abstract

In this study, the thermal, chemical and structural stability of 1*H*,1*H*,2*H*,2*H*-perfluorodecyl acrylate polymers (p-PFDA) synthetized by initiated chemical vapor deposition (iCVD) were investigated. PFDA polymers are known for their interesting crystalline aggregation into a lamellar structure that induces super-hydrophobicity and oleophobicity. Nevertheless, when considering applications which involve chemical, mechanical and thermal stresses, it is important to know the limits under which the crystalline aggregation and the resulting polymer properties are stable. For this, chemical, morphological and structural properties upon multiple heating/cooling cycles were investigated both for linear PFDA polymers and for differently strong cross-linked alterations thereof. Heat treatment leaves the chemical composition of the linear PFDA polymers largely unchanged, while a more ordered crystalline structure with smoother morphology is observed. At the same time, the hydrophobicity and the integrity of the polymer deteriorate upon heating. The integrity and hydrophobicity of cross-linked p-PFDA films was preserved likely because of the lack of internal strain due to the coexistence of both crystalline and amorphous phases. The possibility to finely tune the degree of cross-linking can therefore expand the application portfolio in which PFDA polymers can be utilized.

Introduction

Fluoropolymers, such as polytetrafluoroethylene, are interesting for a variety of different applications due to their low surface energy. The resultant hydrophobic and oleophobic surfaces are used as biocompatible surfaces [1], antifouling coatings [2], and as low dielectric constant materials [3] for microelectronics. Perfluoroacrylates are particularly appealing for such applications, as they combine the hydrophobic properties of the fluorinated pendant groups with easy processability due to an unsaturated acrylate group, allowing for mild processing conditions. One of the greatest limitations to the long-term

stability of perfluoroacrylate-based technologies are mechanical, thermal and chemical stresses on the materials [4-7].

Some super-hydrophobic and oleophobic surfaces based on perfluoroacrylates were previously prepared by initiated chemical vapor deposition (iCVD) [8]. The iCVD technique allows polymerization of the fluorinated monomers, while the chemical structure of the precursor(s) remains intact. Therefore, ultrathin (<100 nm) perfluoropolymers can be easily deposited with high control over the chemistry [9] and crystalline structure [10] of the resulting coatings. Different from other thin film polymer deposition techniques, iCVD takes place in a completely dry environment, eliminating the tedious need of dissolving the fluoropolymers. In addition, it also allows the chemical structure of the monomers to be retained at high deposition rates, especially when compared with pulsed plasma deposition techniques [11]. The mechanism of polymerization by iCVD mirrors that of radical polymerization in solution [12]. An initiator molecule is thermally decomposed into radicals by a filament heated to 250–300 °C. The radicals of the initiator selectively react with the vinyl bonds of monomer species absorbed on the substrate, initiating the polymerization. For this, the substrate is typically held below 60 °C. Chain growth then proceeds on the substrate surface until terminated by another initiator radical or another initiator-monomer fragment.

The mechanical and chemical robustness of iCVD perfluoropolymers at elevated temperature has not yet been investigated. The aim of this study is to identify the limits of the thermal and mechanical stability of the 1*H*,1*H*,2*H*,2*H*-perfluorodecyl acrylate polymer (p-PFDA), and in order to enhance its durability, the copolymerization with ethylene glycol dimethacrylate (EGDMA) as a cross-linker is evaluated (the monomers are depicted in Figure 1). EGDMA is a diester with no free hydrophilic groups, which offers low viscosity, flexibility and high cross-link density in various polymer applications. Differently cross-linked p-PFDA films deposited by iCVD were previously studied, albeit with a somewhat different scope [13]. In contrast to the other cross-linkers that have been studied in combination with perfluropolymers (e.g., divinylbenzene (DVB)), EGDMA has a higher conversion rate, which results in a very low percentage of unreacted vinyl bonds after the deposition. It has been demonstrated that only after annealing, the perfluorinated films were strongly cross-linked by DVB resulting in films that showed low hysteresis between advancing and receding contact angle [14]. The advantage of cross-linking with EGDMA is the elimination of the annealing step, resulting in a cross-linked film already in the as-deposited form. The thermal stability of the thin films was evaluated by ellipsometry, Fourier transform infrared spectroscopy and X-ray diffraction. In situ ellipsometric studies allow the monitoring of the evolution of the thickness and optical constants of the materials during the heating ramp. This is particularly suitable for evidencing thermal transitions in thin films with thickness ranging from a few micrometers to monolayers [15,16].

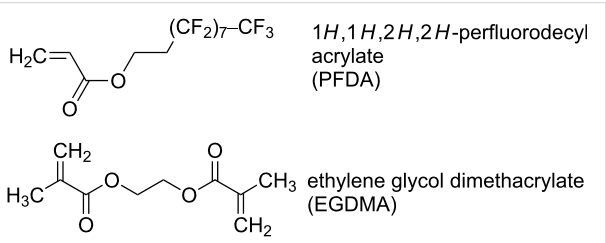

Figure 1: Molecular structure of the monomers PFDA and EGDMA.

Experimental

The monomer precursor 1*H*,1*H*,2*H*,2*H*-perfluorodecyl acrylate (PFDA, purity 97%), the cross-linking agent ethylene glycol dimethacrylate (EGDMA, purity 98%) and the initiator *tert*-butyl peroxide (TBPO, purity 98%) were purchased from Sigma-Aldrich (Germany) and used without further purification. p-PFDA films with different degrees of cross-linking were prepared by initiated chemical vapor deposition (iCVD). The average thickness of the as-deposited polymer films was 350 ± 50 nm. Detailed information on the actual processing conditions are provided in Supporting Information File 1, while a full description of the setup can be found in a previous publication [17]. As substrates, silicon wafers with a native oxide layer (thickness 1.7 nm) were used after being cut into 2 × 2 cm^2 pieces.

Fourier transform infrared spectroscopy (FTIR) was performed on a Bruker IFS 66v/s spectrometer in transmission mode, with all the data being converted to absorption spectra by the OPUS software. The data are automatically baseline corrected by a custom routine written in R, utilizing the algorithms provided in the baseline package [18].

Specular X-ray diffraction (XRD) patterns were recorded on a PANalytical Empyrean diffractometer. The system is equipped with a copper sealed tube (λ = 0.154 nm), a Göbbel mirror, various slits and a PIXcel^{3D} solid state detector. All data were recorded using the same setup and are represented in the scattering vector (q_z) notation, whereby $q_z = 4\pi \cdot \sin(\theta)/\lambda$. The index z indicates that only net planes parallel to the substrate surface were probed in the experiment (specular scan). In situ, temperature-dependent XRD studies were performed with a DHS900 heating stage attachment (Anton-Paar, Austria), using a heating rate of 2 °C/min. The integration time was set to one minute, meaning that a temperature resolution of 2 °C could be achieved.

Atomic force micrographs were taken in noncontact mode on a Nanosurf easyScan 2, equipped with a PPP-NCLR-10 cantilever (NanoWorld AG, Switzerland). The data are corrected for artifacts with the freely available software package Gwyddion [19].

The water contact angle (WCA) of the polymer films was determined by the static sessile drop method on a CAM200 contact angle analyzer (KSV Instruments, Finland). Each sample was probed on five different spots, using a droplet volume of 4 µL.

In situ temperature-dependent spectroscopic ellipsometry measurements were performed on a Woollam M-2000 ellipsometer (J.A. Woollam Co., USA), equipped with a THMS600 temperature stage (Linkam, UK) under nitrogen atmosphere. The samples were investigated in the temperature range between 10 and 150 °C at a heating/cooling rate of 5 °C/min, with a hold time of 5 min between steps. Prior to the measurement, the samples were equilibrated by three subsequent heating and cooling cycles. The optical data were recorded every second at an incidence angle of 75° in the wavelength range of 370 to 1000 nm. The ellipsometric data were modeled using the CompleteEASE® software by a three-layer system consisting of the silicon substrate, the interfacial oxide layer and the transparent top layer. The wavelength- and temperature-dependent refractive indices of silicon and oxide were taken from literature [20], whereas Cauchy's equation was utilized in modeling the polymer film. A nonlinear least squares fit of the experimental data with this model yields the optical constants and thickness of the polymer layers.

Results and Discussion

Chemical composition

The retention of chemical functionality and the degree of cross-linking for the different samples were evaluated by FTIR spectroscopy. In Figure 2, the spectra of the as-prepared samples are depicted (solid lines), where the data are normalized with the polymer layer thickness (i.e., with the sampled volume). Starting with the spectrum of p-PFDA, several characteristic absorption peaks are noted. In the fingerprint region (1500–500 cm^{-1}), the skeletal vibrations of the CH_x and CF_x groups are visible, most prominently featuring the symmetric and antisymmetric stretch of the CF_2 groups at 1251 and 1206 cm^{-1}, respectively. In addition, a strong absorption peak is observed at 1740 cm^{-1}, stemming from the C=O stretching of the ester groups. Upon cross-linking, this peak increases in intensity as EGDMA has twice the number of C=O groups relative to PFDA. In the fingerprint region, the signal of the CF_x groups decreases with increased cross-linking, eventually resulting in two distinct peaks of C–O stretching at 1257 and 1158 cm^{-1} for p-EGDMA. Additional peaks in the regions of

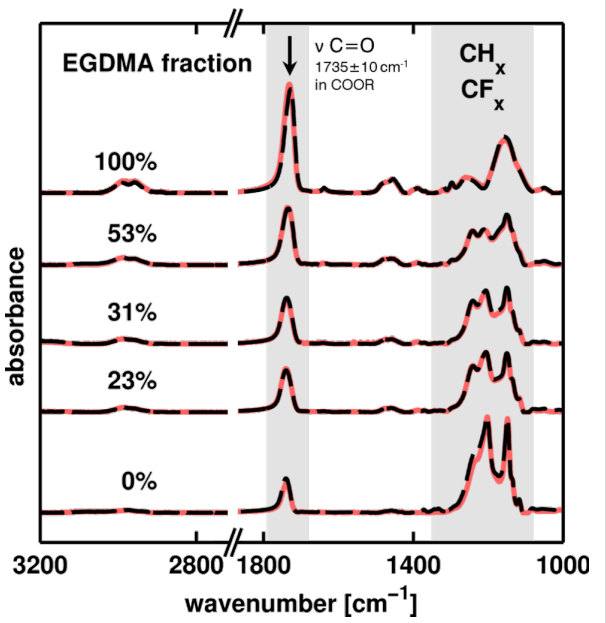

Figure 2: FTIR spectra of p-PFDA films with different EGDMA cross-linker ratios in the as-prepared state (dashed line) and after heat-treatment (solid line). The signal intensity is normalized by the film thickness. Data are shifted on the *y*-axis for clarity.

1480–1450 cm^{-1} and 3000–2800 cm^{-1} in the spectra of the cross-linked polymers are attributed to deformation and stretching vibrations of the CH_x groups, respectively. Interestingly, a small peak at 1638 cm^{-1} is noted to appear exclusively for p-EGDMA, which is characteristic for C=C stretching [21]. This implies that the polymerization of the cross-linker is not completely facilitated as some unreacted vinyl bonds remained in the polymer. Nevertheless, this peak is absent for all other spectra, thus the fraction of unreacted monomer species (in the limit of the experiment) is likely small. This means that the postdeposition annealing steps are superfluous, which is a clear advantage over other cross-linkers such as divinylbenzene; for the latter, iCVD copolymerization with PFDA resulted only in minor conversion rates, necessitating a time-consuming thermal conversion after deposition [14].

To evaluate the degree of cross-linking, each spectrum is treated as a linear combination of the spectra of the p-EGDMA and PFDA homopolymers, each weighted with a factor accounting for its fraction. By a linear fit of these factors, the composition is then obtained (see labels of the spectra in Figure 2).

After repeated heating of such samples to 150 °C under nitrogen atmosphere, the chemical composition of the polymers remained unchanged (dashed lines in Figure 2). This means that both p-PFDA and cross-linked alterations thereof are chemically stable in the investigated temperature range, within the detection limits of the FTIR spectroscopy measurement.

Surface morphology and wettability

The impact of the cross-linker on the surface morphology of p-PFDA films was investigated by atomic force microscopy (AFM) for the as-prepared and heat-treated samples (see Figure 3). For pristine p-PFDA films, the surface consists of randomly distributed spherical aggregations, forming a hillock-like structure. This is also reflected by the root mean square roughness (σ) of the surface, which was 23.7 nm. The mean radius of the spherical structures is about 200 nm, as determined from the autocorrelation length of the micrograph.

Upon addition of EGDMA, the surface morphology is drastically changed. The hillock-like structure of pure p-PFDA is reduced to a few aggregated clusters, interrupting the otherwise smooth polymer film. Except for these grains, the layer's root mean square roughness is below 2 nm, indicating a rather smooth coating of the silicon wafer (roughness below 1 nm). This morphology persists as the EGDMA content increases, suggesting that the transition from spherical aggregations to a smooth coating occurs already at small additions of cross-linker. For the p-EGDMA film, no surface aggregations are observed and a smooth coating results (roughness below 1 nm). The absence of spherical structures in p-EGDMA and the close resemblance to the morphology of p-PFDA films suggest that these aggregations are in fact just due to the PFDA units, as shown also in previous works [10,14]. An interesting detail is observed in the AFM scan of a sample containing 31% EGDMA (third image from left in Figure 3a). Small notches are noted for all the grains, extending twenty to thirty nanometers into the film (a more detailed view is shown in the inset). Possibly, these structures are the result of the degassing of unpolymerized monomer units, which are "buried" within the film during deposition. However, this behavior does not occur for the other samples (or is at least not observable in the respective AFM scans) and is uncharacteristic for iCVD polymers in general. Therefore, it is assumed that such structures are specific for this very sample and not characteristic for this particular EGDMA concentration.

After repeated heating of these polymer films to 150 °C, changes in surface morphology were recorded by AFM (Figure 3b). For the p-PFDA films, a completely different surface morphology results. The spherical aggregates in the as-prepared polymer are completely absent and a relatively smooth surface results instead. The morphology is still reminiscent of the hillock-like structures but on a much smaller scale; the roughness decreases to below 2 nm, comparable to that of cross-linked surfaces. However, multiple cracks have formed in the polymer film, extending several micrometers in the lateral direction (an example is shown in Figure 3, see Supporting Information File 1, Figure S1 for larger scales). The line profiles of these cracks reveal a penetration depth of approximately 20 nm, which means that they are limited to the interfacial area (the film thickness is approximately 350 nm). For cross-linked films, the temperature treatment results in no observable changes, indicating good stability towards temperature variation in the investigated range.

Changes in the surface morphology and chemistry also affect the wettability, as evidenced by a decreasing water contact

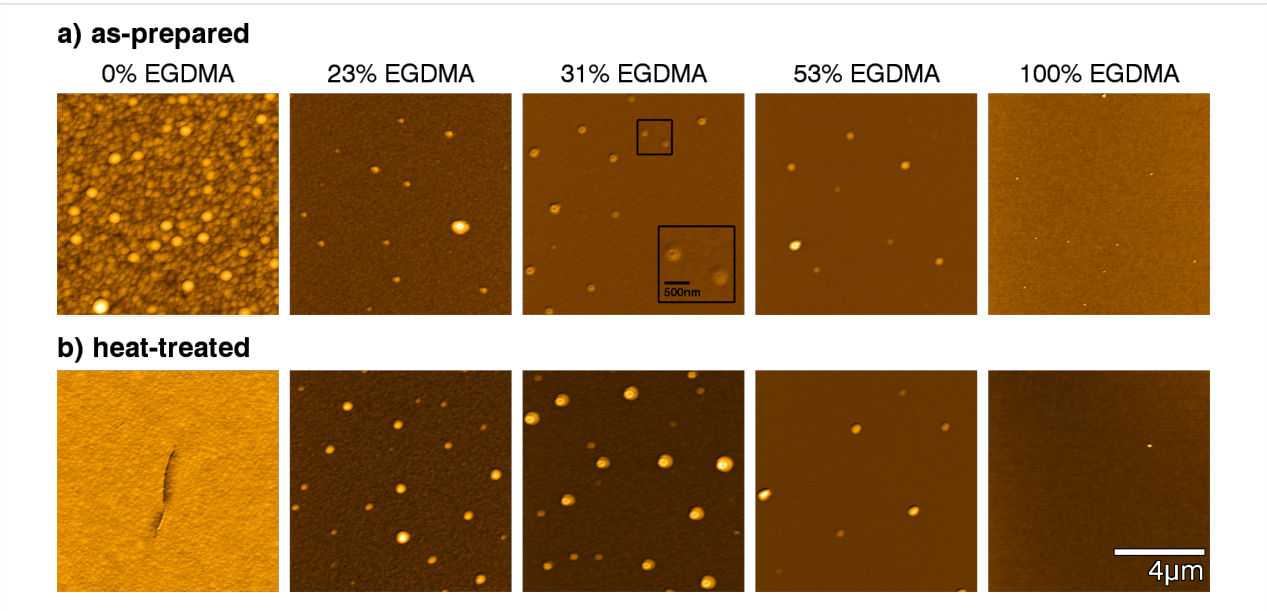

Figure 3: AFM height micrographs of as-prepared (a) and heat-treated (b) p-PFDA films with different degrees of EGDMA cross-linking. The data are represented on individual color scales for clarity.

angle (WCA) upon EGDMA addition to the polymer (Figure 4a). While the PFDA homopolymer forms a highly hydrophobic surface with a WCA of 138 ± 2°, a linear decrease results as the fraction of EGDMA cross-linker is gradually increased. The intercept with the *y*-axis was one of the fit parameters and the fit result, 139°, falls within the error range of the physical measurement of the water contact angle of the PFDA homopolymer. For the EGDMA homopolymer, a WCA of 69 ± 1° was ultimately observed. The change in wettability stems from the (relative) increase of carbonyl groups upon addition of EGDMA, which turns the polymer more hydrophilic. Similar to the morphological changes discussed above, heat treatment predominantly affects the water contact angle of the PFDA homopolymer. A decrease of the WCA to 121 ± 1° results, while the cross-linked polymers show little to no change, independent of the degree of cross-linking.

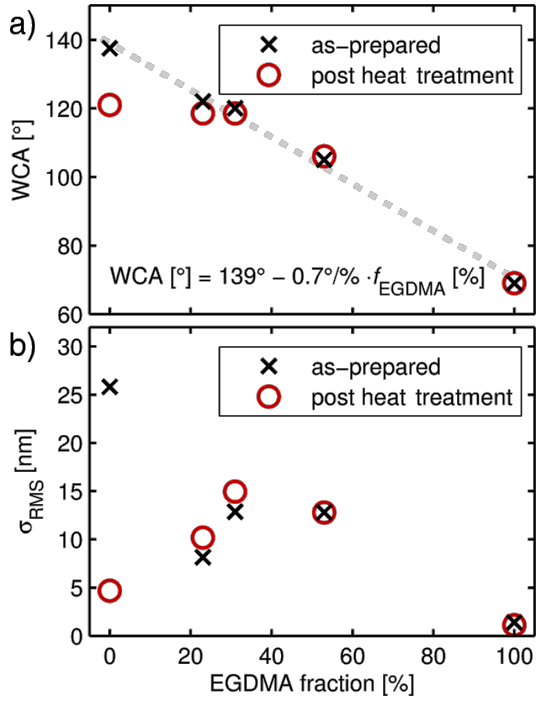

Figure 4: Water contact angle (WCA) (a) and root mean square surface roughness (σ_{RMS}) (b) of p-PFDA films with different degrees of EGDMA cross-linking, as determined by the static sessile drop method and from AFM, respectively. The σ_{RMS} values were calculated from the 50 × 50 µm² AFM micrograph areas presented in Supporting Information File 1, Figure S1. For the as-prepared films, a linear relationship between the contact angle and the cross-linker ratio is found (dashed line). Error bars have been omitted for clarity as the standard deviation of the WCA was less than two degrees.

In Figure 4b, the root mean square surface roughness, σ_{RMS}, of the full-scale AFM micrographs (Supporting Information File 1, Figure S1, 50 × 50 µm^2) is plotted as a function of EGDMA content, both for the as-prepared and heat-treated films. The data evidence that heat treatment predominantly affects the PFDA homopolymer, while only minor changes are noted for cross-linked alterations. Despite the formation of cracks, a pronounced decrease in the σ_{RMS} value was observed for the PFDA homopolymer, resulting in a much smoother film. This suggests that the initial WCA of the p-PFDA films stems in fact from a combination of hydrophobicity by the perfluorinated groups and the high surface roughness present in the as-prepared films. On the other hand, the effect of elevated temperature shows no or only a negligible effect on the morphology and chemical composition of cross-linked polymers (in the investigated range). This means that after deposition, these compositions are already closer to equilibrium so that less internal strain occurs. In turn, this makes these films less prone to rupture formation or surface rearrangement upon exposure to elevated temperatures. The data also show that in thermally annealed films, a water contact angle of approximately 120° can be maintained up to EGDMA fractions of 40%, indicating a surface composition dominated by the fluorinated groups of the PDFA portion.

Structural characterization

The distinct features of pure p-PFDA films and cross-linked alterations thereof are not only limited to the interface but are rather the result of differences in the bulk of the thin films. This is evident from the specular X-ray diffraction data of the as-prepared films, as depicted in Figure 5a. Pristine p-PFDA exhibits a low intensity peak at $q_z = 3.88$ nm^{-1}, meaning that this film is (at least partially) crystalline. This peak is characteristic for the hexagonal packing of the fluorinated pendant chains into a bilayer structure of distance $d = 3.18 \pm 0.02$ nm (corresponding to a scattering vector $q_z = 1.98$ nm^{-1}) [4]. Thus, the Bragg peak in Figure 5a is identified as the 002 reflection of this lamellar packing (data depicting the 001 reflection is provided in Supporting Information File 1, Figure S2). Additionally, the data show a preferred orientation of the lamella that is parallel to the substrate surface, as other reflections are absent in the spectra (measured up to $q_z = 20$ nm^{-1}).

A very different behavior results as the PFDA polymer is cross-linked by the addition of EGDMA to the iCVD process. The crystalline features of the PFDA homopolymer are absent in the cross-linked alterations, independent of the tested EGDMA fraction (thus, only the sample with the lowest EGDMA content is shown). The cross-linked polymers lack a defined repeating unit due to the random nature of the chain interconnects, which constitute a steric hindrance for chain rearrangement, thus limiting the formation of any long-range order.

The structural difference between the PFDA homopolymer and its cross-linked alterations most likely accounts for their distinct thermal response in terms of morphology (see the AFM data in

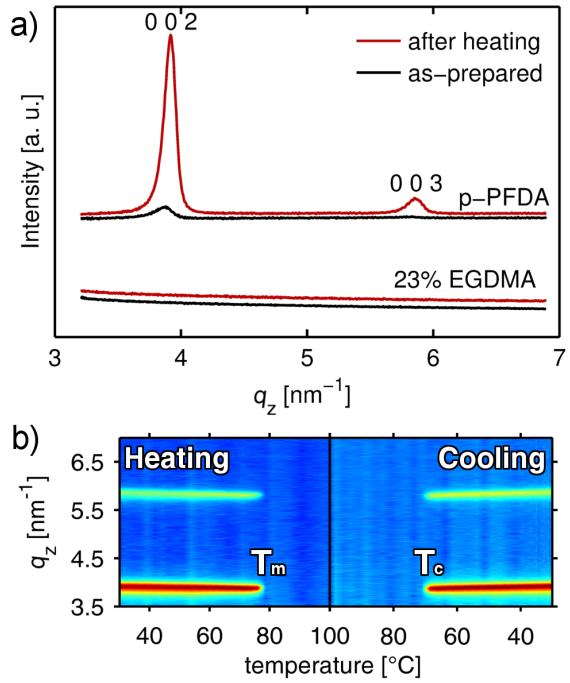

Figure 5: (a) Specular X-ray diffraction patterns of a p-PFDA film and a cross-linked alteration thereof with 23% EGDMA content in the as-prepared state and after heating to 150 °C. For clarity, data are shifted along the *y*-axis (intensity). (b) Temperature-dependent in situ X-ray diffraction measurements of crystalline p-PFDA at a rate of 2 °C/min, with T_m and T_c denoting the onset of melting and of crystallisation at 76 and 69 °C, respectively.

Figure 3), while the chemistry remains unaffected by the heat treatment (see the FTIR data in Figure 2). After heating to 150 °C and cooling back to ambient, the cross-linked polymers do not show any change in the XRD pattern, while the 002 Bragg reflection of the PFDA homopolymer displays a strong increase in intensity. In addition, a further (higher order) reflection of the lamellar structure emerges at $q_z = 5.86$ nm^{-1}, corresponding to the 003 plane. This behavior suggests that thermal treatment greatly improves crystallinity and/or mosaicity of the PFDA homopolymer, but does not lead to the formation of crystalline domains in the cross-linked films. Likely, with a lower cross-linker fraction, some degree of crystallinity might be preserved.

To gain further insight into the thermally induced structural changes of p-PFDA films, in situ X-ray diffraction experiments were performed. In Figure 5b, the specular diffraction pattern of the PFDA homopolymer is depicted in a pseudo-color representation as a function of temperature. The data features most prominently the positions of the 002 and 003 Bragg reflections, which display a shift towards lower *q*-values (and thus larger lattice distances) upon temperature increase, corresponding to thermal expansion of the unit cell. At 76 ± 2 °C, a sudden decrease in the diffracted intensity is then observed, denoting the melting point of the lamella. As the temperature is further increased to 100 °C, no change is observed in the diffraction pattern, that is, the polymer remains in the amorphous state. Upon cooling, recrystallization occurs at 69 ± 2 °C. Once they have emerged, these Bragg peaks display little variation in intensity as a function of temperature, suggesting that the polymer side-chains assume the final lamella arrangement within the resolution of the experiment (2 °C/min). On the other hand, a more pronounced shift of the Bragg peak positions towards higher *q*-values is noted upon cooling.

To quantify the thermal expansion/contraction of the p-PFDA unit cell, the coefficients of linear thermal expansion (CTEs) both for heating ($\alpha_{heating}$) and cooling ($\alpha_{cooling}$) are determined from the data. In general, the CTE is defined as

$$\alpha = \frac{1}{L_0}\frac{dL}{dT}, \quad (1)$$

with dL/dT denoting the rate of change in thickness with temperature, normalized by an initial thickness L_0 (for this work, L_0 refers to the length at 25 °C). From a linear fit to the data in Figure 5b, the linear CTEs are determined to be $\alpha_{heating} = (2.18 \pm 0.05) \times 10^{-4}$ K^{-1} and $\alpha_{cooling} = (3.2 \pm 0.1) \times 10^{-4}$ K^{-1}. The difference between the CTEs of the heating and the cooling run indicates that the sample has not yet reached an equilibrium state, which is expected for an as-prepared sample. Upon recrystallization under cooling, the Bragg peaks are slightly shifted towards higher *q*-values (see Figure 5a,b); the bilayer distance is reduced with respect to the as-prepared state and minor relaxation has occurred in the p-PFDA unit cell. While this difference diminishes in subsequent runs, an increasing peak intensity is still observed after the third run (data not shown).

While X-ray diffraction techniques are perfectly suited to follow structural processes in crystalline materials, their application to amorphous materials is less favorable. To also provide some insight into the amorphous, cross-linked p-(PFDA-*co*-EGDMA) films, in situ spectroscopic ellipsometry was utilized. In Figure 6, the evolution of the film thickness (normalized to the thickness at 25 °C) is depicted as a function of temperature, as determined from ellipsometry data. After several equilibration cycles (as described in the Experimental section), a reversible behavior is recorded. Figure 6a shows a typical measurement for a PFDA homopolymer for a heating and a cooling run. The data features most notably a first-order phase transition, with the onsets at 73 and 71 °C, determined by linear fits to the data. These points correspond to melting, and respectively, crystallization of the lamella. These thermal transition points are in reasonable agreement with those determined from the X-ray

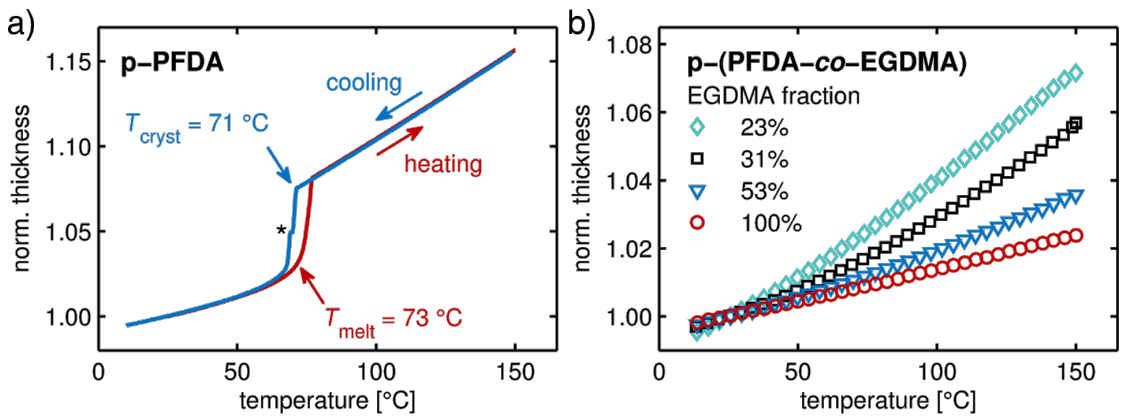

Figure 6: In situ spectroscopic ellipsometry data depicting film thickness evolution as a function of temperature for a PFDA homopolymer (a) and for samples containing different degrees of EGDMA cross-linking (b). The heating/cooling rates were 5 °C/min and data are normalized to the thickness at 25 °C. The data in (b) has been reduced for clarity and only cooling runs are shown. Please note that the discontinuity in (a) is an artefact and has been marked by an asterisk.

diffraction experiment (76 ± 2 and 69 ± 2 °C). The difference is attributed to general sensitivity and temperature resolution differences between these two techniques. While in the X-ray diffraction experiment a resolution of only 2 °C is achieved, the ellipsometric measurement features a ten-times better temperature resolution. In addition, ellipsometry allows even very minor changes in film thickness to be monitored without the need of long integration times.

Above and below the transition point, the data features the thermal expansion of the p-PFDA film. The observed changes do not depend on whether the experiment is performed while heating or cooling, hinting at a reversible behavior. This also means that no thickness loss occurs during the experiment. As this behavior was noted for all the samples (within this temperature regime), only cooling runs are considered from here on.

When EGDMA is added to the polymer, a different behavior was revealed (Figure 6b). A strong thermal transition, as observed for the PDFA homopolymer, is absent. This is expected as X-ray diffraction scans did not show any crystalline fraction (Figure 5a). Instead, the data evidence a gradual decrease in the thermal expansion as the EGDMA content increases. In addition, the thermal expansion features a slight curvature, indicating a thermal transition.

To investigate this in more detail, changes in film thickness and in refractive index are depicted together in Figure 7 as a function of temperature. For a EGDMA fraction of 23% (Figure 7a), a thermal transition at $T = 61 \pm 5$ °C is evidenced by the intersection of two linear fits to the data. With an increasing EGDMA content, this thermal transition shifts to higher temperatures but also becomes less pronounced (Figure 7b,c). Finally, for the EGDMA homopolymer, no transition is observable. While the thermal expansion decreases with increasing EGDMA content, the opposite behavior is noted in the refractive index. Interestingly, this shift in the refractive index (at ambient temperature) shows a linear behavior with the EGDMA fraction and could thus be used to determine the copolymer ratio. The obtained ratios are in good agreement with those determined from FTIR measurements (within a few percent). It is worth noting that another feasible way to evidence such transitions is to determine the thermal expansion coefficient at each temperature by numerical differentiation [22]. This procedure results in comparable transitions points (data not shown) but is very sensitive to noise in the fit/measurement. Thus, measurements should then be performed under stationary (isothermal) conditions for each temperature.

The origin of the thermal transitions could not be unambiguously identified. While crystalline fractions and first-order phase transitions were (in the limit of the experiments) not evident in the present data, the position of the thermal transitions suggests a relation to the crystalline packing present in the PFDA homopolymer. Likely, the thermal transition originates from a collective movement of the perfluorinated PFDA sidechains upon temperature increase. Compared to the liquid–crystalline state, the energy barrier for such chain movement is lowered as lattice energy is absent. This is in agreement with the sample containing 23% EGDMA, which exhibited the lowest transition point at $T = 61 \pm 5$ °C. With stronger cross-linking, the mobility of the fluoroalkyl groups is lowered, thus yielding a shift to higher temperatures while also yielding weaker transitions in general.

There are also several reports in literature which mention a glass transition in the EGDMA homopolymer, located between

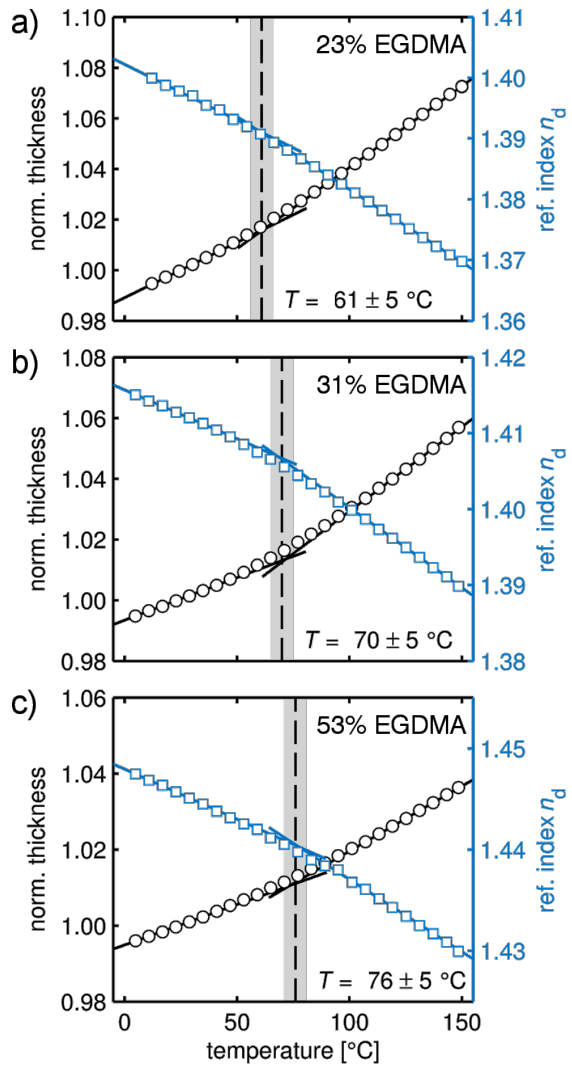

Figure 7: Normalized film thickness and the refractive index n_d (at λ = 589.3 nm) as a function of the temperature for p-(PFDA-*co*-EGDMA) films with (a) 23% EGDMA, (b) 31% EGDMA, and (c) 53% EGDMA content. From the intersection of the linear functions fitted to the data, the thermal transitions are evidenced. The corresponding transition temperatures are annotated in the graph. The shaded area represents the error bar.

130–140 °C [23,24]. However, such a transition is not evident in the present data. While thin films typically do show a different behavior compared to bulk materials, a film thickness greater than 100 nm (such as the ones used in this study) is often found in agreement with the bulk [25,26].

In addition, CTEs are determined for regions in which changes in film thickness depend linearly on temperature. Figure 8 displays the change in thermal expansion coefficients as a function of EGDMA content in the regions below and above the thermal transitions points ((10–45 °C) and 110–150 °C), respectively). Below the melting point, the PFDA homopolymer exhibits the highest thermal expansion coefficient of the systems studied. A comparison with the thermal expansion of the crystallites shows that the thermal expansion of the lamella ($\alpha_{cryst} = 2.18 \pm 0.05 \times 10^{-4}$ K^{-1}) accounts only for about half of the total film thickness increase ($\alpha_{film} = 4.5 \pm 0.5 \times 10^{-4}$ K^{-1}). This suggests that the disordered regions between the layers strongly impact the thermal properties. Possibly, this mixture of amorphous and liquid–crystalline film portions leads to a thermal mismatch, causing the rupture formation noticed within the film. Above 110 °C, the thermal expansion coefficient of p-PFDA is drastically increased as the melting point of the lamella is surpassed ($\alpha_{melt} = 10.6 \pm 0.5 \times 10^{-4}$ K^{-1}).

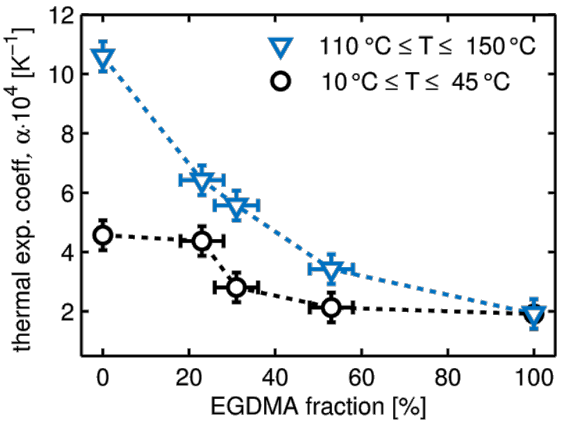

Figure 8: Coefficient of linear thermal expansion, α, as a function of EGDMA cross-linker fraction for various p-(PFDA-*co*-EGDMA) films in two temperature regions. The data points are interconnected by dashed lines as a guide to the eye.

As EGDMA cross-linker is added to the polymer, the CTEs decrease and the difference between CTEs above and below the thermal transition also decreases until it is fully absent for the p-EGDMA homopolymer. This behavior reflects the fact that thermal transitions become weaker with increasing EGDMA content and are fully absent for the p-EGDMA homopolymer (in the investigated temperature range). As the WCA (i.e., the surface energy) displayed little dependence on the EGDMA content (below 40% fraction), this allows for the deposition of highly hydrophobic p-(PFDA-*co*-EGDMA) surfaces with control over the thermal expansion (and mechanical properties) being established by the cross-linker degree.

Conclusion

The morphological and structural properties of linear and cross-linked p-PFDA films deposited by iCVD were investigated with the aim of identifying the limit of thermal stress that these films can sustain before losing integrity. PFDA polymers have indeed shown very interesting properties in terms of repellence of oil and water, due to the formation of a crystalline lamellar structure between the PFDA chains. While this makes the p-PFDA

highly suitable for a large variety of applications, it is interesting to know how these properties change with temperature oscillations that can occur during the everyday use of technologies based on this polymer.

The present study shows that the mechanical stability can be greatly improved by the addition of a cross-linker. When the linear p-PFDA was exposed to the heating cycles, the chemistry remained unchanged while the crystallinity of the films was largely improved and the morphological character of the surface became smoother. Nevertheless, the thermal stress caused some ruptures in the films and reduced the hydrophobic properties. EGDMA, added as a cross-linker, was shown to preserve the chemical stability and hydrophobicity of p-PFDA coatings while making the film more cohesive. The loss of the structural integrity in the PFDA homopolymer was attributed to the different thermal expansion coefficients of the crystalline and amorphous film portions, which caused tension in these films upon heating/cooling. The cross-linked films were fully amorphous, also upon heating, but had more stable hydrophobic properties and showed an increased crack resistance.

In addition, this study demonstrated that EGDMA is a feasible cross-linker for the synthesis of thermally stable hydrophobic polymers. While the ester groups can become a limiting factor at even higher temperatures, EGDMA offers unique advantages for applications below 150 °C. It outperforms previously employed reagents like DVB, allowing for faster deposition rates in the iCVD process and making postdeposition curing unnecessary, as high conversion rates are readily achieved.

The chosen deposition technique, iCVD, allows fine-tuning of the cross-linking ratio, different from other vapor-based deposition techniques (e.g., plasma-enhanced CVD). Therefore, depending on the application and on the desired polymer properties, one can choose to work in conditions that drive crystallinity and hydrophobicity or thermally stable surface properties instead.

Supporting Information

Supporting Information File 1

Additional experimental parameters and results.
iCVD process parameters used in the sample deposition; atomic force micrographs depicting larger scales; X-ray reflectivity scan evidencing the bilayer structure of p-PFDA.
[http://www.beilstein-journals.org/bjnano/content/supplementary/2190-4286-8-95-S1.pdf]

Acknowledgements

The work was funded by the Austrian Science Fund (FWF) [Grant P26993]. The authors gratefully acknowledge Roland Resel for interesting and helpful scientific discussions and for the use of the X-ray diffractometer.

References

1. Sarantopoulou, E.; Kollia, Z.; Cefalas, A. C.; Douvas, A. M.; Chatzichristidi, M.; Argitis, P.; Kobe, S. *Mater. Sci. Eng., C* **2007,** *27,* 1191–1196. doi:10.1016/j.msec.2006.09.044
2. Schmidt, D. L.; Brady, R. F.; Lam, K.; Schmidt, D. C.; Chaudhury, M. K. *Langmuir* **2004,** *20,* 2830–2836. doi:10.1021/la035385o
3. He, F.; Gao, Y.; Jin, K.; Wang, J.; Sun, J.; Fang, Q. *ACS Sustainable Chem. Eng.* **2016,** *4,* 4451–4456. doi:10.1021/acssuschemeng.6b01065
4. Honda, K.; Morita, M.; Otsuka, H.; Takahara, A. *Macromolecules* **2005,** *38,* 5699–5705. doi:10.1021/ma050394k
5. Fujimori, A.; Masuya, R.; Masuko, T.; Ito, E.; Hara, M.; Kanai, K.; Ouchi, Y.; Seki, K.; Nakahara, H. *Polym. Adv. Technol.* **2006,** *17,* 653–663. doi:10.1002/pat.790
6. Kanashima, T.; Maida, O.; Kohma, N.; Okumoto, M.; Ueno, M.; Kitai, S.; Okuyama, M.; Ohashi, H.; Tamenori, Y. *Appl. Surf. Sci.* **2006,** *252,* 7774–7780. doi:10.1016/j.apsusc.2005.06.055
7. Yoo, Y.; You, J. B.; Choi, W.; Im, S. G. *Polym. Chem.* **2013,** *4,* 1664–1671. doi:10.1039/c2py20963b
8. Coclite, A. M.; Shi, Y.; Gleason, K. K. *Adv. Mater.* **2012,** *24,* 4534–4539. doi:10.1002/adma.201200682
9. Gupta, M.; Gleason, K. K. *Langmuir* **2006,** *22,* 10047–10052. doi:10.1021/la061904m
10. Coclite, A. M.; Shi, Y.; Gleason, K. K. *Adv. Funct. Mater.* **2012,** *22,* 2167–2176. doi:10.1002/adfm.201103035
11. Milella, A.; Di Mundo, R.; Palumbo, F.; Favia, P.; Fracassi, F.; d'Agostino, R. *Plasma Processes Polym.* **2009,** *6,* 460–466. doi:10.1002/ppap.200930011
12. Coclite, A. M.; Howden, R. M.; Borrelli, D. C.; Petruczok, C. D.; Yang, R.; Yagüe, J. L.; Ugur, A.; Chen, N.; Lee, S.; Jo, W. J.; Liu, A.; Wang, X.; Gleason, K. K. *Adv. Mater.* **2013,** *25,* 5392–5423. doi:10.1002/adma.201301878
13. Vilaró, I.; Yagüe, J. L.; Borrós, S. *ACS Appl. Mater. Interfaces* **2017,** *9,* 1057–1065. doi:10.1021/acsami.6b12119
14. Yagüe, J. L.; Gleason, K. K. *Macromolecules* **2013,** *46,* 6548–6554. doi:10.1021/ma4010633
15. Beaucage, G.; Composto, R.; Stein, R. S. *J. Polym. Sci., Part B: Polym. Phys.* **1993,** *31,* 319–326. doi:10.1002/polb.1993.090310310
16. Keddie, J. L.; Jones, R. A. L.; Cory, R. A. *Europhys. Lett.* **1994,** *27,* 59. doi:10.1209/0295-5075/27/1/011
17. Christian, P.; Ehmann, H. M. A.; Coclite, A. M.; Werzer, O. *ACS Appl. Mater. Interfaces* **2016,** *8,* 21177–21184. doi:10.1021/acsami.6b06015
18. *baseline: Baseline Correction of Spectra. R package,* Version 1.2-0; 2015.
19. Nečas, D.; Klapetek, P. *Cent. Eur. J. Phys.* **2011,** *10,* 181–188. doi:10.2478/s11534-011-0096-2
20. Herzinger, C. M.; Johs, B.; McGahan, W. A.; Woollam, J. A.; Paulson, W. *J. Appl. Phys.* **1998,** *83,* 3323–3336. doi:10.1063/1.367101

21. Larkin, P. J. *Infrared and Raman Spectroscopy: Principles and Spectral Interpretation;* Elsevier: Amsterdam, Netherlands, 2011.
22. Kawana, S.; Jones, R. A. L. *Phys. Rev. E* **2001,** *63,* 021501. doi:10.1103/PhysRevE.63.021501
23. Loshaek, S. *J. Polym. Sci.* **1955,** *15,* 391–404. doi:10.1002/pol.1955.120158007
24. Horie, K.; Otagawa, A.; Muraoka, M.; Mita, I. *J. Polym. Sci., Polym. Chem. Ed.* **1975,** *13,* 445–454. doi:10.1002/pol.1975.170130217
25. Keddie, L. J.; Jones, R. A. L.; Cory, A. R. *Faraday Discuss.* **1994,** *98,* 219–230. doi:10.1039/fd9949800219
26. Vignaud, G.; Chebil, S. M.; Bal, J. K.; Delorme, N.; Beuvier, T.; Grohens, Y.; Gibaud, A. *Langmuir* **2014,** *30,* 11599–11608. doi:10.1021/la501639z

License and Terms

BEILSTEIN JOURNAL OF NANOTECHNOLOGY

Nanotopographical control of surfaces using chemical vapor deposition processes

Meike Koenig*[1] and Joerg Lahann[1,2]

Review

Open Access

Address:
[1]Karlsruhe Institute of Technology (KIT), Institute of Functional Interfaces (IFG), Hermann-von-Helmholtz-Platz 1, 76344 Eggenstein-Leopoldshafen, Germany and [2]Biointerfaces Institute, University of Michigan (UM), 2800 Plymouth Rd., Ann Arbor, MI 48109, USA

Email:
Meike Koenig* - meike.koenig@kit.edu

* Corresponding author

Keywords:
polymer coatings; polymer structures; structured coatings; vapor deposition polymerization

Beilstein J. Nanotechnol. **2017,** *8,* 1250–1256.
doi:10.3762/bjnano.8.126

Received: 31 January 2017
Accepted: 12 May 2017
Published: 12 June 2017

This article is part of the Thematic Series "Vapor-based polymers: from films to nanostructures".

Associate Editor: M. Stenzel

Abstract

In recent years much work has been conducted in order to create patterned and structured polymer coatings using vapor deposition techniques – not only via post-deposition treatment, but also directly during the deposition process. Two-dimensional and three-dimensional structures can be achieved via various vapor deposition strategies, for instance, using masks, exploiting surface properties that lead to spatially selective deposition, via the use of additional porogens or by employing oblique angle polymerization deposition. Here, we provide a concise review of these studies.

Review

Introduction

Polymer coatings have wide-spread applications, from electronics [1], to sensor systems [2] to biotechnology [3]. The ability to spatially control the surface properties in order to further augment this technological utility has been the subject of intensive research in recent years. In this review, we summarize the work that has been conducted to create patterns and structures using vapor-deposited polymers. Two prominent examples of vapor deposition methods are the thermally activated deposition of poly(*p*-xylylenes) (PPX), as well as plasma-enhanced chemical vapor deposition polymerization, both of which offer many advantages over solution-based deposition methods [4]. Since no solvents are involved, no wetting problems or problems with solvent residues arise, which can potentially interfere with the structuring process. In addition, the process can be applied on thermo- or chemically sensitive substrates and can be used to deposit insoluble polymers. The use of vaporized monomers rather than polymer solutions ensures the conformal coating of the substrate and masks, where required. Many examples exist for the post-deposition structuring of homogeneous coatings, for example, with the use of litho-

graphic techniques [5-7]. Instead, the focus of this review lies on the various methods which can be utilized to form structured coatings during the vapor deposition process.

Masked deposition

Microstructured masks can be applied to cover parts of the substrate in order to prevent deposition of polymer on these locations [8,9]. Chen and Lahann developed the vapor-assisted micropatterning in replica structures (VAMPIR) method using poly(dimethylsiloxane) (PDMS) masks to pattern reactive PPX derivatives on the surface [10]. Compared to metal masks, the PDMS creates a perfect seal to provide smooth surfaces, avoiding the formation of an air gap between the mask and surface, which results in higher pattern fidelity.

Three-dimensional structures can be formed using masks as well. Jang and Oh used anodic aluminum oxide membranes as a template for the production of nanotubes with a tunable wall thickness (Figure 1) [11]. Via chemical oxidation polymerization of vaporized pyrroles, polypyrrole was deposited on the walls of the membrane pores which had been pretreated with ferric chloride. Membranes with a pore diameter of 20 nm or 100 nm were used. Dissolving the membrane in sodium hydroxide resulted in a solution of nanotubes, which were further carbonized to carbon nanotubes. The wall diameter was controlled to be between 12 to 34 nm by using different amounts of the monomer feed. Trujillo et al. produced polymeric nanostructures using colloidal lithography [12]. In this technique, two-dimensional self-assembled monolayer (SAM) arrays of colloidal nanoparticles serve as lithographic templates for "nanobowl" patterns in an initiated chemical vapor deposition (iCVD) process. The colloidal template was removed by ultrasonication after deposition. Structures derived from a broad range of polymers and across a variety of length scales (down to 25 nm) could be fabricated.

Selective deposition

A straightforward method to selectively deposit polymers on prepatterned substrates is the structured coating of the substrate by initiator molecules in surface-initiated vapor-deposition polymerization. With this method, the polymer only grows on those locations on the surface equipped with predeposited initiator molecules. The patterning of the initiator can be achieved using photolithography [13], microcontact printing [14] or inkjet printing [15] for instance.

A second option is the spatially selective in situ activation of the initiator, which has been homogeneously coated on the substrate. Nishida and co-workers created patterns of activated photoinitiator by irradiation of the surface through a mask during the deposition process [16]. In a subsequent report, the use of an auto-drawing system, consisting of an optical fiber irradiation apparatus and a programmed manipulator for the spatially selective activation of the initiator, was demonstrated (Figure 2a) [17].

For PPX, transition metals, as well as their salts or complexes, were found to inhibit the polymer growth on the surface. PPX-n and chlorinated PPX did not grow on metal and metal oxide surfaces. This was likely due to deactivation of the adsorbed

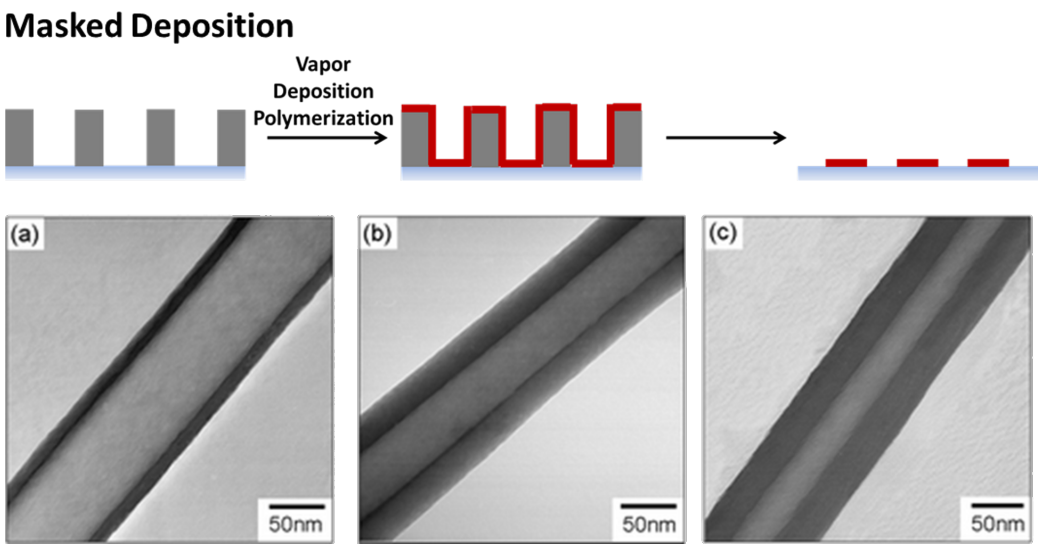

Figure 1: Polymer structures via masked deposition: polypyrrole nanotubes by deposition using aluminum oxide membranes with a pore size of 100 nm as the template. The wall thickness can be varied by variation of the loading amount of monomer (a) 0.07 mL, (b) 0.14 mL, and (c) 0.21 mL. Reproduced with permission from [11], copyright 2004 The Royal Society of Chemistry.

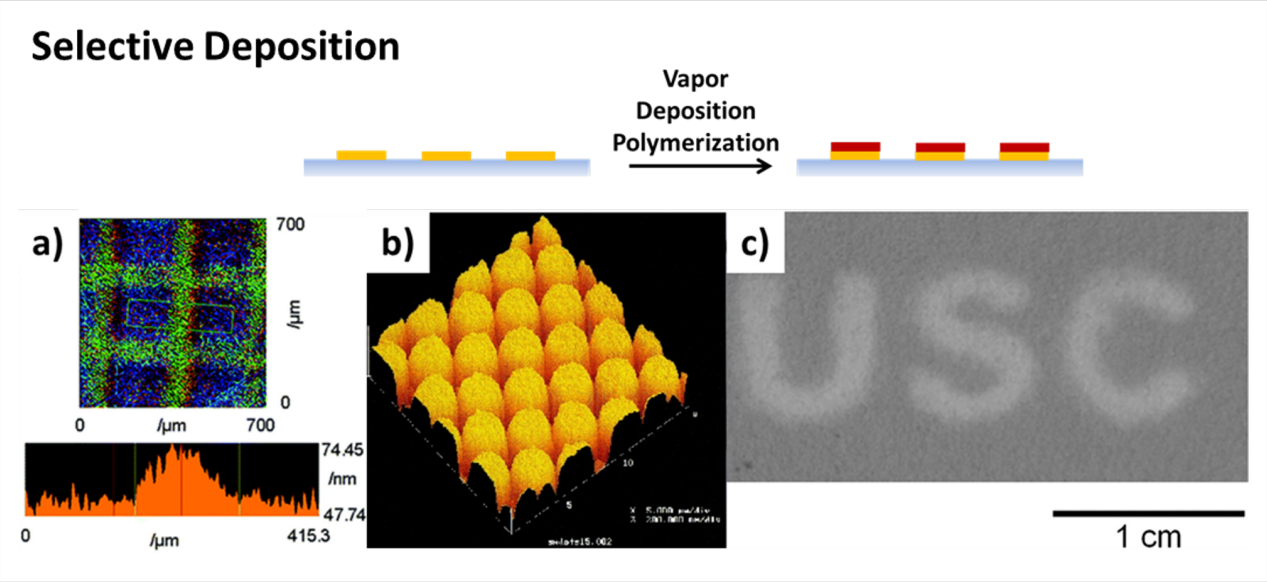

Figure 2: Formation of patterned polymer coatings by selective deposition strategies: a) spatially selective in situ activation of the surface-immobilized initiator in photoinduced vapor-phase-assisted surface polymerization of poly(methyl methacrylate), b) selective deposition of PPX-n on a hexadecanethiol pattern (spot diameter 1.5 µm) on a silver surface, c) selective deposition of poly(4-vinyl pyridine-*co*-divinyl benzene) on copper-free regions (dark area) of chromatography paper. Permissions: (a) was reproduced with permission from [16], copyright 2006 The Royal Society of Chemistry, (b) was reprinted with permission from [18], copyright 2000 American Chemical Society, and (c) was reprinted with permission from [19], copyright 2015, American Vacuum Society.

bi-radical form, which results in quenching of the chain growth [20]. Due to secondary adsorption on deactivated monomers, the authors found a maximum thickness of selectively grown polymer depending on the metal and the monomer type. Iron was found to be the most efficient inhibitor for the investigated polymers. By patterning iron molecules via photolithography or through a shadow mask, microstructured polymer films were fabricated [21]. Inverted structures were created using microcontact printing of alkanethiols on gold or silver surfaces (Figure 2b). These were found to prevent the quenching effect of the metals, thus promoting polymer growth instead. Using carboxylic acid-terminated alkanethiols, iron salt exposure on the surface could be spatially defined, which again prevented polymer growth [18].

Further investigations with a wider variety of PPX derivatives were conducted by Chen et al. [22]. For PPX derivatives containing oxygen or nitrogen, no inhibition of polymer growth was found on transition metals. For this reason, attractive interactions between the metal and the heteroatoms were suggested. The patterned deposition of a reactive PPX derivative could be realized for PPX–vinyl on titanium, and its reactivity in cross-metathesis reactions was demonstrated.

The inhibition of chain growth by transition metals was also demonstrated for different types of monomers by Kwong et al. [19,23]. Various metals and metal salts were found to inhibit the growth of acrylate-based polymers and poly(4-vinylpyridine) (P4VP). Copper salts such as $CuCl_2$ and $Cu(NO_3)_2$ were identified for effective inhibition of all investigated types of polymers. The patterned deposition was demonstrated by screen printing of a solution of the metal salt using a mask. No polymer deposition occurred on locations treated with the metal salt (Figure 2c).

In order to pattern surfaces with PPX derivatives containing nitrogen and oxygen heteroatoms, further work was conducted by Wu et al. [24]. The deposition of various PPX derivatives could be inhibited by electrically charging conducting substrates. Supplying electrical energy to the surface increases the surface energy, which results in the deactivation of the reactive monomer species on the surface. Patterning was realized by placing conducting aluminum metal channels on a nonconductive glass surface [24].

The selective growth of various polymers was also found for surfaces equipped with different functional groups. This results in different adhesion properties of the monomer on the surface. Tsukagoshi et al. used different aminosilanes for locally activating the deposition of polyamide on silicon substrates [25]. On gold surfaces, SAMs of alkanethiolates offer a facile way to supply the surface with various functional groups. Choi et al. directed the growth of poly(isobenzofuran) by patterns of SAMs with different terminal groups [26]. Methyl-terminated SAMs were found to hinder the growth of polymers, while the polymer preferentially grew on carboxylic acid-terminated SAMs. Bally-

Le Gall et al. noted selective growth of PPX derivatives with trifluoroacetyl or chlorine functionality on carboxylic acid- or hydroxyl-terminated alkanethiolates as compared to methyl-terminated SAMs [27]. In this way, free-standing nanosheet membranes were fabricated.

Substrate-induced morphology control

Demiryürek et al. developed a method to produce periodic wrinkle structures on the surface of polymer films using prestrained substrates [28]. Various polymers were deposited on prestrained PDMS substrates using iCVD. The subsequent release of the strain leads to microstructured wrinkles, where the topography is controlled by tuning the elastic modulus of the polymer coating and the substrate. Haller et al. investigated the morphology of vapor-deposited polymers on liquid substrates (Figure 3) [29]. Depending on surface tension, liquid viscosity, deposition rate and deposition time, either film or particle formation was found. Particles tend to form if the surface tension interaction between the liquid and the polymer is energetically unfavorable, promoting aggregation of the polymer. If the interaction is ambiguous, particle formation is observed at low deposition rates and times and with low liquid viscosity.

Introduction of porogen during deposition

Polymer films with porous morphology can be created via the introduction of a porogen into the growth process. Tao and Anthamatten formed open-cell, macroporous poly(glycidyl methacrylate) structures using ethylene glycol as a porogen [30-32]. The inclusion of an inert, condensable species into the gas feed mixture ensures phase separation simultaneously with the polymerization and crosslinking reactions. The porogen is removed in a post-deposition process using vacuum or solvent treatment. Gupta and co-workers demonstrated that in the iCVD process the monomer itself can act as a porogen if unconventional iCVD processing conditions are employed (Figure 4) [33-36]. Increasing the partial pressure of the monomer above its saturation pressure and decreasing the substrate temperature below the freezing point of the monomer results simultaneously in the deposition of solid monomer and polymerization. Following the deposition process, the solid monomer is removed via sublimation, leading to membrane structures with dual-scale porosity. The growth rate and the pore size of the resulting membrane can be controlled by the reactor parameters, such as deposition time, monomer partial pressure and substrate temperature. The three-dimensional growth of pillared microstructures was found at low substrate temperatures, while

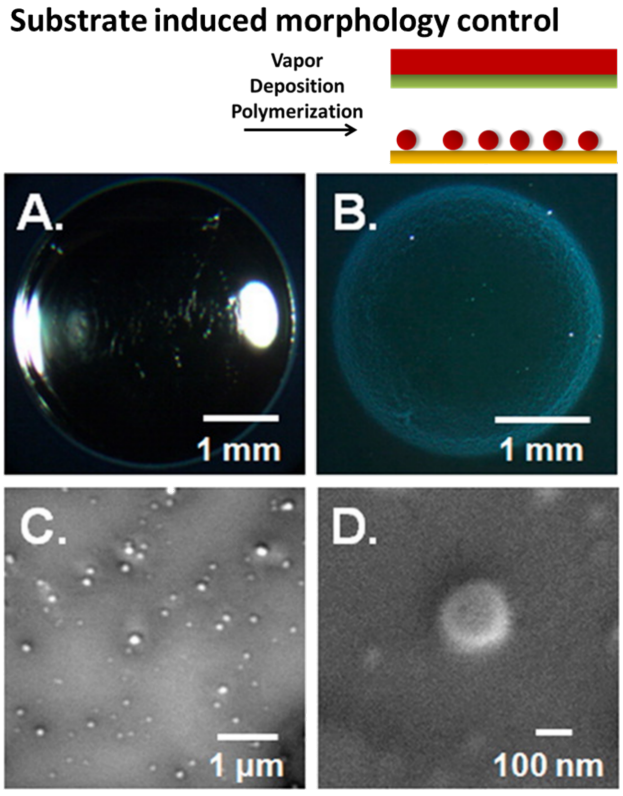

Figure 3: Variation of the polymer structure induced by the substrate: (A) polymer film formed when the spreading of the polymer on the liquid is energetically favorable, poly(1*H*,1*H*,2*H*,2*H*-perfluorodecyl acrylate) on 1-ethyl-3-methylimidazolium tetrafluoroborate, (B) polymer particles formed under energetically unfavorable spreading conditions (poly(4-vinylpyridine) on silicone oil), and (C,D) scanning electron images of poly(4-vinylpyridine) polymer particles. Reprinted with permission from [29], copyright 2013 American Chemical Society.

at increased substrate temperatures, web-like growth occurred. The membrane formation could be spatially controlled by patterning of the surface energy of the underlying substrate using a fluorinated polymer. Minimal nucleation of monomer was found on the fluorinated spots, which led to a dense polymer coating on these sites. These techniques show great promise in the fabrication of membranes [37].

Oblique angle deposition

A significant amount of work was conducted by Demirel and co-workers on the formation of 3D polymer structures using oblique angle polymerization deposition, analogous to the method already widely applied for the formation of inorganic structures [38]. The direction of the monomer vapor flux at an oblique angle of around 10° to the substrate plane results in the formation of slanted nanocolumns via a self-shadowing mechanism with a diameter of around 150 nm [39-41]. The slanting angle can be controlled via the deposition angle. Compared to inorganic oblique angle deposition, more complex algorithms have to be applied in order to successfully predict the growth morphology of the polymer structures, taking into account the chain growth kinetics. The morphology can be further varied by manipulating the substrate rotation, resulting in more complex architectures, such as helices or chevron structures (Figure 5). The nanostructured PPX films produced exhibit a high water contact angle and the use in water droplet transport was demonstrated [42,43]. Further potential applications include biomaterial design [44] and catalytic devices [45].

Conclusion

Vapor deposition polymerization techniques have been successfully applied in order to create patterned and structured polymer coatings. Structuring both in two and three dimensions can be achieved by either using masks or taking advantage of selective deposition properties on prepatterned substrates, exploiting substrate properties such as the surface energy, polarity or interaction with adsorbing monomers. Additionally, the introduction of porogens during the deposition process and the deposition at an oblique angle are methods that have been reported to lead to the formation of three-dimensional polymer structures. With these bottom-up approaches, structured and patterned coatings from a great variety of polymer materials can be created that can be tailored to the respective applications.

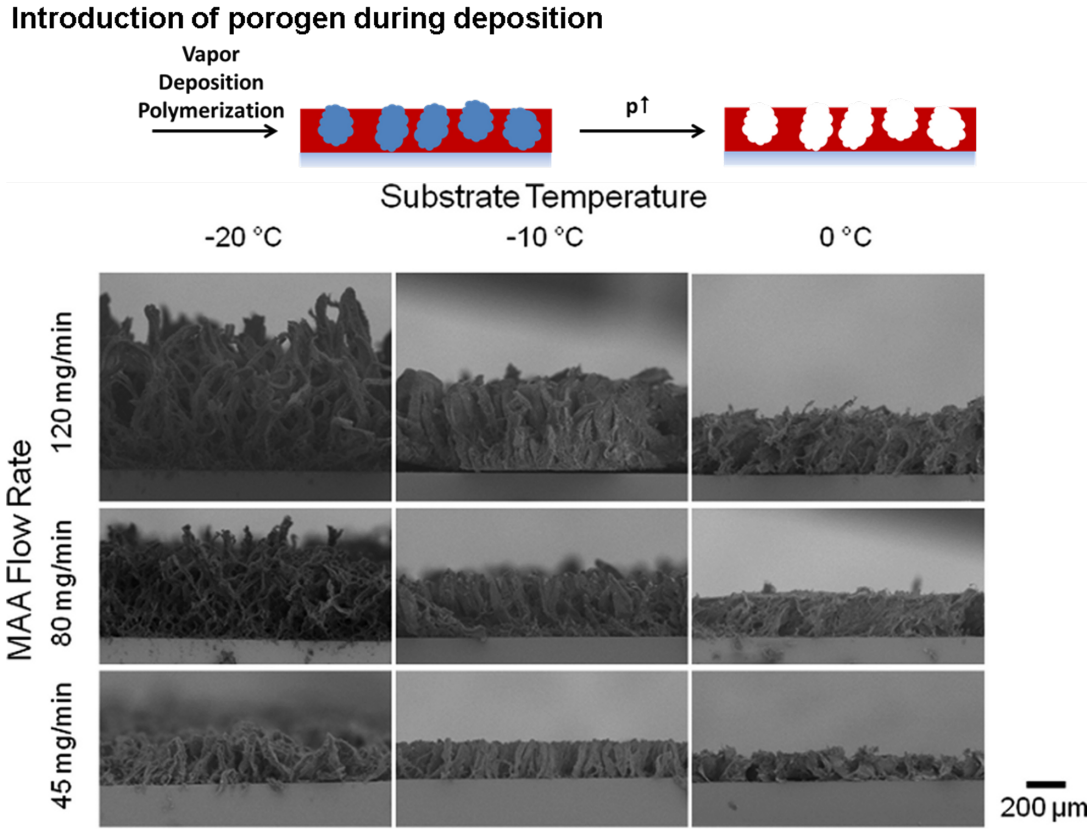

Figure 4: Polymer structures created via introduction of a porogen during the deposition process: the images show the extent of the deposition of solid monomer, which occurs simultaneously with polymerization. Thereby, the resulting morphology can be varied by the monomer flow rates or the substrate temperature. Reprinted with permission from [33], copyright 2014 American Vacuum Society.

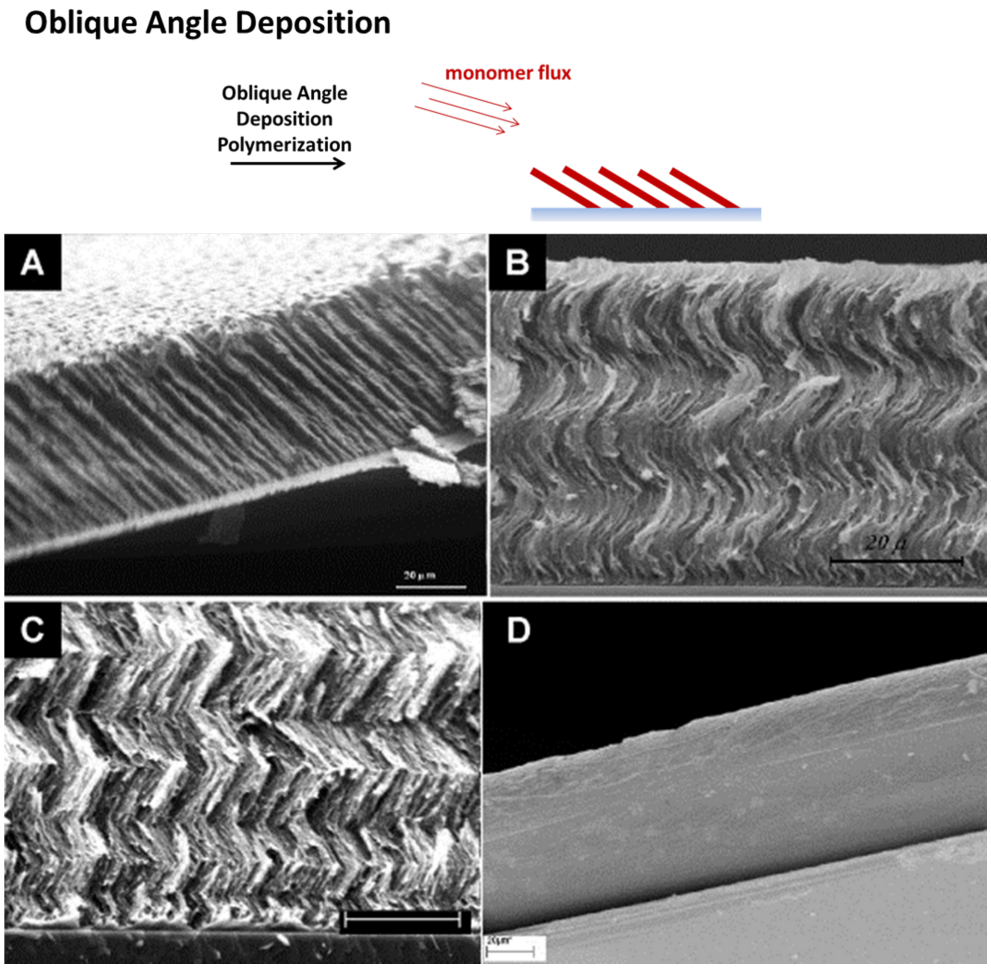

Figure 5: Polymer structures via oblique angle polymerization: by manipulating the substrate rotation during the deposition, complex architectures such as A) columnar, B) helical or C) chevron patterns can be achieved. In contrast to this, D) displays the corresponding cross-sectional scanning electron micrograph of a planar PPX-n film. All scale bars are 20 µm. Reprinted with permission from [40], copyright 2008 Elsevier.

Acknowledgements

The authors acknowledge funding from the Helmholtz Association within the Biointerfaces Program of the Karlsruhe Institute of Technology (KIT) and from the German Science Foundation (DFG) within the framework of the collaborative research center SFB 1176 (Project B3). JL is grateful for support from the Defense Threat Reduction Agency (DTRA) through Grant HDTRA1-12-1-0039 as a part of the interfacial dynamics and reactivity program and from the Army Research Office (ARO) under Grant W911NF-11-1-0251.

References

1. Licari, J. J. *Coating materials for electronic applications. Polymers, processes, reliability, testing;* Noyes Publishing: Norwich, NY, U.S.A., 2003.
2. Adhikari, B.; Majumdar, S. *Prog. Polym. Sci.* **2004,** *29,* 699–766. doi:10.1016/j.progpolymsci.2004.03.002
3. Smith, J. R.; Lamprou, D. A. *Trans. IMF* **2014,** *92,* 9–19. doi:10.1179/0020296713Z.000000000157
4. Asatekin, A.; Barr, M. C.; Baxamusa, S. H.; Lau, K. K. S.; Tenhaeff, W.; Xu, J.; Gleason, K. K. *Mater. Today* **2010,** *13,* 26–33. doi:10.1016/S1369-7021(10)70081-X
5. Chen, H.-Y.; Hirtz, M.; Deng, X.; Laue, T.; Fuchs, H.; Lahann, J. *J. Am. Chem. Soc.* **2010,** *132,* 18023–18025. doi:10.1021/ja108679m
6. Mao, Y.; Felix, N. M.; Nguyen, P. T.; Ober, C. K.; Gleason, K. K. *J. Vac. Sci. Technol., B* **2004,** *22,* 2473. doi:10.1116/1.1800351
7. Yu, J.; Holdcroft, S. *Chem. Commun.* **2001,** 1274–1275. doi:10.1039/b103128g
8. Kim, K. S.; Choi, C.; Kim, S. H.; Choi, K. o.; Kim, J. M.; Kim, H. J.; Yeo, S.; Park, H.; Jung, D. *Appl. Surf. Sci.* **2010,** *257,* 398–403. doi:10.1016/j.apsusc.2010.06.092
9. Lahann, J.; Langer, R. *Macromol. Rapid Commun.* **2001,** *22,* 968–971. doi:10.1002/1521-3927(20010801)22:12<968::AID-MARC968>3.0.CO;2-R
10. Chen, H.-Y.; Lahann, J. *Adv. Mater.* **2007,** *19,* 3801. doi:10.1002/adma.200602830
11. Jang, J.; Oh, J. H. *Chem. Commun.* **2004,** 882–883. doi:10.1039/b316083a
12. Trujillo, N. J.; Baxamusa, S. H.; Gleason, K. K. *Chem. Mater.* **2009,** *21,* 742–750. doi:10.1021/cm803008r

13. Wang, Y.; Chang, Y. C. *Adv. Mater.* **2003,** *15,* 290–293. doi:10.1002/adma.200390069
14. O'Shaughnessy, W. S.; Baxamusa, S.; Gleason, K. K. *Chem. Mater.* **2007,** *19,* 5836–5838. doi:10.1021/cm071381j
15. Cho, J.; Shin, K.-H.; Jang, J. *Thin Solid Films* **2010,** *518,* 5066–5070. doi:10.1016/j.tsf.2010.02.041
16. Andou, Y.; Nishida, H.; Endo, T. *Chem. Commun.* **2006,** 5018–5020. doi:10.1039/b612018k
17. Gomi, S.; Andou, Y.; Nishida, H. *J. Photopolym. Sci. Technol.* **2016,** *29,* 17–23. doi:10.2494/photopolymer.29.17
18. Vaeth, K. M.; Jackman, R. J.; Black, A. J.; Whitesides, G. M.; Jensen, K. F. *Langmuir* **2000,** *16,* 8495–8500. doi:10.1021/la000602w
19. Kwong, P.; Seidel, S.; Gupta, M. *J. Vac. Sci. Technol., A* **2015,** *33,* 31504. doi:10.1116/1.4915247
20. Vaeth, K. M.; Jensen, K. F. *Chem. Mater.* **2000,** *12,* 1305–1313. doi:10.1021/cm990642p
21. Vaeth, K. M.; Jensen, K. F. *Adv. Mater.* **1999,** *11,* 814–820. doi:10.1002/(SICI)1521-4095(199907)11:10<814::AID-ADMA814>3.0.CO;2-Z
22. Chen, H.-Y.; Lai, J. H.; Jiang, X.; Lahann, J. *Adv. Mater.* **2008,** *20,* 3474–3480. doi:10.1002/adma.200800455
23. Kwong, P.; Flowers, C. A.; Gupta, M. *Langmuir* **2011,** *27,* 10634–10641. doi:10.1021/la201532s
24. Wu, C.-Y.; Sun, H.-Y.; Liang, W.-C.; Hsu, H.-L.; Ho, H.-Y.; Chen, Y.-M.; Chen, H.-Y. *Chem. Commun.* **2016,** *52,* 3022–3025. doi:10.1039/C5CC08059B
25. Tsukagoshi, K.; Mizutani, W.; Tokumoto, H.; Miyamae, T.; Nozoye, H. *Surf. Sci.* **2002,** *514,* 48–53. doi:10.1016/S0039-6028(02)01606-0
26. Choi, H.-G.; Amara, J. P.; Swager, T. M.; Jensen, K. F. *Langmuir* **2007,** *23,* 2483–2491. doi:10.1021/la062268v
27. Bally-Le Gall, F.; Friedmann, C.; Heinke, L.; Arslan, H.; Azucena, C.; Welle, A.; Ross, A. M.; Wöll, C.; Lahann, J. *ACS Nano* **2015,** *9,* 1400–1407. doi:10.1021/nn505761x
28. Demiryürek, R.; Ali, M. K.; Ince, G. O. *Smart Mater. Struct.* **2014,** *23,* 95020. doi:10.1088/0964-1726/23/9/095020
29. Haller, P. D.; Bradley, L. C.; Gupta, M. *Langmuir* **2013,** *29,* 11640–11645. doi:10.1021/la402538e
30. Tao, R.; Anthamatten, M. *Macromol. Rapid Commun.* **2013,** *34,* 1755–1760. doi:10.1002/marc.201300566
31. Tao, R.; Anthamatten, M. *Langmuir* **2012,** *28,* 16580–16587. doi:10.1021/la303462q
32. Tao, R.; Anthamatten, M. *Macromol. Mater. Eng.* **2016,** *301,* 99–109. doi:10.1002/mame.201500280
33. Seidel, S.; Gupta, M. *J. Vac. Sci. Technol., A* **2014,** *32,* 41514. doi:10.1116/1.4884559
34. Kwong, P.; Seidel, S.; Gupta, M. *ACS Appl. Mater. Interfaces* **2013,** *5,* 9714–9718. doi:10.1021/am402775r
35. Seidel, S.; Kwong, P.; Gupta, M. *Macromolecules* **2013,** *46,* 2976–2983. doi:10.1021/ma302607c
36. Seidel, S.; Dianat, G.; Gupta, M. *Macromol. Mater. Eng.* **2016,** *301,* 371–376. doi:10.1002/mame.201500340
37. Dianat, G.; Seidel, S.; de Luna, M. M.; Gupta, M. *Macromol. Mater. Eng.* **2016,** *301,* 1037–1043. doi:10.1002/mame.201600124
38. Hawkeye, M. M.; Taschuk, M. T.; Brett, M. J. *Glancing angle deposition of thin films. Engineering the nanoscale;* Wiley: Chichester, West Sussex, United Kingdom, 2014.
39. Cetinkaya, M.; Boduroglu, S.; Demirel, M. C. *Polymer* **2007,** *48,* 4130–4134. doi:10.1016/j.polymer.2007.05.015
40. Demirel, M. C. *Colloids Surf., A* **2008,** *321,* 121–124. doi:10.1016/j.colsurfa.2008.02.028
41. Cetinkaya, M.; Demirel, M. C. *Chem. Vap. Deposition* **2009,** *15,* 101–105. doi:10.1002/cvde.200806747
42. Boduroglu, S.; Cetinkaya, M.; Dressick, W. J.; Singh, A.; Demirel, M. C. *Langmuir* **2007,** *23,* 11391–11395. doi:10.1021/la7025413
43. Sekeroglu, K.; Demirel, M. C. *Polymer* **2015,** *58,* 30–35. doi:10.1016/j.polymer.2014.12.031
44. Demirel, M. C.; So, E.; Ritty, T. M.; Naidu, S. H.; Lakhtakia, A. *J. Biomed. Mater. Res., Part B* **2007,** *81,* 219–223. doi:10.1002/jbm.b.30656
45. Demirel, M. C.; Cetinkaya, M.; Singh, A.; Dressick, W. J. *Adv. Mater.* **2007,** *19,* 4495–4499. doi:10.1002/adma.200701063

License and Terms

BEILSTEIN JOURNAL OF NANOTECHNOLOGY

Oxidative chemical vapor deposition of polyaniline thin films

Yuriy Y. Smolin‡, Masoud Soroush‡ and Kenneth K. S. Lau*,‡

Full Research Paper

Open Access

Address:
Department of Chemical and Biological Engineering, Drexel University, Philadelphia, PA 19104, USA

Email:
Kenneth K. S. Lau* - klau@drexel.edu

* Corresponding author ‡ Equal contributors

Keywords:
conducting polymers; emeraldine oxidation state; oxidative chemical vapor deposition; polyaniline; thin film processing

Beilstein J. Nanotechnol. **2017,** *8,* 1266–1276.
doi:10.3762/bjnano.8.128

Received: 16 January 2017
Accepted: 19 May 2017
Published: 16 June 2017

This article is part of the Thematic Series "Vapor-based polymers: from films to nanostructures".

Guest Editors: M. Koenig and J. Lahann

Abstract

Polyaniline (PANI) is synthesized via oxidative chemical vapor deposition (oCVD) using aniline as monomer and antimony pentachloride as oxidant. Microscopy and spectroscopy indicate that oCVD processing conditions influence the PANI film chemistry, oxidation, and doping level. Fourier transform infrared spectroscopy (FTIR), scanning electron microscopy (SEM), and X-ray photoelectron spectroscopy (XPS) indicate that a substrate temperature of 90 °C is needed to minimize the formation of oligomers during polymerization. Lower substrate temperatures, such as 25 °C, lead to a film that mostly includes oligomers. Increasing the oxidant flowrate to nearly match the monomer flowrate favors the deposition of PANI in the emeraldine state, and varying the oxidant flowrate can directly influence the oxidation state of PANI. Changing the reactor pressure from 700 to 35 mTorr does not have a significant effect on the deposited film chemistry, indicating that the oCVD PANI process is not concentration dependent. This work shows that oCVD can be used for depositing PANI and for effectively controlling the chemical state of PANI.

Introduction

Conducting polymers (CPs) have attracted considerable attention in recent years for their use in solar cells [1-6], batteries [7], supercapacitors [8-12], sensors [13], biosensors [14], and microelectronics [15,16]. As devices continue to decrease in size, the integration of conducting polymers within nanomaterials using conventional solvent-based methods becomes considerably more challenging due to the lack of solubility in common commercial solvents, which limits processability and leads to poor wettability. These challenges can be overcome with oxidative chemical vapor deposition (oCVD). oCVD is a single step, solvent-free polymerization and coating technique, which has previously been used to deposit thin and ultrathin conducting polymer films, including polypyrrole, polythiophene (PTh), and poly(3,4-ethylenedioxythiophene) (PEDOT), without the limitations of solvent-based techniques [17]. The oCVD process provides better control over the deposition (such as film thickness, conformality, uniformity, morphology) than current solution-based techniques such as chemical bath deposition [18],

electrodeposition [19], and casting from suspension [20]. As a result, oCVD has garnered significant attention in recent years as an advantageous route for depositing conducting polymer thin films without the need of a solvent or a conductive substrate, which naturally makes the process amenable in a wide range of applications [17,21]. Other methods such as plasma-enhanced CVD (PECVD) have previously been used to make conformal and uniform polymer films. However, the high energies in PECVD of polymers often result in the loss of functionality and degradation of a stoichiometric linear homopolymer [17]. Laser-based techniques, such as pulsed laser deposition (PLD), matrix-assisted pulsed laser evaporation (MAPLE), and laser-induced forward transfer (LIFT), have also been used to deposit polymer thin films [22]. However, these laser based methods also often lead to polymer degradation or a reduction in molecular weight [23-25]. Resonant infrared laser vapor deposition (RIR-LVP) has been used to deposit PEDOT but conductivity and morphology were highly dependent on the solvent matrix and the laser irradiation wavelength, and MAPLE led to a film that was electrically insulating [26].

Previous studies by Gleason and coworkers highlighted oCVD's advantages in the conformal deposition of PEDOT films with tunable nanoporosity [27], and demonstrated PEDOT as a neutral hole-transporting polymer for enhancing solar cells efficiency and lifetime [28]. oCVD PEDOT was also used to encapsulate flexible organic photovoltaics [29] and in the fabrication of organic photovoltaic circuits on unmodified paper [30]. Likewise, our group demonstrated the utility of oCVD in the synthesis of PTh and showed that the polymer conjugation length and electrical conductivity can be tuned by adjusting the oCVD processing conditions [31]. We further deposited ultrathin (4–6 nm) conformal and uniform PTh coatings within porous nanostructures, including anodized aluminum oxide, mesoporous TiO_2, and activated carbon; these oCVD PTh coatings resulted in enhanced charge storage due to preservation of the surface area and pore space within the nanostructures [32]. As a result, PTh-coated carbon electrodes showed a 50% increase in specific capacitance and excellent cycle life even after 5000 cycles due to the robust ultrathin coatings [32]. In addition, our study of the copolymerization of thiophene and pyrrole via oCVD showed enhanced conductivity and stability of the copolymers [33]. In view of experimental evidence that oCVD conducting polymers show favorable properties and can be easily processed, and that PANI has many advantages over PEDOT and PTh, including high theoretical capacitance (55% higher than PTh), low monomer cost, better stability, and high electrical conductivity [34,35], the deposition of PANI by oCVD is expected to open up new possibilities for significantly improving the performance and stability of energy storage devices along with other device classes such as sensors.

Therefore, this work aims to demonstrate the synthesis of PANI by the oCVD approach, in particular, to investigate systematically how oCVD processing variables influence PANI thin film deposition and chemistry. This processing knowledge is essential for oCVD PANI applications and for optimizing the performance of devices that use PANI coatings. Figure 1 shows the three basic oxidation states of PANI in the base (undoped) form. The fully reduced leucoemeraldine state, which is colorless, is composed fully of benzenoid groups (Figure 1a). At the other extreme, the fully oxidized pernigraniline state, is composed of all quinoid groups and produces a deep blue or violet color (Figure 1c). In between, the partially oxidized emeraldine form is composed of a 1:1 ratio of benzenoid and quinoid groups, which appears as a vivid green (Figure 1b). This emeraldine state is desired from an electrochemical standpoint, because its electrical conductivity is 10 orders of magnitude greater compared with the other two states [36]. Therefore, this work addresses how oCVD can be operated to tune the deposition and chemistry of emeraldine PANI.

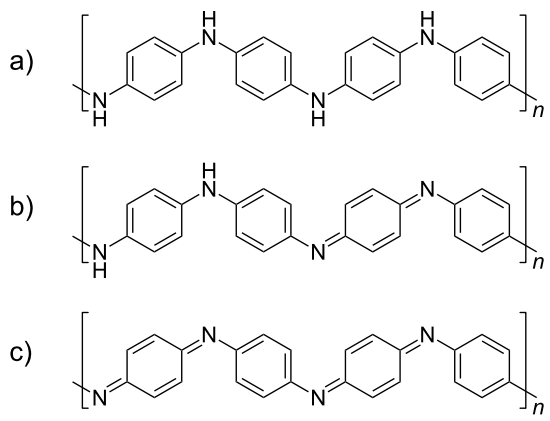

Figure 1: Chemical structure of the primary oxidation states of PANI in the undoped, base form. (a) Fully reduced leucoemeraldine PANI composed of benzenoid groups, (b) emeraldine PANI state composed of a 1:1 ratio of benzenoid and quinoid groups, and (c) fully oxidized pernigraniline PANI composed of quinoid groups.

Experimental

oCVD deposition of polyaniline

The oCVD process for PANI (Figure 2a) involves flowing vapors of the monomer (aniline) and the oxidant (antimony pentachloride, $SbCl_5$) into the reactor continuously. Nitrogen gas is used as an inert carrier to help transport the oxidant and as a diluent to help control polymerization reactions. The monomer and oxidant are delivered in separate quarter-inch stainless-steel tubes to isolate the reactants prior to entering the reaction chamber and minimize polymerization and blockage in the gas delivery manifold system. Upon entry into the oCVD reaction chamber, the monomer and oxidant vapors adsorb onto the sub-

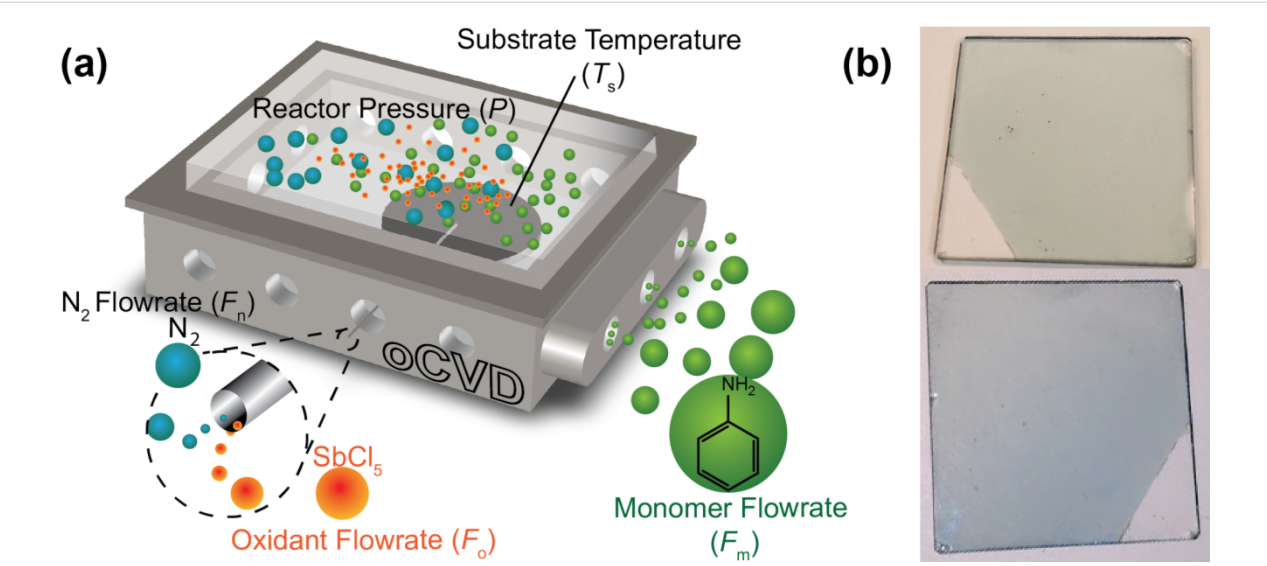

Figure 2: (a) oCVD process highlighting important process parameters, including substrate temperature (T_s), feed flowrates (F_o, F_m, F_n), and reactor pressure (P), for the synthesis of PANI. (b) oCVD PANI deposited on quartz glass (1" × 1") showing the emeraldine (green) and pernigraniline (blue) states. The uncoated portion was masked by tape during deposition.

strate surface and surface polymerize via a step-growth mechanism, which mimics the oxidative chemical polymerization used in solution-based processes to grow conducting polymers [17].

Aniline (Sigma-Aldrich, ACS reagents, >99.5%) and antimony pentachloride oxidant (Sigma-Aldrich, 99%) were used as-received without further purification. Separate source vessels containing antimony pentachloride and aniline were heated to 60 °C to produce sufficient vapors that were metered into the oCVD reaction chamber using low-flow precision metering valves (Swagelok). The "base-case" (BC) deposition conditions were used as a starting point to explore how processing conditions affected film chemistry (Table 1). It had a reactor pressure (P) of 700 mTorr, controlled using a downstream throttle value and pressure controller. The monomer and oxidant flowrates (F_m and F_o, respectively) were set at 1 and 0.8 sccm (standard $cm^3 \cdot min^{-1}$), respectively. Nitrogen gas, maintained at a flowrate (F_n) of 1 sccm by a mass flow controller (MKS 1479A), was also sent through the oxidant line as a diluent. PANI films with a target thickness of 250 nm were deposited on silicon wafers and quartz glass substrates, which were placed on a stage controlled at 90 °C (T_s) using backside contact with a recirculating thermal fluid (distilled H_2O).

oCVD processing conditions were then systematically varied from the base case, according to Table 1, to understand how they affect the resulting polymer film. First, the reactor pressure was varied from the base case of 700 mTorr to 35 mTorr (P series: BC, P1, P2). A lower reactor pressure should lead to more conformal deposition and polymerization given the greater mean free path and lower concentration. Second, the oxidant flowrate was varied from the base case of 0.8 sccm to 0.15 sccm (F series: BC, F1, F2) to investigate possible changes in the oxidization state and doping level of the PANI film due to

Table 1: oCVD process conditions for PANI synthesis and deposition.[a]

Run	P (mTorr)	T_s (°C)	F_o (sccm)	F_m (sccm)	F_n (sccm)	Sample notation
1	700	90	0.80	1	1	BC
2	100	90	0.80	1	1	P1
3	35	90	0.80	1	1	P2
4	700	90	0.30	1	1	F1
5	700	90	0.15	1	1	F2
6	700	25	0.80	1	1	LT-BC
7	700	25	0.30	1	1	LT-F1

[a]P = reactor pressure; T_s = substrate temperature; F_o, F_m, F_n = flowrates of the oxidant (antimony pentachloride), monomer (aniline), and nitrogen gas, respectively.

the antimony pentachloride oxidant. In addition to the reactor pressure and oxidant flowrate series of runs, two additional conditions were carried out at a lower substrate temperature of 25 °C compared to their high temperature counterparts (LT series: LT-BC, LT-F1). The decrease in the temperature may promote surface adsorption over reaction that can impact polymer growth, conjugation length, and chemistry.

In addtion to examining the as-deposited films, deposited samples were also soaked in tetrahydrofuran (THF >99.9%, Sigma-Aldrich) for 3 h and dried in a vacuum oven at 70 °C for 14 h. The washing process has previously been used to improve film properties, such as conductivity and stability, and often results in a much smoother film surface [17]. Besides THF, methanol is a common solvent that is used in the washing process, and acid-washing (e.g., HCl, HBr, H_2SO_4) has also been explored as a way to improve film conductivity by improving chain packing and increased doping [37,38]. The washed films were compared with their as-deposited counterparts to understand how soaking changes the oCVD PANI chemistry. Previous work on other oCVD conducting polymer films have shown that post-deposition rinsing improves film properties such as conductivity and stability by removing residual oxidant, short-chain oligomers, and unreacted monomer [17]. For example, Nejati et al. [31] have shown that washing oCVD PTh films removes the oxidant dopant and soluble portions of the film, which from UV–vis analysis was composed of short chain oligomers of five repeat units or shorter. Work on PEDOT hypothesizes that washing may also lead to tighter chain packing as evident by reduced degradation from water vapor and oxygen exposure [17,37-40]. Therefore, we expect that washing of the oCVD PANI films would remove the antimony pentachloride as well as any soluble oligomeric components that might lead to unfavorable electrochemical properties.

Thin film characterization

As-deposited and washed PANI films were analyzed by Fourier transform infrared spectroscopy (FTIR), X-ray photoelectron spectroscopy (XPS), and scanning electron microscopy (SEM). FTIR spectra were acquired using a Thermo Nicolet 6700 spectrometer in transmission mode using an MCT/A detector at a resolution of 4 cm^{-1} and averaged over 128 scans. An FTIR spectrum of aniline monomer was also acquired in attenuated total reflectance (ATR) mode. Top-down SEM images were taken using a Zeiss Supra 50VP with the in lens detector at 15 kV and a working distance of 4 mm. The images, acquired using line integration with 7 repeats, were used to estimate film thicknesses. Prior to SEM imaging, samples were sputtered with Pt for 30 s. XPS analysis was conducted using a Physical Electronics VersaProbe 5000 with a micro-focused monochromatic scanned X-ray beam from an Al Kα X-ray source (1486 eV photons) at a spot size of 100 µm, 25 W, and 15 kV. High resolution C1s, N1s, Cl2p, and Sb3d spectra were recorded with a pass energy of 23.5 eV and an energy step of 0.05 eV for a total of 512, 2048, 256, and 256 scans, respectively.

Results and Discussion

FTIR of as-deposited oCVD PANI films

Based on the oCVD approach, uniform PANI film depositions were performed on quartz glass substrates, and as seen in Figure 2b, the deposited films can have a vivid green or deep blue color depending on the oCVD conditions. Qualitatively, the colors indicate that PANI in the emeraldine or pernigraniline state, respectively, was formed. To better understand how PANI film chemistry and properties can be influenced by oCVD deposition conditions, a series of deposition runs that systematically looked at some of the critical oCVD processing variables were carried out (Table 1).

For the base case BC, as seen in Figure 3a (0.8 sccm in the *F* series) or Figure 3b (700 mTorr in the *P* series), the FTIR spectrum has peaks that are indicative of the salt form of PANI (doped form, see XPS results below), suggesting that the oxidant dopes the PANI film that is formed. This simultaneous polymerization and doping has been observed previously, for example, with the deposition of oCVD PTh using vanadium oxytrichloride as the oxidant [31]. As discussed in our previous oCVD PANI work [41], the polymerization and doping of polyaniline using oCVD are essentially analogous to chemical oxidative polymerization and acid doping using liquid processing. In the presence of an oxidizing agent, polymerization is believed to proceed via the formation of cation radicals and the electrophilic attack of aniline monomer [42], while in tandem the polymer can be p-doped and charged-balanced with a counterion dopant like chloride [43]. The PANI characteristic peaks are located at 3304, 3064, 1577, 1490, 1382, 1168, 821, and 516 cm^{-1}. The 3304 and 3000–3100 cm^{-1} peaks are assigned to NH and CH stretching, respectively, on the aromatic ring of PANI [44-46]. The 1168 cm^{-1} peak is attributed to $–NH^+=$ stretching and in-plane CH vibrations that suggests the formation of PANI in the salt (doped) form [46,47]. The 821 cm^{-1} peak is typically assigned to out-of-plane CH vibrations [47] that is consistent with high molecular weight PANI due to para-di-substitutions and confirms para-coupling of the constitutive aniline units [48,49]. The quinoid and benzenoid peaks are at 1577 and 1490 cm^{-1}, respectively [50], while the 1382 cm^{-1} peak is specifically CN stretching in the quinoid region of the film. The presence of benzenoid and quinoid peaks implies that both amine (N–C) and imine (N=C) units exist within the polymer chains. From the ratio of the 1577 to 1490 cm^{-1} peak intensities, it is possible to determine the oxidation state of the film [51]. For the as-deposited BC film, the ratio of the peak in-

tensities is 1.77, which suggests that the deposited film is mostly composed of quinoid groups and close to the fully oxidized pernigraniline state, as also shown by the blue color of the film (Figure 2b).

For the *F* series, as the oxidant flowrate (F_o) decreases, there is not a significant change in the FTIR spectra of oCVD PANI until a flowrate of 0.15 sccm is used (Figure 3a). First, the peak at 1579 cm^{-1} dramatically decreased from the higher F_o conditions. This signifies that there is less quinoid groups in the film and therefore the film is much less oxidized. This is expected because the oxidant flowrate is more than 5 times lower than the base case and therefore much less oxidant is available for oxidizing the PANI film. Second, the peaks of the lowest F_o condition (F2) also indicate that some of the film may contain oligomers. For instance, the peak at 1635 cm^{-1} can be assigned to NH scissoring vibrations of the aromatic amines [52] characteristic of an oligomeric structure. Also, the peak at 1382 cm^{-1}, which is the CN stretch in the quinoid structure, becomes nearly indistinguishable and so further confirms that the F2 film contains less quinoid rings. In contrast, the peaks at 749 and 688 cm^{-1}, which correspond to CH out-of-plane bending and out-of-plane ring deformation, respectively, of mono-substituted phenylene rings [48] increase in intensity. These peaks are associated with oligomers of around four repeat units, and indicate that a portion of the film is likely composed of oligomers. In fact, if one looks at the monomer spectrum in Figure 3a, these peaks at 749 and 688 cm^{-1} are strong and very sharp. Also, the broadening of the quinoid and benzenoid ring bands signifies a larger distribution of various quinoid structures, which has been reported for aniline oligomers [53]. Therefore, for the deposition of PANI by oCVD, a sufficiently high oxidant/monomer flowrate ratio (>0.3 for the conditions studied here) is required to deposit a film with more oxidized and higher molecular weight PANI while a lower ratio leads to a film that likely contains soluble oligomeric components.

For the *P* series, as the reactor pressure (*P*) decreases from 700 to 35 mTorr (Figure 3b) while maintaining a sufficient oxidant concentration, there is minimal change in the FTIR spectra. This indicates that the PANI chemistry is not very sensitive to pressure variations, at least when there is enough oxidant. Furthermore, with the deposition time held constant (5 min), the deposited film thickness and therefore the deposition kinetics did not change with pressure. Typically, lower reactor pressures would lead to slower kinetics. However, this does not seem to be the case for the oCVD parameter space studied here. Therefore, our conjecture is that the oCVD PANI process is not sensitive to reactant concentrations under these deposition conditions, and that the monomer and oxidant are most likely in excess to have any influence on deposition behavior.

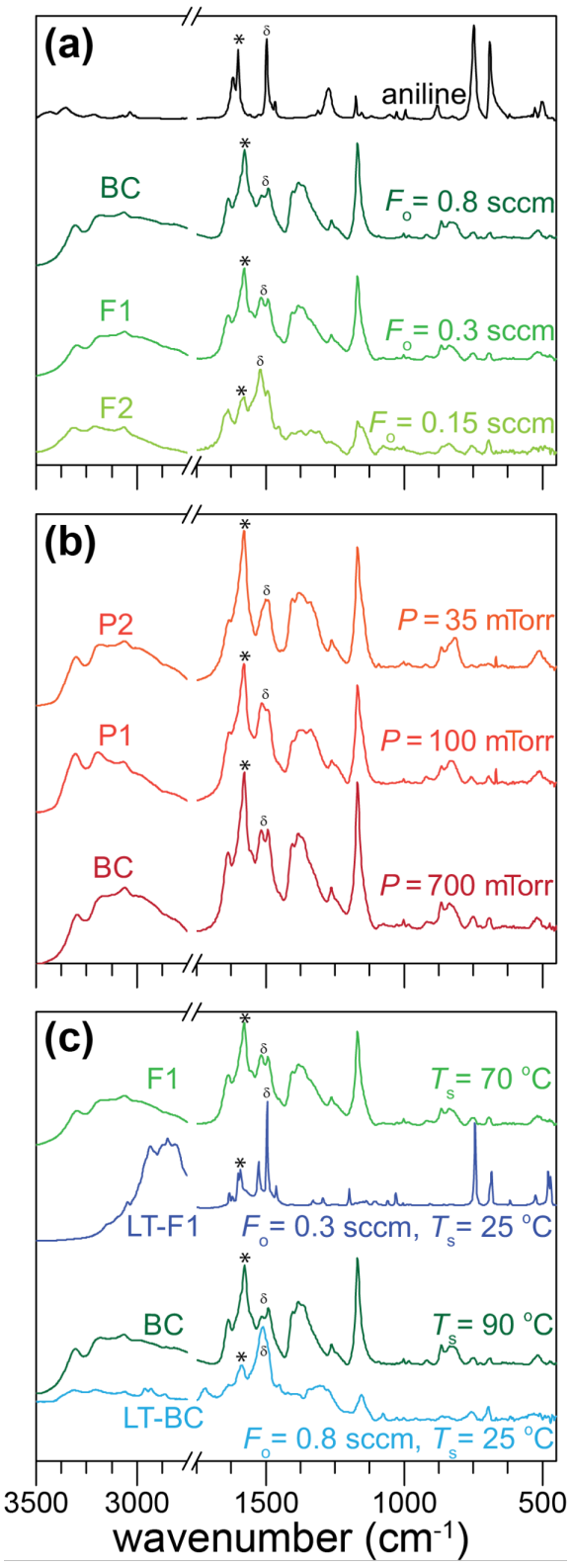

Figure 3: FTIR of as-deposited oCVD PANI films based on the experimental conditions in Table 1. Effect of (a) reactor pressure, (b) oxidant flow rate, and (c) substrate temperature on oCVD PANI chemistry. The quinoid and benzenoid groups are labeled by * and δ, respectively.

For the runs in which substrate temperature (T_s) was varied, their FTIR spectra can be compared, as shown in Figure 3c. For the LT-BC condition at 25 °C compared to BC at 90 °C (with both at the higher 0.8 sccm oxidant flow), there are several changes. First, the intensity of the 1580 cm^{-1} peak decreases, signifying proportionally fewer quinoid groups in the film and a lower oxidation state. Also, the peak at 1382 cm^{-1}, assigned to CN stretching vibration in the quinoid region, is smaller, which further confirms that the LT-BC film contains a smaller amount of quinoid groups. Previous work on oCVD PEDOT showed similar trends with a lower stage temperature yielding lower conjugation length and dopant incorporation [54,55]. Interestingly, the LT-BC spectrum (25 °C, 0.8 sccm oxidant) is very similar to that of F2 (90 °C, 0.15 sccm oxidant), which is believed to have a lower oxidation state and an appreciable amount of oligomers. This suggests that a low substrate temperature has an equivalent effect to reducing the amount of oxidant, which may be the result of more favorable adsorption of short chain oligomers at lower temperatures or slower kinetics at the surface. Further, for the LT-F1 condition, which is now at the low temperature of 25 °C as well as a lower oxidant flow of 0.3 sccm, the film loses most of the FTIR peaks associated with long chain PANI and appears to consist mostly of oligomers, which is supported by the peaks located at 1600, 1525, 1495, 1198, 1030, 684, and 743 cm^{-1}. Previous studies of aniline oligomers revealed that the aromatic ring peaks from 1590 to 1510 cm^{-1} are extremely sensitive to the oligomer chain structure and the relative intensity of the 1600 to 1525–1495 cm^{-1} peaks decreases with fewer quinoid rings in the chain [53]. Therefore, the LT-F1 film likely does not have many quinoid structures. Furthermore, the same work showed that oligomeric films lead to ≈10 cm^{-1} shift to higher wavenumbers for the benzenoid and quinoid peaks. Comparing LT-F1 to F1, we see a 5 and 23 cm^{-1} shift to higher wavenumbers for the benzenoid and quinoid peaks, supporting the hypothesis that a predominantly oligomeric film is formed. In fact, the LT-F1 spectrum is very similar to oligomers that are 2–3 aniline repeat units long [53]. This is also why the LT-F1 film is very similar to aniline monomer, although it is unlikely that the film contains any pure aniline since the monomer is sufficiently volatile under vacuum and most likely pumped out after lowering the reactor pressure to base pressure at the end of the deposition run.

FTIR of washed oCVD PANI films

Besides the as-deposited films, films were also soaked in THF after deposition and dried to investigate the effects of this post-deposition washing step. As mentioned, previous work on other oCVD polymers have shown improved electrochemical properties and stability with washing [17,31]. This has been attributed to the removal of oxidant and soluble oligomers from the films. The washed BC film, as seen in Figure 4a (0.8 sccm in the *F* series) or Figure 4b (700 mTorr in the *P* series), is typical PANI in the base form, with peaks at 1588, 1510, 1315, 1160, 1035, and 824 cm^{-1}. The reduction in peak intensity around 1160 cm^{-1} after washing as compared to the as-deposited BC film suggests a transition from the salt to the base form of PANI (see XPS results below). Furthermore, peak shifts between the as-deposited and washed BC films also indicate that the film transitions from the doped salt form to the undoped base form. For instance, the 865 and 1160 cm^{-1} peaks of as-deposited BC have shifted by 30 and 54 cm^{-1}, respectively, to higher wavenumbers in the washed film, and this indicates that the

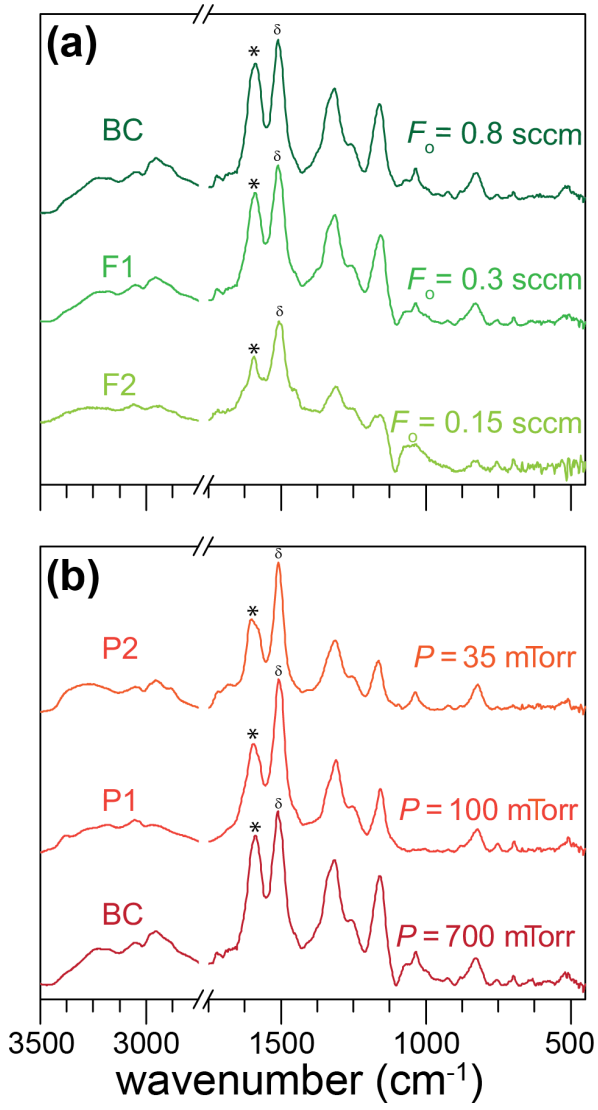

Figure 4: FTIR of washed oCVD PANI films based on the experimental conditions in Table 1. Effect of (a) reactor pressure, and (b) oxidant flow rate on oCVD PANI chemistry after washing. The quinoid and benzenoid groups are labeled by * and δ, respectively.

film has transitioned to the undoped base state [56]. Work by Trchová et al. [47] showed that only the base form of PANI contains a peak at ≈1315 cm^{-1} (the acid doped form of PANI shifts this peak lower by 10 cm^{-1}), which is what is observed for the washed BC film. Similar to the as-deposited film, the peak at 825 cm^{-1} for the washed film is consistent with high molecular weight PANI due to para-di-substitution and suggests para-coupling of the chain units [48,49]. The oxidation state can be derived from the relative intensities of the 1588 quinoid and 1510 cm^{-1} benzenoid peaks, which for the washed film, gives a value of 0.87 and suggests that most of the washed BC polymer is in the emeraldine form. This makes oCVD a highly promising approach for a wide range of applications that can make use of the favorable properties of emeraldine PANI. The presence of emeraldine PANI is further supported by the green color of the washed PANI film (Figure 2b). In addition, previous oCVD PANI UV–vis measurements have also suggested the formation of emeraldine PANI [41].

The *F* series in Figure 4a shows washed films deposited under different oCVD operating conditions. As can be seen, similar to the FTIR spectra for the as-deposited films (Figure 3a), there is minimal influence of the oxidant flowrate down to 0.3 sccm. However, at the lowest oxidant flow rate of 0.15 sccm (washed F2 film), there is a lower peak intensity at 1588 cm^{-1}, suggesting that the film is in the fully reduced leucoemeraldine state. Taking the ratio of the quinoid and benzenoid peak intensities leads to a ratio of 0.41, suggesting that the film is primarily composed of benzenoid groups with a low concentration of quinoid groups. This is expected because, with the much lower oxidant flowrate, there is probably insufficient oxidant available for oxidative polymerization and doping, thus leading to a lower oxidation state of the film. Further, with washing, the film becomes dedoped. For the *P* series (Figure 4b), again similar to the as-deposited counterparts, there does not seem to be a major effect of reactor pressure on film chemistry. As discussed above, we hypothesize that, in general, the oCVD PANI reaction is not pressure or concentration dependent based on the conditions studied. As for washing the lower substrate temperature films, LT-BC and LT-F1, it should be pointed out that both films completely dissolved in THF and therefore no FTIR of the washed films was possible. However, the ease of dissolution further supports our earlier conclusion that these conditions led to films that were primarily soluble oligomers.

SEM and XPS of as-deposited and washed oCVD PANI films

Given that the base case condition (Table 1) seems to have yielded the preferred emeraldine PANI state, further studies were carried out on both the as-deposited and washed BC films to detail their film chemistry and structure. As shown in the top-down SEM images presented in Figure 5, the film morphology did not visibly change after washing. Zoomed-out SEM images in the Supporting Information also show a uniform film morphology before and after washing (Figure S1, Supporting Information File 1). This qualitatively indicates that the BC film is stable and free of oligomers that would most likely alter film morphology if they were dissolved out of the film. Additionally, XPS was performed to understand more quantitatively the oxidation state and doping level of PANI before and after washing. The BC condition was chosen for analysis because our earlier FTIR findings indicated that high substrate temperature, pressure, and oxidant flowrate are favorable for depositing PANI by oCVD. To investigate the presence of the antimony pentachloride oxidant before and after washing, high resolution Cl2p and Sb3d core level XPS spectra were obtained (Figure S2, Supporting Information File 1). From these spectra, the amount of Cl and Sb in the as-deposited film was 6.9 and 11.59 atom %, while after washing, these values decreased to 1.24 and 0.34 atom %, representing a reduction of 82 and 97% reduction,

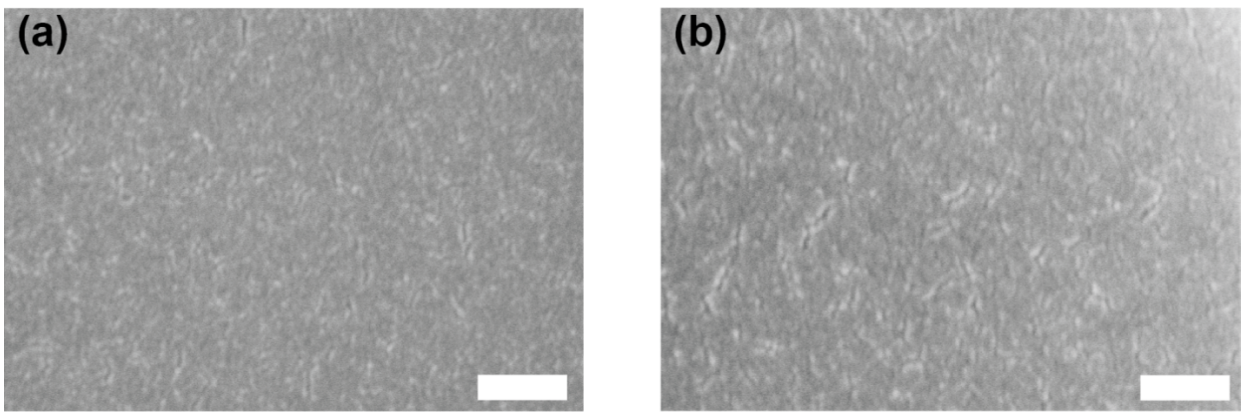

Figure 5: Top-down SEM of (a) as-deposited, and (b) THF-washed oCVD PANI films. Scale bar is 200 nm.

respectively. This indicates that the doping level of the film significantly decreases after the washing process, and corroborates the FTIR finding that showed the BC film transition from the PANI salt to PANI base form when washed with THF.

Further XPS was done to obtain the high resolution N1s XPS spectra of the BC film before and after washing, as shown in Figure 6. For the as-deposited film, the N1s spectrum can be resolved into four unique nitrogen bonding environments, see Table 2. The resolved peak positions and FWHM values are very similar to those reported for PANI [57-60]. The lowest binding energy state (N1) is a neutral imine (–N=) and comes from the base form of the emeraldine and pernigraniline structure of PANI (Figure 1). This peak is associated with the quinoid groups. The next state up (N2) is the neutral amine (–NH–), which is found in the base form of the leucoemeraldine and emeraldine states. It is associated with the benzenoid groups. The third higher energy nitrogen state (N3) is a cation radical amine state and comes most likely from the acid form of the emeraldine state. Finally, the fourth and highest-energy state (N4) can be attributed to a cation amine state, which comes from the salt form of PANI. From the resolved peak analysis, the relative amounts of N1, N2, N3, and N4 are 65.5, 21.5, 11.1, and 2.2 atom %, respectively (Table 2). In addition, by considering the intensity ratio of $(N1 + N3 + N4)/N_{total}$, it is possible to determine the oxidation state of the as-deposited BC film, for example, a value of 0.5 indicates emeraldine PANI. For the as-deposited BC film, a ratio of 0.79 corresponds to a film that is ≈80% oxidized. This indicates that the film has a higher concentration of quinoid groups and therefore is highly oxidized. This validates the FTIR results which give the same conclusion. Upon washing, the resolved N1s spectrum shows the relative proportions of N1, N2, N3, and N4 are 34.2, 50.4, 15.4, and 0 atom %, respectively (Table 2). The most obvious change is the disappearance of N4. Since this aligns with the dramatic reduction in the antimony and chlorine dopant levels after washing and given N4 is a doped cation, this indicates that this state is formed as a result of the oxidant simultaneously enabling polymerization and doping of the growing PANI film. Similar to the as-deposited film, the oxidation state of the washed BC film can be determined by taking the ratio of $(N1 + N3)/N_{total}$. For the washed BC film, this ratio is 0.49, which is very close to the theoretical value of 0.5 for PANI in the emeraldine form. This corroborates the FTIR results, which suggested the emeraldine state of the washed BC film.

Likewise, XPS was carried out to obtain the high resolution C1s XPS spectra of as-deposited and washed BC films, as seen in Figure 6. The carbon signal for the as-deposited BC film can be resolved into four bonding environments, see Table 2. The

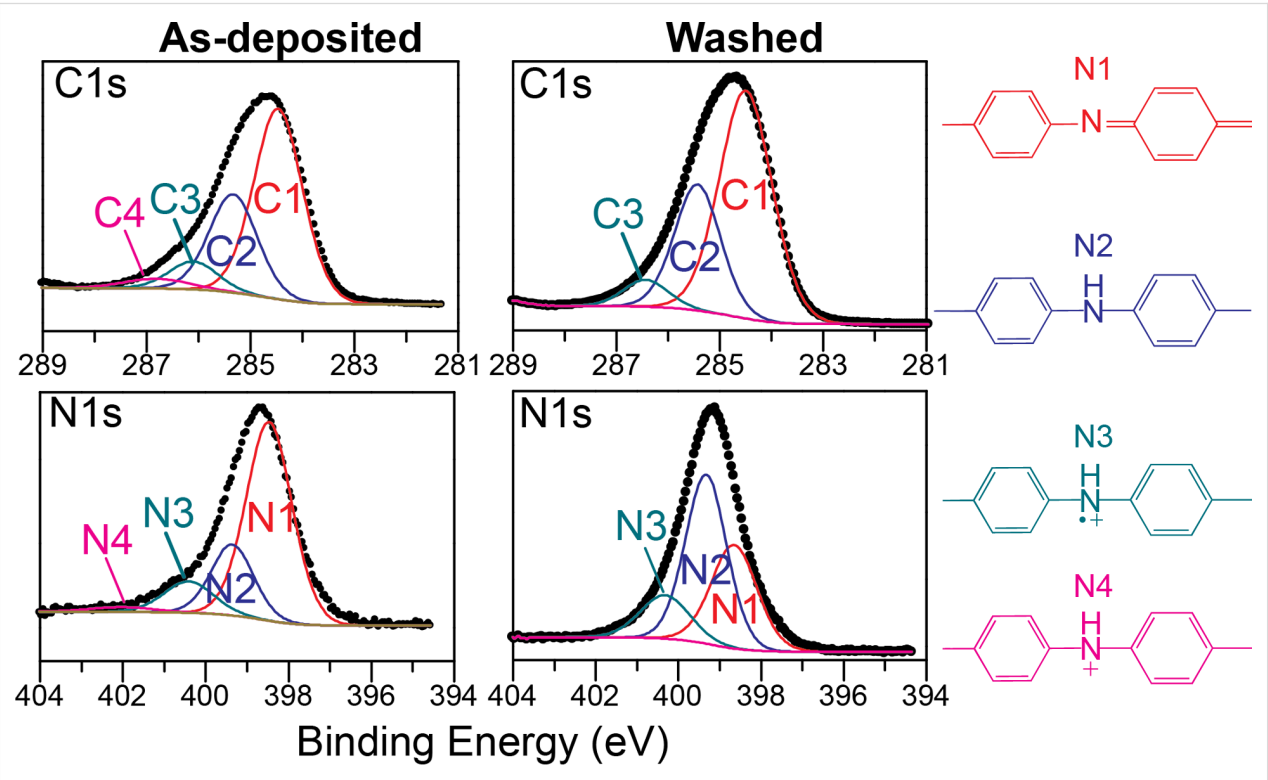

Figure 6: High-resolution C1s and N1s XPS spectra of as-deposited (left) and washed (right) oCVD PANI films. The resolved nitrogen bonding environments are assigned to non-equivalent nitrogen groups in PANI that are color-coordinated to the XPS spectra.

Table 2: Resolved peak data from N1s and C1s XPS spectra of as-deposited and washed oCVD PANI films (BC condition).

	N1	N2	N3	N4	C1	C2	C3	C4
As-deposited								
Binding energy (eV)	398.5	399.4	400.4	402.0	284.5	285.3	286.1	286.8
Atomic %	65.2	21.5	11.1	2.2	58.0	29.6	8.5	3.9
Washed								
Binding energy (eV)	398.7	399.3	400.4	–	284.5	285.3	286.0	–
Atomic %	34.2	50.4	15.4	–	63.2	30.5	6.3	–

lowest binding energy state (C1) corresponds to the C–C and C–H bonds, which for PANI, is due to the =CH– group [61]. The second lowest energy state (C2) can be assigned to neutral C–N bonds, which for PANI are those of N1 and N2, corresponding to the carbons bonded to neutral amine and imine nitrogens. The third, higher energy state (C3) is the carbon that is bound to the cation radical nitrogen (N3), while the highest energy state (C4) is given to a carbon bound to the cation nitrogen (N4). From Table 2, the fractions of C1, C2, C3, and C4 for the as-deposited BC film are 58.0, 29.6, 8.5, and 3.9%, respectively, while after washing, the proportions become 34.2, 50.4, 15.4, and 0%, respectively. Again, the loss of the C4 peak can be attributed to the removal of the dopant due to the washing process. Based on XPS work with electrodeposited PANI, Kumar and coworkers [60,61] stated that the resolved carbon peaks can be used to determine if PANI contains only para-coupling of the repeat unit. Specifically, if the intensity ratio of C1/(C2 + C3 + C4) is equal to 2, only para-coupling takes place within the ring. For our case here, the ratio is 1.4 and 1.7, respectively, for the as-deposited and washed BC films. The washed film is close to 2, which indicates primarily para-coupling. A ratio much lower than 2 suggests that there could be further ortho-coupling in addition to para-coupling of the aniline ring [60,61]. These structures seem to be removed with washing and could be related to less stable oligomer units.

Conclusions

The oCVD process provides a viable approach for a one-step synthesis and deposition of PANI thin films using aniline monomer and antimony pentachloride oxidant. By carefully adjusting oCVD processing parameters, emeraldine PANI with its more desirable electrochemical properties can be formed. By varying the processing conditions, the oxidation level, doping concentration, and film chemistry, as determined by spectroscopy, could be controlled. Specifically, a high substrate temperature (90 °C) and a nearly equimolar ratio of monomer-to-oxidant feed flow rates that provides sufficient amount of oxidant is needed to produce PANI in the emeraldine state. This optimal oCVD condition has been shown to have superb electrochemical performance [41]. Lowering the substrate temperature to 25 °C or reducing the oxidant flowrate below 0.3 sccm leads to predominantly an oligomeric film. However, changing reactor pressure does not have any appreciable effect of the film chemistry. By washing oCVD PANI films with THF, which acts also as a dopant, soluble oligomer components can be removed effectively. This work, for the first time, identified synthesis conditions suitable for making PANI via oCVD, and revealed the influence of different processing parameters on film chemistry. The ability to use oCVD to produce emeraldine PANI is expected to open up new areas and applications, particularly in the field of electrochemical energy storage, which can benefit from the integration of thin PANI films without the issues of liquid processing.

Supporting Information

Supporting Information File 1

Additional data.
[http://www.beilstein-journals.org/bjnano/content/supplementary/2190-4286-8-128-S1.pdf]

Acknowledgements

The authors gratefully acknowledge support from the U.S. National Science Foundation (CBET-1236180, 1264487, and 1463170). We would like to acknowledge the use of Drexel University's Core Facilities and the facilities of Prof. Giuseppe Palmese's laboratory.

References

1. Huynh, W. U.; Dittmer, J. J.; Alivisatos, A. P. *Science* **2002,** *295,* 2425–2427. doi:10.1126/science.1069156
2. Kim, J. Y.; Lee, K.; Coates, N. E.; Moses, D.; Nguyen, T.-Q.; Dante, M.; Heeger, A. J. *Science* **2007,** *317,* 222–225. doi:10.1126/science.1141711

3. Li, G.; Zhu, R.; Yang, Y. *Nat. Photonics* **2012,** *6,* 153–161. doi:10.1038/nphoton.2012.11
4. Chen, H.-Y.; Hou, J.; Zhang, S.; Liang, Y.; Yang, G.; Yang, Y.; Yu, L.; Wu, Y.; Li, G. *Nat. Photonics* **2009,** *3,* 649–653. doi:10.1038/nphoton.2009.192
5. Günes, S.; Neugebauer, H.; Sariciftci, N. S. *Chem. Rev.* **2007,** *107,* 1324–1338. doi:10.1021/cr050149z
6. Smolin, Y. Y.; Nejati, S.; Bavarian, M.; Lee, D.; Lau, K. K. S.; Soroush, M. *J. Power Sources* **2015,** *274,* 156–164. doi:10.1016/j.jpowsour.2014.10.028
7. Wu, H.; Yu, G.; Pan, L.; Liu, N.; McDowell, M. T.; Bao, Z.; Cui, Y. *Nat. Commun.* **2013,** *4,* 1943. doi:10.1038/ncomms2941
8. Zhang, J.; Zhao, X. S. *J. Phys. Chem. C* **2012,** *116,* 5420–5426. doi:10.1021/jp211474e
9. Ramya, R.; Sivasubramanian, R.; Sangaranarayanan, M. V. *Electrochim. Acta* **2013,** *101,* 109–129. doi:10.1016/j.electacta.2012.09.116
10. Wang, K.; Wu, H.; Meng, Y.; Wei, Z. *Small* **2014,** *10,* 14–31. doi:10.1002/smll.201301991
11. Shi, Y.; Pan, L.; Liu, B.; Wang, Y.; Cui, Y.; Bao, Z.; Yu, G. *J. Mater. Chem. A* **2014,** *2,* 6086–6091. doi:10.1039/c4ta00484a
12. Lin, H.; Li, L.; Ren, J.; Cai, Z.; Qiu, L.; Yang, Z.; Peng, H. *Sci. Rep.* **2013,** *3,* 1353. doi:10.1038/srep01353
13. Osada, Y.; De Rossi, D. E. *Polymer Sensors and Actuators;* Springer Science & Business Media, 2013. doi:10.1007/978-3-662-04068-3
14. Ates, M. *Mat. Sci. Eng. C* **2013,** *33,* 1853–1859. doi:10.1016/j.msec.2013.01.035
15. Menard, E.; Meitl, M. A.; Sun, Y.; Park, J.-U.; Shir, D. J.-L.; Nam, Y.-S.; Jeon, S.; Rogers, J. A. *Chem. Rev.* **2007,** *107,* 1117–1160. doi:10.1021/cr050139y
16. Grayson, A. C. R.; Shawgo, R. S.; Johnson, A. M.; Flynn, N. T.; Li, Y.; Cima, M. J.; Langer, R. *Proc. IEEE* **2004,** *92,* 6–21. doi:10.1109/JPROC.2003.820534
17. Gleason, K. K. *CVD Polymers: Fabrication of Organic Surfaces and Devices;* John Wiley & Sons, 2015. doi:10.1002/9783527690275
18. Huang, W.-S.; Humphrey, B. D.; MacDiarmid, A. G. *J. Chem. Soc., Faraday Trans. 1* **1986,** *82,* 2385–2400. doi:10.1039/f19868202385
19. Zotti, G.; Cattarin, S.; Comisso, N. *J. Electroanal. Chem. Interfacial Electrochem.* **1987,** *235,* 259–273. doi:10.1016/0022-0728(87)85212-9
20. Andreatta, A.; Cao, Y.; Chiang, J. C.; Heeger, A. J.; Smith, P. *Synth. Met.* **1988,** *26,* 383–389. doi:10.1016/0379-6779(88)90233-0
21. Wang, M.; Wang, X.; Moni, P.; Liu, A.; Kim, D. H.; Jo, W. J.; Sojoudi, H.; Gleason, K. K. *Adv. Mater.* **2016,** *29,* 1604606. doi:10.1002/adma.201604606
22. Eason, R. *Pulsed Laser Deposition of Thin Films: Applications-Led Growth of Functional Materials;* John Wiley & Sons, 2007. doi:10.1002/0470052120
23. Mercado, A. L.; Allmond, C. E.; Hoekstra, J. G.; Fitz-Gerald, J. M. *Appl. Phys. A* **2005,** *81,* 591–599. doi:10.1007/s00339-004-2994-2
24. Chrisey, D. B.; Piqué, A.; McGill, R. A.; Horwitz, J. S.; Ringeisen, B. R.; Bubb, D. M.; Wu, P. K. *Chem. Rev.* **2003,** *103,* 553–576. doi:10.1021/cr010428w
25. Hansen, S. G.; Robitaille, T. E. *Appl. Phys. Lett.* **1988,** *52,* 81–83. doi:10.1063/1.99332
26. Johnson, S.; Park, H.; Haglund, R. *Appl. Surf. Sci.* **2007,** *253,* 6430–6434. doi:10.1016/j.apsusc.2007.01.084
27. Im, S. G.; Kusters, D.; Choi, W.; Baxamusa, S. H.; van de Sanden, M. C. M.; Gleason, K. K. *ACS Nano* **2008,** *2,* 1959–1967. doi:10.1021/nn800380e
28. Jo, W. J.; Nelson, J. T.; Chang, S.; Bulović, V.; Gradečak, S.; Strano, M. S.; Gleason, K. K. *Adv. Mater.* **2016,** *28,* 6399–6404. doi:10.1002/adma.201601221
29. Chen, N.; Kovacik, P.; Howden, R. M.; Wang, X.; Lee, S.; Gleason, K. K. *Adv. Energy Mater.* **2015,** *5,* 1401442. doi:10.1002/aenm.201401442
30. Barr, M. C.; Rowehl, J. A.; Lunt, R. R.; Xu, J.; Wang, A.; Boyce, C. M.; Im, S. G.; Bulović, V.; Gleason, K. K. *Adv. Mater.* **2011,** *23,* 3500–3505. doi:10.1002/adma.201101263
31. Nejati, S.; Lau, K. K. S. *Langmuir* **2011,** *27,* 15223–15229. doi:10.1021/la203318f
32. Nejati, S.; Minford, T. E.; Smolin, Y. Y.; Lau, K. K. S. *ACS Nano* **2014,** *8,* 5413–5422. doi:10.1021/nn500007c
33. Nejati, S.; Patel, A.; Wallowitch, G. R.; Lau, K. K. *Nanosci. Nanotechnol. Lett.* **2015,** *7,* 50–55. doi:10.1166/nnl.2015.1907
34. Snook, G. A.; Kao, P.; Best, A. S. *J. Power Sources* **2011,** *196,* 1–12. doi:10.1016/j.jpowsour.2010.06.084
35. Bhadra, S.; Khastgir, D.; Singha, N. K.; Lee, J. H. *Prog. Polym. Sci.* **2009,** *34,* 783–810. doi:10.1016/j.progpolymsci.2009.04.003
36. Chiang, J.-C.; MacDiarmid, A. G. *Synth. Met.* **1986,** *13,* 193–205. doi:10.1016/0379-6779(86)90070-6
37. Lee, S.; Paine, D. C.; Gleason, K. K. *Adv. Funct. Mater.* **2014,** *24,* 7187–7196. doi:10.1002/adfm.201401282
38. Howden, R. M.; McVay, E. D.; Gleason, K. K. *J. Mater. Chem. A* **2013,** *1,* 1334–1340. doi:10.1039/C2TA00321J
39. Chelawat, H.; Vaddiraju, S.; Gleason, K. *Chem. Mater.* **2010,** *22,* 2864–2868. doi:10.1021/cm100092c
40. Nardes, A. M.; Kemerink, M.; de Kok, M. M.; Vinken, E.; Maturova, K.; Janssen, R. A. J. *Org. Electron.* **2008,** *9,* 727–734. doi:10.1016/j.orgel.2008.05.006
41. Smolin, Y. Y.; Van Aken, K. L.; Boota, M.; Soroush, M.; Gogotsi, Y.; Lau, K. K. S. *Adv. Mater. Interfaces* **2017,** *4,* 1601201. doi:10.1002/admi.201601201
42. Genies, E. M.; Tsintavis, C. *J. Electroanal. Chem. Interfacial Electrochem.* **1985,** *195,* 109–128. doi:10.1016/0022-0728(85)80009-7
43. Hatchett, D. W.; Josowicz, M.; Janata, J. *J. Phys. Chem. B* **1999,** *103,* 10992–10998. doi:10.1021/jp991110z
44. Neugebauer, H.; Neckel, A.; Sariciftci, N. S.; Kuzmany, H. *Synth. Met.* **1989,** *29,* 185–192. doi:10.1016/0379-6779(89)90295-6
45. Patil, D. S.; Shaikh, J. S.; Dalavi, D. S.; Kalagi, S. S.; Patil, P. S. *Mater. Chem. Phys.* **2011,** *128,* 449–455. doi:10.1016/j.matchemphys.2011.03.029
46. Šeděnková, I.; Trchová, M.; Blinova, N. V.; Stejskal, J. *Thin Solid Films* **2006,** *515,* 1640–1646. doi:10.1016/j.tsf.2006.05.038
47. Trchová, M.; Šeděnková, I.; Tobolková, E.; Stejskal, J. *Polym. Degrad. Stab.* **2004,** *86,* 179–185. doi:10.1016/j.polymdegradstab.2004.04.011
48. Stejskal, J.; Trchová, M. *Polym. Int.* **2012,** *61,* 240–251. doi:10.1002/pi.3179
49. Zaharias, G. A.; Shi, H. H.; Bent, S. F. *Thin Solid Films* **2006,** *501,* 341–345. doi:10.1016/j.tsf.2005.07.145
50. Ping, Z. *J. Chem. Soc., Faraday Trans.* **1992,** *92,* 3063–3067. doi:10.1039/FT9969203063
51. Abdiryim, T.; Xiao-Gang, Z.; Jamal, R. *Mater. Chem. Phys.* **2005,** *90,* 367–372. doi:10.1016/j.matchemphys.2004.10.036

52. Trchová, M.; Stejskal, J. *Pure Appl. Chem.* **2011,** *83,* 1803–1817. doi:10.1351/PAC-REP-10-02-01
53. Cao, Y.; Li, S.; Xue, Z.; Guo, D. *Synth. Met.* **1986,** *16,* 305–315. doi:10.1016/0379-6779(86)90167-0
54. Im, S. G.; Gleason, K. K.; Olivetti, E. A. *Appl. Phys. Lett.* **2007,** *90,* 152112. doi:10.1063/1.2721376
55. Lock, J. P.; Im, S. G.; Gleason, K. K. *Macromolecules* **2006,** *39,* 5326–5329. doi:10.1021/ma060113o
56. Li, J.; Tang, X.; Li, H.; Yan, Y.; Zhang, Q. *Synth. Met.* **2010,** *160,* 1153–1158. doi:10.1016/j.synthmet.2010.03.001
57. Tan, K. L.; Tan, B. T. G.; Kang, E. T.; Neoh, K. G. *Phys. Rev. B* **1989,** *39,* 8070–8073. doi:10.1103/PhysRevB.39.8070
58. Golczak, S.; Kanciurzewska, A.; Fahlman, M.; Langer, K.; Langer, J. J. *Solid State Ionics* **2008,** *179,* 2234–2239. doi:10.1016/j.ssi.2008.08.004
59. Zeng, X.-R.; Ko, T.-M. *Polymer* **1998,** *39,* 1187–1195. doi:10.1016/S0032-3861(97)00381-9
60. Kumar, S. N.; Gaillard, F.; Bouyssoux, G.; Sartre, A. *Synth. Met.* **1990,** *36,* 111–127. doi:10.1016/0379-6779(90)90240-L
61. Kumar, S.; Bouyssoux, G.; Gaillard, F. *Surf. Interface Anal.* **1990,** *15,* 531–536. doi:10.1002/sia.740150906

License and Terms

BEILSTEIN JOURNAL OF NANOTECHNOLOGY

Micro- and nano-surface structures based on vapor-deposited polymers

Hsien-Yeh Chen

Review

Open Access

Address:
Department of Chemical Engineering, National Taiwan University, Taipei 10617, Taiwan

Email:
Hsien-Yeh Chen - hsychen@ntu.edu.tw

Keywords:
multifunctional; polymer coating; surface modification; surface patterning; vapor deposition

Beilstein J. Nanotechnol. **2017,** *8,* 1366–1374.
doi:10.3762/bjnano.8.138

Received: 27 January 2017
Accepted: 09 June 2017
Published: 04 July 2017

This article is part of the Thematic Series "Vapor-based polymers: from films to nanostructures".

Guest Editors: M. Koenig and J. Lahann

Abstract

Vapor-deposition processes and the resulting thin polymer films provide consistent coatings that decouple the underlying substrate surface properties and can be applied for surface modification regardless of the substrate material and geometry. Here, various ways to structure these vapor-deposited polymer thin films are described. Well-established and available photolithography and soft lithography techniques are widely performed for the creation of surface patterns and microstructures on coated substrates. However, because of the requirements for applying a photomask or an elastomeric stamp, these techniques are mostly limited to flat substrates. Attempts are also conducted to produce patterned structures on non-flat surfaces with various maskless methods such as light-directed patterning and direct-writing approaches. The limitations for patterning on non-flat surfaces are resolution and cost. With the requirement of chemical control and/or precise accessibility to the linkage with functional molecules, chemically and topographically defined interfaces have recently attracted considerable attention. The multifunctional, gradient, and/or synergistic activities of using such interfaces are also discussed. Finally, an emerging discovery of selective deposition of polymer coatings and the bottom-up patterning approach by using the selective deposition technology is demonstrated.

Review

Introduction

Vapor-based processes of polymer coating/deposition combine many unique attributes in a dry, solvent-free process, and the deposition protocols as well as the resulting coatings are mostly applicable to a wide range of substrate materials [1]. In addition, the vapor deposition process typically provides excellent coating fidelity, i.e., the resulting polymer coatings are conformal with respect to micrometer- or nanometer-sized topology of the substrate surface. These unique characteristics are due to the absence of dewetting effects [2], which can make the coatings bridge and buckle. In contrast, dewetting is often

encountered in the case of solution-based polymer coatings [3]. Vapor-deposited polymer coatings are widely discussed in interfacial engineering and surface modification technologies for surfaces/devices with sensitive and miniaturized patterns or structures [4,5]. Furthermore, vapor-deposited polymers provide defined chemical control and/or precise accessibility to the linkage with functional molecules at the coating interface. The thrilling developments of such functional activities have recently shown promise to create multiple surface functionalities or gradients that account for the previously mentioned attributes while also rendering the concurrent display of multiple functions and/or synergistic activities to respond to sophisticated microenvironments [6-9].

This review first discusses recent developments in vapor-based polymer deposition and emphasizes the ability to deposit polymers with spatially controlled structures/patterns on the surfaces of substrates regardless of the substrate materials and geometry, i.e., 2D flat substrates or 3D complex substrates. Next, the creation of multiple or gradient structures/patterns on the polymers provides an interfacial template with multifunctional reactivity and gradient information for multifunctional or directional activities. Then, the emerging discovery of the selective deposition of polymer coatings is discussed. This report highlights relevant works and advances by the researchers in the field and is not intended to comprehensively cover the literature from the entire field. Finally, current technological challenges and potential future directions are suggested according to the opinion of the author.

Structuring of conventional 2D surfaces

Over the past decades, extensive effort has been made and successes have been achieved to create topological surface patterns based on light [10], electrons [11], ion beams [12], X-rays [13], or manipulation of atomic beams [14]. Also, printing methods with elastomeric stamps or replica structures to transfer a material from a solution onto a surface, which are collectively related to imprinting lithography [15,16] or soft lithography [17,18], were developed. Thus, the early developments of the patterning and structuring technologies for vapor-based coatings largely depend on adaptation from these lithographical approaches (Figure 1). A DNA array was fabricated in a photolithographical liftoff process on a vapor-deposited (chemical vapor deposition, CVD) poly-*p*-xylylene surface, and the resulting array surface showed excellent uniformity with reduced array-to-array variation [19]. Vapor-phased plasma polymerization to prepare polyacrylic acid has also used to pattern and functionalize microfluidic devices based on wet and dry etching techniques [20]. Combining plasma polymerization and lithographical processes has also been used for the pattern formation of polyethylene glycol (PEG)-like polymer derivatives to guide fibroblast attachment [21]. A photodefinable polymer of poly(4-benzoyl-*p*-xylylene-*co*-*p*-xylylene) was synthesized by CVD, and a combined soft lithographical and UV light process was performed to create the microstructures of PEG hydrogels [22]. In a separate report, this photodefinable polymer was used to pattern protein molecules using a photomask-assisted lithographical approach [23]. Recently, surface patterns were enabled via light-induced thiol-ene/thiol-yne reactions on a poly(4-vinyl-*p*-xylylene-*co*-*p*-xylylene) surface and a poly(4-ethynyl-*p*-xylylene-*co*-*p*-xylylene) surface, respectively. Various substrates were successfully verified for the coating and patterning modifications: metal (silver, titanium, stainless steel), polystyrene (PS), poly(methyl methacrylate) (PMMA), silicon, glass, poly(dimethylsiloxane) (PDMS), and poly(tetrafluoroethylene) (PTFE) [24]. Microcontact printing (μCP) is a commonly exploited technique that uses a PDMS elastomer to stamp patterns of reactive substances on mostly flat surfaces [17]. It is also widely adopted for the confinement of pattern formation on vapor-deposited coating surfaces. For example, surface patterns were created on a CVD-deposited pentafluorophenol ester-functionalized poly-*p*-xylylene coating by μCP with the use of a PDMS elastomeric stamp, and line patterns of functional biotin molecules were formed with stability up to seven days at room temperature. In the same work, spatial control of the cell attachments and patterns were further produced via the biotin/streptavidin conjugation and subsequently immobilized by the cell-binding antibody [25]. A more delicate

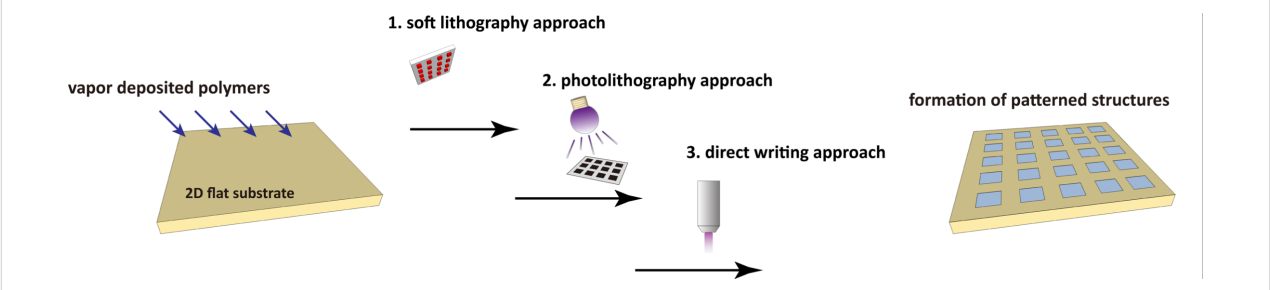

Figure 1: A scheme of creating surface patterns/structures on flat substrates that are modified by vapor-deposited polymer coatings. The patterning methods include soft lithography, photolithography, and direct writing approaches.

pattern formation was generated by combining the μCP technique and the supramolecular nanostamping (SuNS) [26] technology on another vapor-deposited poly(4-formyl-*p*-xylylene-*co*-*p*-xylylene) coating surface, and patterns of DNA molecules were resolved with sizes down to 100 nm. The combination of SuNS with the vapor deposition process enables the extension of the nanopatterning protocols to a range of different substrates, and the nanopatterns were demonstrated on polystyrene, acrylic and PDMS in this work [27]. The aforementioned photolithographical or soft-lithographical methods are simple and straightforward to perform. However, because of the limitation of applying a photomask or an elastomeric stamp, these techniques are mostly limited to flat substrates. The reduced pattern fidelity is resolved from the wider distance of the surface from the photomask or elastomeric stamp on a non-flat or curved surface [23,28-30].

Structuring approaches not limited to flat surfaces

Because vapor polymerization/deposition has the advantage of conformal coverage of substrates, the vapor-phase polymers are freely accessible to deposit on micro- and nano-structured surfaces, curved surfaces, confined microfluidic channels, 3D structures, and substrates with complex geometry [3,31,32]. Although an alternative approach combining vapor deposition of polymers on curved substrates (instead of spin-coating) and a flexible mask to generate polytricosadiynoic acid and poly(4-vinylpyridine) patterns on curvatures has been shown with a conventional lithographic technique [33]. The creation of patterned structures on such non-flat substrates currently requires means different from photomasks or an elastomer stamps to spatially control the modification and construct localized pattern structures, as illustrated in Figure 2. Direct and maskless approaches to apply a patterning at a localized position are attempted by direct electron beam (e-beam) lithography on vapor-deposited PPMA coatings, and 200 nm-sized features were obtained on the vapor-deposited poly(propargyl methacrylate) (PPMA) films [34]. Direct writing using a two-photon laser was also demonstrated on poly(*p*-xylylene) to fabricate 3D nano-/microstructures [35]. Similarly, direct writing using a scanning probe microscopy-based nanolithographic technique (dip-pen nanolithography, DPN) was used to deliver chemical substances with submicrometer features on a wide range of poly(*p*-xylylene) deposited substrates [36]. An array of micro-sized plasma was also used as a maskless method to generate the surface patterning of poly(ethylene oxide) coatings on substrates [37]. An effective maskless approach using directed UV light, for which the light passes through a previously patterned microscopic lens or is projected through a digital micromirror device, was performed to create defined patterns on vapor-deposited poly(*p*-xylylene) surfaces of curved microcolloids [38], microfluidic channels [39], complex stent devices [40-42], and intraocular lens (IOL) devices [43]. Jet deposition was used to prepare a poly(*p*-xylylene) coating under atmospheric conditions and enabled the possibility of direct patterning/writing during the vapor deposition process [44]. A patterning mask made of colloidal crystals has also been demonstrated for the vapor deposition of polymers without requiring photolithographic processes or a stamp [45]. Although most of these techniques remain hampered by the limited resolution of the patterns, they have elegantly contributed to major technological breakthroughs to enable several patterning processes and localized surface modifications on non-flat surfaces for electronics and biotechnology.

Multifunctional structures

The early developments focused on the fabrication of surface patterns and structures with the same physical properties as that

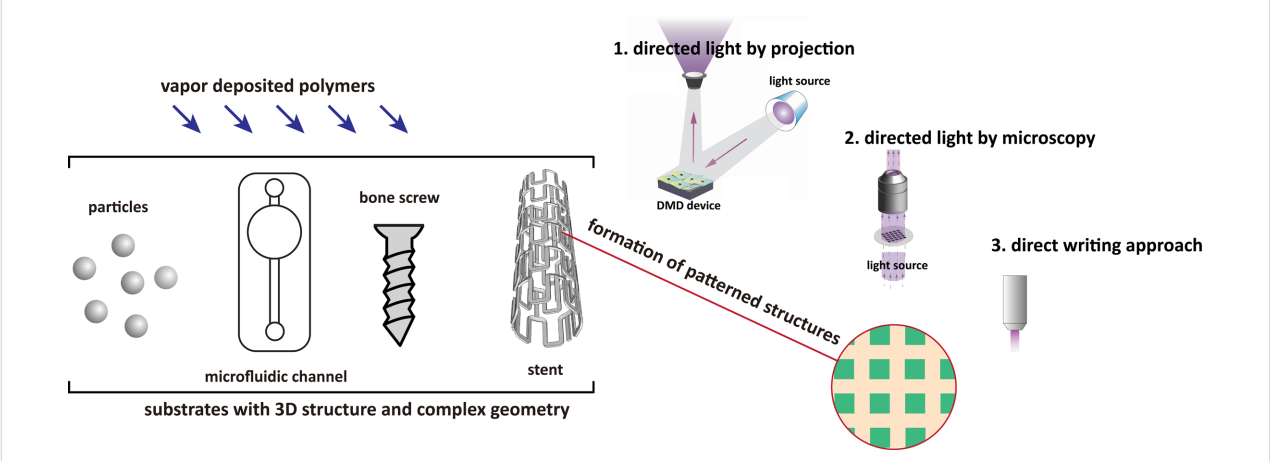

Figure 2: Schematic illustration of creating surface patterns/structures on substrates vapor-coated with polymers with 3D structure and complex geometry. The patterning methods include maskless approaches by light-directed projection, light-directed microscopy and direct writing.

the bulk material, interfacial coating materials, patterning processes, and the aspect ratio of formed surface patterns and structures. In addition, the surface chemistry of such patterns and structures, i.e., chemically and topographically defined interfaces, has recently attracted considerable attention, and multifunctional and/or synergistic activities of using such interfaces were successfully demonstrated. The performed approaches were (i) synthesis/deposition of multicomponent copolymers, which contain two or more addressable functional groups, during the surface modification process for substrates, where the multifunctional patterns/structures were formed by subsequently exploiting the aforementioned patterning process (Figure 3), and (ii) an integrated patterning processes of layered depositions of different functional polymer films; the hierarchical structure of the outer layer and exposed underneath layers forms the multifunctional interface (Figure 4). Vapor-based multicomponent copolymers can be synthesized through CVD in one step by introducing independent monomers into the polymerization chamber to form a multi-phasic reactive species (monomer vapors). The copolymerization processes spontaneously occur when the multicomponent copolymer coatings form on substrates [41,46,47]. A wide range of functionalities was demonstrated: combinations of active esters, carbonyls, amino groups, photoactive benzoyls, maleic derivatives, vinyl and alkyne, and aldehydes. Specific and orthogonal reactions were performed to conjugate various molecules, and multifunctional and/or synergistic activities were demonstrated for many applications [9,48-52]. In order to form chemically and topographically defined patterned structures with multifunctional activities and following approach (i), a poly(*p*-xylylene) copolymer that contained both alkyne and pentafluorophenyl ester functionalities was synthesized via CVD copolymerization. This copolymer was used to co-immobilize the cyclic arginine–glycine–aspartic acid (cRGD) adhesion peptide and epidermal growth factor (EGF) in patterned areas via μCP [51]. Another similar copolymer system, which contained methyl propiolate and maleimide moieties, was also synthesized via CVD copolymerization. The concurrently immobilized μCP-patterned PEG and Cys–Arg–Glu–Asp–Val (CREDV) peptide showed the synergic anti-fouling property and preferentially enhanced attachment of endothelial cells in such patterned areas [50]. In another report, a multifunctional coating was realized via CVD copolymerization to deposit a poly(*p*-xylylene) copolymer, which contained distinct *N*-hydroxysuccinimide (NHS) ester and benzoyl functionalities. The copolymer provided accessibility to the NHS ester–amine coupling reaction and the photochemically induced benzophenone crosslinking reaction. These reactions were confined in selected areas using a combination of μCP and a photomask [53]. Meanwhile, approach (ii) was realized with the layered deposition of polymer coatings with one separate functionality for each coating layer. A multifunctional surface containing “PEG-like” and “non-PEG-like” regions has been created by asymmetric glow discharge plasma polymerization [54]. The multifunctional interfaces with pattern structures were demonstrated by separately depositing alkyne-functionalized poly(*p*-xylylene) and aldehyde-functionalized poly(*p*-xylylene) in selected areas using a vapor-assisted micropatterning in the replica structure (VAMPIR) technique [55,56]. The resulting multifunctional patterned surface could spatially direct a combination of Huisgen cycloaddition and carbonyl–hydrazide coupling in a sequentially devised immobilization procedure [52]. A similar sequential immobilization of molecules on defined areas was also performed on a layered coating of propiolate-functionalized poly(*p*-xylylene) and alkyne-functionalized poly(*p*-xylylene), for which VAMPIR was also applied to pattern the layered surface. Two-step click reactions were accessible by using different reactivities of activated and non-activated alkynyl groups towards the azide groups [57]. The idea of using two-step click reactions with approaches (i) and (ii) was also demonstrated by depositing

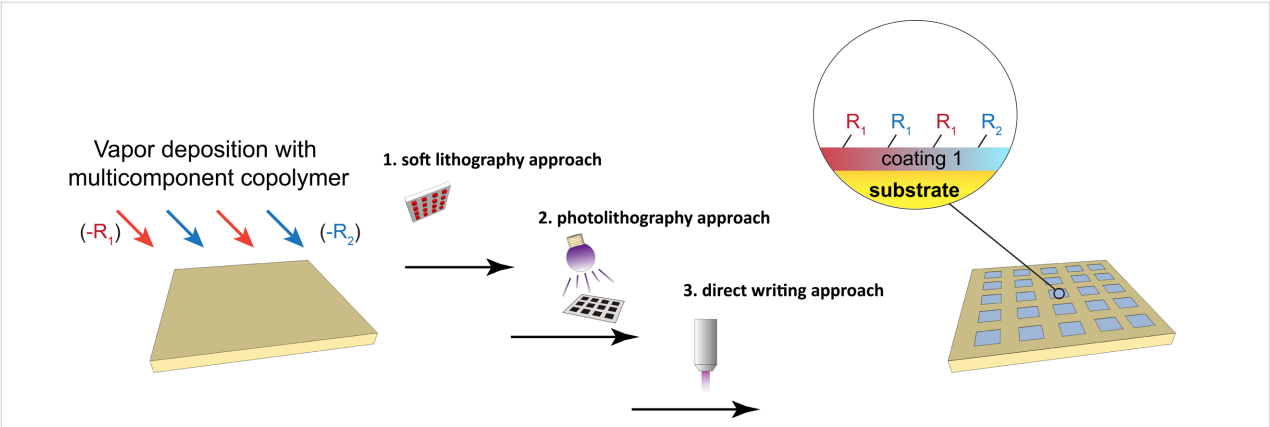

Figure 3: Schematic illustration of creating chemically and topographically defined interfaces with multifunctionality on substrates vapor-coated with polymers. An approach by using multicomponent copolymer coating is demonstrated.

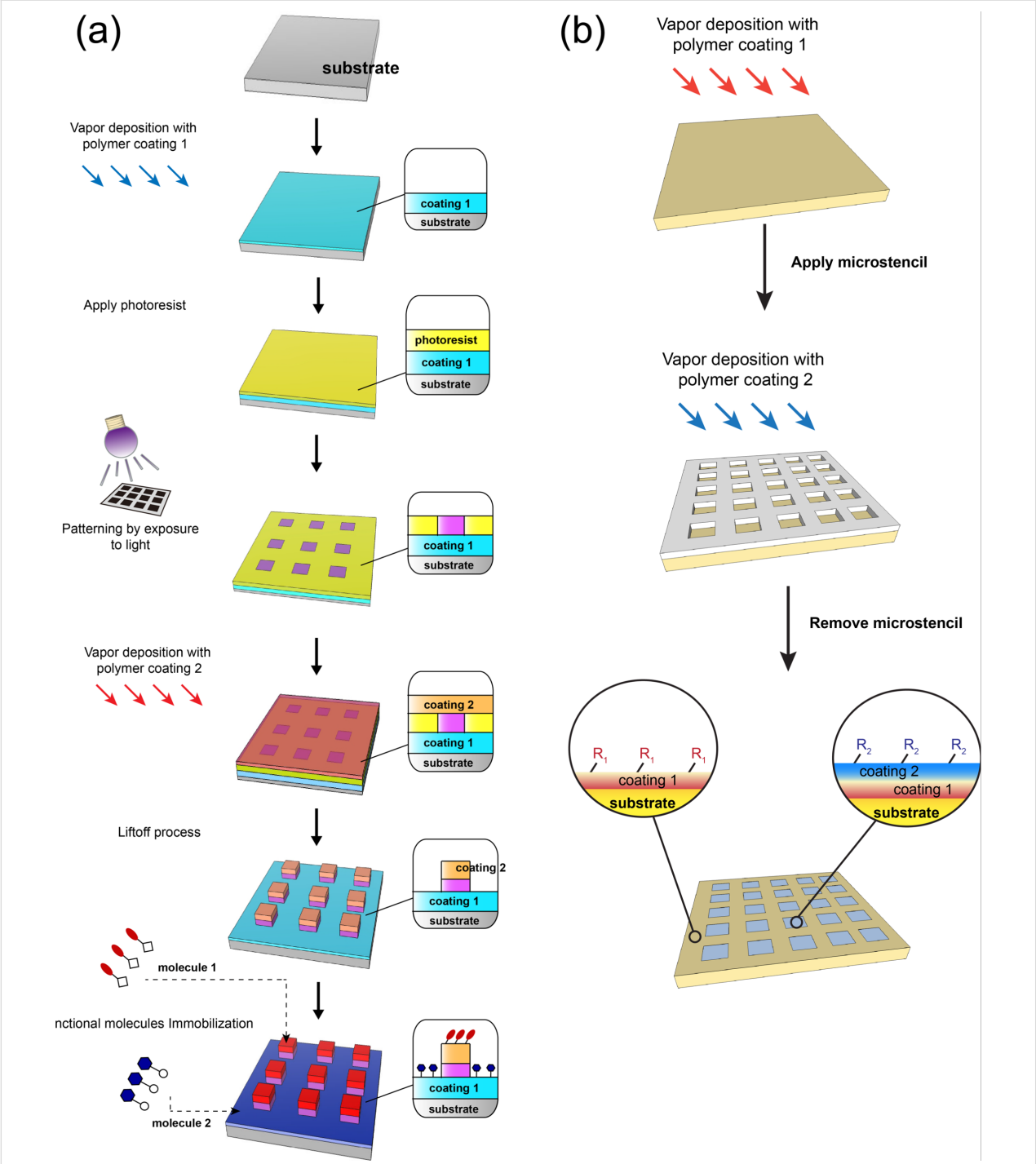

Figure 4: Schematic illustration of creating chemically and topographically defined interfaces with multifunctionality on substrates vapor-coated with polymers. (a) A photolithographic process is performed to prepare chemically and topographically defined surface microstructures on layered functional coatings, and a concept is shown to immobilize multiple functional molecules at corresponding areas. (b) Patterning/structuring on layered polymer coatings by a vapor-assisted micropatterning in the replica structure (VAMPIR) technique, in which a microstencil is exploited during the vapor deposition process. Reproduced with permission from [56], copyright 2014 Wiley-VCH.

alkyne/maleimide-functionalized poly(*p*-xylylene) copolymer or alkyne-functionalized poly(*p*-xylylene) homopolymer, and multifaceted surface patterns were obtained via route-controlled click reactions with μCP or a photomask [49].

Gradient structures

Surface gradients represent an advanced surface modification tool to exert gradient activities and/or communicate with the microenvironment using gradually altered cues. Such gradients

include physical properties such as the wettability, thickness, dielectric constant, temperature, and morphology and various chemical compositions [58-65]. Because of the challenges in fabrication processes, gradients are often generated with solution-based technology. Limitations remain for the ongoing technologies, for example, the lack long-term stability due to degradation or desorption from the modified surface [66,67], or hardly predictable biological outcomes of interactions between the biological environment and the materials interfaces [60]. Moreover, widely used laminated/layered constructs are limited through the boundary discontinuities across layers of dissimilar materials or properties [68]. In addition to the current solution-based techniques, vapor-deposited polymer coatings have been developed to create surface-gradient patterns and provide advantages with precisely controlled chemical or biological compliance without restrictions in selecting substrate materials and geometries [69]. By using corona discharge treatment with gradually increasing power, the density of PEG was controlled with gradients to guide protein adsorption and platelet adhesion [70]. By also controlling polyatomic ion deposition to linearly increase the $C_3F_5^+$ ion fluence across polymer, metal, and silicon substrates, a hydrophobicity gradient was formed along the treatment direction [71]. The chemical gradients of hydrophobic octadiene to a more hydrophilic acrylic acid were produced via plasma polymerization, and the surface was found effective for cell pluripotency against mouse embryonic stem cells [72]. A plasma-polymerized surface with gradient amino functionality was demonstrated to generate density gradients of individual gold (Au) and silver (Ag) nanoparticles on the surfaces [73]. Poly(*p*-xylylene) surfaces with continuously and counter-currently distributed functionality gradients of active carbonyls and amines were synthesized by diffusing individual monomer vapor from the opposite direction during the CVD co-polymerization process [8]. In an extended work, another version of the gradient copolymer containing aldehydes and amine gradients was generated, and a subsequent cell-culture study showed that cell-signaling adenovirus was correlated along the copolymer gradients [74]. A similar combinatorial approach has also been demonstrated to generate poly(diethylaminoethylacrylate) and poly(dimethylaminomethylstyrene) gradients using an initiated CVD system [75]. The route-controlled click reactions, including a thiol-yne reaction and a copper-free alkyne/azide click reaction, were enabled to create continuous and reverse gradients on a CVD deposited poly[(4-methylpropiolate-*p*-xylylene)-*co*-(*p*-xylylene)] surface. The two-click reactions were employed to co-immobilize fibroblast growth factor 2 (FGF-2) and bone morphogenetic protein 2 (BMP-2) and established reverse gradient distributions of the FGF-2 and BMP-2. Furthermore, these two growth factors gradients have demonstrated the corresponding biological activities toward both proliferation (FGF-2) and osteogenic differentiation (BMP-2) for adipose-derived stem cells [76].

Selective deposition

The aforementioned methods rely on physical means to obtain spatially controlled surface modifications and patterned structures. A simpler approach is the selective inhibition of the vapor deposition/polymerization process on substrates, i.e., the polymer coatings are either deposited or not on substrates because of the chemistry below the substrate surface. The mechanism of the polymer deposition selectivity is not conclusive. The inhibition of polymer deposition is believed to occur because of the high surface energy of the substrate, which neutralizes the reactive monomer species that are adsorbed on the substrate surface and prevents further initiation and propagation of the polymerization reaction. For example, non-substituted *p*-xylylene and chlorine-substituted *p*-xylylene (monomers of two types of poly-*p*-xylylenes, which are commercially named parylene™ N and parylene™ C, respectively) were found to deactivate on several high-energy surfaces of several transition metals such as iron, copper, silver, platinum, and the salts of these metals. The monomer deactivation inhibits the deposition of parylene™ N and parylene™ C on these high-energy metal surfaces. The degree of selectivity (there exists an upper limit, where deposition will commence and the relative selectivity is lost) is different for different metal surfaces and correlates with the deposition rate [77]. Based on the discovery, applications have been demonstrated to generate Nomarski poly(*p*-phenylene vinylene) (PPV) patterns from selectively deposited parylene™ N on surfaces with photolithographically fabricated iron structures (inhibitors) [78]. A required pore-sealing process for porous dielectrics was also performed using selectively deposited parylene™ N to avoid the deposition on sub-45 nm copper nodes [79]. The copolymer poly(4-vinyl pyridine-*co*-divinyl benzene) was selectively deposited on a chromatography paper with screen-printed copper(II) chloride patterns [80]. A comprehensive study further examined the deposition of a wide range of functionalized poly(*p*-xylylenes) on high-energy metal surfaces. The study found that the deposition selectivity might have been compromised, and a possible explanation may be that neutralization occurred between the oxygen or nitrogen from the side groups of the functionalized *p*-xylylenes and the high-energy metal substrates by attraction interactions. In contrast, an inhibitor surface experiences neutralization and deactivation at the free radicals for halogen- or non-substituted *p*-xylylenes. A continuum of deposition and polymer chain propagation can thus proceed for the case of functionalized *p*-xylylenes [81]. The compromised selectivity was recently reactivated by supplying electrical energy to the (conducting) substrates. The deposition selectivity was enhanced by increasing the transition of the surface energy instead

of relying on native surface energy of the substrates. In other words, effective selectivity for the deposition of nonfunctional poly(*p*-xylylene) has been achieved, and the family of functionalized poly(*p*-xylylene) is now manageable [82].

Conclusion

As more stringent specifications are required for designing the surface properties of prospective materials, and in addition, the development of new devices is pursued with complicated geometries and minimized sizes, the surface properties of such materials/devices now also require a more defined and flexible presentation of the chemical functionalities (e.g., multifunctional or gradient distribution) and the precise confinement of these chemical conducts in relevant locations of interest. The vapor deposition process and the resulting thin polymer films provide consistent coatings, which decouple the underlying substrate surface properties and can be applied for surface modification on most of the substrate geometry and materials (with the exception for the case of selective deposition on transition metals and charged surfaces). Because of the well-established and available photolithography and soft lithography techniques, promising patterned surface structures have been created. Attempts were conducted to produce patterned structures on non-flat surfaces. However, techniques such as directed light or direct writing approaches currently have limitations regarding the resolution and cost. Thus, new techniques are developed to push the resolution limit and decrease the cost for the possibility of practical applications. An emerging question may have arisen because vapor-deposited species are free of the geometrical limits of the substrate, i.e., vapor species can deposit on curvatures and confined microgeometries. However, the patterning techniques are only available to perform on accessible surfaces but not in overhanging or sealed surfaces. For example, the problem of how to pattern and structure an internal lumen of a microchannel while the surface can be modified using vapor-deposited polymers remains unsolved and is encouraged for dedicated work from researchers in this field. A more general problem of the vapor deposition process us that the process mostly requires vacuum conditions to protect the reactive vapor species (monomers) from side reactions, which hampers the application as a continuous mass production process. A vacuum-free method [44] may solve the problem, but several engineering works and system parameters for other vapor deposition systems must be optimized. Nevertheless, vapor-deposited polymers offer unrivaled coating fidelity and precise control over the surface chemistry. The integration of polymer coatings and patterning technologies results in interface properties that account for both chemically and topologically defined properties, which is a promising tool to design prospective multidisciplinary materials. More applications using these technologies are only limited by imagination.

Acknowledgements

H.-Y. Chen gratefully acknowledges financial support from the Ministry of Science and Technology of Taiwan (MOST 104-2628-E-002-010-MY3) and from National Taiwan University (105R7813 and 104R7745).

References

1. Yang, R.; Asatekin, A.; Gleason, K. K. *Soft Matter* **2012,** *8,* 31–43. doi:10.1039/C1SM06334K
2. Chen, H.-Y.; Lahann, J. *Langmuir* **2011,** *27,* 34–48. doi:10.1021/la101623n
3. Alf, M. E.; Asatekin, A.; Barr, M. C.; Baxamusa, S. H.; Chelawat, H.; Ozaydin-Ince, G.; Petruczok, C. D.; Sreenivasan, R.; Tenhaeff, W. E.; Trujillo, N. J.; Vaddiraju, S.; Xu, J.; Gleason, K. K. *Adv. Mater.* **2010,** *22,* 1993–2027. doi:10.1002/adma.200902765
4. Bazaka, K.; Grant, D. S.; Alancherry, S.; Jacob, M. V. Plasma-Assisted Fabrication and Processing of Biomaterials. In *Biomedical Applications of Polymeric Materials and Composites;* Francis, R.; Kumar, D. S., Eds.; Wiley-VCH: Heidelberg, Germany, 2016; pp 91–124. doi:10.1002/9783527690916.ch4
5. Coclite, A. M. CVD Polymer Surfaces for Biotechnology and Biomedicine. In *CVD Polymers: Fabrication of Organic Surfaces and Devices;* Gleason, K. K., Ed.; Wiley-VCH: Heidelberg, Germany, 2015; pp 301–321. doi:10.1002/9783527690275.ch14
6. Lahann, J. *Polym. Int.* **2006,** *55,* 1361–1370. doi:10.1002/pi.2098
7. Lahann, J. *Chem. Eng. Commun.* **2006,** *193,* 1457–1468. doi:10.1080/00986440500511619
8. Elkasabi, Y.; Lahann, J. *Macromol. Rapid Commun.* **2009,** *30,* 57–63. doi:10.1002/marc.200800578
9. Elkasabi, Y.; Yoshida, M.; Nandivada, H.; Chen, H.-Y.; Lahann, J. *Macromol. Rapid Commun.* **2008,** *29,* 855–870. doi:10.1002/marc.200800101
10. Rai-Choudhury, P. *Handbook of Microlithography, Micromachining, and Microfabrication. Volume 1: Microlithography;* SPIE: Bellingham, WA, U.S.A., 1997.
11. Yao, N.; Wang, Z. L., Eds. *Handbook of Microscopy for Nanotechnology;* Springer: Berlin, Germany, 2005. doi:10.1007/1-4020-8006-9
12. Tseng, A. A. *Small* **2005,** *1,* 594–608. doi:10.1002/smll.200500050
13. Cerrina, F. *J. Phys. D: Appl. Phys.* **2000,** *33,* R103. doi:10.1088/0022-3727/33/12/201
14. Meschede, D.; Metcalf, H. *J. Phys. D: Appl. Phys.* **2003,** *36,* R17. doi:10.1088/0022-3727/36/3/202
15. Chou, S. Y.; Krauss, P. R.; Renstrom, P. J. *Appl. Phys. Lett.* **1995,** *67,* 3114–3116. doi:10.1063/1.114851
16. Chou, S. Y.; Krauss, P. R.; Renstrom, P. J. *Science* **1996,** *272,* 85–87. doi:10.1126/science.272.5258.85
17. Xia, Y.; Whitesides, G. M. *Annu. Rev. Mater. Sci.* **1998,** *28,* 153–184. doi:10.1146/annurev.matsci.28.1.153
18. Kumar, A.; Whitesides, G. M. *Appl. Phys. Lett.* **1993,** *63,* 2002–2004. doi:10.1063/1.110628
19. Moran-Mirabal, J. M.; Tan, C. P.; Orth, R. N.; Williams, E. O.; Craighead, H. G.; Lin, D. M. *Anal. Chem.* **2007,** *79,* 1109–1114. doi:10.1021/ac061898z
20. Dhayal, M.; Jeong, H. G.; Choi, J. S. *Appl. Surf. Sci.* **2005,** *252,* 1710–1715. doi:10.1016/j.apsusc.2005.03.198

21. Brétagnol, F.; Ceriotti, L.; Lejeune, M.; Papadopoulou-Bouraoui, A.; Hasiwa, M.; Gilliland, D.; Ceccone, G.; Colpo, P.; Rossi, F. *Plasma Processes Polym.* **2006,** *3,* 30–38. doi:10.1002/ppap.200500071
22. Suh, K. Y.; Langer, R.; Lahann, J. *Adv. Mater.* **2004,** *16,* 1401–1405. doi:10.1002/adma.200400101
23. Chen, H.-Y.; Lahann, J. *Anal. Chem.* **2005,** *77,* 6909–6914. doi:10.1021/ac050964e
24. Wu, J.-T.; Huang, C.-H.; Liang, W.-C.; Wu, Y.-L.; Yu, J.; Chen, H.-Y. *Macromol. Rapid Commun.* **2012,** *33,* 922–927. doi:10.1002/marc.201200011
25. Lahann, J.; Balcells, M.; Rodon, T.; Lee, J.; Choi, I. S.; Jensen, K. F.; Langer, R. *Langmuir* **2002,** *18,* 3632–3638. doi:10.1021/la011464t
26. Yu, A. A.; Savas, T. A.; Taylor, G. S.; Guiseppe-Elie, A.; Smith, H. I.; Stellacci, F. *Nano Lett.* **2005,** *5,* 1061–1064. doi:10.1021/nl050495w
27. Thévenet, S.; Chen, H.-Y.; Lahann, J.; Stellacci, F. *Adv. Mater.* **2007,** *19,* 4333–4337. doi:10.1002/adma.200701439
28. Graff, M.; Mohanty, S. K.; Moss, E.; Frazier, A. B. *J. Microelectromech. Syst.* **2004,** *13,* 956–962. doi:10.1109/JMEMS.2004.838368
29. Kim, G. M.; van den Boogaart, M. A. F.; Brugger, J. *Microelectron. Eng.* **2003,** *67–68,* 609–614. doi:10.1016/S0167-9317(03)00121-7
30. Zhou, Y. X.; Johnson, A. T., Jr.; Hone, J.; Smith, W. F. *Nano Lett.* **2003,** *3,* 1371–1374. doi:10.1021/nl034512y
31. Liang, Y.; Jordahl, J. H.; Ding, H.; Deng, X.; Lahann, J. *Chem. Vap. Deposition* **2015,** *21,* 288–293. doi:10.1002/cvde.201507197
32. Waterkotte, B.; Bally, F.; Nikolov, P. M.; Waldbaur, A.; Rapp, B. E.; Truckenmüller, R.; Lahann, J.; Schmitz, K.; Giselbrecht, S. *Adv. Funct. Mater.* **2014,** *24,* 442–450. doi:10.1002/adfm.201301093
33. Petruczok, C. D.; Gleason, K. K. *Adv. Mater.* **2012,** *24,* 6445–6450. doi:10.1002/adma.201201975
34. Im, S. G.; Kim, B.-S.; Lee, L. H.; Tenhaeff, W. E.; Hammond, P. T.; Gleason, K. K. *Macromol. Rapid Commun.* **2008,** *29,* 1648–1654. doi:10.1002/marc.200800404
35. Kurihara, M.; Heo, Y. J.; Kuribayashi-Shigetomi, K.; Takeuchi, S. In *Proceesings of the 25th International Conference on Micro Electro Mechanical Systems (MEMS),* Jan 29–Feb 2, 2012; IEEE Publishing: Piscataway, NJ, U.S.A., 2012; pp 196–199. doi:10.1109/MEMSYS.2012.6170124
36. Chen, H.-Y.; Hirtz, M.; Deng, X.; Laue, T.; Fuchs, H.; Lahann, J. *J. Am. Chem. Soc.* **2010,** *132,* 18023–18025. doi:10.1021/ja108679m
37. Yang, Y.-J.; Tsai, M.-Y.; Liang, W.-C.; Chen, H.-Y.; Hsu, C.-C. *ACS Appl. Mater. Interfaces* **2014,** *6,* 12550–12555. doi:10.1021/am502468q
38. Chen, H.-Y.; Rouillard, J.-M.; Gulari, E.; Lahann, J. *Proc. Natl. Acad. Sci. U. S. A.* **2007,** *104,* 11173–11178. doi:10.1073/pnas.0702749104
39. Chen, H.-Y.; Rouillard, J.-M.; Gulari, E.; Lahann, J. High-Precision Surface Modification of Three-Dimensional Geometries Using Photodefinable Ultra-Thin Polymer Coatings. *PMSE Preprints;* American Chemical Society: San Francisco, CA, U.S.A., 2006.
40. Su, C.-T.; Yuan, R.-H.; Chen, Y.-C.; Lin, T.-J.; Chien, H.-W.; Hsieh, C.-C.; Tsai, W.-B.; Chang, C.-H.; Chen, H.-Y. *Colloids Surf., B* **2014,** *116,* 727–733. doi:10.1016/j.colsurfb.2013.11.044
41. Chen, H.-Y.; Lin, T.-J.; Tsai, M.-Y.; Su, C.-T.; Yuan, R.-H.; Hsieh, C.-C.; Yang, Y.-J.; Hsu, C.-C.; Hsiao, H.-M.; Hsu, Y.-C. *Chem. Commun.* **2013,** *49,* 4531–4533. doi:10.1039/c3cc41491d
42. Wu, M.-G.; Hsu, H.-L.; Hsiao, K.-W.; Hsieh, C.-C.; Chen, H.-Y. *Langmuir* **2012,** *28,* 14313–14322. doi:10.1021/la302099y
43. Wu, J.-T.; Wu, C.-Y.; Fan, S.-K.; Hsieh, C.-C.; Hou, Y.-C.; Chen, H.-Y. *Chem. Mater.* **2015,** *27,* 7028–7033. doi:10.1021/acs.chemmater.5b02433
44. Biswas, S.; Shalev, O.; Pipe, K. P.; Shtein, M. *Macromolecules* **2015,** *48,* 5550–5556. doi:10.1021/acs.macromol.5b00505
45. Sletten, E. M.; Bertozzi, C. R. *Angew. Chem., Int. Ed.* **2009,** *48,* 6974–6998. doi:10.1002/anie.200900942
46. Tenhaeff, W. E.; Gleason, K. K. *Langmuir* **2007,** *23,* 6624–6630. doi:10.1021/la070086a
47. Elkasabi, Y.; Chen, H.-Y.; Lahann, J. *Adv. Mater.* **2006,** *18,* 1521–1526. doi:10.1002/adma.200502454
48. Yuan, R.-H.; Li, Y.-J.; Sun, H.-Y.; Wu, C.-Y.; Guan, Z.-Y.; Ho, H.-Y.; Fang, C.-Y.; Chen, H.-Y. *Colloids Surf., B* **2016,** *139,* 259–268. doi:10.1016/j.colsurfb.2015.12.022
49. Sun, T.-P.; Tai, C.-H.; Wu, J.-T.; Wu, C.-Y.; Liang, W.-C.; Chen, H.-Y. *Biomater. Sci.* **2016,** *4,* 265–271. doi:10.1039/C5BM00417A
50. Tsai, M.-Y.; Chen, Y.-C.; Lin, T.-J.; Hsu, Y.-C.; Lin, C.-Y.; Yuan, R.-H.; Yu, J.; Teng, M.-S.; Hirtz, M.; Chen, M. H.-C.; Chang, C.-H.; Chen, H.-Y. *Adv. Funct. Mater.* **2014,** *24,* 2281–2287. doi:10.1002/adfm.201303050
51. Deng, X.; Eyster, T. W.; Elkasabi, Y.; Lahann, J. *Macromol. Rapid Commun.* **2012,** *33,* 640–645. doi:10.1002/marc.201100819
52. Bally, F.; Cheng, K.; Nandivada, H.; Deng, X.; Ross, A. M.; Panades, A.; Lahann, J. *ACS Appl. Mater. Interfaces* **2013,** *5,* 9262–9268. doi:10.1021/am401875x
53. Yuan, R.-H.; Wu, C.-Y.; Tung, H.-Y.; Hsieh, H.-P.; Li, Y.-J.; Chiang, Y.-C.; Chen, H.-Y. *Macromol. Biosci.* **2017,** *17,* 1600322. doi:10.1002/mabi.201600322
54. Menzies, D. J.; Gengenbach, T.; Forsythe, J. S.; Birbilis, N.; Johnson, G.; Charles, C.; McFarland, G.; Williams, R. J.; Fong, C.; Leech, P.; McLean, K.; Muir, B. W. *Chem. Commun.* **2012,** *48,* 1907–1909. doi:10.1039/C2CC15578H
55. Chen, H.-Y.; Lahann, J. *Adv. Mater.* **2007,** *19,* 3801–3808. doi:10.1002/adma.200602830
56. Chen, H.-Y.; Su, C.-T.; Tsai, M.-Y. Nanoscale Functional Polymer Coatings for Biointerface Engineering. In *Advanced Hierarchical Nanostructured Materials;* Zhang, Q.; Wei, F., Eds.; Wiley-VCH: Heidelberg, Germany, 2014; pp 461–478. doi:10.1002/9783527664948.ch13
57. Deng, X.; Friedmann, C.; Lahann, J. *Angew. Chem., Int. Ed.* **2011,** *50,* 6522–6526. doi:10.1002/anie.201101581
58. Ruardy, T. G.; Schakenraad, J. M.; van der Mei, H. C.; Busscher, H. J. *Surf. Sci. Rep.* **1997,** *29,* 3–30. doi:10.1016/S0167-5729(97)00008-3
59. Ma, Y.; Zheng, J.; Amond, E. F.; Stafford, C. M.; Becker, M. L. *Biomacromolecules* **2013,** *14,* 665–671. doi:10.1021/bm301731h
60. Ross, A. M.; Lahann, J. *J. Polym. Sci., Part B: Polym. Phys.* **2013,** *51,* 775–794. doi:10.1002/polb.23275
61. Krabbenborg, S. O.; Nicosia, C.; Chen, P.; Huskens, J. *Nat. Commun.* **2013,** *4,* 1667. doi:10.1038/ncomms2688
62. Efimenko, K.; Genzer, J. *Adv. Mater.* **2001,** *13,* 1560–1563. doi:10.1002/1521-4095(200110)13:20<1560::AID-ADMA1560>3.0.CO;2-Z
63. Khang, G. *Biosurface Biotribology* **2015,** *1,* 202–213. doi:10.1016/j.bsbt.2015.08.004
64. Seidi, A.; Ramalingam, M.; Elloumi-Hannachi, I.; Ostrovidov, S.; Khademhosseini, A. *Acta Biomater.* **2011,** *7,* 1441–1451. doi:10.1016/j.actbio.2011.01.011
65. Wu, J.; Mao, Z.; Tan, H.; Han, L.; Ren, T.; Gao, C. *Interface Focus* **2012,** *2,* 337–355. doi:10.1098/rsfs.2011.0124

66. Greiner, A. M.; Jäckel, M.; Scheiwe, A. C.; Stamow, D. R.; Autenrieth, T. J.; Lahann, J.; Franz, C. M.; Bastmeyer, M. *Biomaterials* **2014,** *35,* 611–619. doi:10.1016/j.biomaterials.2013.09.095
67. Lee, K. Y.; Peters, M. C.; Anderson, K. W.; Mooney, D. J. *Nature* **2000,** *408,* 998–1000. doi:10.1038/35050141
68. Zhu, Y.; Mao, Z.; Gao, C. *Biomacromolecules* **2013,** *14,* 342–349. doi:10.1021/bm301523p
69. Goreham, R. V.; Mierczynska, A.; Pierce, M.; Short, R. D.; Taheri, S.; Bachhuka, A.; Cavallaro, A.; Smith, L. E.; Vasilev, K. *Thin Solid Films* **2013,** *528,* 106–110. doi:10.1016/j.tsf.2012.04.087
70. Lee, J. H.; Jeong, B. J.; Lee, H. B. *J. Biomed. Mater. Res.* **1997,** *34,* 105–114. doi:10.1002/(SICI)1097-4636(199701)34:1<105::AID-JBM14>3.0.CO;2-J
71. Wijesundara, M. B. J.; Fuoco, E.; Hanley, L. *Langmuir* **2001,** *17,* 5721–5726. doi:10.1021/la010592e
72. Wells, N.; Baxter, M. A.; Turnbull, J. E.; Murray, P.; Edgar, D.; Parry, K. L.; Steele, D. A.; Short, R. D. *Biomaterials* **2009,** *30,* 1066–1070. doi:10.1016/j.biomaterials.2008.10.027
73. Goreham, R. V.; Short, R. D.; Vasilev, K. *J. Phys. Chem. C* **2011,** *115,* 3429–3433. doi:10.1021/jp111221g
74. Elkasabi, Y. M.; Lahann, J.; Krebsbach, P. H. *Biomaterials* **2011,** *32,* 1809–1815. doi:10.1016/j.biomaterials.2010.10.046
75. Martin, T. P.; Gleason, K. K. *Chem. Vap. Deposition* **2006,** *12,* 685–691. doi:10.1002/cvde.200606495
76. Guan, Z.-Y.; Wu, C.-Y.; Wu, J.-T.; Tai, C.-H.; Yu, J.; Chen, H.-Y. *ACS Appl. Mater. Interfaces* **2016,** *8,* 13812–13818. doi:10.1021/acsami.6b03908
77. Vaeth, K. M.; Jensen, K. F. *Chem. Mater.* **2000,** *12,* 1305–1313. doi:10.1021/cm990642p
78. Vaeth, K. M.; Jensen, K. F. *Adv. Mater.* **1999,** *11,* 814–820. doi:10.1002/(SICI)1521-4095(199907)11:10<814::AID-ADMA814>3.0.CO;2-Z
79. Senkevich, J. J.; Wiegand, C. J.; Yang, G. R.; Lu, T. M. *Chem. Vap. Deposition* **2004,** *10,* 247–249. doi:10.1002/cvde.200304179
80. Kwong, P.; Seidel, S.; Gupta, M. *J. Vac. Sci. Technol., A* **2015,** *33,* 031504. doi:10.1116/1.4915247
81. Chen, H.-Y.; Lai, J. H.; Jiang, X.; Lahann, J. *Adv. Mater.* **2008,** *20,* 3474–3480. doi:10.1002/adma.200800455
82. Wu, C.-Y.; Sun, H.-Y.; Liang, W.-C.; Hsu, H.-L.; Ho, H.-Y.; Chen, Y.-M.; Chen, H.-Y. *Chem. Commun.* **2016,** *52,* 3022–3025. doi:10.1039/C5CC08059B

License and Terms

BEILSTEIN JOURNAL OF NANOTECHNOLOGY

Parylene C as a versatile dielectric material for organic field-effect transistors

Tomasz Marszalek[1,2,3], Maciej Gazicki-Lipman[*4] and Jacek Ulanski[3]

Review

Open Access

Address:
[1]Organisch-Chemisches Institut, Ruprecht-Karls-Universität Heidelberg, 69120, Heidelberg, Germany, [2]InnovationLab, Speyererstr. 4, 69115 Heidelberg, Germany, [3]Department of Molecular Physics, Lodz University of Technology, Zeromskiego 116, 90-924 Lodz, Poland and [4]Institute for Materials Science and Engineering, Lodz University of Technology, Stefanowskiego 1-15, 90-924 Lodz, Poland

Email:
Maciej Gazicki-Lipman[*] - maciej.gazicki-lipman@p.lodz.pl

* Corresponding author

Keywords:
dielectric; encapsulation layer; flexible substrate; organic field effect transistor; Parylene C

Beilstein J. Nanotechnol. **2017,** *8,* 1532–1545.
doi:10.3762/bjnano.8.155

Received: 14 February 2017
Accepted: 27 June 2017
Published: 28 July 2017

This article is part of the Thematic Series "Vapor-based polymers: from films to nanostructures".

Guest Editors: M. Koenig and J. Lahann

Abstract

An emerging new technology, organic electronics, is approaching the stage of large-scale industrial application. This is due to a remarkable progress in synthesis of a variety of organic semiconductors, allowing one to design and to fabricate, so far on a laboratory scale, different organic electronic devices of satisfactory performance. However, a complete technology requires upgrading of fabrication procedures of all elements of electronic devices and circuits, which not only comprise active layers, but also electrodes, dielectrics, insulators, substrates and protecting/encapsulating coatings. In this review, poly(chloro-*para*-xylylene) known as Parylene C, which appears to become a versatile supporting material especially suitable for applications in flexible organic electronics, is presented. A synthesis and basic properties of Parylene C are described, followed by several examples of use of parylenes as substrates, dielectrics, insulators, or protecting materials in the construction of organic field-effect transistors.

Review

Introduction

An improvement of the performance of organic transistors by means of boosting charge-carrier mobility is one of the main quests in organic electronics, calling for novel design of molecular materials and enhanced processing conditions. Over the past 20 years, the work has been mainly dedicated to the selection and processing of organic semiconductors: either small molecules [1,2] or systems with high molecular weight [3,4]. Nevertheless, it should be pointed out that it is not only semiconductors that constitute crucial elements of organic field-effect transistor (OFET) architecture. The role of both interfaces, namely those of dielectric/semiconductor [5-7] and semiconductor/electrode [8,9] is widely discussed in the literature. In

addition, elements such as electrodes [8], substrate [10] and protective layer [11] are considered to have a significant impact on the transistor performance as well. A particularly important role in the field-effect response is supposed to be played by a dielectric material, a notion that has been accentuated by several reports [12,13]. When this type of material is considered for an application in organic transistors, specific requirements for the gate insulator have to be fulfilled. The most important of these requirements comprise high capacitance, substantial dielectric strength, high purity and processability of the material. In addition the material should yield device characteristics such as high on/off ratio, low hysteresis, and long-term stability. There are only few reports that describe, in a comprehensive way, an influence of each element on the performance of the organic transistor [12,14,15].

At present, one of the most important utility features in the field of potential organic-transistor applications is the flexibility of the semiconductor layer deposited on top of a polymer substrate [16]. In the best case, no degradation of device performance was observed for bending radii as small as ca. 200 μm [17]. Measured variations of the charge-carrier mobility [18] were assigned either to mechanical changes in the semiconductor film or to charge trapping at the dielectric/semiconductor and semiconductor/electrode interfaces. It should be pointed out that the primary element affecting the transistor flexibility is a substrate that is not only flexible (relatively low Young's modulus) but also offers a smooth and pinhole-free structure. An equally important role is played by the encapsulation layer. Firstly, it protects the semiconductor thin film against the negative influence of water and oxygen. Secondly, it makes the semiconductor thin film remain in its initial position during the bending process, which prevents a charge trapping effect induced by the mechanical cracking [19]. For this reason, there is substantial interest in polymer materials that can be successfully applied in flexible organic transistors as both substrate and encapsulation layer.

The present work is focused on the unique performance of one polymer material used in OFETs. This material is poly(chloro-*p*-xylylene) (Parylene C) the applicability of which in the field of OFET manufacturing appears to be continuously growing. Three properties of Parylene C, treated here as independent application fields, are found useful in a fabrication of high performance organic transistors. First of all, major advantages of the chemical structure and the deposition procedure of this polymer are pointed out with the focus on its application as a flexible substrate. Secondly, the electrical insulating properties of this material are presented with emphasis on its use as a gate dielectric material. Last, but not least, an advantage of encapsulation properties of Parylene C, earlier applied in the area of conservation [20-22] are currently utilized in a form of protective layers stabilizing organic electronic devices. It should be pointed out that the requirements for the barrier protecting an organic transistor (about 10^{-2} g/m^2 per day) are not as restricted as those regarding an organic photovoltaic (OPV) device (10^{-4} g/m^2 per day) or an organic light-emitting diode (OLED) (10^{-6} g/m^2 per day) [23]. Nevertheless, some of the organic semiconductors (mostly electron-transporting materials) require an encapsulation layer, in order to observe charge transport in the transistor architecture [24]. According to our knowledge, there is a limited number of materials that can be simultaneously used as a substrate, dielectric and encapsulation layer at the same time while presenting a performance comparable to the materials dedicated to the specific application [25].

Synthesis of Parylene C

The process of deposition of xylylene polymers, known under the commercial name of parylenes, is unique in many ways. It is a synthetic path for polymer formation, at the same time it belongs to the category of chemical vapor deposition (CVD) and, as such, it yields products in a form of conformal solid films depositing at any surface exposed. As a CVD process, on the other hand, it results in the formation of organic polymers with high molecular weight, whereas typical products of these processes are inorganic materials of either metallic or ceramic nature. Perhaps the most unusual feature of the parylene process is the polymerization mechanism itself. The initiation step does not require any external initiator but, instead, it involves a monomer molecule in its diradical triplet first excited state [26]. A natural consequence of this mechanism is the extraordinary purity of parylene coatings, a property of great importance in electronic applications. Yasuda et al. [27] pointed out first that this purity results in a low concentration of localized states at the dielectric/semiconductor interface of the OFET. The authors investigated a number of poly(*para*-xylylene) derivatives with regarding their effectiveness as gate dielectric layers in OFET devices. In each case, independent of the active material used, out of six different xylylene polymers the highest field-effect mobility was exhibited by the transistors equipped with a Parylene C dielectric layer [27]. A schematic diagram, showing the stages of the Parylene C deposition process, together with the accompanying chemical reactions, is presented in Figure 1.

There is a number of advantages of the parylene technology. First of all, being a gas-phase diffusion-controlled process, it yields smooth pinhole-free conformal coatings with excellent penetration abilities. Second, there are several benefits resulting from the fact that the deposition takes place at or around room temperature. The two most important ones are the capability to coat thermolabile substrates [20-22] and the avoidance of mechanical stress otherwise introduced by different thermal

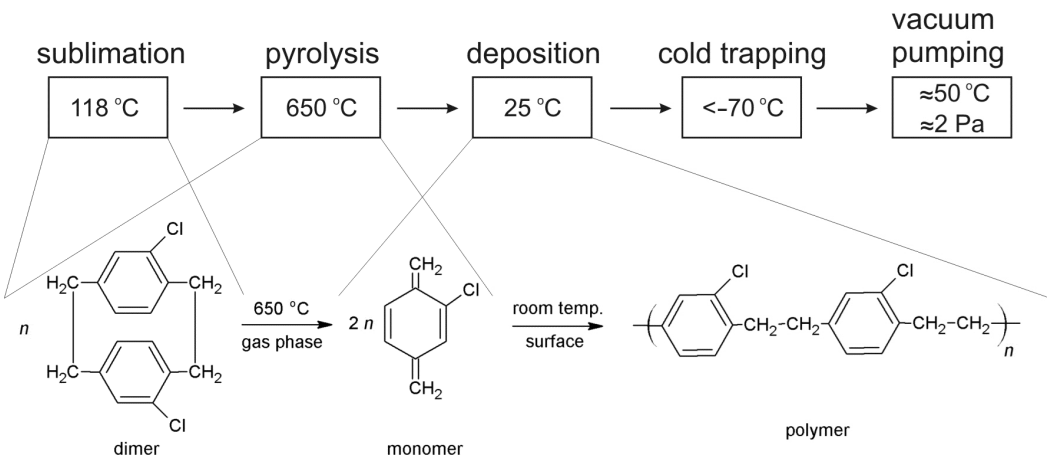

Figure 1: Schematic representation of the deposition process of Parylene C with the respective chemical reactions. Reprinted with permission from [28], copyright 2016 Elsevier.

expansion coefficients of coating and substrate. Finally, as it has been already stressed above, the polymerization reaction is initiated spontaneously and as such it requires no external initiator/catalyst. This unique feature makes the product uncontaminated with impurities influencing electrical conduction. As far as the termination of the reaction is concerned, there is none as long as the growing macromolecules remain under vacuum. The polymerization reaction exhibits a step-growth mechanism with second order kinetics with respect to the active radical sites [26]. Upon exposure to the atmosphere, these radical active centers (sometimes described as "dangling bonds") are quenched with oxygen, forming oxide-type moieties [26]. However, because the gas permeability of parylene coatings is low and the degree of polymerization is very high [26], the concentration of these structures and, therefore, their effect on electrical conduction of the polymer is low.

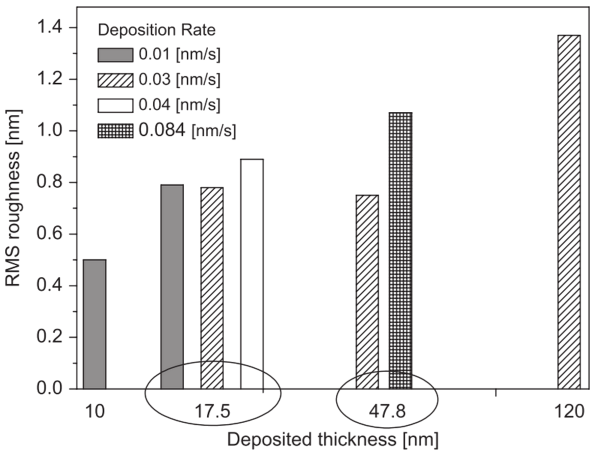

Figure 2: AFM measurements of the surface roughness of Parylene C thin films. Reprinted with permission from [30], copyright 2009 Elsevier.

It is known that Parylene C films deposited at high pressure and high deposition rate are rough and have non-uniform and poor dielectric properties. A small increase of the deposition rate from 0.015 to 0.08 g/min results in a growth of the root-mean-square surface roughness from 5.78 to 9.53 nm [29]. The same effect of an increasing roughness with increasing deposition rate was observed when various film thicknesses were compared (Figure 2) [30]. Therefore, when increasing the sublimation rate, one should be aware of the resulting increase of the film surface roughness.

Xylylene polymers are partially crystalline materials. It was found that both deposition rate and post-deposition thermal treatment significantly affected the crystallinity of the Parylene C films. Both as-deposited and thermally annealed films were subjected to X-ray diffraction (XRD) measurements and showed a maximum at $2\theta \approx 14.5°$ corresponding to the (020) crystalline plane (Figure 3) [29]. It can be seen that the peak height increases with the annealing temperature, while the full width at half maximum (FWHM) is observed to decrease.

The interlayer distance (*d*-spacing), which decreases with increasing temperature, indicates that more ordered polymer chains are formed at higher temperatures. This is due to higher energy available for chain motion and crystallization during thermal annealing. The size of crystalline domains is controlled by a number of defect mechanisms in the polymerization process. The crystallinity of Parylene C films affects their mechanical properties such as elastic modulus and/or Poisson's ratio. The sample with higher crystallinity has approximately 30% greater tensile strength than the as-deposited films, a fea-

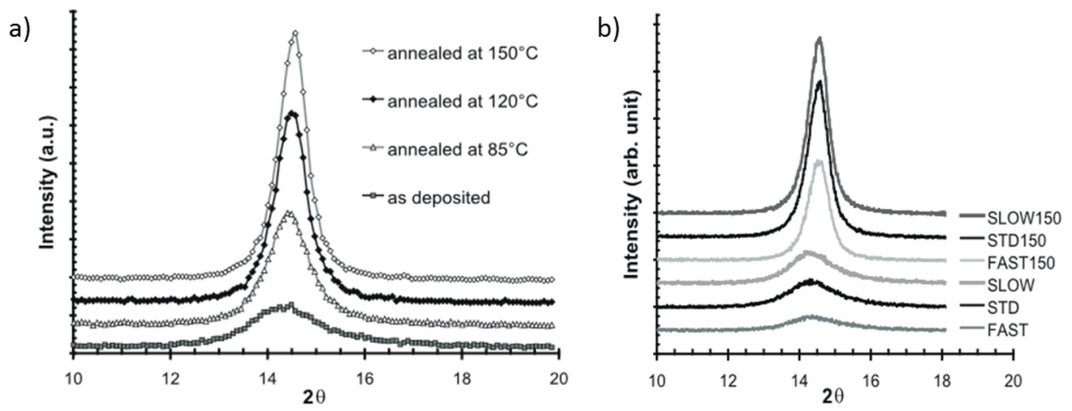

Figure 3: XRD spectra of Parylene C films: as-deposited with constant deposition rate and thermally annealed at different temperatures (a), as-deposited with different deposition rates and thermally annealed at constant temperature (b). Reprinted with permission from [29] copyright 2008 MYU K.K. (reprinted from electronic version).

ture highly required from the point of view of material flexibility. The high quality of Parylene C thin films was confirmed by micro-Raman spectroscopy. The principal Raman band localized at 1336 cm^{-1} was assigned to C–H in-plane deformation in accordance with the results obtained earlier for both a bulk Parylene crystal [31] and micrometer thick layers [32]. Good surface homogeneity in the micrometer range [30] was revealed by means of mapping the layers with micro-Raman spectroscopy, where only small differences in Raman intensity in all measured positions were observed.

Parylene C as substrate material

In the transistor configuration presented in Figure 4, Parylene C is not only used as a gate dielectric material but it also serves as device flexible substrate. Such a flexible substrate allows one to investigate the influence of mechanical bending on charge carrier transport in the zone-cast layer of tetrakis(alkylthio)tetrathiafulvalene [18]. Bending tests carried out for numerous curvature radii clearly demonstrate that the performance of OFET devices (with structure presented in Figure 4(VII)) does not deteriorate irreversibly under these conditions. When sub-

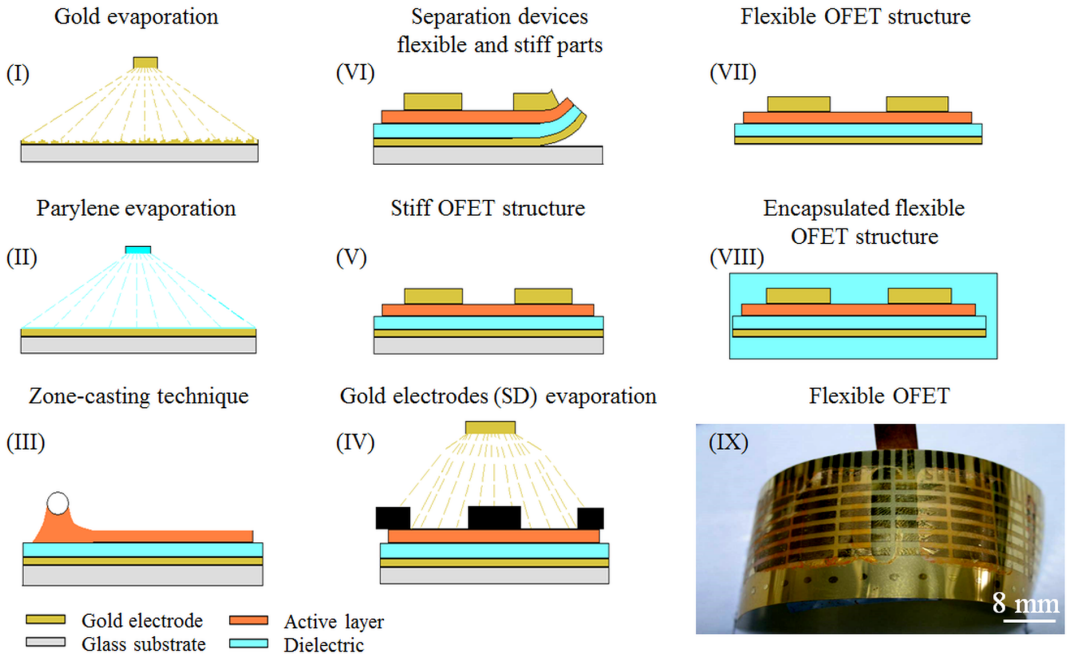

Figure 4: Schematic illustration of the flexible OFET fabrication procedure with Parylene C as a substrate and gate dielectric layer and with zone-cast tetrakis(alkylthio)tetrathiafulvalene as semiconductor. Reprinted with permission from [34].

jected to bending, the devices still work, with the calculated mobility gradually dropping off with a decrease of bending radius. While amounting to 0.1 cm^2/Vs for unbent structures, its magnitude decreases to ca. 0.06 cm^2/Vs for r = 25 mm and to 0.04 cm^2/Vs for r = 5 mm [18]. This effect has been attributed to the influence of stress induced in the tetrathiafulvalene (TTF) semiconductor crystalline films, namely charge trapping caused by mechanical bending [33].

In another work, ultra-thin Parylene C insulating layers were fabricated on Au gate electrodes by reducing the parylene film thickness to 18 nm with the help of oxygen plasma etching [33]. This procedure enabled the manufacturing of OFET devices with a driving voltage as low as 2 V. In fact, the OFETs equipped with the 18 nm thick parylene gate insulator exhibit excellent low gate leakage currents (of the order of picoamperes and below) at 2 V operation. Mechanical tests of OFETs fabricated on a 3 µm thick Parylene C film were carried out. However, the main difference between the results obtained for TTF derivatives, described above, and those obtained in [33] is that the transistor was additionally encapsulated with 3 µm thick Parylene C coating to set it on a strain neutral position. Figure 5a presents a device bent onto a 0.8 mm radius glass tube in the course of a bending test. Transfer characteristics of ten OFET transistors collected before and after the tests are presented in Figure 5d [33].

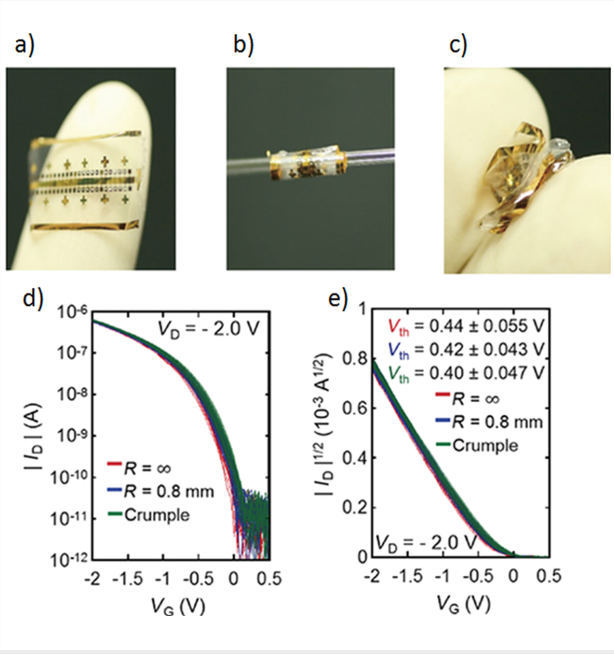

Figure 5: Transfer characteristics of 10 OTFTs after bending and crumpling tests: (a) Photograph of a device before mechanical tests. (b) Photograph of a device rolled onto a cylinder of 0.8 mm radius. (c) Photograph of a crumpled device. (d) and (e) Transfer characteristics of 10 OTFTs before and after bending and crumpling tests. Reprinted with permission from [33] copyright 2016 IOP Publishing Ltd.

As seen in Figure 5, OFET transfer characteristics show a narrow dispersion and a gate leakage current of the order of picoamperes, and these properties do not change after mechanical tests. The remaining transistor parameters such as charge carrier mobility, subthreshold and threshold voltage also remain practically unaffected by mechanical testing. The threshold voltage value, 0.44 V for the unbent device, became slightly reduced down to 0.42 V and 0.40 V after bending and crumpling tests (Figure 5e). The results show that OFET devices with the 18 nm thick parylene gate insulator are characterized by a similar mechanical durability as those equipped with a 100 nm thick layer of the gate insulator [35]. It could be concluded, on a basis of the results obtained for bent transistors, that the encapsulation layer substantially improves mechanical properties of the devices.

Parylene C as a gate insulating layer

The purity of thin dielectric films has a tremendous impact on their electrical properties. Results of electrical breakdown voltage measurements on a 2 mm × 2 mm area capacitor structures equipped with a dielectric layer of Parylene C are presented in Figure 6.

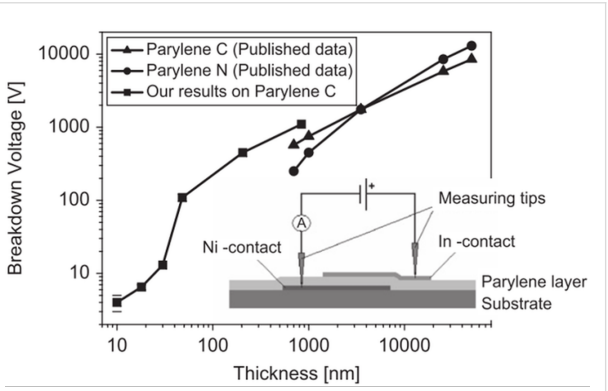

Figure 6: Thin Parylene C layers breakdown voltage as a function of thickness. Reprinted with permission from [30], copyright 2009 Elsevier.

The measurements in Figure 6 reveal the excellent electrical properties of Parylene C layers, particularly in terms of their dielectric strength. An additional advantage of these films is that the breakdown voltage remains constant across the entire capacitor area, which is typical for uniform and pinhole-free layers. The above results show that thin Parylene C films are good candidates for the gate insulating material in organic thin film transistors.

For an application, it is required that a transistor has to be controlled by the lowest possible voltage. A thickness decrease of the dielectric layer allows one to reduce the applied gate

voltage, with a drawback being an increased leakage current [36]. The efficiency of the field effect is dependent on the capacitance of the gate insulating material. The capacitance is determined by the dielectric permittivity (ε) and the thickness of the insulating layer. Currently, two types of dielectric materials are commonly employed in transistor design and construction, either inorganic metal oxides (such as Ta_2O_5, Al_2O_3, SiO_2) or organic polymers [13]. However, it was found that the application of an inorganic insulator with high ε significantly decreases the mobility of charge carriers by interaction with the induced polarization in the gate insulator [37]. The effect of dielectric permittivity of the gate insulating material on field-effect mobility, investigated in rubrene single-crystal transistors equipped with various dielectrics layers, is shown in Figure 7. In Figure 7a, for the device based on Parylene C, the suppression of contact effects requires a larger V_{DS} value (and thus also a larger value of V_{GS}), in order to remain in the linear regime.

To summarize, it should be pointed out that an increase of dielectric permittivity of gate insulating material results in a decrease of field effect mobility (Figure 7b). For all dielectric materials applied, the highest values of charge carrier mobility were obtained for xylylene polymers. In the case of Parylene C (ε = 3.15) it was approximately 10 $cm^2/V{\cdot}s$, while for Parylene N (ε = 2.65) it varied in the range of 10–15 $cm^2/V{\cdot}s$. In contrast, an application of the oxide gate dielectric Ta_2O_5 (ε = 25) resulted in a lower mobility value of 1.5 $cm^2/V{\cdot}s$ [37]. The maximum value of 16–20 $cm^2/V{\cdot}s$, was obtained for vacuum as a dielectric [38].

The deterioration of the dielectric/semiconductor interface was revealed to be due to charge trapping at that interface. This effect could be controlled by an application of self-assembly monolayers (SAM) that significantly reduce the number of traps but they cannot entirely eliminate surface SiOH groups [39]. When polyethylene was used as a buffer dielectric, unhindered charge transport was observed [40], suggesting that thin polymer layers could play the same role as SAMs do. For this reason, polymers are often used as a part of twin dielectric layer systems in which one layer is responsible for dielectric strength and/or capacitance, whereas the other is designed to form a preferred interface for the growth of an organic semiconductor [41]. Due to a substantial charge-trapping effect observed in inorganic dielectrics, the organic polymer insulators bear much higher application potential in organic transistor technology. There are only few commercial dielectric polymer materials that meet the requirements: poly(methylmethacrylate) (PMMA) [42], polyvinylphenol (PVP) [43], amorphous fluoropolymer (CYTOP®) [44] and poly-*p*-xylylene derivatives (parylenes). Because of its unique properties described above, the latter polymer has the potential to outgrow the remaining candidates in its application as a gate dielectric in both single-crystal organic transistors and polycrystalline TFTs.

One of the most cited publications in the field of organic field effect transistors is the work of Podzorov et al. describing rubrene single-crystal transistors with Parylene C used as the gate insulating material [2]. This configuration allowed the authors to fabricate OFET devices with high charge-carrier mobility and reproducible characteristics. Parylene C forms transparent, pinhole-free conformal coatings of thicknesses as low as 0.1 μm with excellent dielectric and mechanical properties. Increasing thickness to 0.2 mm suffices to uniformly cover rough colloidal-graphite contacts. Transistors with rubrene as

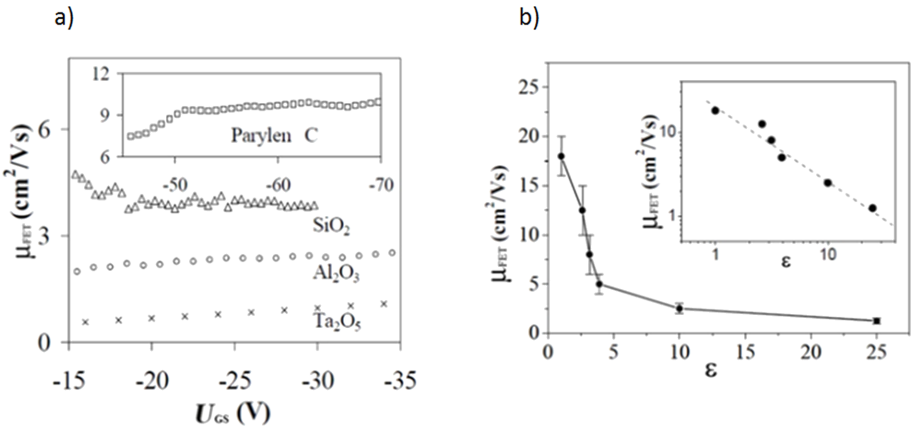

Figure 7: (a) Mobility μ(V_g) curves measured for four different gate insulators. For the device based on Parylene C, the suppression of contact effects often requires a rather large value of V_{DS} (and thus V_{GS}) to remain in the linear regime. (b) Decrease of the mobility with increasing ε, as observed in rubrene single-crystal FETs with different gate insulators. The bars give a measure of the spread in mobility values. Inset: when plotted on a log–log scale, the available data show a linear dependence with slope −1 (i.e., the variation in μ is proportional to ε^{-1}). Reprinted with permission from [37], copyright 2004 of AIP Publishing.

semiconductor and parylene as dielectric exhibit hole-type conductivity with a field-effect mobility up to 1 $cm^2/V{\cdot}s$ and an on/off ratio up to 10^4 at room temperature. Such a good performance has been made possible because of the high quality of both the rubrene crystals and the rubrene/parylene interface. The above results clearly demonstrate how important it is to select a compatible dielectric material with reduced number of charge traps [2].

The effect of the gate dielectric material on charge-carrier transport in single-crystal transistors was also discussed in the case of devices based on TTF derivatives, also characterized as a hole-type semiconductor. In this case, a more effective charge transport was observed when a Parylene C dielectric film was used instead of the Si/SiO_2 combination. An application of parylene insulator also facilitated an evaluation of the influence that the crystalline structure of the semiconductor has on the performance of the single-crystal transistor. Of two crystalline forms of dithiophene-tetrathiafulvalene, the monoclinic alpha polymorph substantially outperformed the hexagonal beta polymorph [45].

The influence of the surface roughness of a dielectric film on the molecular arrangement of the first few semiconductor layers as well as on the size of its crystal grains is a critical factor in high-performance OFET devices. The effect of Parylene C roughness on charge transport has been studied in detail by an observation of submonolayer percolation of a pentacene film during its deposition on a rough dielectric surface. Interestingly enough, electrical properties of such a structure stabilize at the same film thickness as it does when a smooth substrate is used [46]. This suggests that the device performance will not be impaired by surface roughness as long as a conformal deposition of the semiconductor layer is guaranteed. These results are in agreement with the reports presented for a series of transistors with silicon/silicon dioxide substrates of various surface roughness [47-49]. It was found, that charge-carrier transport in relatively thick (multilayer) semiconducting films, obtained by thermal evaporation [47] or from solution [48] is insensitive to the substrate roughness. However, in thin monolayer semiconductor films the surface roughness significantly influences the charge-carrier transport [49]. This is due to the fact that charge-carrier transport in the initial monolayers is directly related to the roughness of a dielectric layer. Thicker films present lower sensitivity to the changes of surface roughness because each next layer away from the dielectric surface contains less and less defects. An increase of the domain size in the upper layers provides sufficient paths for charge carrier transport [48].

Roughness is not the only surface parameter that may influence the supramolecular organization of the semiconductor film. The correlation between surface energy and charge transport in organic semiconductors has been discussed for TTF-based transistors produced on two different silicon dioxide substrates, characterized by surface energies of 51.8 and 40.1 mN/m, respectively [10]. It was found, that the average charge-carrier mobility was considerably higher ($\mu = 0.2$ $cm^2/V{\cdot}s$) when the SiO_2 surface energy was lower. The substrate with the higher surface energy exhibited a mobility of $\mu = 0.006$ $cm^2/V{\cdot}s$. More detailed studies were carried out for tetracene semiconductor films deposited on various dielectric materials, namely organic polystyrene (PS), Parylene C, and poly(methyl methacrylate) (PMMA) as well as on inorganic SiO_2, with and without HMDS modification [50]. AFM measurements of tetracene semiconductor films show that the regularly shaped islands on the polymer dielectrics (PS, Parylene C, PMMA) lead to a complete substrate coverage at low nominal thickness, between 10 and 17 nm (Figure 8). Interconnected islands were formed at thicknesses of 10 nm and 17 nm, respectively, for PS and Parylene C films. This was enough to attain efficient charge transport in the tetracene layer. Certain differences in charge-carrier mobility and threshold voltages between PS and Parylene C were, however, observed.

The slightly lower charge-carrier mobility obtained for Parylene C has been attributed to the surface roughness, which increases the nucleation density and leads to less ordered films. The lower film order of Parylene C is compensated by the low charge trapping at the semiconductor/dielectric interface [50] confirmed by I_{DS} hysteresis observed for all devices, except those equipped with Parylene C.

The weak charge-trapping effect in OFETs with Parylene C dielectric in contrast to the SiO_2 dielectric layer has been well demonstrated in the case of transistors based on poly[bis(4-phenyl)(2,5,6-trimethylphenyl)amine] (PTAA) [51]. The trapping significantly slows down the charge transport when SiO_2 is used. By contrast, the PTAA transistor exhibits a marginal hysteresis between forward and backward sweep with similar transistor performance when the Parylene C is used either as self-standing dielectric (Figure 9a(ii)) instead of the SiO_2 layer (Figure 9a(i)), or as a passivation layer (Figure 9a(iii)). In the latter case, the passivation effect is accomplished by Parylene C film creating a diffusion barrier that separates the conductive channel from electronic trap states in the SiO_2 dielectric.

It is worth noting that the charge-trapping effect is not only connected to the dielectric/semiconductor interface. The effect of grain size and interface dependence of bias stress stability has been studied for C_{60}-fullerene-based, n-type OFETs. It was revealed that, with an increasing grain size of C_{60}, the bias stress induced shift of the threshold voltage can be controlled.

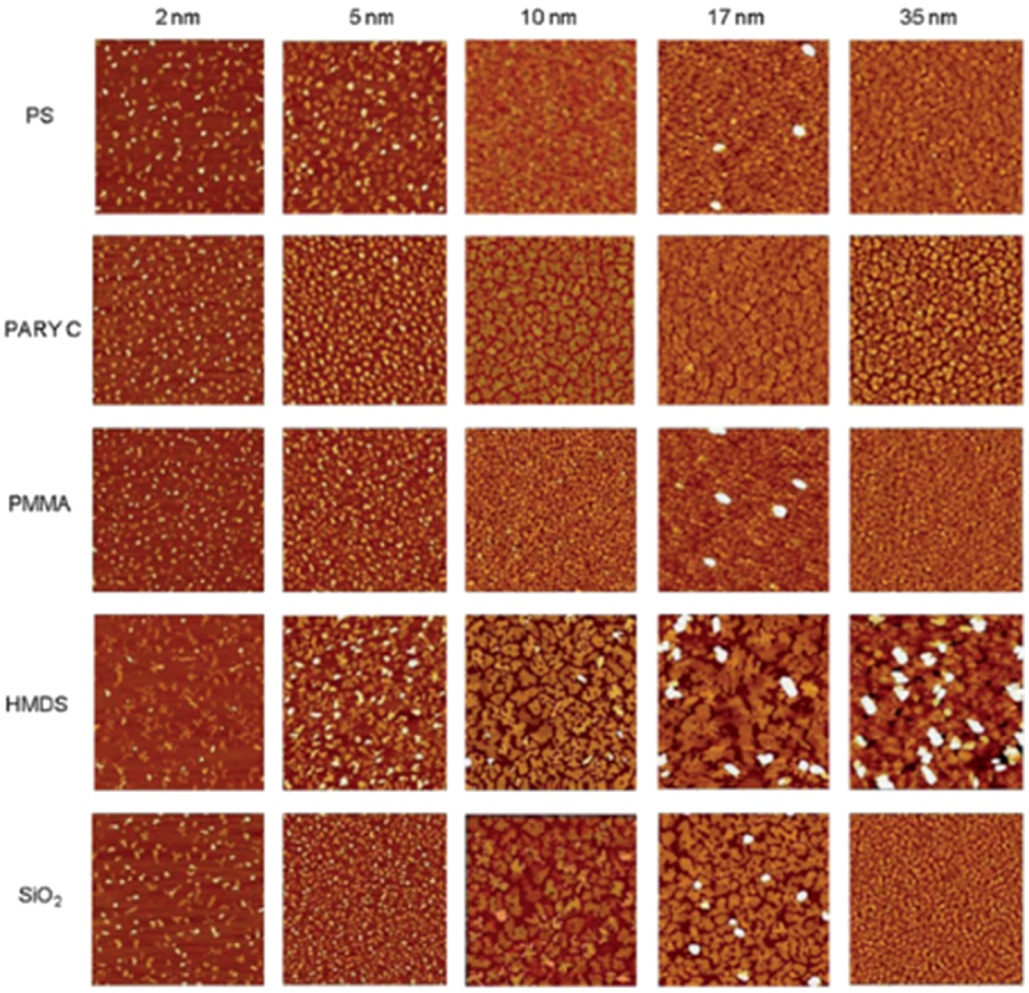

Figure 8: 10 µm × 10 µm AFM images of tetracene thin films on different dielectric surfaces at different nominal thickness. *Z*-scale: 50 nm. Reprinted with permission from [50], copyright 2013 Royal Society of Chemistry.

This effect is mainly attributed to the mechanism of charge trapping at grain boundaries [52]. It was also found in further studies that the growth of C_{60} on the surface of Parylene C at elevated substrate temperatures leads to the creation of radicals at the interface between the active layer and the gate dielectric. The radicals formed during the C_{60} deposition help to improve the bias stress stability of C_{60}-based n-type OFETs [53]. The creation of free radicals was also observed for a double-gate configuration with Parylene C as a dielectric layer [54]. This effect was not observed for the OFETs with top-gate configuration, when the Parylene C film was deposited on a top of the C_{60} layer.

As it was mentioned in the previous section, one of the major advantages of Parylene C films is the fact that they are deposited in a very clean environment, with no solvents and no initiators involved. This is a crucial point during the fabrication of the transistors with top-gate configuration where Parylene C is applied together with highly soluble n-type semiconductors as active material. There is a double advantage of such a combination: First, deposition of Parylene C by CVD method does not disturb the semiconductor surface, and second, the charge-trapping effect caused by oxygen and water is much less pronounced when Parylene C is working as a protecting layer of the semiconductor film. An example of this advantage is given in the abovementioned work with C_{60} fullerene transistors, where a comparison between the bottom-gate, top-gate and double-gate configuration with Parylene C as a dielectric layer is made [54]. The results are shown in Figure 10.

The charge-carrier field-effect mobility for bottom-gate, top-gate, and dual-gate OFETs was determined to be 0.1, 0.2, and 0.9 $cm^2 \cdot V^{-1} \cdot s^{-1}$, respectively. An application of the top-gate or dual-gate configuration not only increases the mobility value but it also brings about a different response to the bias stress. Figure 10 presents the transfer characteristics of the devices re-

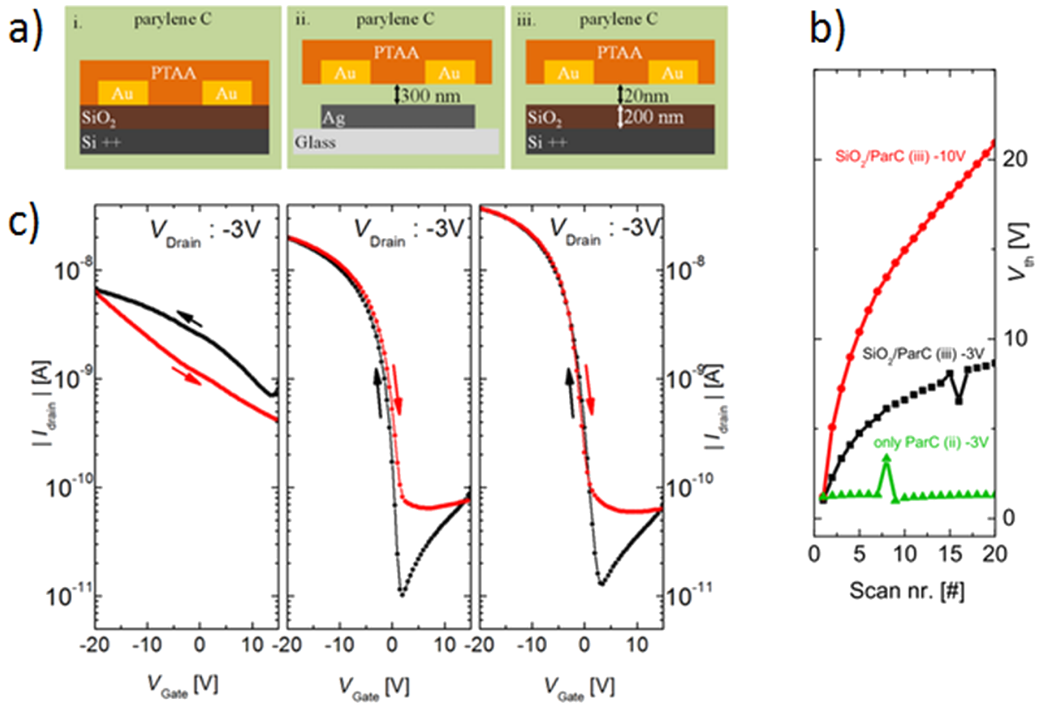

Figure 9: (a) Transistor architecture of the three different transistor stacks investigated, (b) threshold voltage trends of successive transfer sweeps for different V_D, (c) representative transfer *I*–*V* characteristics of the three transistor stacks. The arrows in (c) indicate the sweeping direction of V_G. Reprinted with permission from [51], copyright 2016 Springer.

corded before applying bias stress, and after 24 h and 125 h of bias stress application. While in the case of bottom-gate OFETs the V_{th} value is shifted towards more positive voltage (from 20.7 to 34.6 V), for the top-gate OFET configuration the bias stress results in a V_{th} shift in the opposite direction (from 14.3 to 0.1 V). In the case of dual-gate OFETs, only a small shift of V_{th} (from 11.5 to 8.5 V) was observed. The reason for this behavior is the fact that Parylene can chemically interact with C_{60} when it is being evaporated on top of the C_{60} semiconductor layer. A shift of V_{th} towards negative V_{GS} values implies an accumulation of metastable positive charges at the dielectric/semiconductor interface during the bias stressing. A similar behavior of bidirectional V_{th} shift was also observed in pentacene OFETs on silicon dioxide substrates modified by polydimethylsiloxane and it was assigned to either hole or electron trapping, depending on the bias stress polarity [55].

The top-gate configuration has also an additional advantage of the dielectric film working as a protective layer. In one example, a thin ordered layer of naphthalene bisimide was deposited via a zone-casting solution procedure with Parylene C used as the top-gate dielectric. Parylene was selected as a suitable material because it inflicted no damage to the semiconductor structure, a notion confirmed by relatively high charge carrier mobility of 0.18 $cm^2/V{\cdot}s$ with accompanying threshold voltage below 5 V [24]. As it has already been mentioned, Parylene C plays a role of a protective layer (not only from mechanical point of view) for this *n*-type material for which the LUMO level of −3.77 eV does not assure stability under ambient processing conditions [56]. Interestingly, as it has been established in the course of device manufacturing, OFET parameters such as threshold voltage and charge-carrier mobility of n-channel transistors substantially depend on the material of the dielectric layer. Parylene C is superior for that purpose compared to fluorinated CYTOP polymer [57]. Manufactured via solution processing and equipped with Parylene gate dielectric, OFETs of adequate transport characteristics are operated under ambient conditions with no need of any extra shielding. After an initial period of a decrease of charge-carrier mobility, the long-term performance stabilizes at a satisfactory operational level.

It has to be stressed, however, that not all organic semiconductors show an increase of the charge-carrier mobility when the top-gate configuration is applied. For example, top-gate transistors with solution-processed dibenzo[*d*,*d*]thieno[3,2-*b*;4,5-*b*']dithiophene semiconductor exhibit much lower mobility (0.0001 cm^2/Vs) than a bottom-gate configuration (0.02 cm^2/Vs) [58]. Changes in the surface energy between Parylene C (bottom gate, top contacts) and glass with gold electrodes (top gate, bottom contacts) are the main factor responsi-

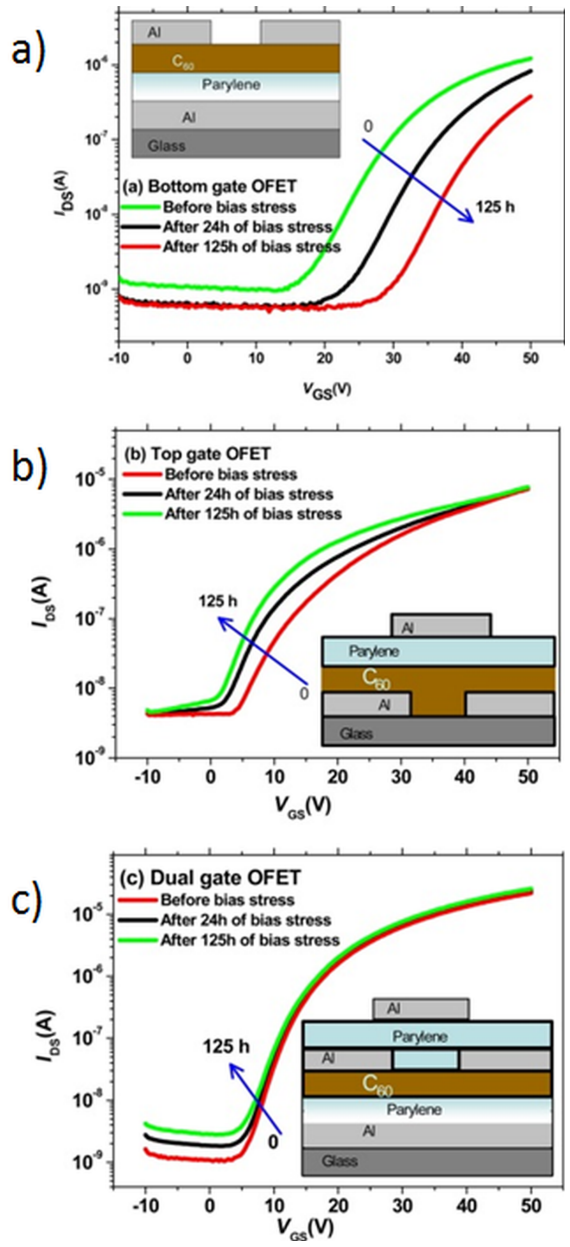

Figure 10: Transfer characteristics measured during the continuous bias stress of 125 h. (a) Bottom-gate, top-contacts, (b) top-gate, bottom-contacts, and (c) dual-gate OFETs. Reprinted from [54], copyright 2014 American Chemical Society.

ble for variations in the organization of semiconductor molecules. Additionally, parameters such as wettability and the corrugated surface can significantly alter the microstructure of semiconducting films and bring about a decrease of the device performance [18]. The effect of surface energy on charge-carrier mobility was discussed above using an example of transistors made of tetrathiafulvalene (TTF) derivatives on silicon dioxide substrates [10].

Parylene C as an encapsulation layer

The origin of electrical instabilities of organic electronic devices is related to absorption of oxygen and/or water by the semiconductor film and to charge trapping in the semiconductor or at the dielectric/semiconductor interface. An efficient encapsulation should protect the organic semiconductor from interactions with gas and moisture and other adverse environmental conditions. Parylene C is one of the encapsulation materials that meet the above requirements [59,60]. However, there is certain ambiguity concerning the adhesion of this polymer to different substrates. According to the literature Parylene C exhibits a satisfactory adherence to gold, platinum and silicon nitride [61], which is, however, in contradiction to older reports [62,63]. Its adherence to polyimide, on the other hand, is found to be very low [61]. It appears that adhesion forces of Parylene C not only depend on the type of substrate, but they can also be easily modified by surface processing, such as oxygen plasma treatment or thermal annealing [64]. Which procedure is to be applied strongly depends on the material used and on the further application of the parylene layer. It should also be pointed out, that when Parylene C is applied as a flexible substrate, its limited adhesion to the temporary rigid support (used in the fabrication process as sacrificial material) constitutes a major advantage of this polymer.

The fact that Parylene C is sensitive to high-temperature treatment, such as thermal annealing, has been discussed in one of the previous chapters. When heated, this material becomes harder, more rigid and more brittle. A simple explanation of this effect is the increase of the degree of polymer crystallinity at elevated temperatures. In a similar way, when deposited at higher pressure, Parylene C layers are more elastic and less brittle because of lower crystallinity. Taking the above consideration into account, care should be taken not to operate at exceedingly high temperatures, which is a likely limitation of the entire field of organic electronics.

One of the early applications of Parylene C encapsulation layer in an electronic structure was that of a microelectrode insulator [65]. The Parylene C-covered iridium and tungsten microelectrodes were investigated by means of in vivo and in vitro impedance tests. In vitro studies were carried out in an especially prepared chamber containing saline, either sterile or plasma-incubated at 37 °C, in order to reproduce the natural environmental. In vivo testing was performed by an implementation of multiple electrode systems in monkey motor cortex [65]. In these studies, an unchanged impedance of the microelectrodes protected by Parylene C layers has been recorded for over four months [66]. As another positive result, no destructive influence of the encapsulation material was observed when Parylene C had been employed to protect a pentacene OFET

device, where no remarkable alteration of the current–voltage characteristics before and after an application of a passivation layer was recorded [67]. Because of the specific properties of the parylene deposition procedure taking place at room temperature, no changes in the semiconducting channel were induced and the device fabricated showed unchanged transfer and output characteristics.

The quality of thin protective films of Parylene C was investigated by optical coherence microscopy (OCT), whereby defects in the encapsulation layer were detected, either by a change of the number of peaks in the interference fringe signal envelope, or as a change in the signal amplitude [68]. Figure 11 presents a glass substrate covered with 1 μm thick Parylene C film, with gas chamber and bad contact areas purposefully created as a reference sample for further investigation of transistors. Transistors with the typical bottom-gate, top-contact configuration and with Parylene C used as the encapsulation layer were investigated. Figure 12 presents a volumetric reconstruction of Parylene C-coated OFET as well as a calculated amplitude map of the Parylene C/semiconductor interface, where zoom-in image (right panel) shows the interface without defects. To summarize, it can be concluded that by optimizing the process of Parylene C deposition no defects in the semiconductor layer and at

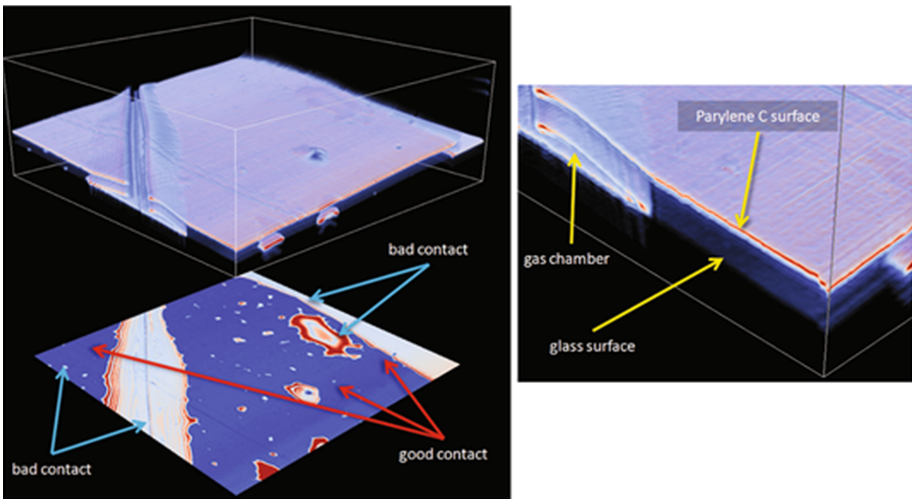

Figure 11: Volumetric reconstruction of the Parylene C-coated microscopy glass (left, atop) and calculated amplitude map of the Parylene C/glass interface (left, bottom). Boundary box indicates the size of the volume 2000 × 2000 × 208 μm. Zoom-in image (right). Coating defects and gas chambers are clearly visible. Reprinted with the permission from [68], copyright 2011 Springer.

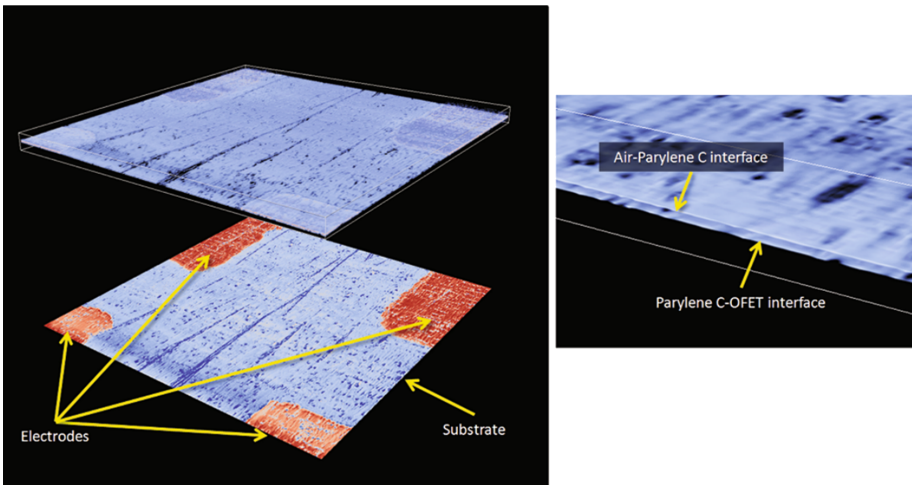

Figure 12: Volumetric reconstruction of the Parylene C-coated OFET structure (left, atop) and calculated amplitude map of the Parylene C/substrate interface (left, bottom). Boundary box indicates the size of the volume 2000 × 2000 × 73 μm. Zoom-in image showing interfaces of 2 μm thin polymer layer (right). Reprinted with the permission from [68], copyright 2011 Springer.

semiconductor/encapsulation layer interface are formed and, therefore, no additional charge traps are created at that interface.

It should be pointed out that the results discussed above were obtained for active materials that were not sensitive to ambient conditions. However, most *n*-type organic semiconductors do not show such stability. One example of an unstable material (characterized by considerable charge trapping) is the previously described fullerene C_{60}. The transistor characteristics of unprotected and Parylene C protected fullerene based devices are presented in Figure 13.

Transfer characteristics, monitored under ambient conditions, of non-protected OFETs are shown in Figure 13a. As seen in the figure, the source–drain current (I_{DS}) of a non-encapsulated OFET decays over 90 min by one order of magnitude, with the gate threshold voltage shifting to higher magnitudes [69]. This behavior strongly indicates that oxygen and/or water vapor create charge trap states the filling of which requires higher gate voltage for a successful OFET operation. The transfer characteristics of OFETs equipped with a protective layer of a sole 1 µm thick Parylene C coating and a combination of 0.5 µm thick Parylene C with 0.5 µm thick benzocyclobutene (BCB) films, monitored under ambient conditions for twelve days, are presented in Figure 13b and Figure 13c, respectively. The encapsulation layer of Parylene C substantially improves the air stability of the C_{60}-based n-type OFET. In this case, the decay of I_{DS} current of one order of magnitude has been recorded after 12 days. The onset voltage remains the same but a small shift in the threshold voltage is observed [69]. The slow degradation of I_{DS}, measured in the OFET encapsulated with Parylene C (1 µm) may be attributed to the slow penetration of water vapor and oxygen through the encapsulation layer. The decrease in the permeability of water vapor and oxygen through the bilayer encapsulation film has been attributed to the sealing of grain boundaries by the smoothness of the BCB layer. However, it only works when Parylene C/BCB bilayer system is used. By applying a bilayer encapsulation system, the defects in the Parylene C film underneath are blocked by the BCB layer. The permeation path for water vapor and oxygen becomes tortuous, which results in an improvement of the barrier performance.

Finally, it is also worth to add, that when Parylene C is used as a gate insulator in OFET transistors with top-gate configuration, its protective properties are considerably enhanced by a metal gate electrode deposited on its top. This feature has been found especially useful in the case of OFETs equipped with either ambipolar [28] or *n*-type [24] channels, since the *n*-type organic semiconductors are particularly sensitive to a deteriorative effect of atmospheric oxygen and water vapor.

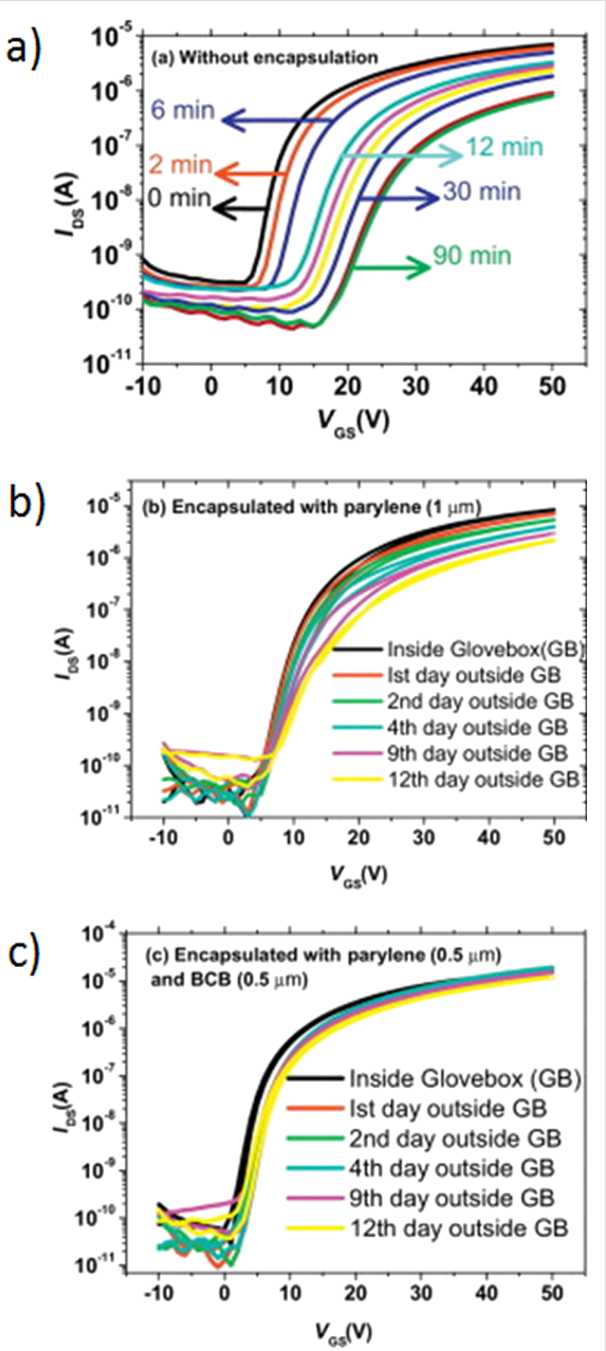

Figure 13: Transfer characteristics recorded under ambient conditions of a fullerene transistor without encapsulation (a), encapsulated with 1 µm thick layer of Parylene C (b) and encapsulated with 0.5 µm thick layer of Parylene C followed by 0.5 µm layer of benzocyclobutene (c). Reprinted with the permission from [69], copyright 2014 Elsevier.

Conclusion

The presented review of literature describing state-of-the-art applications of Parylene C as substrate, dielectric, insulator or protecting and encapsulating material in construction of OFETs demonstrates that poly(*p*-xylylenes) constitute a class of versatile supporting materials particularly suitable for applications in

flexible organic electronics. The properties of greatest importance for such applications are the extraordinary purity and chemical inertness of Parylene layer, its elasticity and ability to form smooth and pinhole-free conformal coatings. Due to high purity and low dielectric permittivity, the concentration of charge-carrier traps at the Parylene/semiconductor interface is very low. This results in enhanced charge-carrier mobility in the OFETs. The flexibility of Parylene C paves the route for flexible electronics, and the continuous and conformal coating, when combined with metal gate electrodes evaporated on the top of parylene layer, assures a sufficient protection of OFETs against oxygen and water, which is especially important for transistors with *n*-type channels.

Acknowledgements

The present work has been supported by the Polish National Research Centre under the projects code of: 2012/07/B/ST8/03789, DEC-2013/08/M/ST5/00914 and UMO-2015/18/E/ST3/00322.

References

1. Xu, X.; Yao, Y.; Shan, B.; Gu, X.; Liu, D.; Liu, J.; Xu, J.; Zhao, N.; Hu, W.; Miao, Q. *Adv. Mater.* **2016,** *28,* 5276–5283. doi:10.1002/adma.201601171
2. Podzorov, V.; Pudalov, V. M.; Gershenson, M. E. *Appl. Phys. Lett.* **2003,** *82,* 1739–1741. doi:10.1063/1.1560869
3. Yamashita, Y.; Hinkel, F.; Marszalek, T.; Zajaczkowski, W.; Pisula, W.; Baumgarten, M.; Matsui, H.; Müllen, K.; Takeya, J. *Chem. Mater.* **2016,** *28,* 420–424. doi:10.1021/acs.chemmater.5b04567
4. Marszalek, T.; Li, M.; Pisula, W. *Chem. Commun.* **2016,** *52,* 10938–10947. doi:10.1039/C6CC04523E
5. Zhang, H.; Guo, X.; Hui, J.; Hu, S.; Xu, W.; Zhu, D. *Nano Lett.* **2011,** *11,* 4939–4946. doi:10.1021/nl2028798
6. Dong, H.; Jiang, L.; Hu, W. *Phys. Chem. Chem. Phys.* **2012,** *14,* 14165–14180. doi:10.1039/c2cp41712j
7. Veres, J.; Ogier, S.; Lloyd, G.; de Leeuw, D. *Chem. Mater.* **2004,** *16,* 4543–4555. doi:10.1021/cm049598q
8. Cheng, X.; Noh, Y.-Y.; Wang, J.; Tello, M.; Frisch, J.; Blum, R.-P.; Vollmer, A.; Rabe, J. P.; Koch, N.; Sirringhaus, H. *Adv. Funct. Mater.* **2009,** *19,* 2407–2415. doi:10.1002/adfm.200900315
9. Liu, C.; Xu, Y.; Noh, Y.-Y. *Mater. Today* **2015,** *18,* 79–96. doi:10.1016/j.mattod.2014.08.037
10. Miskiewicz, P.; Kotarba, S.; Jung, J.; Marszalek, T.; Mas-Torrent, M.; Gomar-Nadal, E.; Amabilino, D. B.; Rovira, C.; Veciana, J.; Maniukiewicz, W.; Ulanski, J. *J. Appl. Phys.* **2008,** *104,* 054509. doi:10.1063/1.2968441
11. Graff, G. L.; Williford, R. E.; Burrows, P. E. *J. Appl. Phys.* **2004,** *96,* 1840–1849. doi:10.1063/1.1768610
12. Ortiz, R. P.; Facchetti, A.; Marks, T. J. *Chem. Rev.* **2010,** *110,* 205–239. doi:10.1021/cr9001275
13. Facchetti, A.; Yoon, M.-H.; Marks, T. J. *Adv. Mater.* **2005,** *17,* 1705–1725. doi:10.1002/adma.200500517
14. Klauk, H. *Chem. Soc. Rev.* **2010,** *39,* 2643–2666. doi:10.1039/b909902f
15. Małachowski, M. J.; Żmija, J. *Opto-Electron. Rev.* **2010,** *18,* 121–136. doi:10.2478/s11772-010-0008-9
16. Sekitani, T.; Zschieschang, U.; Klauk, H.; Someya, T. *Nat. Mater.* **2010,** *9,* 1015–1022. doi:10.1038/nmat2896
17. Yi, H. T.; Payne, M. M.; Anthony, J. E.; Podzorov, V. *Nat. Commun.* **2012,** *3,* 1259. doi:10.1038/ncomms2263
18. Marszalek, T.; Nosal, A.; Pfattner, R.; Jung, J.; Kotarba, S.; Mas-Torrent, M.; Krause, B.; Veciana, J.; Gazicki-Lipman, M.; Crickert, C.; Schmidt, G.; Rovira, C.; Ulanski, J. *Org. Electron.* **2012,** *13,* 121–128. doi:10.1016/j.orgel.2011.10.001
19. Fukuda, K.; Sekine, T.; Shiwaku, R.; Morimoto, T.; Kumaki, D.; Tokito, S. *Sci. Rep.* **2016,** *6,* 27450. doi:10.1038/srep27450
20. Humphrey, B. J. *Restaurator* **1990,** *11,* 48–68. doi:10.1515/rest.1990.11.1.48
21. Halvorson, B. G.; Kerr, N. *Stud. Conserv.* **1994,** *39,* 45–56.
22. Dobroussina, S. A.; Rybalchenko, O. V.; Velikova, T. D.; Kochkin, V. F. *Mikol. Fitopatol.* **1996,** *30,* 87–95.
23. Reese, M. O.; Dameron, A. A.; Kempe, M. D. *Rev. Sci. Instrum.* **2011,** *82,* 085101. doi:10.1063/1.3606644
24. Tszydel, I.; Kucinska, M.; Marszalek, T.; Rybakiewicz, R.; Nosal, A.; Jung, J.; Gazicki-Lipman, M.; Pitsalidis, C.; Gravalidis, C.; Logothetidis, S.; Zagorska, M.; Ulanski, J. *Adv. Funct. Mater.* **2012,** *22,* 3840–3844. doi:10.1002/adfm.201200258
25. Nawrocki, R. A.; Matsuhisa, N.; Yokota, T.; Someya, T. *Adv. Electron. Mater.* **2016,** *2,* 1500452. doi:10.1002/aelm.201500452
26. Gazicki, M.; James, W. J.; Yasuda, H. K. *J. Polym. Sci., Polym. Lett. Ed.* **1985,** *23,* 639–645. doi:10.1002/pol.1985.130231207
27. Takeshi, Y.; Katsuhiko, F.; Hiroshi, N.; Tetsuo, T. *Jpn. J. Appl. Phys.* **2003,** *42,* 6614–6618. doi:10.1143/JJAP.42.6614
28. Frac, I.; Kucinska, M.; Gawrys, P.; Zagorska, M.; Maniukiewicz, W.; Nosal, A.; Ulanski, J.; Gazicki-Lipman, M. *Synth. Met.* **2016,** *220,* 194–201. doi:10.1016/j.synthmet.2016.05.025
29. Hsu, J. M.; Rieth, L.; Kammer, S.; Orthner, M.; Solzbacher, F. *Sens. Mater.* **2008,** *20,* 87–102.
30. Jakabovič, J.; Kováč, J.; Weis, M.; Haško, D.; Srnánek, R.; Valent, P.; Resel, R. *Microelectron. J.* **2009,** *40,* 595–597. doi:10.1016/j.mejo.2008.06.029
31. Mathur, M. S.; Weir, N. A. *J. Mol. Struct.* **1973,** *15,* 459–463. doi:10.1016/0022-2860(73)80016-X
32. Balss, K. M.; Llanos, G.; Papandreou, G.; Maryanoff, C. A. *J. Biomed. Mater. Res., Part A* **2008,** *85,* 258–270. doi:10.1002/jbm.a.31535
33. Kondo, M.; Uemura, T.; Matsumoto, T.; Araki, T.; Yoshimoto, S.; Sekitani, T. *Appl. Phys. Express* **2016,** *9,* 061602. doi:10.7567/APEX.9.061602
34. Marszalek, T. Właściwości elektryczne organicznych tranzystorów polowych otrzymanych metodą wylewania strefowego. Ph.D. Thesis, Lodz University of Technology, Lodz, Poland, 2012.
35. Reuveny, A.; Yokota, T.; Sekitani, T.; Someya, T. *Appl. Phys. Express* **2015,** *8,* 091601. doi:10.7567/APEX.8.091601
36. Ando, M.; Wakagi, M.; Onisawa, K. *J. Appl. Phys.* **2015,** *118,* 234505. doi:10.1063/1.4938014
37. Stassen, A. F.; de Boer, R. W. I.; Iosad, N. N.; Morpurgo, A. F. *Appl. Phys. Lett.* **2004,** *85,* 3899–3901. doi:10.1063/1.1812368
38. Sundar, V. C.; Zaumseil, J.; Podzorov, V.; Menard, E.; Willett, R. L.; Someya, T.; Gershenson, M. E.; Rogers, J. A. *Science* **2004,** *303,* 1644–1646. doi:10.1126/science.1094196
39. Aswal, D. K.; Lenfant, S.; Guerin, D.; Yakhmi, J. V.; Vuillaume, D. *Anal. Chim. Acta* **2006,** *568,* 84–108. doi:10.1016/j.aca.2005.10.027

40. Chua, L.-L.; Zaumseil, J.; Chang, J.-F.; Ou, E. C.-W.; Ho, P. K.-H.; Sirringhaus, H.; Friend, R. H. *Nature* **2005,** *434,* 194–199. doi:10.1038/nature03376
41. Cosseddu, P.; Lai, S.; Barbaro, M.; Bonfiglio, A. *Appl. Phys. Lett.* **2012,** *100,* 093305. doi:10.1063/1.3691181
42. Kang, G.-W.; Park, K.-M.; Song, J.-H.; Lee, C. H.; Hwang, D. H. *Curr. Appl. Phys.* **2005,** *5,* 297–301. doi:10.1016/j.cap.2004.02.012
43. Hwang, M.; Lee, H. S.; Jang, Y.; Cho, J. H.; Lee, S.; Kim, D. H.; Cho, K. *Macromol. Res.* **2009,** *17,* 436–440. doi:10.1007/BF03218886
44. Cheng, X.; Caironi, M.; Noh, Y.-Y.; Wang, J.; Newman, C.; Yan, H.; Facchetti, A.; Sirringhaus, H. *Chem. Mater.* **2010,** *22,* 1559–1566. doi:10.1021/cm902929b
45. Pfattner, R.; Mas-Torrent, M.; Bilotti, I.; Brillante, A.; Milita, S.; Liscio, F.; Biscarini, F.; Marszalek, T.; Ulanski, J.; Nosal, A.; Gazicki-Lipman, M.; Leufgen, M.; Schmidt, G.; Molenkamp, L. W.; Laukhin, V.; Veciana, J.; Rovira, C. *Adv. Mater.* **2010,** *22,* 4198–4203. doi:10.1002/adma.201001446
46. Werkmeister, F. X.; Noever, S. J.; Nickel, B. A. *Org. Electron.* **2015,** *26,* 439–442. doi:10.1016/j.orgel.2015.08.009
47. Li, M.; Marszalek, T.; Müllen, K.; Pisula, W. *ACS Appl. Mater. Interfaces* **2016,** *8,* 16200–16206. doi:10.1021/acsami.6b03233
48. Li, M.; An, C.; Marszalek, T.; Baumgarten, M.; Müllen, K.; Pisula, W. *Adv. Mater.* **2016,** *28,* 2245–2252. doi:10.1002/adma.201503552
49. Li, M.; Marszalek, T.; Zheng, Y.; Lieberwirth, I.; Müllen, K.; Pisula, W. *ACS Nano* **2016,** *10,* 4268–4273. doi:10.1021/acsnano.5b07742
50. Wünsche, J.; Tarabella, G.; Bertolazzi, S.; Bocoum, M.; Coppedé, N.; Barba, L.; Arrighetti, G.; Lutterotti, L.; Iannotta, S.; Cicoira, F.; Santato, C. *J. Mater. Chem. C* **2013,** *1,* 967–976. doi:10.1039/C2TC00337F
51. Alt, M.; Melzer, C.; Mathies, F.; Deing, K.; Hernandez-Sosa, G.; Lemmer, U. *Appl. Phys. A* **2016,** *122,* 204. doi:10.1007/s00339-016-9678-6
52. Bobbert, P. A.; Sharma, A.; Mathijssen, S. G. J.; Kemerink, M.; de Leeuw, D. M. *Adv. Mater.* **2012,** *24,* 1146–1158. doi:10.1002/adma.201104580
53. Ahmed, R.; Simbrunner, C.; Baig, M. A.; Sitter, H. *ACS Appl. Mater. Interfaces* **2015,** *7,* 22380–22384. doi:10.1021/acsami.5b06210
54. Ahmed, R.; Kadashchuk, A.; Simbrunner, C.; Schwabegger, G.; Baig, M. A.; Sitter, H. *ACS Appl. Mater. Interfaces* **2014,** *6,* 15148–15153. doi:10.1021/am5032192
55. Debucquoy, M.; Rockelé, M.; Genoe, J.; Gelinck, G. H.; Heremans, P. *Org. Electron.* **2009,** *10,* 1252–1258. doi:10.1016/j.orgel.2009.07.005
56. Usta, H.; Facchetti, A.; Marks, T. J. *Acc. Chem. Res.* **2011,** *44,* 501–510. doi:10.1021/ar200006r
57. Rybakiewicz, R.; Tszydel, I.; Zapala, J.; Skorka, L.; Wamil, D.; Djurado, D.; Pécaut, J.; Ulanski, J.; Zagorska, M.; Pron, A. *RSC Adv.* **2014,** *4,* 14089. doi:10.1039/C4RA00052H
58. Marszalek, T.; Kucinska, M.; Tszydel, I.; Gravalidis, C.; Kalfagiannis, N.; Logothetidis, S.; Yassar, A.; Miozzo, L.; Nosal, A.; Gazicki-Lipman, M.; Jung, J.; Ulanski, J. *Opt. Mater.* **2012,** *34,* 1660–1663. doi:10.1016/j.optmat.2012.03.008
59. Chen, T.-N.; Wuu, D.-S.; Wu, C.-C.; Chiang, C.-C.; Chen, Y.-P.; Horng, R.-H. *Plasma Processes Polym.* **2007,** *4,* 180–185. doi:10.1002/ppap.200600158
60. Jin-Woo, H.; Hee-Jin, K.; Jong-Hwan, K.; Dae-Shik, S. *Jpn. J. Appl. Phys.* **2006,** *45,* L827–L829. doi:10.1143/JJAP.45.L827
61. Hassler, C.; von Metzen, R. P.; Ruther, P.; Stieglitz, T. *J. Biomed. Mater. Res., Part B* **2010,** *93,* 266–274. doi:10.1002/jbm.b.31584
62. Sharma, A. K.; Yasuda, H. *J. Adhes.* **1982,** *13,* 201–214. doi:10.1080/00218468208073187
63. Yeh, Y.-S.; James, W. J.; Yasuda, H. *J. Polym. Sci., Part B: Polym. Phys.* **1990,** *28,* 545–568. doi:10.1002/polb.1990.090280409
64. von Metzen, R. P.; Stieglitz, T. *Biomed. Microdevices* **2013,** *15,* 727–735. doi:10.1007/s10544-013-9758-8
65. Salcman, M.; Bak, M. J. *Med. Biol. Eng.* **1976,** *14,* 42–50. doi:10.1007/BF02477088
66. Loeb, G. E.; Bak, M. J.; Salcman, M.; Schmidt, E. M. *IEEE Trans. Biomed. Eng.* **1977,** *BME–24,* 121–128. doi:10.1109/TBME.1977.326115
67. Tsukagoshi, K.; Yagi, I.; Shigeto, K.; Yanagisawa, K.; Tanabe, J.; Aoyagi, Y. *Appl. Phys. Lett.* **2005,** *87,* 183502. doi:10.1063/1.2120894
68. Czajkowski, J.; Fabritius, T.; Ulański, J.; Marszałek, T.; Gazicki-Lipman, M.; Nosal, A.; Śliż, R.; Alarousu, E.; Prykäri, T.; Myllylä, R.; Jabbour, G. *Appl. Phys. B* **2011,** *105,* 649–657. doi:10.1007/s00340-011-4699-5
69. Ahmed, R.; Simbrunner, C.; Schwabegger, G.; Baig, M. A.; Sitter, H. *Synth. Met.* **2014,** *188,* 136–139. doi:10.1016/j.synthmet.2013.12.007

License and Terms

BEILSTEIN JOURNAL OF NANOTECHNOLOGY

Surface functionalization of 3D-printed plastics via initiated chemical vapor deposition

Christine Cheng and Malancha Gupta*

Full Research Paper

Open Access

Address:
Mork Family Department of Chemical Engineering and Material Science, University of Southern California, 925 Bloom Walk, Los Angeles, California 90089, USA

Email:
Malancha Gupta* - malanchg@usc.edu

* Corresponding author

Keywords:
3D printing; chemical vapor deposition; coatings; functional polymers; surface modification

Beilstein J. Nanotechnol. **2017,** *8,* 1629–1636.
doi:10.3762/bjnano.8.162

Received: 02 March 2017
Accepted: 05 July 2017
Published: 08 August 2017

This article is part of the Thematic Series "Vapor-based polymers: from films to nanostructures".

Guest Editors: M. Koenig and J. Lahann

Abstract

3D printing is a useful fabrication technique because it offers design flexibility and rapid prototyping. The ability to functionalize the surfaces of 3D-printed objects allows the bulk properties, such as material strength or printability, to be chosen separately from surface properties, which is critical to expanding the breadth of 3D printing applications. In this work, we studied the ability of the initiated chemical vapor deposition (iCVD) process to coat 3D-printed shapes composed of poly(lactic acid) and acrylonitrile butadiene styrene. The thermally insulating properties of 3D-printed plastics pose a challenge to the iCVD process due to large thermal gradients along the structures during processing. In this study, processing parameters such as the substrate temperature and the filament temperature were systematically varied to understand how these parameters affect the uniformity of the coatings along the 3D-printed objects. The 3D-printed objects were coated with both hydrophobic and hydrophilic polymers. Contact angle goniometry and X-ray photoelectron spectroscopy were used to characterize the functionalized surfaces. Our results can enable the use of iCVD to functionalize 3D-printed materials for a range of applications such as tissue scaffolds and microfluidics.

Introduction

Three-dimensional printing (3DP) is a useful fabrication technique that offers rapid and low-cost prototyping, high levels of design complexity, and resolution on the micron scale [1,2]. These attractive features have led to applications of 3DP in diverse fields including tissue engineering [2,3], microfluidics [4], robotics [5], and batteries [6,7]. 3DP involves a computer-aided design of the target structure sliced into 2D layers and printed layer-by-layer [2,3]. Four methods of 3DP are most common. Fused deposition modeling (FDM) involves heating a feed filament past the melting point of the material and extruding it onto a platform, which moves progressively downwards as layers are printed [8,9]. Inkjet printing deposits droplets of ink onto a platform, with ink flow regulated by a piezoelectric actuator [10,11]. Selective laser sintering uses a

laser beam to heat a layer of powder above its melting point, fusing it to the previous layers, and then new powder is subsequently rolled over the printed object [12,13]. In stereolithography (SLA), a laser or UV beam selectively hardens layers of photocurable resin and then the object is covered with another layer of fresh resin [14,15].

Though the number of printable functional materials is burgeoning [1,16,17], tuning the materials properties within the constraints of printability is still a challenge. This limitation presents a problem for application-driven print objects, because consideration of material printability must supersede other functionalities, such as biocompatibility or responsiveness to stimuli. Thus, controlling post-printing surface properties is critical to expanding the breadth of 3DP applications, because it allows for tuning of bulk properties, such as cost-effectiveness or structural rigidity, independently of sophisticated surface functionalization. For example, in scaffolds for bone tissue engineering, angiogenesis is a major challenge, because printed scaffolds have hydrophobic surface properties and do not promote cellular differentiation [3,18]. Surface modification of printed scaffolds can allow for the tuning of surface functionalization to promote vascularization and tissue regeneration while maintaining control over the mechanical robustness of the bulk structure. Hong et al. demonstrated that simply dipping polycaprolactone/poly(lactic-*co*-glycolic acid) 3D scaffolds in mussel adhesive proteins promoted cellular adhesion, proliferation and differentiation, showing that a facile surface modification improved the viability of using 3D-printed scaffolds for tissue engineering applications [18]. In another example of surface functionalization, Wang et al. reported a method for modifying the surfaces of 3DP structures fabricated via SLA by using a UV-curable resin with an embedded alkyl bromide initiator from which atom transfer radical polymerization was initiated [19,20]. They demonstrated that complex 3D-printed structures could be coated with hydrophobic polymers and various metals. However, this coating technique is limited to photocurable resins into which the polymerization initiator has already been incorporated, which restricts surface modification to only SLA-printed objects and wastes unused initiator embedded within the bulk structure. The breadth of materials and feature sizes of 3D-printed objects presents a challenge to finding a universal method for surface functionalization.

Initiated chemical vapor deposition (iCVD) is a technique that can be used to deposit functional polymer coatings [21,22]. In the iCVD process, monomer and *tert*-butyl peroxide (TBPO) initiator are introduced in the vapor phase to a reactor chamber under vacuum, whereupon the initiator is thermally cleaved by a heated filament array. Monomer and initiator radicals adsorb to substrates on a cooled stage where polymerization occurs. The molecular weight increases with decreasing substrate temperature and typical molecular weights are in the range of 50,000 to 200,000 [23,24]. The iCVD process is solventless and therefore effects of surface tension are avoided, allowing for conformal coating on complex surfaces such as mictrotrenches [25] and nanopore membranes [26]. Since the rate of reaction in iCVD is limited by adsorption of monomer to the substrate, a lower substrate temperature results in a faster polymerization rate [24]. Thus, the thermally insulating properties of macro-scale 3D-printed plastics pose a challenge to the iCVD process. Although there have been previous reports of iCVD deposition onto thermally insulating substrates such as tissue wipes [27], glass [28], and poly(ethylene naphthalate) [29], these substrates were typically less than 1 mm in thickness and therefore the thermal gradients were modest. In contrast to these previous studies, our 3D-printed objects are over 5 mm in thickness and therefore the significant thermal gradients may impact the deposition process.

In this study, we printed the 3D objects using both poly(lactic acid) (PLA) and acrylonitrile butadiene styrene (ABS) in order to study the generality of the coating process for modifying the surfaces of different plastics. We investigated the deposition of poly(1*H*,1*H*,2*H*,2*H*-perfluorodecyl acrylate) (PPFDA) [23] and poly((2-hydroxyethyl methacrylate)-*co*-(ethylene glycol diacrylate)) (P(HEMA-*co*-EGDA)) [30] onto 3D objects of a variety of shapes and sizes to study the capabilities and limitations of the iCVD process. X-ray photoelectron spectroscopy (XPS) and contact angle goniometry were used to study the surface properties before and after coating.

Results and Discussion

A schematic of the iCVD deposition process onto 3D-printed substrates is shown in Figure 1. To systematically study the uniformity of the iCVD coatings, PPFDA was deposited onto 3D-printed PLA lattices of 7.5 mm in height. PPFDA was chosen as a model polymer because it is easily discernable from

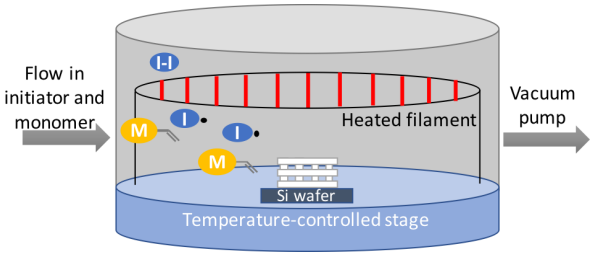

Figure 1: Schematic of the iCVD process. The 3D-printed substrate (white lattice) is placed on a silicon wafer piece on a temperature-controlled stage. Initiator (I–I) and monomer (M) in vapor phase are introduced into the reactor and the filament array is heated to thermally cleave the initiator.

the underlying substrate via XPS [23]. Additionally, the relatively high water contact angle on flat PPFDA (121°) [31] compared to that on flat PLA (72.5°) [32] allows for the use of contact angle goniometry to verify polymer deposition. Substrates were printed with PLA because of its ease of printing, low cost, and prior use in biomedical applications [33]. A silicon wafer piece was placed under the substrate to visually observe the penetration of polymer through the lattice.

To measure the change in hydrophobicity of the 7.5 mm PLA lattice after the deposition of PPFDA, contact angle changes were monitored (Figure 2a). Variations in contact angle measurements at the top and bottom of the pieces and among different pieces can be attributed to slight variations in geometry during the printing process. During deposition, the top side was closer to the heated filament array and the bottom side was placed on a silicon wafer piece on the stage. After coating, the contact angle changed from (110 ± 2)° to (122 ± 2)° at the top of the lattice and from (103 ± 2)° to (131 ± 8)° at the bottom, indicating that both the top and bottom of the lattice were coated with PPFDA. The contact angles are higher than that of flat PLA and flat PPFDA due to surface roughness [34]. Penetration of polymer through the lattice was also confirmed by deposition on the silicon wafer piece underneath the lattice. We used Fourier transform infrared spectroscopy (FTIR) (Figure 2b) to compare the spectra of the PPFDA film deposited on the silicon wafer (top) and the liquid monomer (bottom). The peaks at 1250, 1200, and 1150 cm^{-1} in the polymer confirm the presence of the CF_2 and CF_3 groups and the absence of signals from the vinyl bond in the polymer spectrum at 1640, 1620, 1410, 1400, 1300, 1080, 986, and 971 cm^{-1} indicates that all the vinyl bonds were completely reacted. Additionally, the presence of PPFDA at the top of the lattice was verified using X-ray photoelectron spectroscopy (XPS) to analyze the chemical composition of the surface (Figure 2c). The survey spectrum of the top of the PPFDA-coated lattice had atomic percentages of 51.2 atom % F, 6.2 atom % O, and 42.6 atom % C on a hydrogen-free basis, which agreed well with the theoretical composition of PPFDA (53.1 atom % F, 6.3 atom % O, 40.6 atom % C) rather than that of PLA (40 atom % O, 60 atom % C) indicating that there is at least 5 nm of PPFDA coating at the top of the lattice since XPS probes the top 5 nm of the surface. Scanning electron microscopy (SEM) images of the lattice (Figure 3) reveal that the appearance before modification (left) and after PPFDA coating (right) are similar since the thickness of the polymer coating is much smaller than the feature size.

The stage temperature can impact the thermal gradient during polymerization. The concentration of monomer at the surface of the substrate increases with decreasing temperature as previously shown by quartz crystal microbalance experiments by Lau and Gleason [24]. At a given stage temperature, we expect different temperatures at the top and bottom of the 3D-printed objects due to the heat from the filament array. To systematically study this effect, we studied depositions at stage temperatures of 15 °C, 35 °C and 45 °C (Table 1). For these stage temperatures, the temperature at the bottom of a 7.5 mm lattice was measured to be 31 °C, 43 °C and 48 °C, respectively, and the

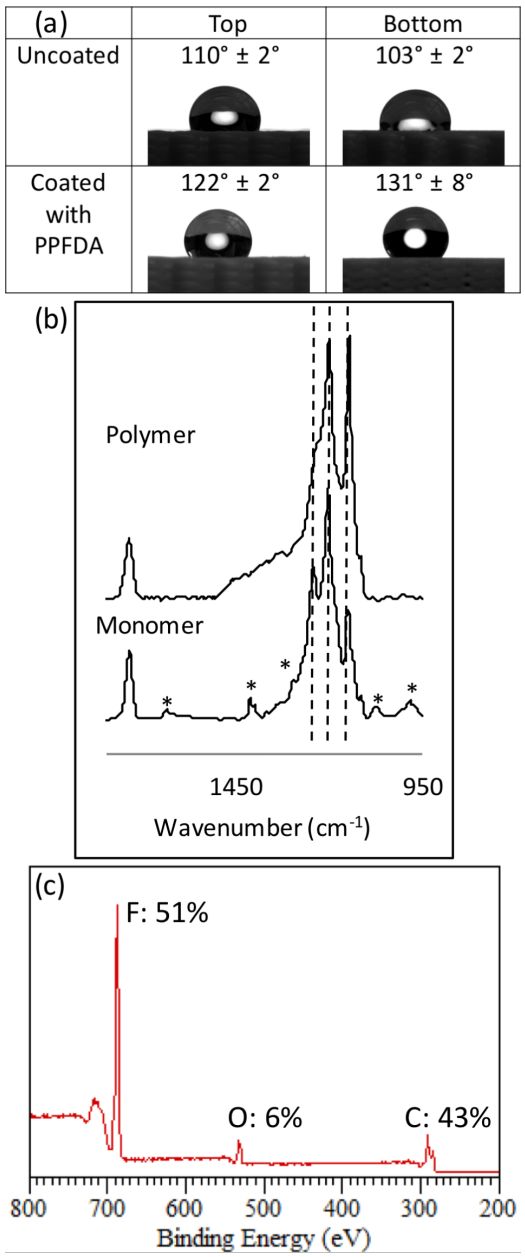

Figure 2: (a) Static contact angles for a 7.5 mm tall PLA lattice that was uncoated and coated with PPFDA. (b) FTIR spectra of the PPFDA film (top) and liquid monomer (bottom). Dashed lines correspond to the CF_2 and CF_3 signals, and the asterisks in the monomer spectrum correspond to the vinyl signals. (c) Representative XPS survey spectrum of the top of the lattice coated with PPFDA.

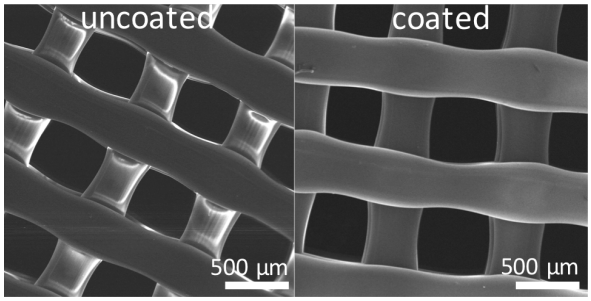

Figure 3: SEM images of the lattice before (left) and after (right) PPFDA coating.

temperature at the top of the lattice was measured to be 62 °C, 77 °C and 80 °C, respectively. These temperature differences of ca. 30 °C are due to the large height and thermally insulating properties of the PLA lattice. After PPFDA deposition at a stage temperature of 15 °C (sample S1), the contact angle of the lattice increased from (105 ± 2)° to (126 ± 5)° at the top and from (99 ± 8)° to (131 ± 4)° at the bottom. After PPFDA deposition at a stage temperature of 35 °C (sample S2), the contact angle at the top of the lattice increased from (109 ± 5)° to (127 ± 3)° at the top and from (104 ± 2)° to (139 ± 3)° at the bottom. After PPFDA deposition at a stage temperature of 45 °C (sample S3), the contact angle of the lattice increased from (111 ± 6)° to (125 ± 4)° at the top and from (105 ± 2)° to (133 ± 4)° at the bottom. These increases of the contact angle indicate that the lattices were coated at both the top and bottom at the three stage temperatures, despite the large temperature gradients. To further verify the presence of the PPFDA coatings, XPS was used to measure the atomic composition at the top and bottom of the lattices (Table 1). For the three stage temperatures, the atomic compositions of the bottom match well with the theoretical composition of PPFDA, again indicating that there is at least 5 nm of coating at the bottom of the lattice, however the top sides of S1 and S2 have slightly less fluorine indicating less coating.

Another challenge for iCVD deposition onto plastic materials is the potential for precursor molecules to absorb into the substrate. To verify that our XPS signals are due to polymer and not due to monomer, a PLA lattice was placed in the reactor and exposed to the same deposition conditions except without the presence of initiator. Polymerization does not occur because of the absence of the initiator, but the heated filament causes the same thermal gradients in the PLA lattice that were present during depositions. After monomer exposure, the contact angle changed from (106 ± 3)° to (119 ± 5)° at the top of the lattice and from (107 ± 4)° to (119 ± 4)° at the bottom of the lattice. This contact-angle increase indicates that some monomer was absorbed into the lattice. XPS of the sample (Table 1) shows the presence of a fluorine signal, which is absent in PLA, confirming the presence of monomer in the lattice. However, this fluorine signal is much less than that for the PPFDA polymer. Therefore, we can conclude that although there may be some monomer absorption during deposition, the large fluorine signals from the samples S1–S3 match the theoretical PPFDA values and therefore confirm the presence of a polymer coating of more than 5 nm.

Table 1: XPS survey spectra for PLA lattices.

sample	stage temperature (°C)	filament temperature (°C)	position	atom % F	atom % O	atom % C
reference PPFDA				53.1	6.3	40.6
S1	15	250	top	43.8	8.1	48.1
			bottom	49.6	6.6	43.8
S2	35	250	top	46.4	6.6	47.0
			bottom	51.1	6.2	42.7
S3	45	250	top	53.0	7.0	40.0
			bottom	51.6	6.2	42.2
F1	35	220	top	50.7	6.9	42.4
			bottom	50.1	6.5	43.4
F2	35	190	top	49.7	6.8	43.5
			bottom	53.9	6.3	39.8
H1	15	250	top	27.9	15.7	56.4
			bottom	52.9	6.4	40.7
H2	45	250	top	43.8	7.9	48.3
			bottom	53.3	6.5	40.2
absorption	45	250	top	19.0	15.3	65.7
			bottom	26.2	13.8	60.0

To decrease thermal gradients during the deposition of PPFDA onto the PLA lattices, the filament temperature can be reduced. We therefore investigated whether a uniform coating could still be achieved with lower filament temperatures. The filament temperature was lowered to 220 °C (sample F1) and the contact angles changed from (106 ± 5)° to (127 ± 3)° at the top of the lattice and from (102 ± 6)° to (140 ± 3)° at the bottom of the lattice. The filament temperature was further lowered to 190 °C (sample F2) and the contact angles changed from (106 ± 3)° to (128 ± 2)° at the top of the lattice and from (99 ± 6)° to (133 ± 5)° at the bottom of the lattice. At both filament temperatures, the top and bottom of the lattice exhibited increasing contact angles, indicating that the lattices could be coated at lower filament temperatures. Additionally, XPS of the lattices (Table 1) showed that the atomic composition agreed well with that of PPFDA, indicating that there is at least 5 nm of PPFDA at the top and bottom of both samples F1 and F2.

To further investigate the effects of thermal gradients, the lattice size was increased to 25 mm, which reaches to 6 mm below the filament array. For stage temperatures of 15 °C and 45 °C, the temperature at the top of the lattice was measured to be 97 °C and 103 °C, respectively. At a stage temperature of 15 °C (sample H1), the contact angle changed from (107 ± 5)° to (118 ± 4)° at the top of the lattice and from (103 ± 8)° to (125 ± 5)° at the bottom of the lattice. XPS of the sample (Table 1) showed that the atomic composition at the bottom agreed well with PPFDA, however, the composition at the top was similar to the signal found for monomer absorption, indicating that deposition did not occur. For a stage temperature of 45 °C (sample H2), the contact angle changed from (101 ± 3)° to (123 ± 2)° at the top of the lattice and from (93 ± 7)° to (134 ± 6)° at the bottom of the lattice. XPS of the sample (Table 1) showed that the bottom was coated, however, the decreased fluorine coating at the top demonstrated less coating. These samples indicate that the thermal gradients in very tall 3D objects can inhibit polymerization close to the filament. These thermal effects could be combatted by increasing the height of the filament array, optimizing substrate orientation, or lowering the substrate temperature.

To demonstrate the generality of the iCVD process for depositing different functional polymers onto 3D-printed substrates, 7.5 mm tall lattices were also coated with a hydrophilic, cross-linked polymer. PHEMA was chosen as the model hydrophilic polymer because it is biocompatible and has been used in biomedical applications [35,36]. However, because PHEMA is water soluble, the cross-linker EGDA was incorporated during the deposition to ensure that the hydrophilic polymer coating would not dissolve in water. As shown in Figure 4, an uncoated PLA lattice did not sink in water, despite PLA having a density

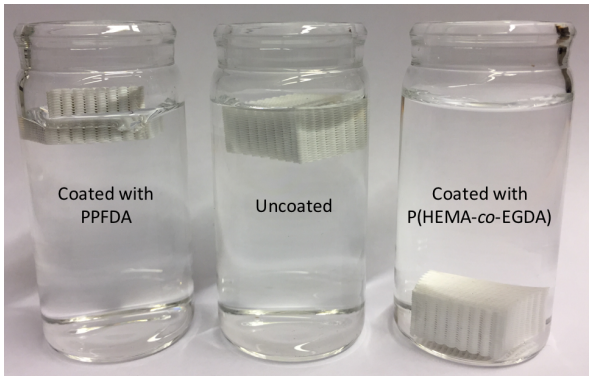

Figure 4: PLA lattices coated with PPFDA (left), uncoated (center), and coated with P(HEMA-*co*-EGDA) (right) in water.

of 1.25 g/cm^3. Since the uncoated PLA is hydrophobic, the pores of the lattice remained filled with air instead of wetting readily, which sufficiently reduced the overall density of the lattice causing it to float. Similarly, a lattice coated with PPFDA did not sink, because its enhanced hydrophobicity caused its pores to also remain filled with air. Unlike the hydrophobic lattices, the lattice coated with P(HEMA-*co*-EGDA) wicked water into its pores because of the hydrophilicity and the lattice sank in the water. To demonstrate the efficacy of the incorporated cross-linker for preventing dissolution of the polymer coating, the lattice coated with P(HEMA-*co*-EGDA) was soaked in water for three days and then was dried and placed back into the water, whereupon it sank, demonstrating the retention of its hydrophilicity.

To study the limitations of the iCVD process for coating macroscale plastics, P(HEMA-*co*-EGDA) was deposited onto a 25 mm tall lattice. In Figure 5, the bottom of the lattice was placed on the silicon wafer piece on the stage and the top of the lattice was nearest to the filament. From Figure 5, the bottom of

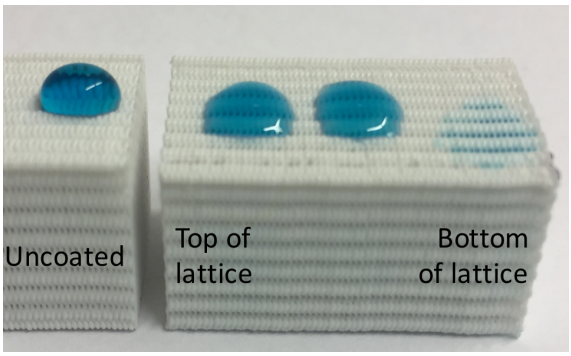

Figure 5: Water droplets (colored with blue food coloring) on an uncoated lattice and on a 25 mm tall PLA lattice coated with P(HEMA-*co*-EGDA).

the lattice exhibited hydrophilic properties verifying that it was coated with P(HEMA-*co*-EGDA). The middle and top of the lattice wicked water, but less readily than the bottom of the lattice, indicating partial polymer coverage. Comparison of the droplets on the coated lattice show that the coated lattice is more hydrophilic than the uncoated lattice.

A unique feature of the iCVD process is facile layering of polymer coatings with different chemistries, which allows for tuning of surface properties. To demonstrate this feature, substrates were coated with a hydrophilic copolymer followed by a hydrophobic polymer. Substrates were printed with ABS to demonstrate the generality of the substrate material. A comb, nut, and bolt were all coated in the same deposition to show that objects with complex features can be easily coated using the iCVD process (Figure 6a). The uncoated ABS substrate surfaces were hydrophobic (Figure 6b). The substrates were first coated with P(HEMA-*co*-EGDA), after which the comb, nut, and bolt all were readily wetted (Figure 6c). Following the coating with hydrophilic polymer, the substrates were then coated with PPFDA, and the substrate surfaces regain hydrophobicity (Figure 6d). These sequential depositions of polymers with different chemistries show that the substrate surface properties can be readily tuned using the iCVD process.

Conclusion

The iCVD process was used to modify the surfaces of 3D-printed polymer substrates with complex geometries. The lattices studied were 7.5 mm and 25 mm tall, which were significantly larger than insulating substrates that were coated in previous iCVD reports. Both hydrophobic (PPFDA) and hydrophilic (P(HEMA-*co*-EGDA)) polymer coatings were deposited onto substrates made of PLA and ABS. Thermal gradients over PLA lattices were studied and shown to decrease polymer coverage on 25 mm substrates, but these effects can be overcome by optimizing substrate orientation and lowering the substrate temperature. Additionally, the surface properties of the substrates can be tuned using sequential polymer depositions. This coating process can be generalized to modify the surface properties of a variety of 3D-printed materials for potential applications in tissue grafting, microfluidics, and electronics.

Experimental

1*H*,1*H*,2*H*,2*H*-Perfluorodecyl acrylate (PFDA) (SynQuest Laboratories, 97%), 2-hydroxyethyl methacrylate (HEMA) (Aldrich, 97%), ethylene glycol diacrylate (EGDA) (Polysciences, Inc.), and *tert*-butyl peroxide (TBPO) (Aldrich, 98%), were used as received without further purification. 3D-printed PLA lattices (Invention's Hub, Mission Hills, CA) were also used as received. The comb, nut, and bolt were printed on a MakerBot Replicator 2X using ABS filament in True Red.

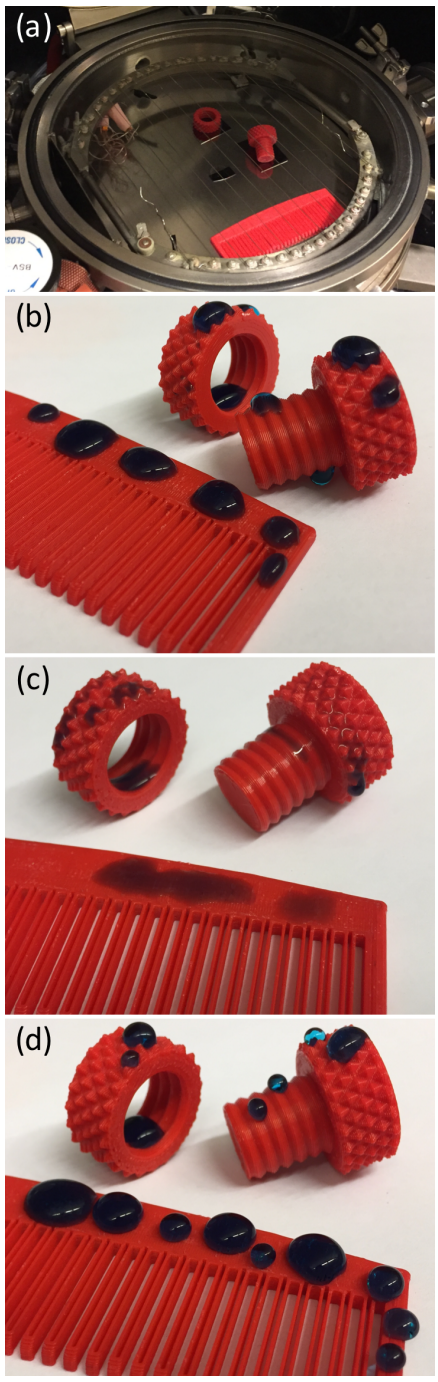

Figure 6: Sequential deposition of P(HEMA-*co*-EGDA) and PPFDA. (a) Nut, bolt, and comb in the iCVD reactor. Water droplets (colored with blue food coloring) on ABS substrates (b) without coating, (c) coated with P(HEMA-*co*-EGDA), and (d) coated with PPFDA.

Polymerization was carried out in a custom-built iCVD reactor (GVD Corporation, 250 mm diameter, 48 mm height). Substrates were placed on silicon wafer pieces (Wafer World, 100 mm) on a stage that was temperature-controlled by a backside recirculating chiller (Thermo Scientific NESLAB RTE 7). The orientation of the lattice during polymer deposition was

controlled for consistency. In FDM, the first layer is printed onto a heated, flat build plate which causes the bottom of the layer to be discernably flatter than subsequent extruded layers. This first printed layer was placed facing downwards during all iCVD depositions. Prior to polymer deposition, the stage was cooled to 14 °C for an hour to reduce the temperature of the substrates. Reactor pressure was achieved by a rotary vane vacuum pump (Edwards E2M40) controlled by a throttle valve (MKS 153D) and measured with an ambient temperature capacitance manometer (MKS 622C01TDE Baratron). Monomers were loaded into stainless steel jars and subsequently attached to the reactor chamber. To achieve appropriate monomer vapor pressure, PFDA was heated to 60 °C or 50 °C (for S1-S3, F1-F2, H1-H2), HEMA was heated to 50 °C, and EGDA was heated to 35 °C. TBPO was kept at room temperature of 25 °C and introduced into the reactor using a mass flow controller (MKS Type 1152C).

Immediately before polymer deposition, the stage temperature was raised to the appropriate temperature for deposition, which was 35 °C unless otherwise stated. During deposition, a nichrome filament (Omega Engineering, 80%/20% Ni/Cr) array held at 31 mm above the substrates was resistively heated to 250 °C, unless otherwise stated, to thermally cleave the peroxide bond of the initiator. The deposition rate was monitored in situ via interferometry on a reference silicon wafer using a He–Ne laser (Industrial Fiber Optics, 633 nm). For the samples S1–S3, F1–F2 and H1–H2, PFDA and TBPO were introduced into the reactor at flow rates of 0.26 sccm and 1.8 sccm, respectively. Reactor pressure was maintained at 50 mTorr, and deposition was carried out for 1 h. For the other depositions of the hydrophobic coating, PFDA and TBPO were introduced into the reactor at flow rates of 0.6 sccm and 1.0 sccm, respectively. Reactor pressure was maintained at 100 mTorr and deposition proceeded for 1 h. For the deposition of the cross-linked hydrophilic coating, HEMA was introduced at a flow rate of 1.0 sccm, EGDA was introduced at 0.14 sccm, and TBPO was introduced at 1.3 sccm. Reactor pressure was maintained at 130 mTorr and deposition was carried out for 1.5 h. To coat samples with multiple polymer layers, the substrates were removed from the reactor, rinsed with deionized water, and characterized between polymer layers.

Contact angles were measured on a goniometer (ramé-hart 290) with 10 μL droplets of deionized water. Five measurements were taken per sample and averaged and profile images were taken using the goniometer camera. Additionally, because the lattice structure consists of alternating, crosshatched layers, the structure has visible grooves depending on the viewing orientation. Therefore, to measure contact angles, the lattice was oriented such that the grooves were orthogonal to the goniometer camera. The chemical functionality of samples was studied using a Fourier transform infrared spectrometer (Thermo Scientific i510), with a resolution of 4 scans over a total of 32 scans. The surface composition of samples was studied using X-ray photoelectron spectrometer (Kratos Axis Ultra DLD) with a monochromatic Al Kα source. Survey spectra were taken from 0 to 800 eV in steps of 1 eV, averaged over five scans. Sample morphology was studied using a scanning electron microscope (Topcon Aquila), and samples were sputtered with a thin layer of silver (Cressington Sputter Coater 108) prior to imaging.

Acknowledgements

This work was supported by the National Science Foundation under Award No. 1332394. The authors thank June Park for her assistance.

References

1. Kalsoom, U.; Nesterenkoab, P. N.; Paull, B. *RSC Adv.* **2016,** *6,* 60355–60371. doi:10.1039/C6RA11334F
2. Guvendiren, M.; Molde, J.; Soares, R. M. D.; Kohn, J. *ACS Biomater. Sci. Eng.* **2016,** *2,* 1679–1693. doi:10.1021/acsbiomaterials.6b00121
3. Short, A. R.; Koralla, D.; Deshmukh, A.; Wissel, B.; Stocker, B.; Calhoun, M.; Deand, D.; Winter, J. O. *J. Mater. Chem. B* **2015,** *3,* 7818–7830. doi:10.1039/C5TB01043H
4. Bhattacharjee, N.; Urrios, A.; Kanga, S.; Folch, A. *Lab Chip* **2016,** *16,* 1720–1742. doi:10.1039/C6LC00163G
5. Rus, D.; Tolley, M. T. *Nature* **2015,** *521,* 467–475. doi:10.1038/nature14543
6. Sun, K.; Wei, T.-S.; Ahn, B. Y.; Seo, J. Y.; Dillion, S. J.; Lewis, J. A. *Adv. Mater.* **2013,** *25,* 4539–4543. doi:10.1002/adma.201301036
7. Fu, K.; Wang, Y.; Yan, C.; Yao, Y.; Chen, Y.; Dai, J.; Lacey, S.; Wang, Y.; Wan, J.; Li, T.; Wang, Z.; Xu, Y.; Hu, L. *Adv. Mater.* **2016,** *28,* 2587–2594. doi:10.1002/adma.201505391
8. Crump, S. S. Apparatus and method for creating three-dimensional objects. U.S. Patent US5121329, June 9, 1992.
9. Zein, I.; Hutmacher, D. W.; Tan, K. C.; Teoh, S. H. *Biomaterials* **2002,** *23,* 1169–1185. doi:10.1016/S0142-9612(01)00232-0
10. Menhennet, H. E.; Brown, R. B. Apparatus and method for making three-dimensional articles using bursts of droplets. U.S. Patent US5555176, Sept 10, 1996.
11. Derby, B. *Annu. Rev. Mater. Res.* **2010,** *40,* 395–414. doi:10.1146/annurev-matsci-070909-104502
12. Deckard, C. R. Method and apparatus for producing parts by selective sintering. U.S. Patent US4863538, Sept 5, 1989.
13. Beaman, J. J.; Deckard, C. R. Selective laser sintering with assisted powder handling. U.S. Patent US4938816, July 3, 1990.
14. Hull, C. W. Apparatus for production of three-dimensional objects by stereolithography. U.S. Patent US4575330, March 11, 1984.
15. Tumbleston, J. R.; Shirvanyants, D.; Ermoshkin, N.; Janusziewicz, R.; Johnson, A. R.; Kelly, D.; Chen, K.; Pinschmidt, R.; Rolland, J. P.; Ermoshkin, A.; Samulski, E. T.; DeSimone, J. M. *Science* **2015,** *347,* 1349–1352. doi:10.1126/science.aaa2397
16. Jungst, T.; Smolan, W.; Schacht, K.; Scheibel, T.; Groll, J. *Chem. Rev.* **2016,** *116,* 1496–1539. doi:10.1021/acs.chemrev.5b00303

17. Nadgorny, M.; Xiao, Z.; Chen, C.; Connal, L. A. *ACS Appl. Mater. Interfaces* **2016,** *8,* 28946–28954. doi:10.1021/acsami.6b07388
18. Hong, J. M.; Kim, B. J.; Shim, J.-H.; Kang, K. S.; Kim, K.-J.; Rhie, J. W.; Cha, H. J.; Cho, D.-W. *Acta Biomater.* **2012,** *8,* 2578–2586. doi:10.1016/j.actbio.2012.03.041
19. Wang, X.; Cai, X.; Guo, Q.; Zhang, T.; Kobe, B.; Yang, J. *Chem. Commun.* **2013,** *49,* 10064–10066. doi:10.1039/c3cc45817b
20. Wang, X.; Guo, Q.; Cai, X.; Zhou, S.; Kobe, B.; Yang, J. *ACS Appl. Mater. Interfaces* **2014,** *6,* 2583–2587. doi:10.1021/am4050822
21. Alf, M. E.; Asatekin, A.; Barr, M. C.; Baxamusa, S. H.; Chelawat, H.; Ozaydin-Ince, G.; Petruczok, C. D.; Sreenivasan, R.; Tenhaeff, W. E.; Trujillo, N. J.; Vaddiraju, S.; Xu, J.; Gleason, K. K. *Adv. Mater.* **2010,** *22,* 1993–2027. doi:10.1002/adma.200902765
22. Asatekin, A.; Barr, M. C.; Baxamusa, S. H.; Lau, K. K. S.; Tenhaef, W.; Xu, J.; Gleason, K. K. *Mater. Today* **2010,** *13,* 26–33. doi:10.1016/S1369-7021(10)70081-X
23. Gupta, M.; Gleason, K. K. *Langmuir* **2006,** *22,* 10047–10052. doi:10.1021/la061904m
24. Lau, K. K. S.; Gleason, K. K. *Macromolecules* **2006,** *39,* 3688–3694. doi:10.1021/ma0601619
25. Baxamusa, S. H.; Gleason, K. K. *Chem. Vap. Deposition* **2008,** *14,* 313–318. doi:10.1002/cvde.200806713
26. Asatekin, A.; Gleason, K. K. *Nano Lett.* **2011,** *11,* 677–686. doi:10.1021/nl103799d
27. Seidel, S.; Riche, C.; Gupta, M. Chemical Vapor Deposition of Polymer Films. *Encyclopedia of Polymer Science and Technology,* 4th ed.; Wiley: New York, NY, U.S.A.. doi:10.1002/0471440264.pst467
28. Bakker, R.; Verlaan, V.; van der Werf, C. H. M.; Rath, J. K.; Gleason, K. K.; Schropp, R. E. I. *Surf. Coat. Technol.* **2007,** *201,* 9422–9425. doi:10.1016/j.surfcoat.2007.03.058
29. Seong, H.; Choi, J.; Jang, B. C.; Kim, M.; Yoo, S.; Choi, S.-Y.; Im, S. G. *Adv. Electron. Mater.* **2016,** *2,* 1500385. doi:10.1002/aelm.201500385
30. Chan, K.; Gleason, K. K. *Langmuir* **2005,** *21,* 8930–8939. doi:10.1021/la051004q
31. Gupta, M.; Kapur, V.; Pinkerton, N. M.; Gleason, K. K. *Chem. Mater.* **2008,** *20,* 1646–1651. doi:10.1021/cm702810j
32. Jacobs, T.; Declercq, H.; De Geyter, N.; Cornelissen, R.; Dubruel, P.; Leys, C.; Beaurain, A.; Payen, E.; Morent, R. *J. Mater. Sci.: Mater. Med.* **2013,** *24,* 469–478. doi:10.1007/s10856-012-4807-z
33. Alves, C. M.; Yang, Y.; Marton, D.; Carnes, D. L.; Ong, J. L.; Sylvia, V. L.; Dean, D. D.; Reis, R. L.; Agrawal, C. M. *J. Biomed. Mater. Res., Part B* **2008,** *87B,* 59–66. doi:10.1002/jbm.b.31068
34. Feng, L.; Li, S.; Li, Y.; Li, H.; Zhang, L.; Zhai, J.; Song, Y.; Liu, B.; Jiang, L.; Zhu, D. *Adv. Mater.* **2002,** *14,* 1857–1860. doi:10.1002/adma.200290020
35. Khytoryanskaya, O. V.; Mayeva, Z. A.; Mun, G. A.; Khutoryanskiy, V. V. *Biomacromolecules* **2008,** *9,* 3353–3361. doi:10.1021/bm8006242
36. Lou, X.; Muro, S.; Wang, S. *Biomaterials* **2004,** *25,* 5071–5080. doi:10.1016/j.biomaterials.2004.01.058

License and Terms

BEILSTEIN JOURNAL OF NANOTECHNOLOGY

Bi-layer sandwich film for antibacterial catheters

Gerhard Franz*[1], Florian Schamberger[2], Hamideh Heidari Zare[1], Sara Felicitas Bröskamp[1] and Dieter Jocham[3]

Full Research Paper

Open Access

Address:
[1]Munich University of Applied Sciences, Munich, D-80335, Bavaria, Germany, [2]Plasma Parylene Systems, Pang, D-83026, Bavaria, Germany and [3]University Hospital of Schleswig Holstein at Lübeck, Lübeck, D-23538, Schleswig-Holstein, Germany

Email:
Gerhard Franz* - gerhard.franz@hm.edu

* Corresponding author

Keywords:
catheters; chemical vapor deposition; parylene; sandwich films

Beilstein J. Nanotechnol. **2017,** *8,* 1982–2001.
doi:10.3762/bjnano.8.199

Received: 28 February 2017
Accepted: 25 August 2017
Published: 22 September 2017

This article is part of the Thematic Series "Vapor-based polymers: from films to nanostructures".

Guest Editors: M. Koenig and J. Lahann

Abstract

Background: Approximately one quarter of all nosocomial infections can be attributed to the urinary tract. The infections are supposed to be mainly caused by implantations of urethral catheters and stents. A new catheter design is introduced with the aim to lower the high number of nosocomial urethral infections. In order to avoid limitations to use, the design is first applied to conventional commercially available balloon catheters.

Results: The main feature of the design is a sandwich layer on both sides of the catheter wall, which is composed of a fragmented base layer of silver capped by a thin film of poly(*p*-xylylene). This top layer is mainly designed to release a controlled amount of Ag^+ ions, which is bactericidal, but not toxic to humans. Simultaneously, the lifetime is prolonged to at least one year. The base layer is electrolessly deposited applying Tollens' reagens, the cap layer is deposited by using chemical vapor deposition.

Conclusion: The three main problems of this process, electroless deposition of a fragmented silver film on the surface of an electrically insulating organic polymer, irreproducible evaporation during heating of the precursor, and exponential decrease of the layer thickness along the capillary, have been solved trough the application of a simple electrochemical reaction and two standard principles of physics: Papin's pot and the principle of Le Chatelier.

Introduction

In 2014, nosocomial infections caused the death of more than 2000 patients in Swiss hospitals. About one quarter of the deaths were due to infections of the urethral tract. Applying this number to Germany with 10 times the size in population, these infections would have caused the death of approximately 5000 hospitalized patients. As the main reason for these infections, the urethral balloon catheters have been identified, which are implanted into the urethra to almost every sixth hospitalized patient, especially those who undergo a surgery [1]. According to Saint et al., catheter-associated urinary tract infection

(CAUTI) is the most frequent health care-associated infection in the USA [2].

In the year 2015, a total of 19.2 million patients were hospitalized in Germany, which meant a consumption of more than three million balloon catheters [3]. To this figure, about 350,000 ureteral stents, which are implanted in the ureters between kidneys and bladder to ensure the drainage of urine, have to be added for those patients with even worse illnesses involving also the kidneys. To emphasize the importance of this issue, the federal government of Germany has launched a program in 2015 that addresses some of these topics, including the conduct in intensive care units but also the development of new devices [4].

For the urethral system, huge efforts has been taken to fight these infections at the root. The most simple and most promising vehicles are antibacterial balloon catheters and ureteral stents. The antibacterial coating of these stents should not only prevent the ascend of bacteria into the renal pelvis, but also the formation of encrustations. Bacteria, especially *proteus mirabilis*, release urease, an enzyme that is capable to hydrolyze urea into ammonia, thereby enlarging the pH value. In turn, the formation of inorganic deposits (mainly hydroxyapatite, calcium oxalate and struvite) is promoted [5]. In ureteral stents with their maximum lumen of 1 mm, these deposits can completely block the drainage [6]. In both systems, the initial colonization of bacteria can be fought relatively easily. Once the invasion is permitted and the small islands have grown to a highly structured biofilm with a protecting polysaccharide, the prospects for an effective attack are severely diminished [7].

Because catheterization was a giant step towards a better mobility of patients, combined with a reduced need for care that saves time for the health care personnel, the strategy could only be an improvement of already existing catheters, which means a highly sophisticated wall material. In this course, two main strategies have been evolved: doping the viscous polymer, which will be subsequently formed to an infinite catheter (capillary) by extruding, with an active reagent or developing a coating of the interior and exterior side of the capillary. For the first alternative, it is imperative that the active species must not be coated by the organic polymer, so it remains free to act as antibacterial source.

The “Erlanger Silberkatheter” (silver catheter of Erlangen)

The “Erlanger Silberkatheter” was described by Guggenbichler et al. in the 1990’s [8,9]. Remembering that for more than 2000 years, the antibacterial impact of silver has been known, and that bacteria have developed antibiotic resistance against several antibiotics, but not against silver, he also emphasized that silver is also known for its oligodynamic impact, because it can interact with a bacterium in a versatile way. In 2003, however, it was communicated by Silver et al. that they had detected a bacterial resistance against silver by molecular genetics [10]. The impact is not predictable, because this was a single result of research.

Briefly, plates of organic polymers (polyurethane) were coated with evaporated silver films, hatched into small pieces and added to the highly viscous pastry that was subjected to the extruding process, yielding randomly distributed silver particles in the wall of the capillary (Figure 1). The charm of this technique is its simplicity which offers potential for a large production scale, and large numbers are demanded by the market.

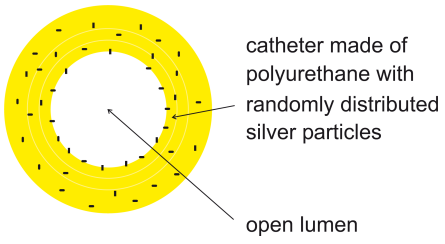

Figure 1: Cross section of Guggenbichler’s “Erlanger Silberkatheter”.

Although it was rapturously applauded by an interested public when it was introduced, it was withdrawn from the public after only a short time of use. Evidently, the clinical trials did not fulfil the promises that were fueled by electrochemical analyses around the Münstedt group [11,12]. The reason is still unclear [13].

Drug-release catheters

All other trials can be subsumed under drug-release catheters being at least bacteriostatic or even bactericidal. The first trials consisted of dipping catheters into a solution of an antibiotic drug (e.g., ciprofloxacin [14]) and subsequent drying of the solvent. Although, by this simple technique with its variant of impregnating the surface, the idea of drug-releasing devices could be realized, it was prone to generate local concentrations above a tolerable level for adjacent human cells. Since no protecting layer was deposited on top of these deposits, only short-term applications were possible. Therefore, the inorganic alternative silver was proposed again, but now as silver coating [7,15]. This deposit dissolves with a lower time constant, thereby reducing the toxic potential combined with longer lifetime. However, the catheters were coated only on their external skin, and again, no protecting layer was deposited. It should be mentioned that all these alternative tracks are based on conven-

tional catheters, which are modified in various ways and methods. Such a currently commercially available catheter is also our substrate (Figure 2).

Figure 2: Terminals of a typical balloon catheter. The pipe that connects the terminals has a typical length of 30 cm. After implantation, the blown-up balloon will stick in the urinal bladder (top).

Deficits and our answers

The above mentioned concepts do not address these deficits:

1. The exterior side of the catheter has intimate contact to the urethra along its whole length. Therefore, it is most likely that contamination with bacteria only happens during its implantation. Depositing an antibacterial layer only on the exterior side of the capillary neglects the fact that bacteria mainly ascend through the interior of the catheter.

2. Ag and its ions are well known as antibacterial reagent, but also to precipitate with Cl^- ions to AgCl. Since urine is a 0.1 M solution of sodium chloride, silver ions could never work in the intended manner.

3. Simple deposition techniques, such as impregnation and dipping, do not generate a film that steadily sticks on the substrate. Other methods, such as sputtering and evaporation of silver, only affect the exterior of the catheter.

4. In addition to its antibacterial potential, silver is also toxic.

5. The whole film may not deteriorate the qualities of conventional catheters, in particular, it must remain biocompatible with materials that are admitted by the FDA regulations.

Our answers to these challenges are:

1. We consider necessary a double-sided coating for optimum impact, irrespective of whether the catheter is utilized as urethral balloon catheter or as ureteral stent. Due to the high aspect ratio of the catheters (20 to 30 cm in length at with a small lumen of maximal 1 or 3 mm), the only technique to achieve a double-sided coating is chemical vapor deposition (CVD). A homogeneous film would mean co-deposition with at least two molecules, one to build up the film and one medical drug. To act as vapor, this drug has to be evaporated. None of the commonly used organic molecules (antibiotica, heparine, gendine [16-18]) is sufficiently stable to withstand this process. Only an inorganic reagent, i.e., silver or copper, could be used as metallorganic compound. Hence, a homogeneous coating is almost impossible, and the best solution would be a sandwich system of at least two sublayers.

2. Especially for urine, silver can be used as antibacterial reagent. Ag^+ ions are easily precipitated by Cl^- ions. The solubility product is 10^{-10} mol^2/L^2. Urine contains approximately 0.1 M of Cl^-. Silver and silver ions can only be used because urine also contains urease and urea, which generate ammonia, NH_3. Ammonia is responsible for a successful application of the antibacterial coating, because it forms the very stable complex $[Ag(NH_3)_2]^+$, which dissolves a possible precipitate of AgCl [19].

3. Among the various deposition techniques, chemical vapor deposition (CVD) is known for its outstanding conformal coatings, in particular on three-dimensional substrates. Because the substrates discussed here are unstable at high temperatures, no inorganic films can be deposited.

4. Silver is known to act as an effective oligodynamic antibacterial reagent with almost no deficiencies, in particular an ineffectiveness against several bacteria that have developed a resistance against this drug. However, its toxic behavior is also well known. Unfortunately, systematic investigations referring to toxicity and long-term exposition are rare. In 1996, the U.S. Environmental Protection Agency (EPA) published values for the long-term oral reference dose (RfD) [20,21]. These values are based on the assumption that certain illnesses, such as necrosis are triggered by silver ions, but only for concentrations beyond a certain threshold value. These values are explicitly denoted as “estimated” and are given with an uncertainty of approximately one order of magnitude (averaged for all human beings of mean age). For argyria, the RfD value was stated to 5 μg/kg/day, referring to a value that was communicated by Gaul and Staud in 1935 [22,23]. Later on, it evidently became more difficult to work on this topic.Argyria is mostly developed by persons who extensively incorporate colloidal silver [24]. Colloidal silver can be prepared by electrolytical or chemical reduction of a silver salt solution and consists of positively charged silver clusters exhibiting a diameter of typically

between 5 and 15 nm and, containing approx. 10^3 to 10^9 atoms/cluster. From the generation process, it is evident that the clusters mainly consist of atoms, the residual ions are responsible for keeping the clusters apart, thereby suppressing the aggregation to larger units. The ions fight the bacteria in a multifold manner and are evidently replenished from the cluster after having reacted. Finally, toxicity in the uriniferous system is different from oral ingestion or intravenous injections.

5. Among the thousands of possible organic materials, just a few remain fulfilling the requirements of biocompatibility and of the FDA regulations. For the CVD deposition we chose poly(*p*-xylylene) N, PPX-N or parylene N (N denotes an unsubstituted benzene ring, in contrast to, e.g., PPX-C, which denotes a benzene ring with one Cl atom). PPX, a material with teflon-like properties, has been certified as harmless by the FDA.

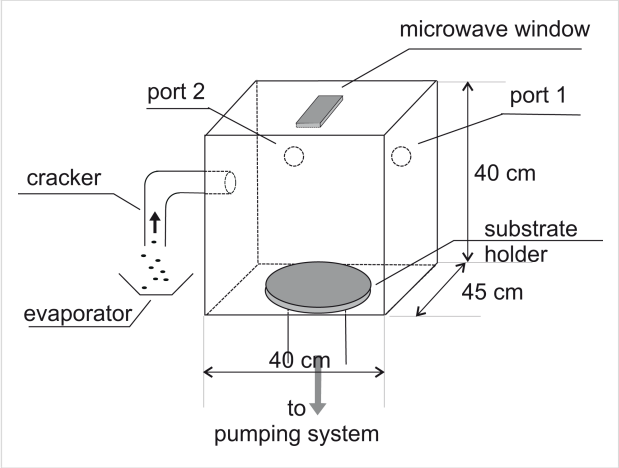

Figure 3: CVD reactor used to deposit PPX. The film-building monomers enter the reactor on the left-hand side and will be pumped out through the annular gap below the circular substrate holder at the bottom. Reprinted with permission from [26], copyright 2013 American Vacuum Society.

Poly(*p*-xylylene)

PPX is deposited by low-pressure chemical vapor deposition (CVD) in a vacuum apparatus. Chemical vapor deposition differs from physical vapor deposition by the fact that one or more substances are evaporated and undergo a chemical reaction during transport to a surface. The main advantage of CVD is conformal coating even on heavily rugged surfaces, which makes it the perfect candidate even for the interior deposition on narrow tubes.

Two types of reactors are in use, steady-state reactors and flow reactors. In the first type, a process is started by pressure reduction to a certain level by a vacuum pump. After that the pump is switched off, and the reaction is started [25]). In a flow reactor, the pump is acting during the whole process time, sometimes with reduced pumping power. It is evident that in the first case, the vacuum deteriorates by the presence of inevitable leaks during the process. Especially high-quality layers can be generated only in flow reactors (Figure 3).

Following Gorham, PPX is deposited by thermally cracking the precursor di(parylene N) (DPX) at 700 °C [27,28] (Figure 4). According to Figure 4, the radical polymerization reaction occurs at the two methylene groups in *para*-position of the benzene ring. This is one of the very rare reactions in organic chemistry with only one reaction route.

Design of the sandwich layer

In principle, two layer designs are possible: one homogeneous layer with immersed silver particles, or a sandwich system with at least two layers, one silver depot layer and one protecting top layer. Doping with silver would require copolymerization with a silver-organic compound that has to be decomposed simultaneously. However, silver-organic compounds that can easily be applied are commercially not available. Therefore, fabrication of a homogeneous antibacterial layer is not feasible, and a sandwich system must be developed, which consists of a depot layer of silver capped by a protective layer.

Silver layer: Depositing a metallic layer atop a material that is electrically isolating and an organic polymer that is classified as elastomer generates at least two interface problems: (1) How can a film of metallic silver be deposited electrolessly on a surface of an insulating material? and (2) How can the very differ-

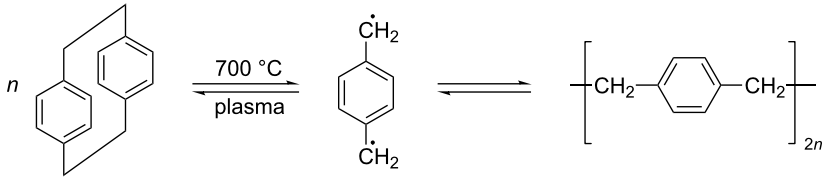

Figure 4: CVD process: The dimeric species di(*p*-xylylene) (DPX, left), which contains two ethyl bridges in each *para*-position, is cracked to form the *p*-xylylene diradical (PX, middle), which forms polymeric chains of poly(*p*-xylylene) (PPX, right) [27]. This reaction can occur either in the gas phase (volume polymerization) or on a cold surface (surface polymerization).

ent Young's moduli be adapted in such a way that bending and torsion, which are inevitable during the implantation process or during usage, do not cause exfoliation of the silver film? The bendability of the polymer is larger by orders of magnitude than that of the coating. Therefore, a special design has to be applied to avoid cracks and exfoliation (Figure 5).

Our designs are called "zebra stripe pattern" and "leopard skin". In both cases, only fractions of the total area are coated. Here, we describe the first design.

In the literature, two different coatings are discussed: metallic layers consisting of Ag^0, and layers containing ionic Ag^+ salts [10]. Coatings of silver halides are difficult to prepare, the most commonly applied process is impregnation, dipping into a solution or aqueous slurry of a silver salt [17,18,29]. The main issue is the low adhesion of these films. Therefore, the deposition of metallic silver has come to the fore. Because the substrate (organic polymer) is electrically insulating, the most common technique, electrolysis, is not applicable. Only an electroless deposition can lead to the intended pattern. We chose Tollens's reaction to deposit fragmented metallic silver layers, which is described elsewhere [30,31]. The recipe (concentration and reaction conditions) was adopted from the textbook "Organikum" [32]. Briefly, the redox reaction consists of the oxidation of monosaccharides or disaccharides, accompanied by a reduction of silver ions to elementary silver. The silver forms a fine grained, mirror-like deposit, provided the film-building Ag^+ can form complex ions, preventing the coagulation to large grains. To classify this method in terms of nanotechnology, it is a bottom-up technique. Layer growth from zero level passes through several stages until the single grains have built a coherent film. This process is visualized with scanning electron microscopy (SEM).

PPX layer: The cap layer must meet at least two requirements. First, it must protect the silver from unintended corrosion. Second, it must ensure a certain release rate of the reagent Ag^+, which is below the toxic level but sufficiently high to fight bacteria, germs and fungi successfully. The minimum inhibitory concentration (MIC) must be exceeded. For this purpose, the coating must be conformal. This means it needs to exhibit a certain constant porosity along the capillary, i.e., a certain and reliable thickness along the catheter, irrespective of whether the surface of the bottom layer is bent or parallel to the wall.

Since the exterior wall surface of the catheter is in intimate contact to the urethra, the antibacterial coating must be applied not only to the interior wall of the capillary but to the exterior wall as well. It is evident that fabrication of an even thickness along the interior wall of a closed-end pipe with an aspect ratio of up to 1:100 (diameter/length) is a challenging issue (Figure 6).

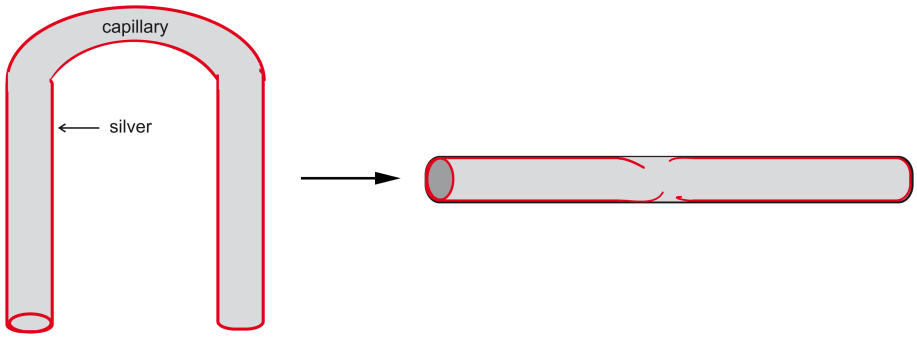

Figure 5: Bending and torsion of the capillary during implantation or usage lead to delamination of the silver-containing layer.

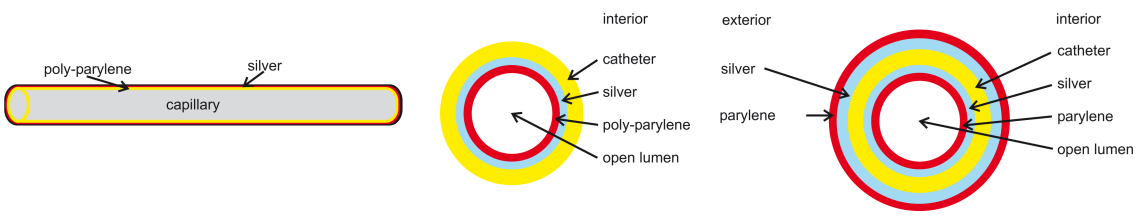

Figure 6: Left: The challenge of coating the interior wall of a closed-end capillary with an aspect ratio of up to 1:100 (diameter/length) with a sandwich system consisting of two layers with a thickness of significantly less than 1 µm (middle). Right: Cross section of the complete system, interior wall and surface of the capillary are coated.

The transport of the film-building species (cf. Equation 1) happens through diffusion (random walk), not through convection (flow). Even for molecules that do not form a deposit, a linear density gradient will form. But deposition of film-building molecules will reduce their density in the vapor, thereby decreasing the growth rate of the forming layer.

At first glance, coating of the exterior wall seems to be easier. However, coating with a layer-forming vapor also deliberately reduces the density of the chain-building species, which causes a reduction of the deposition rate from the vapor entrance (Figure 3, top left) to the pumping port (Figure 3, bottom, distance approx. 50 cm). Although between these points, there exists a gradient in density, the compensation does happen by diffusion, not by convective flow.

For an actual pumping speed of 2.7 L/sec and a gas flow of 5 sccm Ar (1 sccm equals 2.7×10^{19} molecules per minute under standard conditions STP (0 °C, 1 bar), which results in a pressure of 22 mTorr (3 Pa) in the reactor (V = 72 L), a residence time τ of 42 s can be calculated. Compared to the process of diffusion (mean free path λ ≈ 2 mm, cross section σ = 108 Å^2, diffusion coefficient D = 3750 cm^2/s with a thermal speed of 550 m/sec), the diffusion length Λ is calculated via the equation for the random walk $\Lambda = 2\sqrt{D\tau} = 796\,\text{cm}$. This means diffusion predominates convective flow, and the loss of monomers that will form a polymeric chain via Figure 4 has to be taken into account by setting up the equation of diffusion. Therefore, suspended catheters are expected to be inhomogeneously coated, at least after one shot.

During the deposition of layers within a polymeric tube of a small curvature with a closed end, several challenges have to be faced. First, the number density of the depositing molecules decreases exponentially with penetration depth not only by diffusion but also by deposition losses, which causes a steeply dropping layer thickness. The reaction can occur in the gas phase as well as during or after the process of condensation (physisorption). By diluting the evaporated dimer with argon, the first reaction is suppressed, and the polymeric growth happens only after the condensation of the monomeric species. Irrespective of the route followed, the concentration c is described through the diffusion equation reduced by a linear loss term L due to the deposition reaction (Equation 1 [33]):

$$\frac{\partial c}{\partial t} = D\Delta c - Lc, \tag{1}$$

where c scales with the partial pressure of the monomeric vapor. Equation 1 is solved by standard methods and is the sum of the two terms in Equation 2

$$\frac{c(x,t)}{c_0} = \frac{1}{2}\exp\left(-x\sqrt{\frac{L}{D}}\right)\operatorname{erfc}\left(\frac{x}{2\sqrt{Dt}} - \sqrt{Lt}\right) + \frac{1}{2}\exp\left(x\sqrt{\frac{L}{D}}\right)\operatorname{erfc}\left(\frac{x}{2\sqrt{Dt}} + \sqrt{Lt}\right), \tag{2}$$

with erfc being the complementary error function.

This issue is the prerequisite for the application of the "temperature seesaw". Condensation is an exothermic reaction. According to the principle of Le Chatelier, a (phase) equilibrium can be influenced by temperature and pressure. Here, rising the temperature favors the density of the energy-rich side, i.e., the vapor side. Hence, condensation and subsequent polymerization can be forced back or can even be suppressed by an increase of temperature, if the temperature is raised beyond the so-called ceiling temperature [34]. This is the basis for the construction of a temperature seesaw (Figure 7). It consists of a metallic rail with a semi-circular groove cut, which hosts the closed-end capillary. Above this configuration, several Peltier elements (up to five, shown here are two) with thermocouples are located through which a temperature gradient of ±30 °C can be obtained. This gradient is sufficient to counterbalance the density loss of monomeric diradicals along the capillary.

Another challenge is that the degree of porosity depends on the preparation conditions for the protecting layer, in particular of

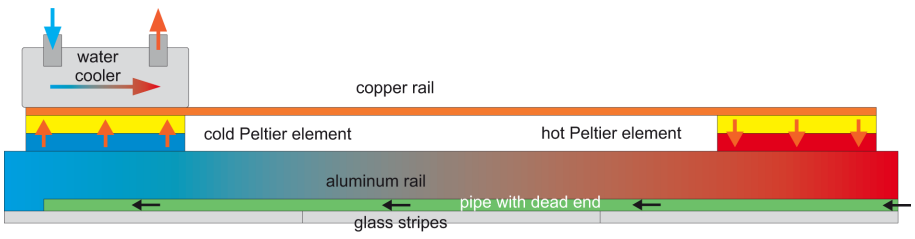

Figure 7: A "temperature seesaw" with several heating or cooling elements can equalize the density gradient that will develop as consequence of diffusion and simultaneous loss of diffusing molecules. Reprinted with permission from [35], copyright 2017 American Institute of Physics.

its thickness. The vague expression porosity must be brought into a quantitative relation to the thickness and to the release rate of Ag^+ ions.

Thickness ratio of the sandwich layers: After having determined the thickness of the cap layer, the thickness of the depot layer has to be fixed. This thickness is a trade-off between durability and adhesion of the sandwich system. It is evident that the adhesion of the silver layer is significantly improved if this layer does not consist of a continuous film on top of the substrate (polysilicone or polyurethane), but if small grains or stripes are encased by the organic polymer. This polymer is deposited directly on the substrate, and the adhesion between an organic substrate and the organic polymer is expected to be far better than the adhesion of silver atop polysilicone or polyurethane. Also, the thickness of the protecting porous layer determines the maximum of the depot layer. For a long durability, the thickness should be as high as possible. For a stable and reliable sandwich system, the thickness of both the layers should be similar (Figure 8).

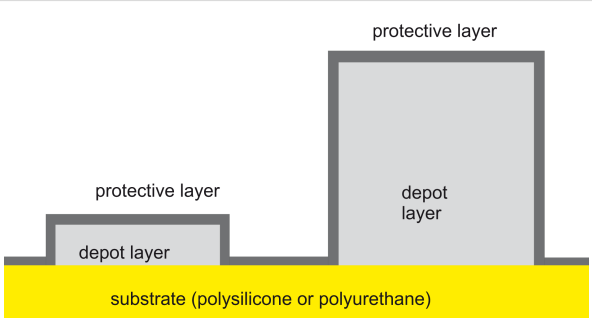

Figure 8: The thickness of the protecting cap layer with its retarding effect determines the thickness of the silver layer with its antibacterial impact. Since the adhesion of the organic polymer atop an organic substrate is far better than the adhesion of silver, the silver depot should consists of grains or stripes, which are encased by an evenly thick layer of PPX.

Summary: To coat a catheter with an antibacterial layer, several obstacles have to be overcome:

- the need for biocompatible coating material,
- an antibacterial agent that must be effective against several bacterial strains that have developed resistances against antibiotics,
- a tunable release rate of the agent,
- the deposition of layers with uniform thickness on both sides of the catheter, especially on the interior.

In this paper, the most important steps of the fabrication of urethral catheters with an antibacterial coating are addressed and described:

- the deposition of the silver film,
- the deposition of an organic polymer (PPX) by chemical vapor deposition (CVD),
- the deposition of the interior PPX film,
- and the characterization of the films, in particular the grain size of the silver clusters, the determination of thickness of the PPX film and its influence on the porosity,
- and the influence of the above properties on the release rate of antibacterial Ag^+ ions.

Experimental

Silver film

Deposition

The deposition of metallic silver is an electroless reaction in aqueous solution. Silver ions are reduced by a saccharide (glucose or maltose) at elevated temperatures, typically at 70 °C. Of paramount importance is the pre-treatment of the hydrophobic substrates (polyurethane and polysilicon), which can be carried out with an oxygen plasma, either by microwave generation (100 E TechnicsPlasma, Kirchheim, Germany), or by RF generation (PlasmaLab 80, Oxford Plasma Technology, Yatton, UK). Another method involves exposing the substrates (polysilicon) to diluted nitric acid (30%) for approximately 30 min. The latter procedure was preferred, mainly because the process could be controlled visually, and the reproducibility is far better. By this treatment, the nature of the surface is switched from hydrophobic to hydrophilic through the generation of carboxy and hydroxy groups at the surface [36].

The silver deposition itself was carried out by applying a pneumatic apparatus. The capillary was attached to a small peristaltic pump that draws a mixture of an Ag^+ solution ($AgNO_3$ dissolved in a surplus of aqueous ammonia (type TL, Medorex, Nörten-Hardenberg, Germany), to which a certain amount of a monosaccharide (glucose) or a disaccharide (maltose) is added (denoted as Tollens' reagent) and air (Figure 9), by which a chain of bubbles is generated, consisting of alternating packages of air and reagent (PD 5101, Heidolph Instruments GmbH &Co. KG, Schwabach, Germany). The volume ratio of these bubbles could be adjusted by a small Arduino controller and was visually inspected (Arduino Proto Sield REV3). The minimum length was the diameter of the capillary. The silver layers were deposited in a water bath (temperature between 70 and 85 °C, mainly at the former value).

Analysis

Because the roughness of the polymeric substrates does not allow for an exact measurement of the layer thickness and the growth rate as well as the assessment of the morphology, smooth substrates are required. We deposited a silver layer on

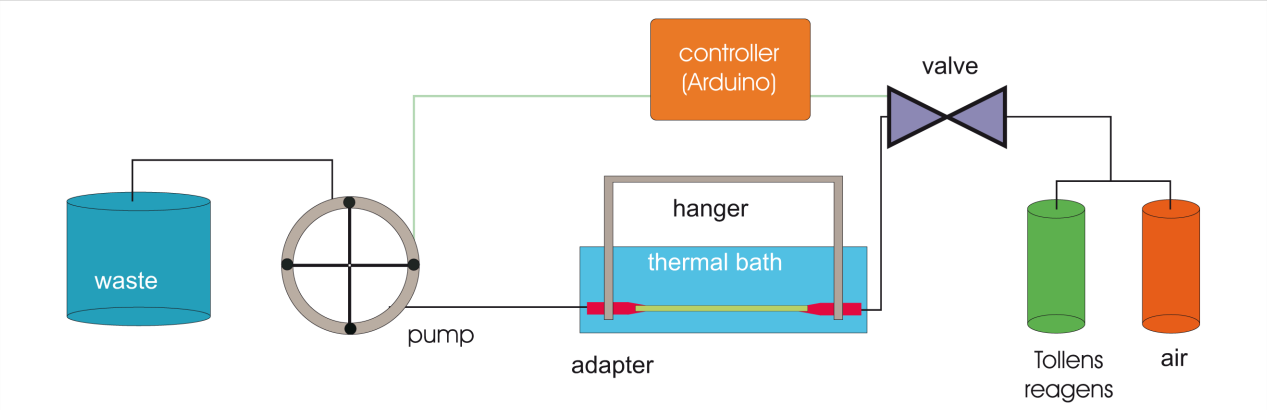

Figure 9: Apparatus for deposition of fragmented silver layers. Reprinted with permission from [19], copyright 2016 American Vacuum Society.

microscope glass slides. The layer thickness was measured with mechanical profilometry (α-step, KLA-Tencor, Milpitas, Calif., U.S.A.). The glass slides have the advantage that the exact silver volume of the deposited layers can be measured. For thick layers, the density of the precipitate can be calculated by measuring the different weights before and after deposition.

PPX layer

Deposition

The subsequent deposition of the porous cap layer consisting of PPX is performed with a slightly modified Gorham process [26,27]. In a CVD reactor (Plasma Parylene Systems, Rosenheim, Germany), the dimeric precursor is evaporated at temperatures between 130 and 140 °C and monomerized in the cracking zone at 700 °C (Figure 3). In contrast to a steady-state reactor, this vessel is continuously perfused by the polymer-generating vapor and additional doping gases. Vapor enters through a heated pipe and reacts either in the volume (gas-phase reaction) or on cold surfaces (solid-state reaction) to a polymer by chain-building.

To prevent evaporation during the heating ramp (approx. 45 min), which would cause an irreproducible layer thickness, a flow of argon generates a pressure of approximately 300 mTorr (mass flow controller 1179B, MKS GmbH, Munich, Germany). After having reached the evaporation temperature, the argon flow is suddenly lowered, and the deposition starts at a constant rate. At steady state, the entrance flow of the monomer is approximately 9 sccm. The monomer is highly diluted with argon (flows between 2 and 4 sccm), approaching epitaxial conditions, i.e., volume polymerization is suppressed to favor surface polymerization (Figure 10).

For a flow of 10 sccm argon, the pressure would rise to 156 mTorr, and the residence time in the reactor with $V = 72$ L would be 135 s. The velocity of flow in the cracking tube with a

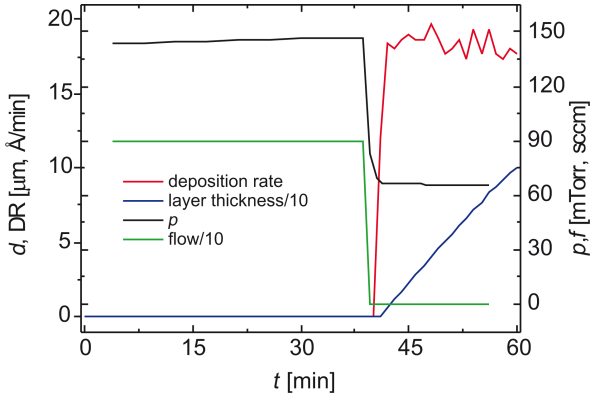

Figure 10: Deposition rate of PPX and counteracting argon pressure during the heating ramp [26,37]. Reprinted with permission from [26], copyright 2013 American Vacuum Society.

cross section of approximately 72 L is 10 cm/s, and the mean free path λ of nitrogen at this pressure would be 0.25 mm. The length l of the cracking zone is 30 cm, i.e., a ratio l/λ of 1200, which is expected more than sufficient for a complete cleavage of the dimeric precursor DPX. Diluting the organic vapor with an equal amount of inert gas doubles the flow velocity and halves λ.

Analysis

Thickness: The thickness of the film can easily be evaluated with a mechanic profilometer, but only on a plain hard substrate (glass). Its principle consists of creating an acute step in the film without hurting the substrate. This step is traced with a sharp needle of diamond as in a conventional cartridge of an old-fashioned turntable. Because of the softness of the catheters, no exact measurement is feasible. Therefore, only optical methods can be applied, either in transmission (absorption due to the law of Lambert and Beer) or in reflection (interferometric measurement). In both cases, the capillary has to be

sliced to get access to the layer. Because the thickness of the wall is large compared to the thickness of the deposited layer (1,500 µm vs 0.3 µm), this method is hardly applicable. But recording the broad-band reflectance of the capillary will lead to success. We applied the spectrometer F20e from Filmetrics (Unterhaching, Germany) using a light spot with a diameter d of 30 µm. For a radius r of the capillary of 1.5 mm, the substrate can be regarded plain ($r >> d$). The reflected light is diffracted by a diffraction grating and recorded by a photodiode array. By relating the recorded spectrum of the coated substrate to a previously recorded spectrum of the pure substrate, a background-corrected signal is accessible, which yields thickness and refractive index of the probed layer [35]. Statements of the film thickness refer to the mechanical measurement in the case of porosity and microbiological context, and the optical measurement is used for the homogeneous coating of the interior of the capillary.

Porosity: Porosity can be evaluated qualitatively and quantitatively. The qualitative approach comprises visual inspection and scanning of surface areas with atomic force microscopy (AFM). When automatic evaluation procedures are applied, the roughness of the surface can be quantitatively validated. Physical methods involve measurement of the impedance of an incompletely isolating layer on top of an electrode.

Applying AFM, the small areas of the surface can be scanned and evaluated regarding parameters like roughness and porosity. While the first parameter is the standard output of AFM and is displayed as 3D topographical map with mountains and valleys, porosity only regards those valleys that extend to the substrate (holes). To discriminate between valleys and holes, we applied the evaluation software GWYDDION [38], which extracts height profiles h_{profile} along a scanned line l_{scan}, for which we chose the largest possible measurement area (130 µm × 130 µm). We set the threshold for a hole to 90% of the total thickness measured with mechanical profilometry.

Physical inspection comprises measurements that make use of electric currents flowing through the pores and holes of an imperfect dielectric medium. This method is called electrical impedance spectroscopy (EIS) and is a widespread technique to evaluate the quality of coatings quantitatively. In contrast to the first method, larger areas can be easily tested, and a quantitative result is yielded, under the expense of spatial resolution. A simple electrochemical cell, which consists of two electrodes in an electrolyte with defined concentration and DC conductivity, is used as basis. One electrode, the device under test, is coated with a porous layer of a dielectric medium, here PPX, which would yield an infinite DC resistance for perfect coverage. Increasing the frequency of the voltage would only generate a displacement current. For a porous layer, however, ions are attracted by the potential and generate a conduction current. This additional current scales inversely with the square root of the applied frequency, because the ionic current depends on the distance the ions can travel during their attractive half period. Hence, the total resistance of this electrode is the sum of ohmic resistance of the PPX film, R_{f} and the frequency-dependent Warburg resistance, Z_{W}, because R_{f} is in series with Z_{W}. Parallel to this series resistance is the capacitance of the electrochemical double layer, C_{dl}. R_{Ω} is the ohmic resistance of the solution of the electrolyte (Figure 11).

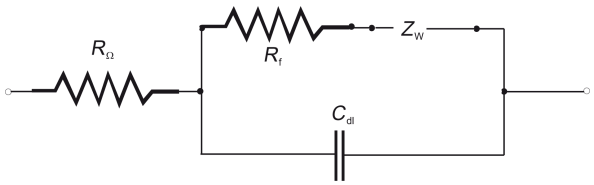

Figure 11: Equivalent circuit of the electrode covered by a porous membrane with capacitance C_{dl} and ohmic resistance R_{f} in series with the Warburg impedance Z_{W} in an aqueous electrolyte (R_{Ω}). Reprinted with permission from [39], copyright 2012 American Vacuum Society.

To measure the impedance of the system the electrodes are connected to a HP 4192A Impedance Analyzer, which measures the impedance Z and the phase angle φ between test voltage and resulting current. The HP 4192A Impedance Analyzer (Hewlett-Packard, Palo Alto, Calif., U.S.A.) is able to sweep the frequency from a fraction of a Hertz up to 12 MHz (Figure 12).

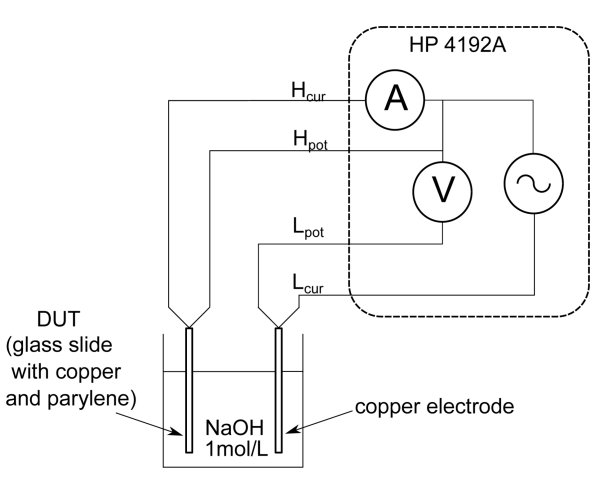

Figure 12: Experimental setup for electrochemical impedance spectroscopy: Between two copper electrodes in an aqueous solution of an electrolyte, here 1 mol/L NaOH, one coated with a porous layer (Device Under Test, DUT), a $I(V)$ measurement can be carried out, which yields the frequency-dependent impedance. To get a precise measurement, a four-probe device is required (H_{cur} and L_{cur} denote the current terminals, H_{pot} and L_{pot} the voltage terminals). Reprinted with permission from [39], copyright 2012 American Vacuum Society.

This measurement is the basis for the determination of the frequency-dependent capacitance, which is obtained with the same measurement setup as in Figure 12. The measurement frequency was 1 MHz to minimize the influence of the Warburg capacitance. As the dimensions of the glass slide are known (area, film thickness), the permittivity ε was calculated according to Equation 3:

$$C = \varepsilon_0 \cdot \varepsilon \cdot \frac{A}{d_{\text{coat}}}. \quad (3)$$

Sandwich layer silver + PPX

Analysis

To investigate the antibacterial impact, two data sets have to be compiled, the time-dependent release rate of Ag^+ ions, and its effect on bacteria. Several standard methods are in use to measure the released concentration of Ag^+ ions, always at the detection limit. Among the physical and chemical standard methods to detect traces are inductively coupled plasma optical emission spectroscopy (ICP-OES), cyclic voltammetry, and atomic absorption spectroscopy (AAS). The former two methods have been extensively used and are described in [19,40,41].

The biological methods are the determination of the zone of inhibition around a spot of the subjected material, and the measurement of the optical density as a function of the time, i.e., absorption spectroscopy at a fixed wavelength (mostly used OD_{600}). After having exposed a colony of bacteria with a certain starting density against solutions of Ag^+ of known concentration or against solutions with Ag^+ ions releasing catheters, the raising absorption is caused by exponential bacteria growth, which eventually becomes saturated. With this method, however, a decision is not possible whether the bacteria are already dead or still alive but have lost their ability for proliferation (the difference between bactericidic and bacteriostatic character). With the measured Ag^+ concentrations, the minimum inhibitory concentration (MIC) against certain bacteria in certain solvents is established. In this article, we focus on the latter method because it allows for quantitative conclusions.

The medium of choice is artificial urine because our catheter should be applied to the uriniferous system [41,42]. Although urine is mainly a solution of NaCl (approx. 0.1 M), no precipitation of AgCl occurs because urine always contains ammonia (which is the reaction product of urea and urease). Only by the complexing reaction of Ag^+ and NH_3 to $[Ag(NH_3)_2]^+$, the amount of free Ag^+ can be kept below the level that forces Ag^0 into its oxidic state Ag^+ even in an anaerobic environment (the oxygen content of fresh urine in the renal pelvis is still unknown because it was never studied [19]). Physiological sodium salt solution, for example, never passes the limit of the solubility product at concentrations that are typical for these drug-release systems.

Release rate: The coated substrates [two catheter pieces (outer diameter: 5.3 mm) with a length of 2 cm (13% of the length of a normal balloon catheter, inner diameter: 2.3 mm) and completely coated with silver] were subjected to equal amounts (2 mL) of artificial urine for defined exposure times in 50 mL tubes (37 °C, 120 rpm) in the incubator [43]. After 24 h of incubation, the catheters were placed in fresh artificial urine. After one week of additional incubation, catheters were placed again in fresh artificial urine for another three weeks. The silver concentration in all three samples was measured by ICP-OES using an ICP710-ES (Varian Medical Systems, Willich, Germany), which covers a range of typically more than five orders of magnitude [40]. This method has become standard for determining atomic concentrations in highly diluted solutions at the detection limit (5 µg/L = 50 nmol/L) [44]. Summing up all three values resulted in the total amount of silver released over a period of four weeks [45]. Additionally, voltammetry was used to measure the ionic concentration only [41].

Antibacterial impact (optical density): The sterile specimens were catheter pieces (outer diameter: 5.3 mm) or one catheter piece (outer diameter: 5.3 mm) of a length of 5 mm (inner diameter: 2.3 mm), completely coated with silver and coated with PPX layers of different thicknesses. The specimens were incubated in 1 mL of artificial urine for 24 h at 37 °C. After having removed the samples, 450 µL of the supernatant was transferred into a sterile 48-well plate and inoculated with 10^3 CFU/mL of *E. coli* or *S. cohni*. Bacterial growth was measured photometrically at a wavelength of 600 nm every 20 min for 21 h (TECAN Infinite M200 PRO Nano Quant, Tecan Trading AG, Männedorf, Switzerland) [41].

Results and Discussion

Silver film

Absolute prerequisite is the hydrophilization of the surface. Bi et al. have shown by X-ray photoelectronic spectroscopy (XPS) that O_2 treatment of PPX under similar exposure conditions causes the origin of two new peaks at 287.8 eV and 289.3 eV in the C *1s* spectrum, which they attributed to the carbon atoms in the free carbonyl group (C=O) and carbonate group (O_2C=O), respectively [36].

On smooth substrates, the growth can be evaluated without any distortion. In Figure 13, silver grains on thermoplastic polyurethane are depicted.

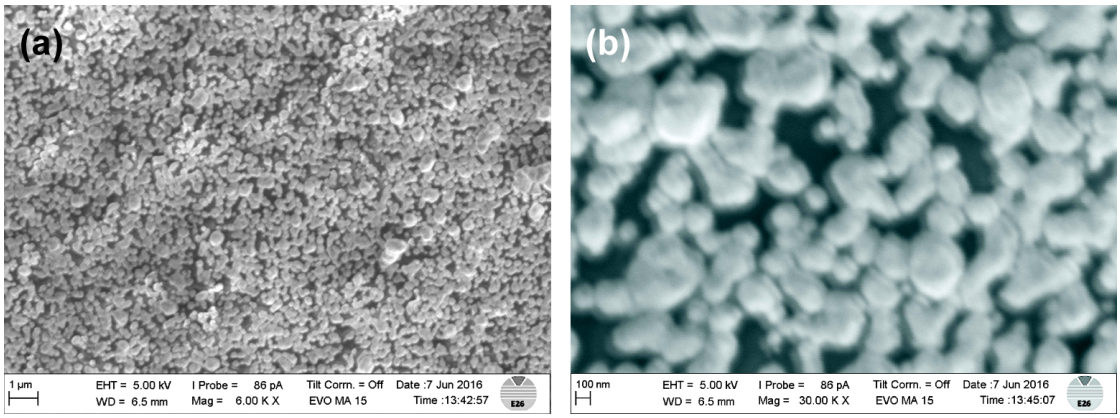

Figure 13: (a) The low-resolution SEM micrograph of silver on a surface of thermoplastic polyurethane (TPU) shows small adjacent grains of silver (5 min deposition time), saccharide: maltose. (b) The high-resolution SEM micrograph reveals a typical grain size between 50 and 200 nm.

The surface is covered with adjacent silver grains, which are composed of small clusters with a typical diameter between 50 and 200 nm. Under the same reaction conditions but with longer exposure times, capillaries made of polysilicone were treated by Tollens' reagens, and these thick layers have been subjected to SEM and EDX analysis (Figure 14). In Figure 14a, a cross section of an urethral catheter is displayed. Figure 14b shows the silver layer ($d \approx 4$ µm) on the interior wall, and in Figure 14c, an EDX scan of the Ag Lα line along the yellow line in Figure 14b is shown.

As is evident from Figure 8, the thicknesses of the two layers, the silvery depot film and the polymeric cap layer, must match to avoid poor adhesion of the silver layer. Also, silver is exposed to an aggressive liquid that could passivate the reagent, thereby reducing the impact of retarded controlled release of Ag^+ ions. An upper thickness limit of 500 nm is required to deliver an Ag^+ concentration into the urine that suppresses the density of bacteria below a certain level, the minimum inhibitory concentration (MIC). This has been topic of our recent research [19,41]. However, for these low thicknesses, the Tollens' reaction does not generate a continuous film on the rough surface of the catheters.

Morphology

In the following, we focus on these sub-micrometer layers on relatively rough surfaces. After a deposition time of 5–10 min, the resulting total silver layer on glass substrates exhibits a thickness between 200 and 500 nm. On polysilicone, however, incoherent spots of Ag are deposited, and the resulting grain size amounts to 50–200 nm (Figure 15). The grain size delicately depends on the pH value, on the type of sugar (monosaccharide or disaccharide), and to a lesser extent on the deposition time.

These micrographs justify these grains to be classified as nanoparticles [46-49]. Irrespective of how they have been generated, one of the main issues is their significantly enhanced surface, compared with thick coatings, although they have definitely passed the state of islands and have already coalesced [50]. This

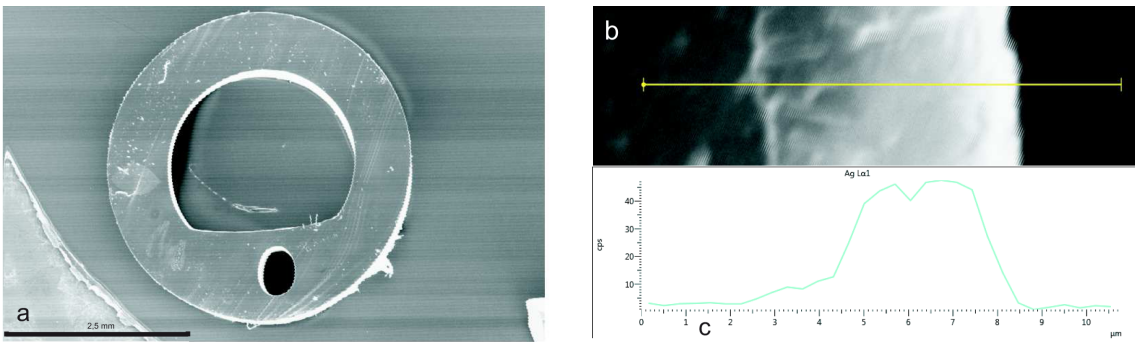

Figure 14: Silver layer deposited on the interior wall of a balloon catheter. (a) SEM micrograph of the cross section, (b) SEM micrograph of the silver layer, (c): EDX scan through the silver layer. Reprinted with permission from [19], copyright 2016 American Vacuum Society.

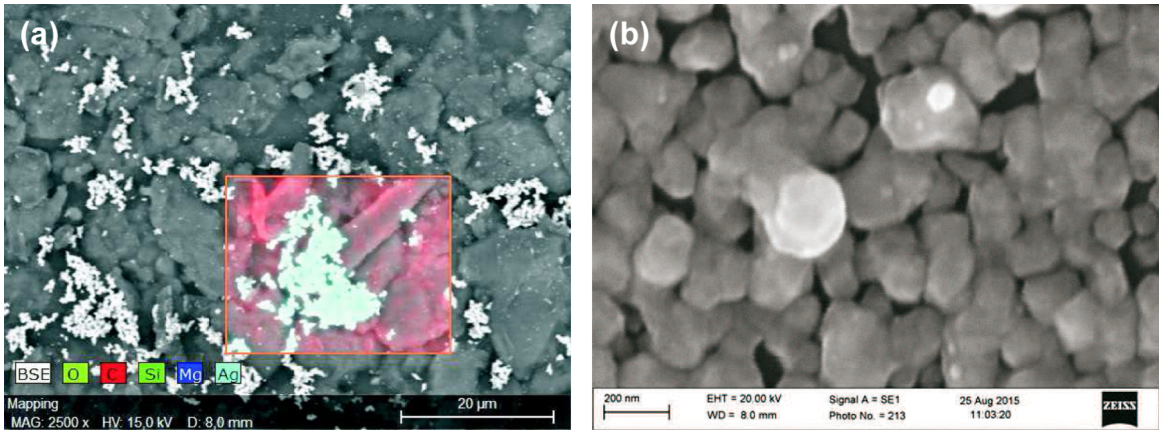

Figure 15: (a) The low-resolution SEM micrograph of silver on a rough polysilicone surface shows disconnected spots of silver (10 min deposition time, disaccharide: maltose). (b) The high-resolution SEM micrograph reveals a typical grain size of 50–200 nm. Reprinted with permission from [19], copyright 2016 American Vacuum Society.

larger surface area should increase the release rate and therefore the antibacterial activity.

PPX by CVD

Surface polymerization vs volume polymerization

The silver depot is capped by a layer, which acts in a threefold way: It should encase the silver grains completely and should touch the organic substrate. Only by meeting the first requirement, no direct access of the medium to the silver depot is ensured, which could cause uncontrolled solvation of Ag^+ ions. By fulfilling the second demand, the adhesion of the grains is improved. But the main purpose of the cap layer is the exact control of the release rate of Ag^+ ions. This is achieved by tuning the porosity of the cap layer as a function of the layer thickness.

Chemical vapor deposition differs from physical vapor deposition by the fact that one or more substances are evaporated and undergo a chemical reaction during transport to a surface. According to Figure 4, the radical polymerization reaction occurs at the two methylene groups in *para*-position of the benzene ring. The chain length can vary (molecular weights are typically in the 200000 to 400000 range [27,51,52]), and the reaction can occur in the vapor phase as well as during the process of condensation.

Therefore, the deposition must be steered into the direction of surface polymerization to avoid formation of larger clusters already in the vapor phase (volume polymerization). This problem was addressed for the first time by Yasuda et al. who diluted the chain-building vapor by an inert gas [53]. They found the expected reduced deposition rate. Additionally, they observed a vertical gradient from the vapor entrance to the pumping flange. According to them, the kinetic energy of the film-building species at substrate level had been reduced by collisions with the atoms of the inert gas [54].

The existence of these two competing processes in the volume and at the surface is a main issue in epitaxy, and the transition from simple chemical vapor deposition to advanced epitactic layer formation can be managed only by pushing back reactions in the vapor phase [55]. This can be easily achieved by dilution of the layer-forming gas(es) with an inert gas. In our case, the exact control of the porosity is mandatory and diluting the gases leads to high-quality, homogeneous layers with a high conformity, albeit at slow growth rates [39].

Growth rate as function of pressure

The reactor spatially separates the regions of activation (cleavage of dimers) and polymerization (oligomers or polymers in the vapor vs deposition as surface reaction). The growth rate, GR, depends on two parameters: the availability or density of monomers and on a steric factor. Two monomers are generated by the homogeneous fission of the dimeric precursor in the cracking unit. For the geometry of this reactor, a complete turnover to monomers is expected.

For the dependence on pressure, several experimental findings differ between an exponent of 1.5 [33] and 2 [56]. Models for the polymerization have been developed by Ganguli [33], Beach [57] and Fortin [58]. For a surface reaction, the diffusion of reactive species to an active site plays an important role. After the initial reaction of three monomers, which form a triple unit with two reactive centers, chain growth is proportional to the density of the monomers and the diffusivity of the monomer in the film. This leads to an exponent of only 3/2 for the

overall pressure dependence [33,57]. It is remarkable that in the small pressure interval covered, the experimental data can be fitted well by both approaches.

At low vapor densities, surface polymerization is favored, and if the pressure is raised volume polymerization will predominate. This behavior defines an upper limit of the operating pressure due to the onset of parasitic snow formation (approx. 100 mTorr) [33].

It should be noted that the reaction is not diffusion-controlled [59]. The rate at which the radicals strike the surface was estimated to exceed that at which a radical is effectively absorbed by the growing chain by approximately three orders of magnitude [57]. This low sticking coefficient is mandatory for the excellent conformal coating, and the rate-limiting step happens on the surface.

As our interest is focused on layers with a defined porosity, which can only be achieved by a low deposition rate, diluting the chain-building vapor with an inert gas is one possibility to enhance the film quality. This is analyzed by variation of the evaporation temperature of the dimeric precursor (following the Clausius–Clapeyron equation), and diluting the reactive gas with argon. In Figure 16, the deposition rate is given as function of the total pressure (Figure 16a: linear scale and Figure 16b: logarithmic scale) and as function of the percentage of the partial pressure of the monomer for two models. The equilibrium constant between monomer PX and dimer DPX (Figure 4) is given by Equation 4

$$K_{\text{diss}} = \frac{p_{\text{PX}}^2}{p_{\text{DPX}}}, \tag{4}$$

which is followed by the (intended) surface reaction PX→PPX. The equilibrium is written inverted (as in the derivation of the solubility product, Equation 5):

$$K'_{\text{p}} = \frac{p_{PX}}{p_{\text{PPX}}}. \tag{5}$$

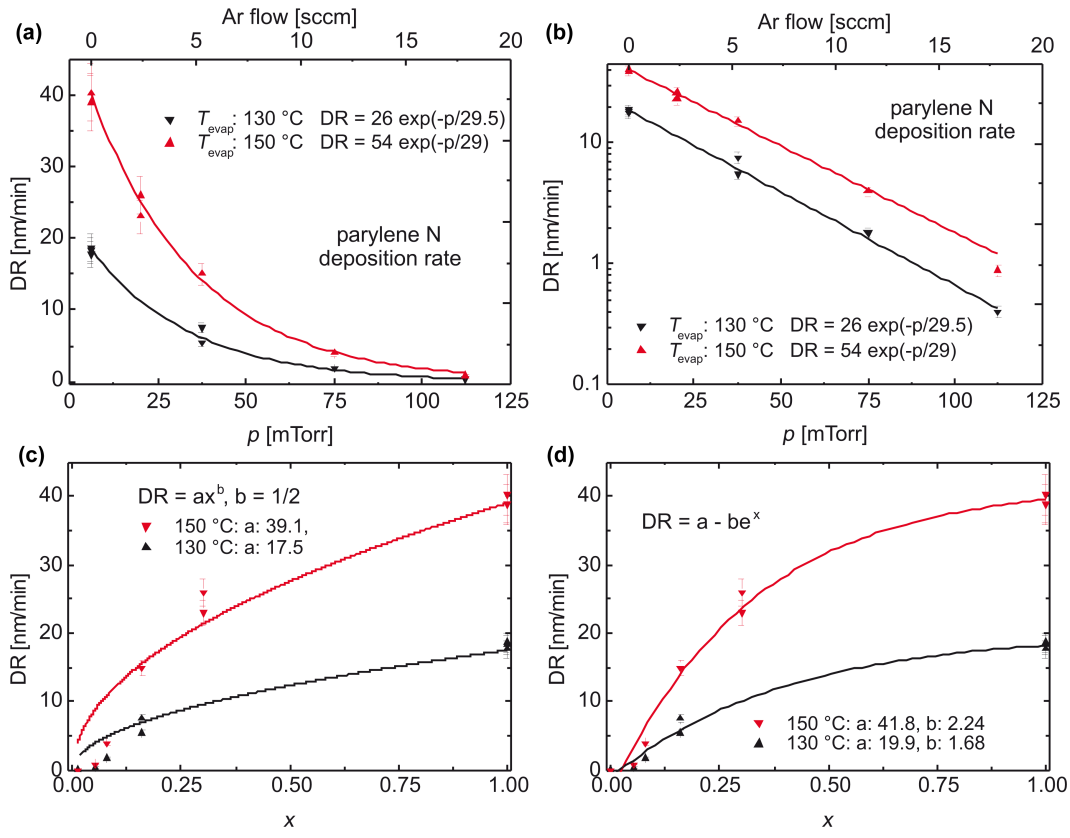

Figure 16: (a,b) Deposition rate of parylene-N as a function of the reactor pressure; (c,d) deposition rate of parylene-N as a function of the percentage of the partial pressure of parylene-N $p_p = f_{PX}/(f_{PX} + f_{Ar})$ for two models. By diluting the vapor with argon, the reaction is forced to surface polymerization (reaction of first order), best visible by the linear logarithmic slope [60]. In the model in panel c, the rate-limiting step is the condensation of the monomer; in the Beach model in panel (d) surface diffusion is the rate-limiting step.

Because PPX is a solid with an activity of 1, it is integrated into the equilibrium constant K_p yielding Equation 6, which expresses diffusion control

$$K_p = K'_p p_{PPX} = p_{PX}. \quad (6)$$

The condensation is followed by a chemical reaction (enlargement of the polymeric chain) with quantitative yield. Including Equation 4, this leads to the final Equation 7:

$$K_p = p_{PX} \vee \sqrt{K_{diss} p_{DPX}}. \quad (7)$$

This dependence is shown in Figure 16c. Figure 16d shows the model of Beach, which connects the terminating value for PPX, here denoted a, with an exponential term c^x and a pre-exponential factor b. b describes mainly the surface diffusivity, and e^x includes the order of the surface diffusion reaction with its diffusion coefficient [57]. Evidently the experimental data can be fitted with that model.

Morphology (grain size)

By diluting the chain-building vapor with argon, collisions between the monomers, which lead to unwanted reactions are reduced. These unwanted reactions lead to polymerization and grain formation in the gas phase. Eventually, these grains arrive at the surface, which is clearly revealed by SEM inspection (Figure 17a).

Properties of sub-micrometer layers

As our interest is focused on very thin high-quality layers, visual inspection via SEM is only one method, which has to be flanked by electrical methods. AFM micrographs are shown across an area of 130 µm × 130 µm in Figure 18. Again, increasing smoothness of the film with increasing dilution with argon is shown.

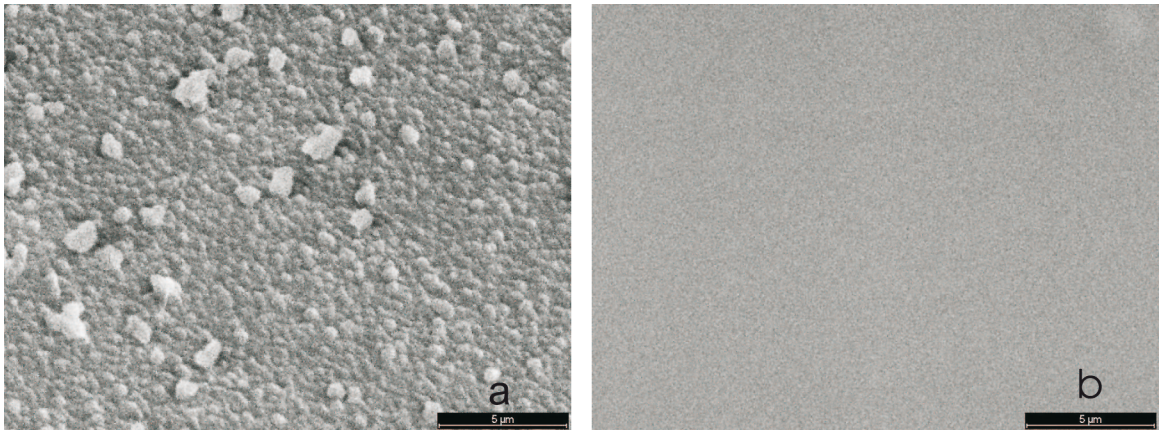

Figure 17: (a) Parylene N deposited in pure atmosphere of *p*-xylylene at a total pressure of 6 mTorr; (b) parylene N deposited in *p*-xylylene diluted with at a total pressure of 50 mTorr. At constant partial pressure of the monomer, the volume polymerization at low pressure is effectively suppressed. Reprinted from [60], copyright 2015 the authors.

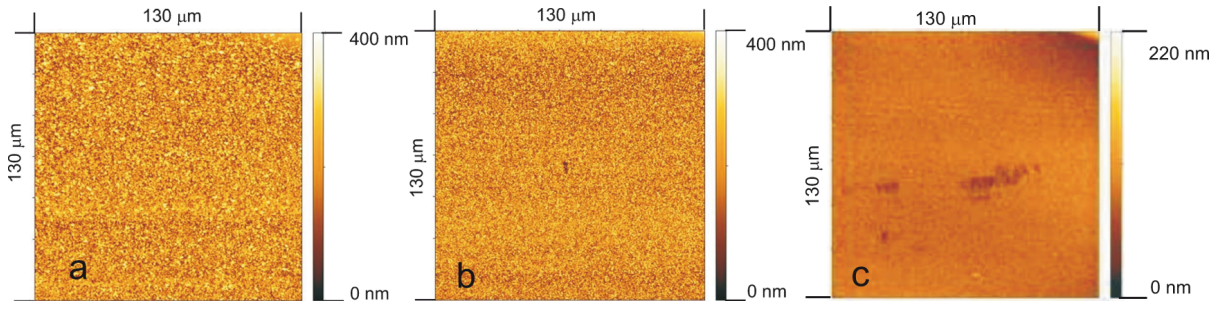

Figure 18: Surface morphology of parylene films deposited at various deposition pressures. Flow of the monomeric species was fixed to 9 sccm. Process pressure was established by adding argon to the ambient. (a) Without diluent, 6 mTorr (0.8 Pa), (b) 37.5 mTorr (5 Pa), (c) 75 mTorr (10 Pa). Reprinted from [60], copyright 2015 the authors.

Evaluating the AFM micrographs with GWYDDION reveals the imperative necessity to dilute the monomer by an inert gas (Figure 19). In pure monomeric vapor, the hole density increases steeply but almost uncontrollably.

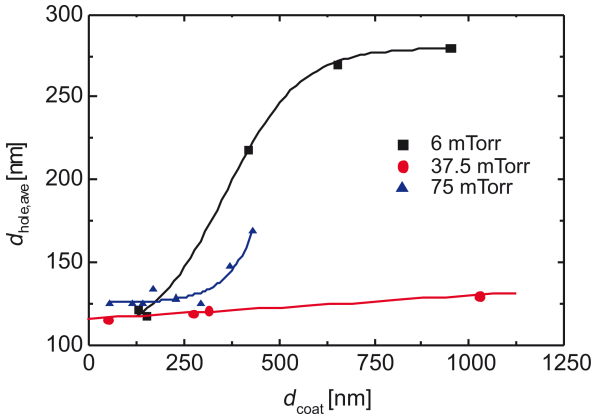

Figure 19: Averaged pin hole density of PPX-N at 90% scan depth of AFM [61].

The EIS measurement results are shown in a Nyquist diagram (Figure 20), where the device under test was a copper layer, which had been coated by PPX-N (1650 and 2240 nm).

According to the equivalent circuit in Figure 11, the intersection of the graph with the real axis close to the origin is related to the serial ohmic resistance R_Ω of the NaOH solution. The semi-circle trajectory, which approaches the shape of a straight line for lower measurement frequencies, is caused by the capacitance C_{dl} of the NaOH–PPX–Cu double layer. The slope of the straight line is caused by the so called Warburg Z_W impedance.

Without the influence of Z_W, the half-circle would intersect the abscissa for low frequencies at $R_f + R_\Omega$, since R_f represents the ohmic behavior of the coating. The local minimum at Re(Z) = 3250 Ω is caused by the measuring frequency of 100 Hz. Hence, all capacitance measurements of the PPX layer have to be carried out at freqencies significantly above 100 Hz to avoid confusing C_{dl} and Z_W. Because the silver ions were expected to move slowly in the porous membrane, the measurement cycle was repeated every 5 min.

Applying electrochemical impedance spectroscopy, the areal capacitance of layers of PPX-C is measured and ε is calculated with Equation 3. The striking increase below a thickness of 350 nm is caused by the increasing porosity. For thicker layers, ε reaches its limit of 3 (literature value at 1 MHz: 2.95 [62], Figure 21a). This value matches perfectly the low-frequency capacitance. In Figure 21b, the capacitance as function of frequency is shown in the low-frequency regime up to 100 kHz. The value starts at an almost constant bottom level of 3.1 at 100 kHz to rise to lower frequency values (literature value at 1 kHz: 3.10 [62]).

Deposition of layers with longitudinally uniform thickness

From Equation 1 and Equation 2, it has become evident that deposition on the interior of a long pipe is inevitably connected with a steep gradient in layer thickness. The simple approach of these equations does not take into account a steric factor: The probability of a radical to be caught at the terminal position of the polymeric chain is assumed to decrease strongly with the growing length of the chain. This leads to a complicated dependence, which was extensively discussed by Broer and Luijks, and Tolstopyatov et al. [63-65].

This steep thickness gradient is fought by the application of Le Chatelier's principle. The principal sketch of the temperature seesaw with two Peltier elements along the groove in which the pipe is embedded takes the exothermal principle of the con-

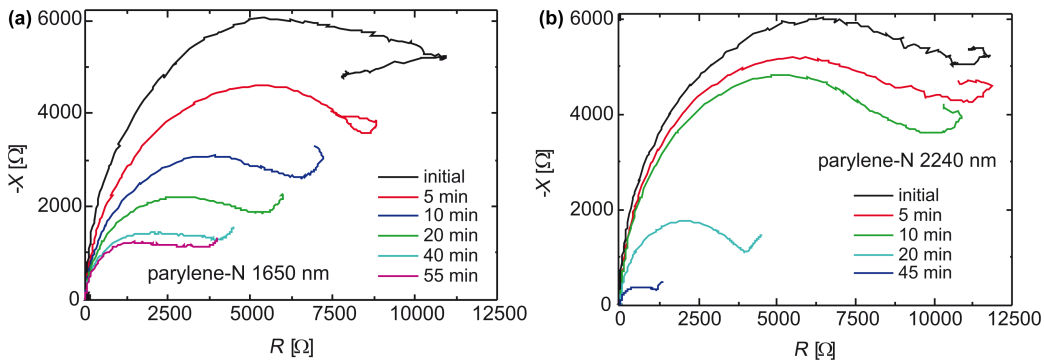

Figure 20: Nyquist diagrams of an metallic electrode covered by a porous membrane of PPX exhibiting a thickness of (a) 1650 nm and (b) 2240 nm. Imaginary part −X as a function of the real part R of the impedance. Reprinted with permission from [39], copyright 2012 American Vacuum Society.

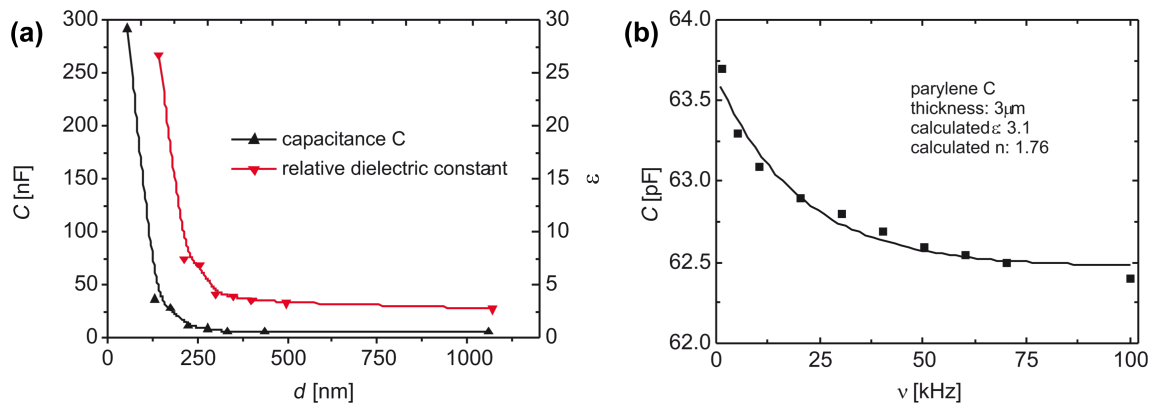

Figure 21: (a) Areal capacitance of CVD layers of PPX-C and resulting permittivity as function of thickness as measured with electrochemical impedance spectroscopy at 1 MHz. (b) Capacitance of CVD layers of PPX-C and resulting permittivity as function of frequency in the low-frequency regime. Reprinted with permission from [39], copyright 2012 American Vacuum Society.

densation reaction into account (cf. Figure 7). A higher temperature at the opening of the pipe prevents condensation and the subsequent polymerization. Hence, it should be possible to shift the maximum in deposition rate towards the center of the capillary by establishing an appropriate temperature gradient. In Figure 22, the deposition maximum is moved from the opening of the capillary 5 cm towards the inside.

Our construction of a temperature seesaw with five Peltier elements establishes a very effective temperature gradient, which eliminates the concentration gradient. Thus, the layer thickness is almost constant between opening and closed end of the capillary, at the cost of reduced deposition rate. This gradient is easy to apply at atmospheric pressure, but turns out to be difficult to control in vacuum. In Figure 23, a comparison is carried out of dependence of the layer thickness along a capillary without and with temperature balance.

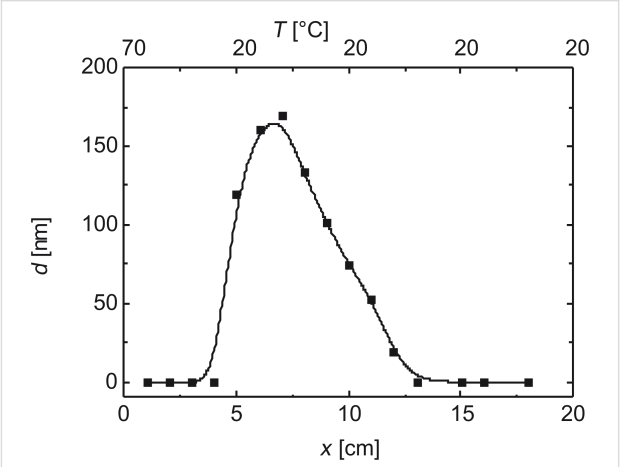

Figure 22: The maximum in deposition rate is moved to the center of the capillary by establishing an appropriate temperature gradient. The figures at the top denote the temperature of the Peltier elements.

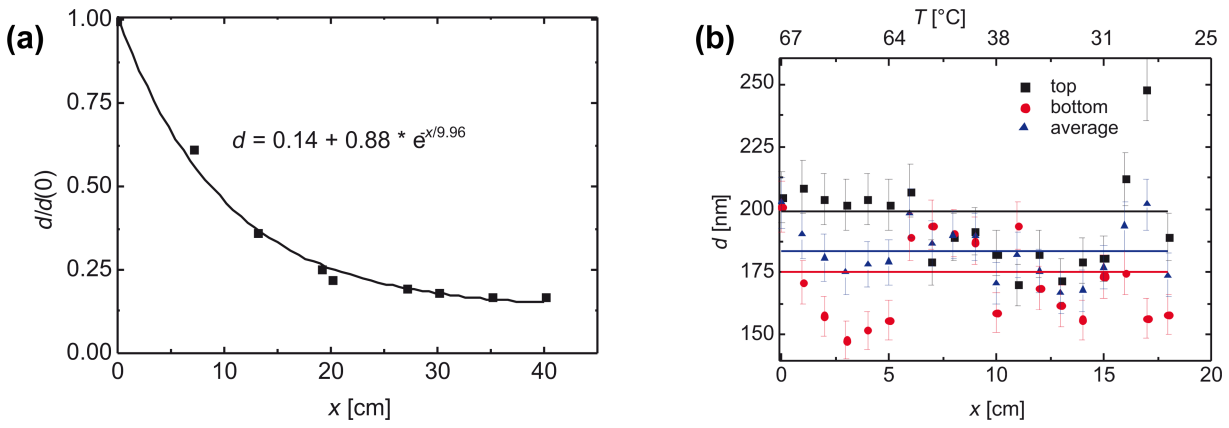

Figure 23: (a) Relative layer thickness (referred to the starting value at the mouth) as a function of the capillary length without a temperature gradient. (b) Layer thickness as a function of the capillary length after application of a counteracting temperature profile [66], error bars are ±5%. Reprinted with permission from [35], copyright 2017 American Institute of Physics.

Thin coatings as porous membranes

During a parallel work, the minimum inhibitory concentration of Ag^+ ions against the bacterium *E. coli*, which is responsible for approximately 80% of the nosocomial infections [1], was evaluated up to 30 µg/L in artificial urine measuring the optical density [19,41].

Although it is widely accepted that only Ag^+ ions are soluble in water and can pass through the channels of the porous cap layer, it might be possible that also very small clusters of metallic silver could succeed in moving through the barrier [67]. Whereas with ICP-OES, it is not possible to distinguish between Ag^0 and Ag^+, because both species are excited by an inductively coupled plasma, with voltammetry, only ions are detected.

In Figure 24, the silver release as measured by OES is depicted for an exposure of the sandwich layer against artificial urine for four different times: 24 h, 7 days, 14 days, and 21 days [68]. The release from the PPX layer is almost constant over time. Note that for this experiment, two pieces of a fully coated catheter were used. Their total length equaled only 13% of a complete balloon catheter (12”).

With these measurements, it could be shown that the desired thickness of the cap layer is between 150 and 300 nm [40], which, in turn, determines the upper limit for the thickness of the silver depot. In fact, the mean value of 50 µg/L or 0.45 µmol/L corresponds exactly to the results, which are possible in an environment that is determined by the presence of Cl^-, but also of urea and urease. Small amounts of Ag^+ ions are soluble in artificial urine as complexed $[Ag(NH_3)_2]^+$, and the value is always above the MIC of 30 µg/L. [19].

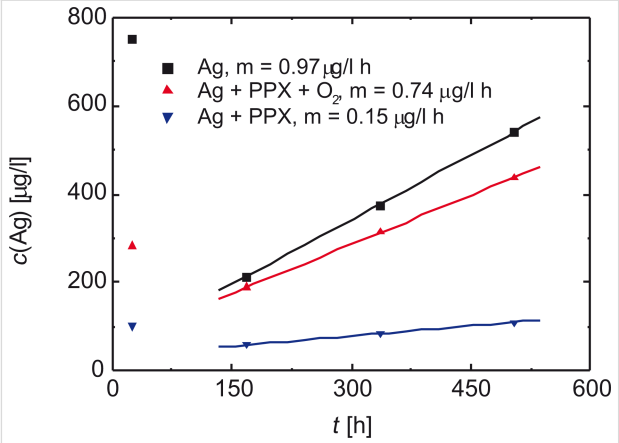

Figure 24: After 24 h, the released amount of Ag^+ ions from the PPX layer does not depend on time and is almost constant. Reprinted with permission from [19], copyright 2016 American Vacuum Society.

Antibacterial activity

Measuring the optical density is a preferred method to determine quantitatively the bactericidic power of a reagent as function of time. One can distinguish the lag phase at the begin of the treatment when the bacteria adopt to the new environment, which causes a very low division rate. It is followed by the exponential growth phase, leading to typical log values of 0.4–0.6. A further increase is suppressed by the increasing competition for nutrition, which leads to the plateau phase and eventually to a darkening of the medium. Although this effect is known to be caused by a large number of dead bacteria, a distinction between active cells and those who are either still alive but not capable to divide themselves or are already dead is impossible. In the case of successful antibacterial treatment, no increase in optical density is expected, and the antibacterial activity can be quantitatively evaluated (Figure 25).

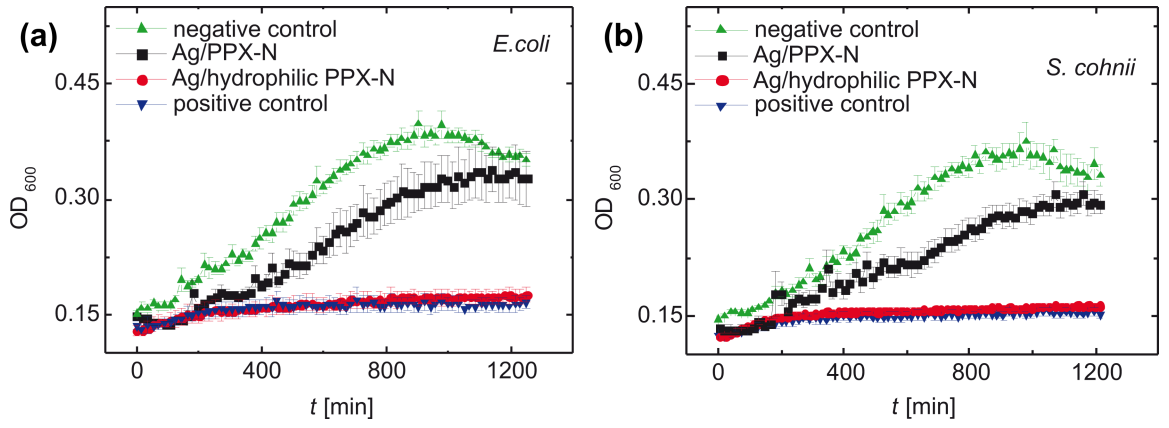

Figure 25: Growth of (a) *E. coli* and (b) *S. cohnii* in artificial urine, exposed to a defined catheter area with two different antibacterial sandwich layers. Positive control with untreated catheter and penicilline–streptomycine, negative control with untreated catheter. Optical density as a function of the exposure time. Urine was inoculated with 10^3 CFU/mL, $n = 6$, $p < 10^{-4}$ (ANOVA). Reprinted with permission from [41], copyright 2017 American Vacuum Society.

Conclusion

One of the most underestimated issues in clinical treatment is the ubiquitousness of aggressive bacteria that cause thousands of victims after a successful surgery. Urological inflammations are responsible for approximately one quarter of all nosocomial infections. These infections are most often attributed to the balloon catheter, which has been implanted to more than three million patients in Germany in 2015. Since many bacteria have developed a highly effective resistance against most antibiotics, other strategies are highly welcome, strategies that act on-site.

The construction and fabrication of a new antibacterial system, which belongs to the category of drug-release devices, has been described. Starting with commercially available catheters, its main feature is a layered sandwich coating, which is composed of a fragmented base layer of silver capped by a thin film of poly(*p*-xylylene). This top layer is designed to release a controlled current of Ag^+ ions. With this feature, it is possible to tune their concentration to a level, which is bacteriostatic, but well below the toxic level for humans.

For an effective protection, this sandwich layer has to be deposited on the interior and the exterior side of the capillary. Coatings out of the liquid phase are always possible, provided that the surface is sufficiently wetted, but most vacuum-based methods fail to coat the inner surface (sputtering, evaporation), only vapor phase deposition is an appropriate technique.

With these restrictions in mind, the recipe for this microsystem has been elaborated. The base layer has been deposited electrolessly applying Tollens' reagent, the cap layer has been coated using chemical vapor deposition. The three main problems of this process, which are electroless coating of a hydrophobic substrate with a silver layer with an aqueous solution of a silver salt, irreproducible evaporation during heating of the precursor, and exponential decrease of the layer thickness along the capillary, have been solved by application of three standard principles of chemistry and physics: electrochemical reactions applying simple redox equations, Papin's pot and the principle of Le Chatelier.

These sub-micrometer layers are permeable for Ag^+ ions and small Ag^0 clusters. The diffusion coefficient can be tuned by the thickness of this film. The sandwich system acts antimicrobially against conventional bacteria on-site and avoids the application of antibiotics by substituting them by oligodynamic silver.

This sandwich technique of a drug-releasing system has been realized with a device, which is a challenge for the coating technology due to its high aspect ratio. With the same approach, a perforated tube, e.g., a coronary stent, could be modified far more easily to become a "real" restenotic stent. The critical issue here is the roughening of a smooth surface to enhance its area for a higher load of an antistenotic drug. Increasing the aspect ratio, which is the case for urethral stents (1 mm open lumen at 150–200 mm in length), requires to overcome increased difficulties during coating. Such works are currently ongoing.

Acknowledgements

The SEM micrographs of Figure 14 were recorded by C. Eulenkamp. Valuable work was done by our students A. Edlfurtner, Ph. Frischauf, D. Graupner, M. Haertling, M. Hintereder, Th. Huber, J. Klamt, M. Klimt, A. Kutschera, V. Loidl, I. Lukashov, M. Madfai, J. Malais, D. Malisch, A. Möhlmann, M. Ott, F. Pavic, D. Redka, S. Seyedi, S. Steiner, M. Trowbridge, S. Wiedemann, and A. Ziegler. The microbiological investigations were carried out at "Deutsches Herzzentrum München" (DHM) and at the "Institut für medizinische Mikrobiologie, Immunologie und Hygiene" of the hospital "Rechts der Isar" (RdI), both in Munich and both run by Technische Universität München. We thank A. Kastrati and A. Dietrich (DHM) and M. Gerhard and H. Meyer ("Institut für medizinische Mikrobiologie, Immunologie und Hygiene") for their altruistic support. The experimental setups were fabricated by W. Preisser and A. Hadzimujic. We would like to thank our colleagues H. Huber, St. Kleemann, U. Koch, Chr. Schindler, E. Steinhauser, St. Sudhop, and K. Trebesius. Without their support, this work would have been impossible.

References

1. Vincent, J.-L. *Lancet* **2003,** *361,* 2068–2077. doi:10.1016/S0140-6736(03)13644-6
2. Saint, S.; Meddings, J. A.; Calfee, D.; Kowalski, C. P.; Krein, S. L. *Ann. Intern. Med.* **2009,** *150,* 877–884. doi:10.7326/0003-4819-150-12-200906160-00013
3. Pressemitteilungen - 19,2 Millionen Patienten 2015 stationär im Krankenhaus behandelt - Statistisches Bundesamt (Destatis). https://www.destatis.de/DE/PresseService/Presse/Pressemitteilungen/2016/08/PD16_283_231.html (accessed Aug 24, 2017).
4. 10-Punkte-Plan zur Vermeidung behandlungsassoziierter Infektionen und Antibiotika-Resistenzen. https://www.bundesgesundheitsministerium.de/ministerium/meldungen/2015/10-punkte-plan-zu-antibiotika-resistenzen.html (accessed Aug 24, 2017).
5. Morris, N. S.; Stickler, D. J.; McLean, R. J. C. *World J. Urol.* **1999,** *17,* 345–350. doi:10.1007/s003450050159
6. Tenke, P.; Köves, B.; Nagy, K.; Hultgren, S. J.; Mendling, W.; Wullt, B.; Grabe, M.; Wagenlehner, F. M. E.; Cek, M.; Pickard, R.; Botto, H.; Naber, K. G.; Johansen, T. E. J. *World J. Urol.* **2012,** *30,* 51–57. doi:10.1007/s00345-011-0689-9
7. Høiby, N.; Ciofu, O.; Johansen, H. K.; Song, Z.-j.; Moser, C. Ø.; Jensen, P.; Molin, S.; Givskov, M.; Tolker-Nielsen, T.; Bjarnsholt, T. *Int. J. Oral Sci.* **2011,** *3,* 55–65. doi:10.4248/IJOS11026

8. Guggenbichler, J.-P.; Böswald, M.; Lugauer, S.; Krall, T. *Infection (Munich, Ger.)* **1999,** *27* (Suppl. 1), S16–S22. doi:10.1007/BF02561612
9. Samuel, U.; Guggenbichler, J. P. *Int. J. Antimicrob. Agents* **2004,** *23* (Suppl. 1), S75–S81. doi:10.1016/j.ijantimicag.2003.12.004
10. Silver, S. *FEMS Microbiol. Rev.* **2003,** *27,* 341–351. doi:10.1016/S0168-6445(03)00047-0
11. Joyce-Wöhrmann, R. M.; Münstedt, H. *Infection (Munich, Ger.)* **1999,** *27* (Suppl. 1), S46–S48. doi:10.1007/BF02561618
12. Joyce-Wöhrmann, R. M.; Hentschel, T.; Münstedt, H. *Adv. Eng. Mater.* **2000,** *2,* 380–386.
13. Guggenbichler, J. P., private communication, July 1, 2015.
14. Reid, G.; Sharma, S.; Advikolanu, K.; Tieszer, C.; Martin, R. A.; Bruce, A. W. *Antimicrob. Agents Chemother.* **1994,** *38,* 1490–1495. doi:10.1128/AAC.38.7.1490
15. Prithiviraj, B.; Bais, H. P.; Jha, A. K.; Vivanco, J. M. *Plant J.* **2005,** *42,* 417–432. doi:10.1111/j.1365-313X.2005.02385.x
16. Naber, K.; Fünfstück, R.; Hofstetter, A.; Brühl, P.; Hoyme, U. *Chemother. J.* **2000,** *9,* 193–199.
17. Schumm, K.; Lam, T. B. L. *Types of urethral catheters for management of short-term voiding problems in hospitalised adults;* The Cochrane Library: New York, NY, U.S.A., 2008.
18. Lam, T. B. L.; Omar, M. I.; Fisher, E.; Gillies, K.; MacLennan, S. *Types of indwelling urethral catheters for short-term catheterisation in hospitalised adults;* The Cochrane Library: New York, NY, U.S.A., 2014.
19. Heidari Zare, H.; Düttmann, O.; Vass, A.; Franz, G.; Jocham, D. *Biointerphases* **2016,** *11,* 031002. doi:10.1116/1.4955467
20. *An Exposure and Risk Assessment for Silver, EPA Report # 440-8-81017;* U.S. Environmental Protection Agency, USEPA Office for Water: Washington, DC, U.S.A., 1981.
21. *International Risk Information System, Silver, CASRN-7440-22-4;* U.S. Environmental Protection Agency: Washington, DC, U.S.A., 1996. Last revised Jan 12, 1996.
22. Gaul, L. E.; Staud, A. H. *Arch. Dermatol. Syphilol.* **1935,** *32,* 775–779. doi:10.1001/archderm.1935.01470050071011
23. Gaul, L. E.; Staud, A. H. *JAMA, J. Am. Med. Assoc.* **1935,** *104,* 1387–1395. doi:10.1001/jama.1935.02760160011004
24. Lansdown, A. *Silver in Healthcare;* The Royal Society of Chemistry: Cambridge, United Kingdom, 2010.
25. Bier, A. K. Erzeugung substituierter Poly(*p*-xylylen)e durch Gasphasenabscheidung. Ph.D. Thesis, Philipps-Universität, Marburg/Lahn, Germany, 2011.
26. Franz, G.; Schamberger, F. *J. Vac. Sci. Technol., A* **2013,** *31,* 061602. doi:10.1116/1.4816942
27. Gorham, W. F. *J. Polym. Sci.* **1966,** *4,* 3027–3039. doi:10.1002/pol.1966.150041209
28. Franz, G.; Rauter, F.; Dribinskiy, S. F. *J. Vac. Sci. Technol., A* **2009,** *27,* 1035–1041. doi:10.1116/1.3148825
29. Darouiche, O. R.; Raad, I. Antimikrobisch imprägnierte Katheter und medizinische Implantate sowie entsprechende Imprägnierungsverfahren. DE 69633177 T2, Aug 11, 2005.
30. Franz, G.; Schamberger, F.; Kutschera, A.; Seyedi, S.; Jocham, D. Strukturierte Beschichtung eines Substrats. German Patent Disclosure DE 10 2012 023 349.3, Nov 29, 2012.
31. Franz, G.; Schamberger, F.; Jocham, D. Schichtstruktur zur Abgabe mindestens eines Wirkstoffes. German Patent Disclosure DE 10 2012 023 343.3, Nov 29, 2012.
32. Schwedtlick, K. *Organikum,* 11th ed.; VEB Deutscher Verlag der Wissenschaften: Berlin, Germany, 1973.
33. Ganguli, S.; Agrawal, H.; Wang, B.; McDonald, J. F.; Lu, T.-M.; Yang, G.-R.; Gill, W. N. *J. Vac. Sci. Technol., A* **1997,** *15,* 3138–3142. doi:10.1116/1.580858
34. Yang, G.-R.; Ganguli, S.; Karcz, J.; Gill, W. N.; Lu, T.-M. *J. Cryst. Growth* **1998,** *183,* 385–390. doi:10.1016/S0022-0248(97)00428-4
35. Bröskamp, S. F.; Redka, D.; Möhlmann, A.; Franz, G.; Jocham, D. *AIP Adv.* **2017,** *7,* 075005. doi:10.1063/1.4994678
36. Bi, X.; Crum, B. P.; Li, W. *J. Microelectromech. Syst.* **2014,** *23,* 628–635. doi:10.1109/JMEMS.2013.2283634
37. Franz, G.; Schamberger, F.; Voss, D. Druckgesteuerte Abscheiderate. German Patent Disclosure DE 2012 014 915.8, July 29, 2012.
38. *Gwyddion,* v02; Gwyddion, 2012, http://www.gwyddion.net.
39. Schamberger, F.; Ziegler, A.; Franz, G. *J. Vac. Sci. Technol., B* **2012,** *30,* 051801. doi:10.1116/1.4740049
40. Heidari Zare, H.; Sudhop, S.; Schamberger, F.; Franz, G. *Biointerphases* **2014,** *9,* 031002. doi:10.1116/1.4876736
41. Heidari Zare, H.; Juhart, V.; Vass, A.; Franz, G.; Jocham, D. *Biointerphases* **2017,** *12,* 011001. doi:10.1116/1.4974197
42. Rose, C.; Parker, A.; Jefferson, B.; Cartmell, E. *Crit. Rev. Environ. Sci. Technol.* **2015,** *45,* 1827–1879. doi:10.1080/10643389.2014.1000761
43. Kark, R.; Lawrence, J.; Pollack, V. *A primer of urinalysis,* 2nd ed.; Harper & Row, Publishers: New York, NY, U.S.A., 1964.
44. ICP-OES and ICP-MS Detection Limit Guidance — EAG Laboratories. http://www.eag.com/icp-oes-and-icp-ms-detection-limit-guidance/ (accessed Aug 24, 2017).
45. Wang, R.; Neoh, K. G.; Kang, E.-T.; Tambyah, P. A.; Chiong, E. *J. Biomed. Mater. Res., Part B* **2015,** *103,* 519–528. doi:10.1002/jbm.b.33230
46. Matsumura, Y.; Yoshikata, K.; Kunisaki, S.-i.; Tsuchido, T. *Appl. Environ. Microbiol.* **2003,** *69,* 4278–4281. doi:10.1128/AEM.69.7.4278-4281.2003
47. Morones, J. R.; Elechiguerra, J. L.; Camacho, A.; Holt, K.; Kouri, J. B.; Ramìrez, J. T.; Yacaman, M. J. *Nanotechnology* **2005,** *16,* 2346–2353. doi:10.1088/0957-4484/16/10/059
48. Kim, J. S.; Kuk, E.; Yu, K. N.; Kim, J.-H.; Park, S. J.; Lee, H. J.; Kim, S. H.; Park, Y. K.; Hwang, C.-Y.; Kim, Y.-K.; Lee, Y.-S.; Jeong, D. H.; Cho, M.-H. *Nanomedicine* **2007,** *3,* 95–101. doi:10.1016/j.nano.2006.12.001
49. Prabhu, S.; Poulose, E. K. *Int. Nano Lett.* **2012,** *2,* 32. doi:10.1186/2228-5326-2-32
50. Kaganer, K. G.; Ploog, K. H.; Sabelfeld, K. K. *Phys. Rev. B* **2006,** *73,* 115425. doi:10.1103/PhysRevB.73.115425
51. Errede, L. A.; Hoyt, J. M. *J. Am. Chem. Soc.* **1960,** *82,* 436–439. doi:10.1021/ja01487a047
52. Errede, L. A.; Gregorian, R. S.; Hoyt, J. M. *J. Am. Chem. Soc.* **1960,** *82,* 5218–5223. doi:10.1021/ja01504a048
53. Kramer, P.; Sharma, A. K.; Hennecke, E. E.; Yasuda, H. *J. Polym. Sci., Polym. Chem. Ed.* **1984,** *22,* 475–491. doi:10.1002/pol.1984.170220218
54. Yasuda, H. K.; Yeh, Y. S.; Fusselman, S. *Pure Appl. Chem.* **1990,** *62,* 1689–1698. doi:10.1351/pac199062091689
55. Boehm, G.; Katz, S.; Meyer, R.; Amann, M.-C. *J. Cryst. Growth* **2009,** *311,* 1932–1934. doi:10.1016/j.jcrysgro.2008.10.082
56. Cariou, F. E.; Valley, D. J.; Loeb, W. E. *IEEE Trans. Parts, Mater. Packag.* **1965,** *1,* 54–62. doi:10.1109/TPMP.1965.1135388
57. Beach, W. F. *Macromolecules* **1978,** *11,* 72–76. doi:10.1021/ma60061a014

58. Fortin, J. B.; Lu, T.-M. *Chem. Mater.* **2002,** *14,* 1945–1949. doi:10.1021/cm010454a
59. Semlyen, J. A. *Adv. Polym. Sci.* **1976,** *21,* 41–75. doi:10.1007/3-540-07727-8_3
60. Reichel, A. J.; Franz, G.; Amann, M.-C. *Coatings* **2015,** *5,* 142–171. doi:10.3390/coatings5020142
61. Ziegler, A. Investigation of Physical Parameters of Polyparylene. Master Thesis, Munich University of Applied Sciences, Munich, Germany, 2011.
62. Olson, R. Xylylene Polymers. *Encyclopedia of Polymer Science and Engineering,* 2nd ed.; Wiley: New York, NY, U.S.A., 1989; Vol. 17, pp 990–1024.
63. Broer, D. J.; Luijks, W. *J. Appl. Polym. Sci.* **1981,** *26,* 2415–2422. doi:10.1002/app.1981.070260727
64. Tolstopyatov, E. M. *J. Phys. D: Appl. Phys.* **2002,** *35,* 1516–1525. doi:10.1088/0022-3727/35/13/311
65. Tolstopyatov, E. M.; Yang, S. H.; Kim, M. C. *J. Phys. D: Appl. Phys.* **2002,** *35,* 2723–2730. doi:10.1088/0022-3727/35/21/306
66. Franz, G.; Heidari Zare, H.; Resch, K. Heiße CVD-Abscheidung. German Patent Disclosure DE 10 2014 019, Dec 19, 2014.
67. Behra, R.; Sigg, L.; Clift, M. J. D.; Herzog, F.; Minghetti, M.; Johnston, B.; Petri-Fink, A.; Rothen-Rutishauser, B. *J. R. Soc., Interface* **2013,** *10,* 20130396. doi:10.1098/rsif.2013.0396
68. Brooks, T.; Keevil, C. W. *Lett. Appl. Microbiol.* **1997,** *24,* 203–210. doi:10.1046/j.1472-765X.1997.00378.x

License and Terms